

Carnegie Mellon University
MELLON COLLEGE OF SCIENCE

THESIS

SUBMITTED IN PARTIAL FULFILLMENT OF THE REQUIREMENTS
FOR THE DEGREE OF

DOCTOR OF PHILOSOPHY IN THE FIELD OF PHYSICS

TITLE: "Thermodynamics from First Principles: Prediction of Phase Diagrams
and Materials Properties Using Density Functional Theory."

PRESENTED BY: William Huhn

ACCEPTED BY THE DEPARTMENT OF PHYSICS

| | |
|--------------------------------|----------|
| Michael Widom | 5/5/2014 |
| <hr/> | |
| MICHAEL WIDOM, CHAIR PROFESSOR | DATE |

| | |
|---------------------------|----------|
| Stephen Garoff | 5/5/2014 |
| <hr/> | |
| STEPHEN GAROFF, DEPT HEAD | DATE |

APPROVED BY THE COLLEGE COUNCIL

| | |
|-------------------|----------|
| Fred Gilman | 5/5/2014 |
| <hr/> | |
| FRED GILMAN, DEAN | DATE |

**Thermodynamics from First Principles:
Prediction of Phase Diagrams and
Materials Properties Using Density
Functional Theory**

by

William Paul Huhn

Submitted in partial fulfillment of the
requirements for the degree of
Doctor of Philosophy
at
Carnegie Mellon University
Department of Physics
Pittsburgh, Pennsylvania

Advised by Professor Michael Widom

April 28th, 2014

Abstract

First principles calculations have become one of the main computational methods in condensed matter physics and physical chemistry due to their high degree of accuracy without the usage of any fitting parameters. Interest has been growing in the engineering disciplines to exploit these properties to predict new materials with desired material properties, greatly accelerating the prototyping of materials over experimental methods with a degree of accuracy not found in other computational methods. In this thesis, first principles calculations will be applied to understand material properties of four classes of chemical systems with promising mechanical or thermodynamic applications, but whose experimental characterizations are either incomplete or questionable: boron carbide, molybdenum-niobium-tantalum-tungsten, copper-palladium-sulfur, and various early-late transition metal alloys. For all classes, the phase stability will be examined, of particular interest B-C and Mo-Nb-Ta-W due to the controversy surrounding the phase diagram of the former and the interesting “high-entropy alloy” behavior of the later. In addition, for Cu-Pd-S, various thermodynamic quantities associated with resistance to sulfur poisoning will be calculated, and for the early-late transition metal alloys, the elasticity will be examined, with attention paid towards possible transferability to the field of amorphous materials. All four of these disparate systems show overall semi-quantitative agreement with known experimental results, highlighting the versatility of first principles calculations.

Acknowledgments

We thank Nathalie Vast, Helmut Werheit and Koun Shirai for useful discussions regarding boron carbide.

We thank Marek Mihalkovič and Michael Gao for useful discussions regarding high entropy alloys. This work was supported in part by grant DTRA1-11-1-0064.

We would like to thank our fellow collaborators Andrew M. Cheung, Gary J. Shiflet, S. Joseph Poon, and John Lewandowski on elasticity of transition metal alloys. This work was funded by DOD-DTRA under contract number DTRA-11-1-0064.

We thank Brian Gleeson, Marek Mihalkovič, and John Kitchin for useful discussion regarding sulfidization of copper-palladium membranes. This work was performed in support of the Fuels Program of Strategic Center for Coal at DOE National Energy Technology Laboratory under the RES contract DE-FE0004000.

I would also like to thank my doctoral committee: Michael Widom (chair), John Kichin, Sara Majetich, and Robert Suter.

Contents

| | | |
|----------|--|----------|
| 1 | Introduction | 1 |
| 1.1 | The Trouble With Trials: Why Computational Studies Are Necessary For Materials Research | 1 |
| 2 | Formalism and Methods | 7 |
| 2.1 | Density Functional Theory | 7 |
| 2.1.1 | The Problem | 7 |
| 2.1.2 | Slater Determinants and Single Particle Wavefunctions | 8 |
| 2.1.3 | The Hohenberg-Kohn Equations | 11 |
| 2.1.4 | The Kohn-Sham Equations | 14 |
| 2.1.5 | Exchange and Correlation | 16 |
| 2.1.6 | Basis Sets In Density Functional Theory | 21 |
| 2.1.7 | Motion of the Nuclei: Forces and Phonons | 26 |
| 2.2 | Phase Stability and Phase Diagrams | 30 |
| 2.2.1 | A Brief Review of Thermodynamics and Statistical Mechanics | 30 |
| 2.2.2 | Thermodynamic Quantities | 31 |
| 2.2.3 | Consequences of the Four Laws of Thermodynamics | 32 |
| 2.2.4 | Entropy Maximization, Stability Conditions, and Equilibrium | 33 |
| 2.2.5 | Legendre Transforms and Free Energies | 35 |
| 2.2.6 | Stability of Free Energies and Additional Thermodynamic Quan- tities | 37 |

| | | |
|----------|---|-----------|
| 2.2.7 | Ensemble Averages, the Microcanonical Ensemble, and the Ideal Solution | 38 |
| 2.2.8 | The Canonical Ensemble | 42 |
| 2.2.9 | The Partition Function in Detail | 43 |
| 2.3 | The (Classical) Theory of Phase Transitions and Free Energy Modeling | 47 |
| 2.3.1 | Phase Transitions: An Overview | 48 |
| 2.3.2 | Phase Competition and Free Energy Minimization | 48 |
| 2.3.3 | Phase Segregation, Coexistence, and the General Behavior of Phase Transitions | 50 |
| 2.3.4 | The Landau Formalism for Phase Transitions | 52 |
| 2.3.5 | Free Energy Modeling | 56 |
| 2.3.6 | The Convex Hull | 65 |
| 2.4 | Ensemble Average Approaches: Monte Carlo and Molecular Dynamics | 67 |
| 2.4.1 | Ensemble Average Approaches for Phase Transitions: An Overview | 67 |
| 2.4.2 | The “Modern” Theory of Phase Transitions and Critical Exponents | 69 |
| 2.4.3 | Metropolis Monte Carlo and Molecular Dynamics | 72 |
| 2.4.4 | Finite Size Effects | 75 |
| 3 | On the Structure of Boron Carbide | 78 |
| 3.1 | What is Boron Carbide? | 78 |
| 3.2 | What Does Density Functional Theory Predict for Boron Carbide? | 85 |
| 3.3 | Method 1: Partition Function Enumeration | 85 |
| 3.3.1 | First Principles Total Energy Calculations | 85 |
| 3.3.2 | Configurational Free Energy via the Partition Function | 87 |
| 3.4 | Method 2: Analytic Free Energy Models | 92 |
| 3.4.1 | The Free Energy Models | 92 |
| 3.4.2 | $T \rightarrow 0$ K Limit | 96 |
| 3.4.3 | Analytic $T = \infty$ Limit | 100 |

| | | |
|----------|--|------------|
| 3.4.4 | Results of the Free Energy Models | 100 |
| 4 | On the Stability of the High-Entropy Alloy Mo-Nb-Ta-W | 104 |
| 4.1 | The High-Entropy Alloy Mo-Nb-Ta-W: A Vague Phase Diagram . . . | 104 |
| 4.2 | A Pairwise Bond Model | 108 |
| 4.3 | A Search for the T=0 K States | 110 |
| 4.3.1 | Mo-Nb | 111 |
| 4.3.2 | Mo-Ta | 113 |
| 4.3.3 | Mo-W and Nb-Ta | 113 |
| 4.3.4 | Nb-W | 114 |
| 4.3.5 | Ta-W | 114 |
| 4.3.6 | T=0 K Mo-Nb-Ta-W | 115 |
| 4.4 | Hybrid Monte Carlo/Molecular Dynamics | 115 |
| 4.5 | A Proposed Nearest Neighbor Model and Its Mean Field Reduction . | 121 |
| 4.6 | Results of the Mean Field Model | 125 |
| 4.7 | Results of Monte Carlo Simulations | 130 |
| 5 | On the Elasticity of Transition Metal Alloys | 136 |
| 5.1 | Elasticity of Transition Metal Alloys: Too Many Phase Diagrams . . | 136 |
| 5.2 | The Basics: Elasticity | 141 |
| 5.3 | The Raw Data | 143 |
| 5.3.1 | Structures | 145 |
| 5.3.2 | Convex Hulls | 147 |
| 5.3.3 | Binary Elastic Moduli | 150 |
| 5.4 | Trends in the Data | 152 |
| 5.4.1 | Force Constants and COHP | 156 |
| 5.4.2 | Microstructural Details: Ternaries and Quaternaries | 157 |
| 6 | On Bulk Sulfidization of the Cu-Pd System | 162 |

| | | |
|----------|---|------------|
| 6.1 | Sulfidization of Copper-Palladium Membranes: What Do These Numbers Mean? | 162 |
| 6.2 | What Does Density Functional Theory Predict? | 166 |
| 6.3 | Proposed Ternary Phase Diagrams | 173 |
| 6.4 | Two Phases of Interest: Pd ₄ S and Pd ₁₆ S ₇ | 181 |
| 6.4.1 | Electronic Structure | 184 |
| 6.5 | Sulfidization Thresholds and Predominance Diagrams | 185 |
| 6.6 | Activity Calculations | 189 |
| 7 | Summary, Difficulties, And Future Outlook | 193 |
| 7.1 | The Structure of Boron Carbide | 193 |
| 7.1.1 | A New Phase? | 195 |
| 7.2 | The Stability of the High-Entropy Alloys Mo-Nb-Ta-W | 197 |
| 7.3 | Elasticity of Transition Metal Alloys | 199 |
| 7.4 | Bulk Sulfidization of the Cu-Pd System | 201 |

List of Tables

| | | |
|-----|--|-----|
| 3.1 | Table of low ΔE structures for pure elements and the hexagonal boron carbide cell. In our naming scheme, adapted from the primitive cell, sites listed are those containing carbons. t and t' denotes the two ends of the chain (so that tt' denotes a C-B-C chain), $p\{0,1,2\}$ denotes the polar atoms on the "north" side of the icosahedra, $p'\{0,1,2\}$ denotes the polar atoms on the opposite ("south") side of the icosahedra. Likewise $e\{0,1,2\}$ and $e'\{0,1,2\}$ denotes the atoms just to the north and south of the equator. Ω is the multiplicity. | 88 |
| 3.2 | Parameters for the rhombohedral phase obtained from first principles calculations. | 101 |
| 4.1 | Optimal structures and enthalpies for pairwise interactions at 50-50% composition. Elements are ordered in decreasing atomic volume. Pearson symbol of stable compound followed by negative enthalpy of formation (units meV/atom). | 109 |
| 4.2 | Nearest neighbor bond strengths $b_{\alpha\beta}$ used in modeling the Mo-Nb-Ta-W BCC phase, in units of meV/atom. | 126 |
| 4.3 | The eigenvalues and associated eigenvectors of θ using bond strengths given in Table 4.2. λ is in units of meV/atom. The final column is the selected dependent species and is not part of the associated eigenvector; it is shown here to give physical intuition to how the particular mode is ordering the system. | 127 |

| | | |
|-----|--|-----|
| 5.1 | Structure types considered listing common prototype, and Strukturbericht and Pearson notations. Frank-Kasper phases list common names. * indicates symmetry-breaking distortion. "Non-FK" indicates non-canonical Frank-Kasper phase containing CN=10 Bernal Hole. The final column contains a list of coordination numbers from Voronoi polyhedra appearing in the structure [1, 2, 3]. | 146 |
| 5.2 | Measures of anisotropy for materials of interest. $A_G = A_E = 1$ for cubic structures. | 153 |
| 5.3 | Correlation coefficients for linear regressions involving elastic moduli and thermodynamic quantities of interest, where rows denote independent variables and columns dependent variables for a given regression. | 153 |
| 5.4 | Data for tI12. R are average bond lengths for nearest neighbors under 4 Å. k are averaged over atoms (i.e. weighted by the number of bonds per atom) in units $\text{eV}/\text{Å}^2$, ρ_{COHP} is iCOHP volume density in units $\text{eV}/\text{Å}^3$, and K is the calculated bulk moduli in units GPa. | 156 |
| 5.5 | Elastic moduli for pure elements and binary hR13 structures. | 158 |
| 5.6 | Comparison of calculated ternary and quaternary hR13 moduli with averaged values of binaries. Moduli are given in GPa, and deviations in percentages. | 160 |
| 6.1 | A partial list of calculated structures, focusing on "base" structures with no substitutions. All energetic quantities are given in units of meV/atom. $\text{Cu}_2\text{Pd}_3\text{S}_4$ is a hypothetical structure based on $\text{Cu}_2\text{Pd}_3\text{Se}_4$.mP18 [4]. Cu.cI2 and CuPd.cP2 are hypothetical structures used to model the β -CuPd phase. ΔH and dE are defined in eqs. 6.8 and 6.9 | 171 |
| 6.2 | A list of substitutions into binary structures to produce ternary structures. Only low enthalpic cost substitutions are shown. Impurity concentration denotes the concentration in the appropriate sublattice, not concentration in the structure as a whole. | 178 |

| | | |
|-----|--|-----|
| 6.3 | Description of our phase models. γ denotes the number concentration of the sublattice in the total lattice and is used for scaling the entropic contribution to energy (see equation 6.7). "Phonon concentrations" denotes the concentrations for which phonon free energies were calculated. x denotes the copper composition. | 179 |
| 6.4 | Sulfidization threshold pressures for the Pd-S ₂ system. Calculated values with and without phonon contributions are separately shown. Values * are liquid experimentally, but were extrapolated from the solid region of the predominance diagram for comparison purposes. ** not indicated in experimental results. | 188 |

List of Figures

| | | |
|-----|--|-----|
| 3.1 | Assessed phase digram of the boron carbide system [5]. | 79 |
| 3.2 | The two predicted 0 K structures. Green denotes borons, grey denotes carbons on the chain terminator sites, and pink denotes carbons on polar sites. | 81 |
| 3.3 | Cohesive energies of boron carbide structures. Heavy black circles at $x_C = 0.133$ and 0.20 , respectively, correspond to the ideal $B_{13}C_2$ and B_4C structures displayed in Figure 3.2. Data points in blue have $0 < \Delta E < 0.015$ eV/atom, while red has 0.015 eV/atom $< \Delta E$ | 87 |
| 3.4 | Heat capacities for $\delta\mu$'s of interest. | 91 |
| 3.5 | Components of free energy model. Details in text. | 95 |
| 3.6 | Predicted phase boundaries for our model using calculated parameters as listed in Table 3.2 and a selection of values of β . Line compounds are β -boron at $x = 0$, graphite (not shown) at $x = 1$ and monoclinic boron carbide at $x = 3/15$. Carbon-rich phase boundaries of rhombohedral boron carbide are shown as solid lines, while boron-rich phase boundaries are shown as dashed lines. | 102 |

| | | |
|-----|--|-----|
| 4.1 | First principles enthalpies of formation for binaries. Black squares denotes structures on the convex hull, blue squares denotes structures within 2 meV/atom of the convex hull, and red squares above 2 meV/atom. Filled green diamonds denote 16 atom BCC SQS structures [6]. The scales of Mo-W and Nb-Ta differ from the scales from the other four binaries. | 112 |
| 4.2 | Monte Carlo acceptance rates (ratio of accepted to attempted species swaps) for each species pair vs. temperature. | 117 |
| 4.3 | Partial density functions obtained from MC/MD for the Mo-Nb-Ta-W BCC phase, showing first and second nearest neighbors. Solid lines denote PDFs between species from differing groups, dashed lines between differing species from the same group, and dotted lines between the same species. The main figure shows results for 300 K, and the inset for 1800 K. | 119 |
| 4.4 | The vertex sublattice occupancy as a function of temperature for the mean field model. See text for information on inset. | 128 |
| 4.5 | The normal coordinates of the system as function of temperature. . . | 129 |
| 4.6 | The vertex sublattice occupancy as a function of temperature for our Monte Carlo simulations. | 131 |
| 4.7 | Comparison of Mo and Ta vertex occupancies to the expected form for the order parameter in a 3D Ising model. The red line denotes an estimate for the behavior of the order parameter at critical temperature 1280 K with the expected 3D Ising critical exponent $\beta = 0.327$ | 132 |
| 4.8 | Specific heat as a function of temperature for various supercell sizes. . | 133 |
| 4.9 | The specific heat peak height as a function of supercell dimension. The green line denotes a fit to an exponential scaling law with both the prefactor and exponent free to vary, and red a fit imposing the expected 3D Ising critical exponent $\alpha/\nu = 0.175$ | 134 |

| | | |
|-----|--|-----|
| 5.1 | Frank-Kasper Voronoi polyhedra, listing coordination numbers and polyhedron codes. | 140 |
| 5.2 | Stacked bar chart of Honeycutt-Andersen common neighbor statistics [7, 8]. | 145 |
| 5.3 | Enthalpies of formation for (Co,Ni)-(Ta,W) alloys. Values for Ta shown in black, for W shown in green. Plotting symbols explained in text. . | 148 |
| 5.4 | Elastic moduli for (Co,Ni)-(Ta,W) compounds. Lines show CPA estimates. Data points are our DFT calculations. Asterisks are experimental values from our experiments on Ni-Ta alloys and from the literature for pure elements. | 151 |
| 5.5 | Calculated Poisson ratios. Dashed line at $\nu=0.32$ is putative threshold for ductility. | 155 |
| 5.6 | Electronic densities of states for hR13 structures. Line segments indicate the mean and standard deviations of the element projected <i>d</i> -bands. | 158 |
| 6.1 | Binary enthalpies of formation for Pd-S, Cu-S, and Cu-Pd. The x axis corresponds to concentration, and y axis corresponds to enthalpy of formation. Black symbols denote stable structures, blue correspond to structures within 3 meV of the convex hull, and red to structures above 3 meV. Circles with thick borders are known low temperature stable structures, circles with thin borders are known high temperature stable structures, and squares denotes all other cases (including hypothetical structures). For Cu-Pd, to better distinguish phases, filled symbols corresponding to bcc structures, empty symbols to fcc, and dashed for the three other structures (Cu ₃ Pd.tP28, Cu ₄ Pd.tP20, and the SQS configuration for fcc at 50% Pd). | 172 |
| 6.2 | Crystal structures for P ₄ S.tP10 and P ₁₆ S ₇ .cI46. The unit cells are outlined. Atomic sizes indicate vertical height. | 174 |

| | | |
|-----|---|-----|
| 6.3 | The calculated $T = 0$ K phase diagram for the Cu-Pd-S system. Plotting symbols as in Fig. 6.1. | 177 |
| 6.4 | The experimental phase diagram for the Cu-Pd-S system at $T = 673$ K, and our calculated phase diagram. | 180 |
| 6.5 | The experimental phase diagram for the Cu-Pd-S system at $T = 823$ K, and our calculated phase diagram. | 180 |
| 6.6 | Comparison for the enthalpy of formations for filling 8c sites versus filling 24g sites in $\text{Pd}_{16}\text{S}_7\text{cI46}$ | 182 |
| 6.7 | Calculated electronic densities of states for $\text{Pd}_{16}\text{S}_7\text{cI46}$ with copper substitutions at the palladium 8c sites. Dashed lines indicate the Fermi level E_F . The inset shows the DOS relative to E_F and enlarges the pseudogap region. | 184 |
| 6.8 | The chemical potential of S_2 dimers. Black is NIST-JANAF, and red is our linear fit. | 187 |
| 6.9 | Activities of Pd in the Cu-Pd binary. First principles results are denoted with solid lines, and CALPHAD with dashed lines. | 192 |

Chapter 1

Introduction

1.1 The Trouble With Trials: Why Computational Studies Are Necessary For Materials Research

Material research's fundamental problem is that nature loves diversity. The statement "a system consists of N_C carbon atoms in a solid state" is useless. A given collection of atoms can arrange themselves into a variety of phases, different configurations of atoms with different periodic lattices, or perhaps no lattice at all, and these configurations can have dramatically different properties. Carbon in the graphite phase (a layered hexagonal structure with interlayer van der Waals bonding and intralayer sp^2 bonding) is soft enough to form pencil lead, but carbon in the diamond phase (a diamond structure with sp^3 bonding) is one of the hardest materials known to man.

For practical applications, it is necessary to know what phase is *expected* to be present at a given set of conditions, that is, which phase is "stable". The stable phase is the phase that minimizes the free energy of the system at those conditions. However, this does not preclude the existence of other phases. Using the previous example, diamond is only stable at high pressure, and graphite is stable at standard atmospheric conditions. Diamonds should eventually decompose into graphite, but diamonds are

still able to command a premium as they are sufficiently ‘metastable’ to buy and sell. Although eventually diamonds will undergo a phase transition into graphite, the probability of observing this event in a human lifetime is vanishingly small. A precise definition of metastability is rather hard to come by, as it is by definition a non-equilibrium property. Equilibrium statistical mechanics, the framework that predicts structural stability, exists in the infinite time, infinite volume limit. Under such conditions, a phase is either stable or unstable for a given set of conditions, and different phases will be stable under different conditions. If there is a phase with a lower free energy than the phase the system is currently in, a phase transition to the lower free energy phase will occur in the infinite time limit.

It may be objected that, if metastability exists, why bother worrying about true thermodynamic stability? If carbon atoms are arranged into a diamond structure, and they will continue to remain in a diamond structure for the remainder of our lifetimes, why worry about it? While it is true that under relatively static conditions, metastable structures will continue to be metastable, their metastability is due to inhabiting local free energy minimums in the free energy landscape, whereas stable structures are the global free energy minimums in the free energy landscape under a particular set of conditions¹. Small distortions of a metastable phase are energetically unfavorable, and when made the system will eventually return to the metastable phase. However, if a metastable phase undergoes a large enough distortion, it is possible to move far enough from the local energy minimum that the system will not return to the metastable phase; it has overcome the free energy barrier keeping it in the metastable phase. Thus metastable phases can be destabilized by large external shocks of some kind to the system, whether it be mechanical shock, rapid changes in temperature, large chemical potential gradients, and so on. But for systems in a stable phase, that they reside in global free energy minimums favors the system

¹Commonly, a phase that is stable for one set of conditions (i.e. the global minimum) will be metastable under conditions where it is not stable (i.e. it will convert into a local minimum).

returning to its original configuration after a shock.

So why are computations necessary for determining if a particular phase is stable? Why not measure what phase the system is in? The first reason has already been given. Just because a particular phase is experimentally observed does not mean that it is stable. To determine the stability of a phase, it is necessary to find its free energy and show that out of all possible phases, it is this phase that has the lowest free energy, a process known as “free energy minimization”. Computations can be used to determine the free energy for a system directly, as they can directly yield the total energy, the total energy’s pressure dependence, phonon band structure, electronic state occupations, and other such quantities that can be used to calculate the free energy for a given phase. Determination of these quantities from experiments, on the other hand, are always constrained by the particular technique used, and it may be difficult to compare quantities derived from different techniques. Even though first principles calculations may end up being inaccurate, the various quantities used to derive free energy models are calculable (at least in principle) and internally consistent.

The second reason is that experimental identification of a phase is non-trivial. Growing a single phase experimentally is possible for relatively few phases, and this process is often arcane.² For such phases, Bragg diffraction patterns may be easily indexed to identify the phase. Most determinations of phase existence come from powders, yielding angle-averaged diffraction which is hard to index to uniquely determine the phase. There may be multiple phases within a material which, when combined, mimic another phase. Or there may be a single phase that mimics a mixture of phases. Or the experimental apparatus may add a spurious peak. Or a particular sample may have a defect that eliminates a peak. Or maybe the growth chamber really does not like Mondays. The list goes on. Structural determination is more of an art than the science we wish it were. What is commonly done to narrow

²Crystal growth lies somewhere between an art and alchemy, with otherwise sane and rational individuals making bizarre statements like a given growth chamber “liking” Mondays.

down the possible candidates for phase identification is to assume only *known* stable and metastable phases are possible, and match peaks accordingly. It is possible for bad results to seep into the literature in this way. A group incorrectly predicts a phase to exist. Other groups use that phase's Bragg patterns or diffraction peaks for phase matching. Upon (incorrectly) finding that phase in their material as well, they propagate the m \hat{e} me of the phase's stability further. Accurate structural determination is difficult enough to do with "binaries", phases containing only two chemical species. For "ternaries" and higher, it becomes virtually impossible, and the literature on ternaries is relatively small and treated skeptically. Whereas most possible binary phase diagrams have been published, relatively few ternary phase diagrams exist.

There is no possible ambiguity in structure determination with computational methods. The phase under consideration for stability is determined in advance, and there is no difficulty handling three or more chemical species. However, this requires one either know the candidate phases for stability or have some notion of what they might be. This is especially troublesome when calculating ternary (or higher) phase diagrams. This is one major issue confronting computational materials research, but it is not as major an impediment as it appears at first glance. Often insight can be gained into a particular chemical family by examining chemical families with similar chemistries that are better understood (i.e. substituting Ni for Co, both fourth row late transition metals). Computational prediction of new phases is a growing field, and in practice reliable interpretation of experimental results also requires the experimentalist to have some previous knowledge about candidate phases.

The previous two issues combined gave rise to an embarrassment in the materials literature. There are many experimentally assessed phase diagrams that have some feature(s) that violate the laws of thermodynamics and must therefore be incorrect. Okamoto [9] has tabulated 20 such commonly observed features (and 3 that are not formally forbidden but are suspect) in phase diagrams peer-reviewed and accepted in the literature. This is a serious problem for materials research, as the initial input

for materials research is frequently some form of phase diagram. The confidence in binary phase diagrams was shattered. Computational research has helped rebuild confidence by resolving issues with experimental phase diagrams.

The third reason is more practical in origin. Experimental methods take time. Machines that perform very specific experimental techniques can cost millions of dollars. An experimentalist must carefully plan in advance what material she³ will examine, as she will likely be spending months if not years looking at that material, and she might need a capital investment to do so. Graduate students can take years to perfect a method to grow one particular phase.

On the other hand, the computational researcher can move from material to material nearly at will. He can try new materials on a hunch. He can scan through databases of thousands or even millions of materials to find the diamond in the rough. He only requires one capital investment at any given time: an increase in the resource currently bottlenecking calculations (usually number of processors, memory capacity/bandwidth, or graduate students). He does not need to worry about wasted capital investments nearly as much as the experimentalist. There will always be some future application that will make use of the present investment in capital. The only specialized training the junior computational researcher needs is computer programming and knowledge of computational algorithms, and this training is highly transferable.

The computational researcher's main advantage is his versatility. Such versatility is meaningless if his computations have poor predictive value. This was the case for most of the 20th century, limiting computational research to basic science research and a lot of toy models. What computational materials research was possible lagged behind experiment, as it was necessary to use experimental data as input into the calculations to obtain any degree of accuracy. With the advent of quantum chemistry codes, in particular the relatively efficient density functional theory, computational

³Gender has been assigned using a random number generator.

materials research underwent a radical transformation. Density functional theory can be used to perform first principles calculations, that is, calculations with no fitted parameters and some degree of accuracy. While the accuracy of first principles methods depends on the chosen approximation and the system under consideration, first principles calculations have proven successful enough that experimentalists have come to rely on computational researchers to predict new candidate systems, rather than the other way around.

My thesis will be organized as follows. I will give a brief explanation of the formalism underlying density functional theory. I will next move to the formalism and practical implementation of phase stability and phase transitions, using both free energy modeling and ensemble averaging. Finally, I will present my results. Representative of computational materials research, I have not spent time narrowly focused on one particular subject, and thus my “thesis” is better describe as a body of work rather than a single document: the phase diagram of boron carbide, phase stability in high entropy alloys, elasticity of early-late transition metal alloys, and sulfidization of copper-palladium membranes. Though diverse in origin, all have the common theme of calculating materials properties, with a special focus on thermodynamic quantities, from first principles.

Chapter 2

Formalism and Methods

2.1 Density Functional Theory¹

2.1.1 The Problem

The time-independent Schrödinger equation (1926) for N particles is

$$\left(\sum_{j=1}^N -\frac{\hbar^2}{2m_j} \nabla_{\mathbf{r}_j}^2 + V(\mathbf{r}_1, \mathbf{r}_2, \dots, \mathbf{r}_N) \right) \Psi(\mathbf{r}_1, \mathbf{r}_2, \dots, \mathbf{r}_N) = E\Psi(\mathbf{r}_1, \mathbf{r}_2, \dots, \mathbf{r}_N), \quad (2.1)$$

where $\hbar \approx 6.582 \times 10^{-16} \text{ eV} \cdot \text{s}$ is Planck's constant, m_j is the mass of particle j , \mathbf{r}_j is the position operator of particle j , and V is the potential of the system. This is the only known equation governing the behavior of nature for stationary states in the non-relativistic limit. Here only the time-independent Schrödinger equation will be used and will be referred to as “the” Schrödinger equation, and the wavefunction will always be expressed in the position representation $\Psi = \Psi(\{\mathbf{r}_i\})$.

In theory, one can completely determine the evolution of any condensed matter system using this equation and standard differential equation techniques. However,

¹Excellent books and review articles on density function theory include [10, 11, 12, 13], and in particular Martin [14] whose notation will mostly be used here, and, for more general condensed matter references, [15, 16].

the wavefunction in this form depends on the spatial coordinates of every particle in the system, each additional particle adding four degrees of freedom, three for position and one for spin. Neglecting the spin degree of freedom for the moment, for a single gram of carbon-12, by definition there are Avagadro’s number of nucleons, $N_{av} = 6.022 \times 10^{23}$, and N_{av} electrons. The associated Schrödinger equation would have 3.613×10^{24} coordinates to solve over, making such a brute force method completely intractable.

The first simplification is the Born-Oppenheimer approximation (1927). Due to the mass ratio between electrons and nucleons, the time scales of the dynamics decouple and the wavefunction is decomposable into a product of nuclear and electronic wavefunctions. From the standpoint of the electronic properties of the system, the nucleons may be merged into fixed point-like nuclei² and Equation 2.1 may be taken to refer exclusively to electrons, the nuclei relegated to the potential function. For a gram of carbon-12, there are still N_{av} electrons and thus $3N_{av}$ degrees of freedom, and this equation is still not suitable for computation.

2.1.2 Slater Determinants and Single Particle Wavefunctions

The major difficulty in computing the wavefunction is that it is a “many-particle” wavefunction. However, electrons are indistinguishable fermions and satisfy the Pauli exclusion principle (antisymmetry). Formally, the wavefunction reverses sign under the interchange of any two position operators,

$$\Psi(\mathbf{r}_1, \dots, \mathbf{r}_m, \dots, \mathbf{r}_n, \dots, \mathbf{r}_N) = -\Psi(\mathbf{r}_1, \dots, \mathbf{r}_n, \dots, \mathbf{r}_m, \dots, \mathbf{r}_N). \quad (2.2)$$

Inspired by the method of separation of variables, Slater (1929) suggested that the many-particle wavefunction may be approximated as sums and differences of products

²In pseudopotential methods, one freeze core states onto the nuclei and treats them as one unit, and thus it is common to refer to nuclei as ions. As a nucleus is a fully ionized ion, this usage may be rather odd in certain cases but is technically correct, the best kind of correct, and this terminology will be used from here on.

of functions,

$$\psi_1(\mathbf{r}_1)\psi_2(\mathbf{r}_2)\dots\psi_N(\mathbf{r}_N). \quad (2.3)$$

Each function ψ will be referred to as a single-electron wavefunction for reasons that will become clear shortly. To satisfy antisymmetry, these monomial terms can be combined in the form of a determinant of a matrix,

$$\Psi(\mathbf{r}_1, \mathbf{r}_2, \dots, \mathbf{r}_N) = \frac{1}{\sqrt{N!}} \begin{vmatrix} \psi_1(\mathbf{r}_1) & \psi_1(\mathbf{r}_2) & \dots & \psi_1(\mathbf{r}_N) \\ \psi_2(\mathbf{r}_1) & \psi_2(\mathbf{r}_2) & \dots & \psi_2(\mathbf{r}_N) \\ \dots & \dots & \dots & \dots \\ \psi_N(\mathbf{r}_1) & \psi_N(\mathbf{r}_2) & \dots & \psi_N(\mathbf{r}_N) \end{vmatrix}, \quad (2.4)$$

known as the ‘‘Slater determinant’’, where the ψ_i ’s normalize to 1, and where the spin state is implicitly absorbed into the ψ_i ’s. This system will have an electron density of

$$n(\mathbf{r}) = \sum_{i=1}^N |\psi_i(\mathbf{r})|^2. \quad (2.5)$$

Suppose the electrons are *effectively* non-interacting, that is, the potential $V(\mathbf{r}_1, \mathbf{r}_2, \dots, \mathbf{r}_N)$ may be broken into a sum of single-particle potentials V_i . As the electrons are identical, the potential on each electron must be identical, and

$$V(\mathbf{r}_1, \mathbf{r}_2, \dots, \mathbf{r}_N) = \sum_i V(\mathbf{r}_i). \quad (2.6)$$

The Hamiltonian is then reducible to a sum of single-particle Hamiltonians, and after some manipulation it can be shown that the wavefunction of the system is a Slater determinant of eigenstates of the single-particle Schrödinger equation,

$$-\frac{\hbar^2}{2m_e} \nabla^2 \psi_m(\mathbf{r}) + V(\mathbf{r})\psi_m = E_m \psi_m(\mathbf{r}), \quad (2.7)$$

with an energy for the many-particle wavefunction

$$E = \sum_m E_m, \quad (2.8)$$

where the sum is taken over all occupied states.

But what if the potential is not separable? And even if it is separable, the system is infinite in extent, and $V(\mathbf{r})$ is not generally localized. No computer program can hold a wavefunction with infinite spacial extent in memory, let alone calculate it. The main theorem that makes the study of condensed matter physics possible is Bloch's theorem (1928). Bloch's theorem states that, for a single particle under a periodic potential with an associated lattice $\{\mathbf{R}\}$ which obeys

$$V(\mathbf{r} + \mathbf{R}) = V(\mathbf{r}), \quad (2.9)$$

where \mathbf{R} is any lattice vector, the eigenstates of energy may be written as the product of two pieces: a function $u(\mathbf{r})$ with the same periodicity of the potential, and a plane wave with wave vector \mathbf{K} belonging to the reciprocal lattice,

$$\psi_{\mathbf{K}}(\mathbf{r}) = e^{i\mathbf{K}\cdot\mathbf{r}}u(\mathbf{r}), \quad (2.10)$$

where \mathbf{K} is the “lattice” or “crystal” wavevector. This changes the quantity of interest in the solution of the Schrödinger equation from ψ , a wavefunction with infinite spatial extent, to u , an orbital that is periodic and thus needs to be calculated (and stored in memory) for only one cell of the periodic potential.

This approximation is critical for the study of condensed matter physics because, to first approximation, many condensed matter structures of interest are formed from a regular lattice of nuclei. For carbon in a graphite structure, a cell of the lattice contains only two nuclei and twelve electrons. No material is perfectly periodic; any practical material contains defects, and all materials are of finite size and thus have edges. However, defects within an otherwise periodic structure generally have localized wavefunctions near the defect, decaying exponentially to the perfectly periodic crystal wavefunction as one moves away from the defect. In practice, for a localized defect (say a chemical substitution or the edge of a material), 1-2 nm away from a boundary or a defect, the local wavefunction is identical to the wavefunction of the perfect crystal, commonly referred to as the “bulk wavefunction”. Calculation of the bulk wavefunction is an important first step for understanding the properties of any

real material. This line of argumentation may also be reversed: if one wishes to understand the physics of a system near a defect, one may take as the computational cell the configuration of the system near that defect. With periodic boundary conditions this corresponds to the physical picture of a regular lattice of that defect infinitely repeated throughout space (defeating identification of the “defect” as such), but if the cell is large enough, the localization of the wavefunction near that defect ensures that the defect will interact negligibly with its periodic images.

2.1.3 The Hohenberg-Kohn Equations

As electrons are identical particles, perhaps having each electron contribute three independent spacial degrees of freedom is redundant, even in the case of an interacting system. Instead, only three degrees of freedom should be needed to properly model the system, each electron contributing “its” three degrees of freedom equally to some function at that location in space:

$$\Psi(\mathbf{r}_1, \mathbf{r}_2, \dots, \mathbf{r}_N) \rightarrow n(\mathbf{r}). \quad (2.11)$$

Hohenberg and Kohn (1964) [17] showed that this is indeed possible. The quantity of importance is the ground state electron density $n_0(\mathbf{r})$, and all properties of the system may be computed from this function. This was beautifully presented in the two Hohenberg-Kohn theorems. The original formulation was in second-quantized form, but here it will be presented in Levy’s constrained search formalism [18]. Besides being easier to understand and sidestepping the issue of ground state degeneracy, Levy’s formulation has the advantage of only imposing the (entirely reasonable) condition that trial densities be N-representable, i.e. obtainable from some anti-symmetric wavefunction with N electrons. The original Hohenberg-Kohn formulation required the stronger condition that trial densities be v-representable, i.e. derivable from some external potential, which may be violated even for sensible trial densities [19].

Consider a many-electron Hamiltonian of general form

$$\hat{H} = \hat{T} + \hat{V}_{ee} + \sum_i V_{ext}(\mathbf{r}_i), \quad (2.12)$$

where \hat{T} is the kinetic energy operator, V_{ee} is the electron-electron interaction operator, and $V_{ext}(\mathbf{r})$ is some single-body external potential (including the Coulomb attraction of electrons to the nuclei of the system). The energy for a general many-body wavefunction Ψ is

$$E[\Psi] = \langle \Psi | (\hat{T} + \hat{V}_{ee}) | \Psi \rangle + \int d\mathbf{r} V_{ext}(\mathbf{r}) n(\mathbf{r}), \quad (2.13)$$

where

$$n(\mathbf{r}) = N \int d\mathbf{r}_2 \dots d\mathbf{r}_N |\Psi(\mathbf{r}, \mathbf{r}_2, \dots, \mathbf{r}_N)|^2. \quad (2.14)$$

By Equation 2.14, given any Ψ , one may find a corresponding n . Now suppose instead a particular charge density $n(\mathbf{r})$ is imposed on the system, and the energy is desired. In general, many Ψ may map to the same n , and Equation 2.14 is non-invertible. However, by the principle of energy minimization, we may recover the energy of the system as³

$$E[n] = \min_{\Psi \rightarrow n} E[\Psi], \quad (2.15)$$

where minimization is done over all wavefunctions Ψ that are consistent with Equation 2.14, giving Equation 2.13 a functional form of

$$E[n] = F[n] + \int d\mathbf{r} V_{ext}(\mathbf{r}) n(\mathbf{r}), \quad (2.16)$$

where

$$F[n] \equiv \min_{\Psi \rightarrow n} \langle \Psi | (\hat{T} + \hat{V}_{ee}) | \Psi \rangle. \quad (2.17)$$

³It is critical to understand that, although energy minimization is being invoked, here we are not attempting to find the ground state energy of the system. Rather, given a particular $n(\mathbf{r})$, we are attempting to find the lowest possible energy consistent with this charge density. In general, this charge density will correspond to an excited state of the system (assuming the charge density is physical to begin with, which it need not be), and only in the case where the ground state charge density is given will the resulting energy be the ground state energy.

It is important to note that $F[n]$ is completely independent of V_{ext} , and thus it is a universal functional depending only on the total number of electrons N . The Hohenburg-Kohn theorems can now be stated (and proven quite easily) as:

The First Hohenburg-Kohn Theorem: $V_{ext}(\mathbf{r})$ is a unique functional of $n_0(\mathbf{r})$, the exact ground state electronic density, apart from a trivial additive constant.

The Second Hohenburg-Kohn Theorem: For any particular $V_{ext}(\mathbf{r})$, the exact ground state energy E_0 of the system is the global minimum value of the functional $E[n]$, and the density $n(\mathbf{r})$ that minimizes the functional is $n_0(\mathbf{r})$.

The first theorem states that once a particular $n_0(\mathbf{r})$ has been found (or proposed), it may be mapped back to a unique $V_{ext}(\mathbf{r})$ term in the Schrödinger equation. However, all electron-electron interactions are contained in $F[n]$, which is a universal functional independent of V_{ext} . The $V_{ext}(\mathbf{r})$ term in the Hamiltonian is the only term that differs between systems with the same number of electrons. Thus by the second Hohenburg-Kohn theorem, $n_0(\mathbf{r})$ uniquely determines the Hamiltonian for the system, which in turn uniquely determines the (possibly degenerate) ground and excited many-body wavefunctions. Therefore, if $n_0(\mathbf{r})$ is known, it is in principle possible to determine all properties of the system, and thus it is in principle possible to compute all properties of the system from $n_0(\mathbf{r})$.

However, the form of the functional $F[n]$ given is so general as to be practically useless, and the important question of how exactly to determine system properties from $n_0(\mathbf{r})$ without re-solving the Schrödinger equation is left unaddressed. The second Hohenburg-Kohn theorem gives $E[n]$ from which the ground state energy and $n_0(\mathbf{r})$ may be found via functional minimization, but the first Hohenburg-Kohn theorem only asserts that it is *in principle* possible to calculate all other properties of the system.

2.1.4 The Kohn-Sham Equations

To derive the single-electron Schrödinger equation (Equation 2.7), it was assumed that the electrons were effectively non-interacting. The key word here is *effectively*. If for an interacting system, all details of the electron-electron interactions can be moved into a potential term that is single-electron-like, shoving the electron-electron interactions of the interacting system into the external potential of the non-interacting system⁴, a single-electron Schrödinger equation for “non-physical” non-interacting electrons may be solved to generate the many-particle wavefunction for the “physical” interacting electrons. This is the main idea behind the Kohn-Sham Ansatz [20]:

The Kohn-Sham Ansatz (1965): For every interacting system, there is a non-interacting system with the same ground state electron density.

With this ansatz in hand, Kohn and Sham broke the Hohenberg-Kohn functional into three pieces. First, they factored out the classical electrostatic interaction between electrons, the “Hartree” term, which for many (but not all!) systems will be the only significant long-range electron-electron interaction. Next, they broke the other terms into two pieces, one piece corresponding to the functional operating on the Slater determinant of non-interacting electron wavefunctions with equivalent electron density, and the second measuring deviation of the energy of the multi-particle wavefunction from the Slater determinant, yielding a functional form of (in Hartree atomic units)

$$E_{HK} = T_{NI} + E_{II} + \int d\mathbf{r} V_{ext}(\mathbf{r})n(\mathbf{r}) + E_{Hartree} + \delta T + \delta V, \quad (2.18)$$

where

$$T_{NI} = -\frac{1}{2} \sum_i |\nabla \psi_i|^2 \quad (2.19)$$

⁴The usage of “non-interacting” here is a misnomer, though common in the literature, as the classical Coulombic energy for the electronic density will be retained through the Hartree energy term, whereas truly non-interacting electrons would have no charge and thus no Coulomb interaction.

is the kinetic energy for the non-interacting Slater determinant, δT is the deviation of T_{NI} from the true kinetic energy for the interacting system, $\{\psi_i\}$ are the single-electron wavefunctions (where spin has been merged into index i), E_{II} is the interaction energy between ions, $E_{Hartree}$ is the Hartree energy,

$$E_{Hartree} = \frac{1}{2} \int d\mathbf{r} d\mathbf{r}' \frac{n(\mathbf{r})n(\mathbf{r}')}{|\mathbf{r} - \mathbf{r}'|}, \quad (2.20)$$

and δV is the deviation of the Hartree energy from the electron-electron interaction energy for the interacting system. This is an exact equation as all many-body effects have been incorporated into δT and δV . These two terms combined form the exchange-correlation functional

$$E_{xc}[n] \equiv \delta T[n] + \delta V[n]. \quad (2.21)$$

Carrying out functional minimization on the Kohn-Sham functional while imposing the constraint that different occupied single-particle states are orthogonal via Lagrange multipliers yields the Kohn-Sham equation,

$$H_{KS}\psi_i(\mathbf{r}) = \epsilon_i\psi_i(\mathbf{r}), \quad (2.22)$$

where H_{KS} is the Kohn-Sham single-electron Hamiltonian,

$$H_{KS} = -\frac{1}{2}\nabla^2 + \left(V_{ext}(\mathbf{r}) + \int d\mathbf{r}' \frac{n(\mathbf{r}')}{|\mathbf{r} - \mathbf{r}'|} + V_{xc}(\mathbf{r}) \right) \equiv -\frac{1}{2}\nabla^2 + V_{KS}(\mathbf{r}), \quad (2.23)$$

and

$$V_{xc}(\mathbf{r}) \equiv \frac{\delta E_{xc}}{\delta n(\mathbf{r})} \quad (2.24)$$

is the exchange-correlation energy.

The Kohn-Sham equation may be in principle solved exactly to find the non-physical single-particle wavefunctions ψ_i . These wavefunctions may then be put into equation 2.5 to determine $n_0(\mathbf{r})$, from which all properties of the system may be derived via the first Hohenberg-Kohn theorem. However, moving from functional minimization to the Kohn-Sham equation adds one complication. The Hartree term,

used in Equation 2.23 to derive $\{\psi_i\}$, is an integral operator depending on $n(\mathbf{r})$. By equation 2.5, however, $n(\mathbf{r})$ itself depends on the set $\{\psi_i\}$, and thus the equations are coupled. In practice, this is not a major impediment, as self-consistency can be used, where one iteratively solves the Kohn-Sham equation for a charge density, using the resulting wavefunctions (as well as previous charge densities for reasons of computational stability) to derive a new charge density, continuously repeating this cycle until convergence is reached.

2.1.5 Exchange and Correlation

In principle, if the exchange-correlation functional $E_{xc}[n]$ was known exactly, the Kohn-Sham equation could be solved exactly. The exchange-correlation functional is the contribution to $F[n]$ that explicitly encodes the electron-electron interactions over and above that of a classical charge distribution. Like $F[n]$, it is a universal functional that only depends on the number of electrons N in the system. This “stupidity energy” [21] incorporates too much physics to be given a simple closed form solution. However, it can be shown via a thought experiment of varying the electron charge adiabatically from 0 (the true non-interacting case) to e (the physical case) [22] that the exchange-correlation energy has the general form

$$E_{xc}[n] = \frac{1}{2} \int d\mathbf{r} d\mathbf{r}' \frac{n(\mathbf{r})n_{xc}(\mathbf{r}, \mathbf{r}')}{|\mathbf{r} - \mathbf{r}'|}, \quad (2.25)$$

where n_{xc} is the “exchange-correlation hole”, a pair correlation function obeying

$$\int d\mathbf{r}' n_{xc}(\mathbf{r}, \mathbf{r}') = -1. \quad (2.26)$$

The exchange-correlation hole has physical significance as a spatial representation of the exchange and correlation effects. The response of the system to an electron at \mathbf{r} is to repulse electrons at \mathbf{r}' , creating a hole n_{xc} with unit total charge, and the exchange-correlation energy is the classical Coulomb interaction of the electron with this charge distribution [10]. n_{xc} is still too complicated for a closed form solution, however. Now

the major approximation underlying practical implementation of density functional theory is made:

Guess what $n_{xc}(\mathbf{r}, \mathbf{r}')$ is, yielding an assumed form for E_{xc} .

The major source of error in all electronic structure codes is this approximation. This guess is known as a “functional”. This approximation is plausible because the terms treated exactly in density functional theory, the Hartree term and kinetic energy term for the Slater determinant, are large compared to the approximated exchange-correlation energy [11]. One test of the accuracy of a functional is to perform quantum Monte Carlo on atoms and small molecules, and compare the results to the functional. Another is to examine the energy of highest occupied single-electron state, as its energy relative to the next highest occupied single-electron state is the negative of the ionization energy (despite the single-particle state having formally no physical meaning)⁵ Some examples of functional follows.

First Order: Local Density Approximation (LDA)

If electrons are weakly interacting, locally the system should behave like the uniform electron gas. This led Kohn and Sham to propose using the exchange energy density for a homogeneous electric gas with density n , which can be given exactly as [12]

$$e_x(n) = -0.458\left(\frac{4\pi}{3}\right)^{\frac{1}{3}}n^{\frac{1}{3}}. \quad (2.27)$$

Even in this simple case, the correlation energy density must be estimated, as Wigner (1938) first did, to obtain

$$e_c(n) \approx \frac{-0.44}{\left(\frac{4\pi}{3}\right)^{\frac{1}{3}}n^{\frac{1}{3}} + 7.8}, \quad (2.28)$$

giving an exchange-correlation energy density of

$$e_{xc}(n) = e_x(n) + e_c(n). \quad (2.29)$$

⁵It must be noted that the electron affinity *cannot* be found using the lowest unoccupied single-particle state, as the Kohn-Sham prescription does not optimize unoccupied states.

To make the Local Density Approximation (LDA)⁶, assume that the exchange-correlation energy density may be approximated by the exchange-correlation energy a homogeneous electron gas would have at the local electron density, so that the total exchange-correlation energy for the electronic density will be

$$E_{xc}[n] = \int d\mathbf{r} n(\mathbf{r})(e_x(n) + e_c(n)). \quad (2.30)$$

Due to its reliance on the homogeneous electron gas, LDA was expected to be valid only in the case of charge densities slowly varying relative to the local Fermi wavelength, which is the only length scale present in the homogeneous electron gas. The Fermi wavelength is often much larger than the oscillations in the charge density, so LDA was expected to be a poor approximation. Surprisingly, LDA gives reasonable results for ionization energy of atoms, dissociation energies of molecules, and cohesive energies of solids, typically within 10% to 20%, with a preference towards overbinding [23]. Bond lengths are usually accurate to within 1%.⁷ For atoms and molecules, exchange energies are generally underestimated by around 10-20% and correlation energies are overestimated by a factor of 2. The opposite trends in errors, combined with the exchange energy being an order of magnitude larger than the correlation energy, results in “error cancellation” enhancing accuracy. For solids, volumes are systematically underestimated by 5% and bulk moduli overestimated by 20%.

This surprising basic agreement for a relatively crude functional is possible because LDA was derived from the uniform electron gas. It can be re-expressed in the form of Equation 2.25, in particular as being associated with the exchange-correlation hole for some system. For weakly interacting systems, the dependence of the properties of the system on the precise form of the exchange-correlation functional should be weak, and ensuring that the gross, averaged features of the exchange-correlation hole are

⁶There is somewhat of a nomenclature issue here, as LDA may refer to the general family of functionals that depend only on local electron density or the special case of the specific functional that reproduces the homogeneous electron gas. The usage should be obvious from context.

⁷LDA is often the most accurate traditional functional for bond lengths.

obeyed should be important for qualitative understanding the physics of the system. For strongly interacting systems, however, the precise form of the exchange-correlation functional plays an important role in the physics of the system, and indeed for these system LDA (and, in fact, all traditional functionals) fails.

As written, LDA does not allow for any type of magnetic ordering, but spin-decomposed variants using the Local Spin Density Approximation (LSDA) exist. Magnetism is currently density functional theory’s Achilles’ Heel, as approximate functionals without long-range interactions excessively delocalize electron densities, and results regarding magnetism will have qualitative accuracy at best. In these cases, methods like LDA+U, which include Hubbard terms to impose proper electron localization, are necessary to get precise magnetic ordering, but these methods are phenomenological in nature, and thus not “first principles”.

Higher Orders: Generalized Gradient Approximation (GGA)

So how can the exchange-correlation functional be further improved? The kneejerk reaction of any physicist is to “Taylor expand it”. The next set of terms to include in the approximation would be the gradient and higher order derivatives of the electron density, or more specifically their magnitude, yielding the Gradient Expansion Approximation (GEA),

$$E_{xc}[n] = \int d\mathbf{r} n(\mathbf{r}) e_{xc}(n(\mathbf{r}), |\nabla n(\mathbf{r})|, \dots). \quad (2.31)$$

Surprisingly, early implementations of GEA gave worse results than LDA for most realistic materials. The problem was poor treatment of the gradient. Where the electron density is rapidly varying (such as near nuclei), gradients will become large, amplifying errors in the approximate exchange-correlation functional. To eliminate this flaw, it is necessary to explicitly dampen out the dependence of the functional on the gradient as the gradient grows large. Equation 2.31 is rearranged to read

$$E_{xc}[n] \equiv \int d\mathbf{r} n(\mathbf{r}) e_{xc}(n(\mathbf{r})) F_{xc}(n(\mathbf{r}), |\nabla n(\mathbf{r})|, \dots), \quad (2.32)$$

where $e_{xc}(n)$ again refers to the exchange energy for a homogeneous electron gas of density n , and F_{xc} is some dimensionless function. F_{xc} is constructed so it dampens out when the higher-order terms grow large, but this requires a dimensionless measure of the relative magnitude of the higher-order terms. The only length scale available is given by the inverse of the Fermi wavevector of the homogeneous electron gas for the local density, so a measure of the relative magnitude of the higher-order terms in dimensionless units is

$$s_m = \frac{|\nabla^m n|}{(2k_f(n))^m n}, \quad (2.33)$$

and Equation 2.32 becomes

$$E_{xc}[n] = \int d\mathbf{r} n(\mathbf{r}) e_{xc}(n(\mathbf{r})) F_{xc}(n(\mathbf{r}), s_1, \dots). \quad (2.34)$$

GEA in this form is now rechristened the Generalized Gradient Approximation (GGA)⁸, as the focus has shifted from a Taylor expansion of the exchange-correlation energy to a dimensionless function F_{xc} , the “enhancement factor”, whose inputs are the local electron density and the relative magnitudes of the higher-order terms. Popular implementations of this method only retain $s_1 \equiv s$ and are constructed to obey certain physical limiting cases (such as high and low density homogeneous electron gases), such as Perdew-Wang [24] (PW91, 1991) and Perdew-Burke-Enzerhof [25] (PBE, 1996). It is a general feature of GGA functionals to give much improved estimates for exchange-correlation energy over L(S)DA functionals [23], with PBE having slight trend toward overestimating volume by 5% and underestimating bulk moduli by 10%.

Beyond DFT: Hybrid Functionals

As can be seen from Equations 2.27 and 2.28, the exchange energy is generally the dominant portion of the exchange-correlation energy, the approximated quantity in

⁸Spin-decomposed versions of GGA also exist, but unlike LDA/LSDA they are not given a special name.

practical density functional theory, and to increase the accuracy of calculated energies, one should be primarily concerned with the exchange energy. In fact, the exchange energy in the absence of correlation effects for the Kohn-Sham eigenfunctions, E_{xx} , can be given exactly from Hartree-Fock theory as a function of the orbitals $\{\psi\}$. Technically, such a quantity does not belong in proper density functional theory as it explicitly depends on the calculated orbitals $\{\psi\}$ and thus is not a proper functional, which by the Hohenberg-Kohn theorems can be written exclusively in terms of the density. However, to increase the accuracy of the calculated energies, it is useful to go past density functional theory and reintroduce the exact exchange energy. The correlation energy is still needed, however. It may be argued using the adiabatic construction that the proper way to construct the “hybrid” or “exact-exchange” functional is [26]:

$$E_{xc}[n, \{\psi\}] = \beta E_{xx}[\{\psi\}] + (1 - \beta) E_{xc}[n], \quad (2.35)$$

where β is a variational mixing parameter that can be varied by hand.⁹ These hybrid functionals give the most accurate energies of the functionals listed. However, for most applications in physics when accuracy in energy isn’t absolutely critical, the $O(N^4)$ scaling (due to the appearance of four orbitals terms in the Hartree-Fock equations) makes these functionals computational overkill unless very accurate energies are needed.

2.1.6 Basis Sets In Density Functional Theory

With a functional chosen, one may now solve the single-particle Schrödinger’s equation to obtain the single-particle wavefunctions from which the Slater determinant may be determined. Electronic structure codes with the accuracy necessary for thermodynamic calculations use a basis to convert this differential equation into matrix equations. This is not an approximation if the basis set is complete. For realistic

⁹It is necessary to use a mixing parameter rather than taking only the correlation portion of the traditional functions, as the correlation energy on its own has no physical meaning.

calculations, computational constraints require the basis set to be truncated, which when performed intelligently (i.e. with basis functions that approximate the expected wavefunctions of the system) is not a major impediment. Two examples will be shown here. We here only consider plane-wave-based methods, though real-space methods also exist and scale better as computational cell size increases.

The Knee-Jerk Reaction: Plane Waves

Because the potential energy function in condensed matter physics is almost always taken to be periodic, a naive first guess would be to expand the potential in a plane wave basis. Expansion of the wavefunction in this basis set is its Fourier decomposition,

$$\psi(\mathbf{r}) = \sum_{\mathbf{q}} c_{\mathbf{q}} \frac{1}{\sqrt{V}} e^{i\mathbf{q}\cdot\mathbf{r}} = \sum_{\mathbf{q}} c_{\mathbf{q}} |\mathbf{q}\rangle, \quad (2.36)$$

with

$$|\mathbf{q}\rangle \equiv \frac{1}{\sqrt{V}} e^{i\mathbf{q}\cdot\mathbf{r}}, \quad (2.37)$$

where the unit cell of the system is defined over a volume V . Similarly, the potential is Fourier-decomposed,

$$V(\mathbf{r}) = \sum_{\mathbf{G}} V(\mathbf{G}) e^{i\mathbf{G}\cdot\mathbf{r}}, \quad (2.38)$$

with matrix elements in the $|\mathbf{q}\rangle$ basis of

$$\langle \mathbf{q}' | V(\mathbf{r}) | \mathbf{q} \rangle = \frac{1}{V} \sum_{\mathbf{G}} V(\mathbf{G}) \int_V d\mathbf{r} e^{i(\mathbf{G}+\mathbf{q}-\mathbf{q}')\cdot\mathbf{r}} = V(\mathbf{q} - \mathbf{q}'). \quad (2.39)$$

The Bloch theorem allows restriction to eigenfunctions of form

$$\psi_{\mathbf{k}}(\mathbf{r}) = \sum_{\mathbf{G}} c_{\mathbf{G}}(\mathbf{k}) |\mathbf{k} + \mathbf{G}\rangle, \quad (2.40)$$

where $c_{\mathbf{k}+\mathbf{G}}$ has been relabeled $c_{\mathbf{G}}(\mathbf{k})$ to stress that the sum is over all reciprocal lattice vectors. To find these eigenfunctions, diagonalize the H matrix in the $|\mathbf{k} + \mathbf{G}\rangle$ basis, which from Equation 2.39 for $\langle \mathbf{k} + \mathbf{G}' | V(\mathbf{r}) | \mathbf{k} + \mathbf{G} \rangle$ is

$$H_{\mathbf{G},\mathbf{G}'}(\mathbf{k}) = \langle \mathbf{k} + \mathbf{G}' | H | \mathbf{k} + \mathbf{G} \rangle = \frac{|\mathbf{k} + \mathbf{G}|^2}{2} \delta_{\mathbf{G},\mathbf{G}'} + V(\mathbf{G}' - \mathbf{G}). \quad (2.41)$$

The plane wave basis is efficient when relatively few $V(\mathbf{G}' - \mathbf{G})$ terms are non-zero. If the potential is decomposable into a small number of plane waves, however, it must be delocalized. The ionic potentials considered here, on the contrary, are highly localized, as the electron-ion interaction term has a $1/r$ divergence at the origin. Such a potential will require a large number of plane waves to approximate and a large number of scattering interactions to calculate, even when the band structure turns out to be nearly free-electron-like. While the various integrals will be trivial, as they involve only plane waves, using such a large basis set will generate extremely large matrices with many non-zero entries, which are memory-intensive and difficult to diagonalize.

Pseudopotentials: Projector Augmented Waves (PAW)

To better approximate the general behavior of a system, it is useful to decompose space into two regions, the “core region” where the wavefunctions wildly vary and show strong localized behavior, and an “interstitial” region where wavefunctions are nearly plane-wave-like. This is done by Projector Augmented Waves [27, 28] (1994), a generalization of the “pseudo-potential” formalism, where the Coulomb potential within the core is replaced with a pseudo-potential that is designed to capture the essential details of the core-electron interaction. The complicated nodal structure of the core states can be replaced by smooth states, which have the added benefit of simplifying calculations, and only scattering off these core regions affects the wavefunctions in the interstitial regions¹⁰. It is commonly observed that because they are smooth, pseudo-potentials are “transferable”, that is, pseudo-potentials can be fit from a small set of systems (usually one isolated atom), but the resulting pseudo-potential can be transferred to a wide number of systems.

¹⁰This is why effectively free-electron-like bands can be observed in metals. When the scattering amplitudes off the core regions are small, the electronic wavefunction in the interstitial region is essentially free with minor perturbations due to the core region, even though the electronic wavefunction in the core region is strongly localized and far from free-electron-like.

The general spirit of pseudopotential approaches is to change the potential $V(\mathbf{r})$ to a pseudopotential $V'(\mathbf{r})$. This changes the wavefunctions from the “all-electron valence wavefunctions”¹¹ ψ to pseudo-wavefunctions ψ' , but those that faithfully represent the all-electron valence wavefunctions outside the cores and interact properly with the cores. This implies that a one-to-one mapping \hat{T} exists between the two sets of wavefunctions with an associated operator,

$$\psi = \hat{T}\psi'. \quad (2.42)$$

In the PAW method, the wavefunction in the interstitial region is taken to be identical for both the all-electron valence wavefunctions and the pseudo-wavefunction. In this case, \hat{T} becomes

$$\hat{T} = 1 + \sum_i (|\phi_i\rangle - |\phi'_i\rangle) \langle p'_i|, \quad (2.43)$$

where $\{\phi'_i\}$ are the basis functions for the pseudo-potentials and $\{p'_i\}$ is some set of projectors such that $\langle p'_i|\phi'_j\rangle = \delta_{ij}$. \hat{T} defines a transformation between the pseudo-potential basis and the all-electron valence basis.¹² Expectation values of a (local) operator \hat{A} for the all-electron valence wavefunctions may be transformed into expectation values of an operator $\hat{A}' = \hat{T}^\dagger \hat{A} \hat{T}$ for the pseudo-wavefunction using

$$\hat{A}' = \hat{A} + \sum_{ij} |p'_i\rangle (\langle \phi_i|\hat{A}|\phi_j\rangle - \langle \phi'_i|\hat{A}|\phi'_j\rangle) \langle p'_j|. \quad (2.44)$$

All expectation values in the PAW formalism for (local) operators can be reduced to (at most) three different terms. The first term is the operator acting on the pseudo-wavefunction basis functions. The second reintroduces the all-electron core states,

¹¹The nomenclature here is tricky. “Valence” does not refer to the valence band from solid state theory but rather to non-core states (which also includes the conduction band and higher) and “all-electron” refers to the solutions of the exact one-electron Schrödinger wavefunction with the exact one-body potential, and not the many-particle wavefunction.

¹²More precisely, it defines the estimate of the all-electron valence basis from the given pseudo-wavefunction basis.

and the third compensates for the pseudo-wavefunction core states from the first term. Of particular interest for density functional theory is the electron density,

$$n(\mathbf{r}) = n'(\mathbf{r}) + n^1(\mathbf{r}) - n'^1(\mathbf{r}), \quad (2.45)$$

where n is the electron density, n' is the electron density for the pseudo-wavefunction eigenstates, n^1 is the electron density for the core region of the all-electron basis functions, and n'^1 is the electron density of the core region of the pseudo-wavefunction basis functions.

In the PAW formalism, it is not required that the core states for the pseudo-wavefunction basis be orthonormal, as the \hat{T} operator will reimpose orthonormality when calculating expectation values. The price paid by ignoring orthonormality is the introduction of an “overlap” matrix in the single-particle Schrödinger equation, leading to a generalized eigenfunction equation

$$\hat{H}'\psi' = \epsilon\hat{O}'\psi', \quad (2.46)$$

where H' is the transformed Hamiltonian operator and

$$\hat{O}' = 1 + \sum_{i,j} |p'_i\rangle (\langle\phi_i|\phi_j\rangle - \langle\phi'_i|\phi'_j\rangle) \langle p'_j| \quad (2.47)$$

is the overlap matrix. The overlap matrix is the transformation of the identity matrix in the all-electron valence basis, and in the case where norm conservation is imposed, the overlap matrix is equivalent to the identity matrix.

Violation of orthonormality is useful when valence states interact with high-energy core states, known as “semi-core states,” and accurate knowledge of the nodal structure of the semi-core states is necessary. As previously noted, the wavefunctions within the core region can have a complicated nodal structure. If orthonormality is imposed, upon removing the semi-core levels from the core, part of this complicated nodal structure will be recovered if orthonormality is imposed, increasing the number of Fourier modes necessary to model the pseudo-wavefunction core region. If

the number of Fourier modes is fixed, relaxing orthonormality doubles the number of calculations necessary, as two sets of matrix elements must be calculated, the Hamiltonian matrix and the overlap matrix. However, relaxing orthonormality reduces the number of Fourier modes needed to model the core region, with the introduction of the overlap matrix re-establishing the proper norms when calculating physical properties. This not only reduces the total number of calculations necessary but also increases transferability, as the resulting core states will be smoother.

2.1.7 Motion of the Nuclei: Forces and Phonons

Having found the electronic ground state density, one may not only calculate the electronic band structure but also the ionic forces and subsequently the equilibrium ion positions. Using the Hellmann-Feynman theorem, the force on a given ion i is

$$\mathbf{F}_i = -\frac{\partial E}{\partial \mathbf{R}_i} = -\langle \Psi | \frac{\partial \hat{H}}{\partial \mathbf{R}_i} | \Psi \rangle + \frac{\partial E_I}{\partial \mathbf{R}_i}, \quad (2.48)$$

where Ψ here denotes the non-interacting ground state wavefunction (the Slater determinant of occupied Kohn-Sham eigenstates) and E_I is the electrostatic potential between ions.

These forces have multiple applications. It is likely that the initial positions for the ions will not be the equilibrium positions predicted by the particular functional used, and the forces on ions will be non-zero. The energy as a function of $\{\mathbf{R}_i\}$ forms a surface called the “energy landscape”, and the forces are the gradients of the energy landscape, going to zero where the energy is locally minimized. One may use a whole suite of functional minimization techniques (quasi-Newton, steepest descent, conjugate gradient, etc.) to find the ionic positions that locally minimizes the energy, a process known as “relaxation”. It should be stressed that the energy landscape has innumerable local minimums, and all commonly used methods for relaxation are local minimization methods. They will always find an equilibrium structure close to the initial structure and not necessarily the true global minimum structure.

The second application is molecular dynamics. Knowledge of the forces combined with initial momentum is sufficient to directly integrate Newton’s laws of motion using one of the many classical molecular dynamics algorithms available (Verlet, leapfrog, etc.), yielding molecular dynamics at fixed volume¹³, particle number, and energy. This is equivalent to the microcanonical ensemble, as will be discussed later. This way of performing molecular dynamics is known in atomistic-level modeling as “Born-Oppenheimer molecular dynamics”, as it is the Born-Oppenheimer approximation that makes it possible to apply classical molecular dynamics methods to fundamentally quantum mechanical systems. It suffers from the problem that it is necessary to recompute the self-consistent electronic band structure each time step. The need for self-consistency may be circumvented by adding fictitious kinetic energy terms for the electrons to the Hamiltonian, as well as Lagrange multiplier terms to enforce orthogonality of the electronic wavefunctions. The quantum electronic and classical ionic degrees of freedom are then coupled, and the electrons roughly follow the ions each time step, resulting what is known as Car-Parrinello dynamics [29]. Alternatively, one may use the method of “wavefunction prediction” to speed up Born-Oppenheimer molecular dynamics. As the changes in wavefunctions are expected to be small for small time steps, one may propose a candidate wavefunction for the system after a time step has been performed, extrapolated from previous wavefunctions. The self-consistency cycle is then performed to calculate the actual wavefunction; however, the cycle usually requires much less steps than usual, as the initial predicted wavefunction is (hopefully) close to the converged wavefunction.

To perform the molecular dynamics at fixed temperature instead of energy, various “thermostats” can be used, such as Langevin [30] which adds white noise, consistent with the desired temperature, to the equations of motion and Nosé-Hoover [31, 32], which adds fictitious degrees of freedom to the Hamiltonian to regulate the kinetic en-

¹³More specifically, fixed lattice, but the difference between fixed lattice and fixed volume is commonly neglected except near phase transitions.

ergy of the ions. Similarly, to perform molecular dynamics at fixed pressure instead of volume, “barostats” may be introduced, such as Parrinello-Rahman [33] which adds fictitious degrees of degree to the Hamiltonian to impose a particular pressure via regulation of the strain tensor. One major problem with all *ab initio* molecular dynamics methods is the time scale required. As molecular oscillations have frequencies between 10^{12} to 10^{14} Hz, time steps to accurately model the motion of ions are on the order of 1 fs, and current computational resources only allow for maximum run times on the order of 100 ps, limiting the phenomena observable to relatively rapid processes.

The last application that will be considered is the phonon band structure. In the harmonic approximation [15], small changes in the ion position away from equilibrium, $\mathbf{u}_\mu(\mathbf{R})$, induce a quadratic term in energy,

$$E = E_0 + \sum_{\mathbf{R}\mu} \sum_{\mathbf{R}'\mu'} \frac{1}{2} \mathbf{u}_\mu(\mathbf{R}) \frac{\partial^2 E}{\partial \mathbf{u}_\mu(\mathbf{R}) \partial \mathbf{u}_{\mu'}(\mathbf{R}')} \mathbf{u}_{\mu'}(\mathbf{R}'), \quad (2.49)$$

where E_0 is the energy for the unperturbed lattice $\mathbf{u}_\mu(\mathbf{R}) = \mathbf{0}$ and, due to periodicity, it is convenient to break up an ion’s position into two pieces: the coordinate of the Bravais cell it resides in, \mathbf{R} , and an index for the particular site of the ion within a single Bravais cell, μ . Defining the “interatomic force constants matrix” as

$$D_{\mu\mu'}(\mathbf{R}, \mathbf{R}') \equiv \frac{\partial^2 E}{\partial \mathbf{u}_\mu(\mathbf{R}) \partial \mathbf{u}_{\mu'}(\mathbf{R}')} = D_{\mu\mu'}(\mathbf{R} - \mathbf{R}'), \quad (2.50)$$

where the last equality arises due to translational symmetry, and taking its Fourier transform,

$$D_{\mu\mu'}(\mathbf{k}) \equiv \sum_{\mathbf{R}} e^{-i\mathbf{k}\cdot\mathbf{R}} D_{\mu\mu'}(\mathbf{R}), \quad (2.51)$$

where the sum is taken over all Bravis lattice vectors, the phonons of the system may be derived in the usual way from the solution to the set of coupled equations

$$\sum_{\mu'} D_{\mu\mu'}(\mathbf{k}) \mathbf{U}_{m\mu'}(\mathbf{k}) = M_\mu \omega_{m\mathbf{k}}^2 \mathbf{U}_{m\mu}(\mathbf{k}), \quad (2.52)$$

where $\mathbf{U}_{m\mu}(\mathbf{k})$ is the polarization for ion μ of the m^{th} phonon at wavevector \mathbf{k} , M_μ is the mass of ion μ , and $\omega_{m,\mathbf{k}}$ is the frequency of the m^{th} mode at wavevector \mathbf{k} .

The only unknown quantities in these equations are the interatomic force constants matrices. The simplest way to calculate the interatomic force constant matrices is the “finite differences” methods, where small displacements are made in the ionic positions. The resulting forces are numerical derivatives of the energy, from which the interatomic force constants matrices may be approximated. Another method is density functional perturbation theory. It may be shown via the “2n+1 theorem” that in perturbation theory, second-order corrections to energy with respect to a small perturbation may be calculated from the first-order correction to the wavefunction. If one uses as a perturbation a small change in ion position from equilibrium, the second-order correction to energy will consist of second derivatives with respect to ion position, the interatomic force constants matrices. DFPT has the advantage that it is analytically exact and computationally efficient, but when properly implemented, both methods have similar accuracy.

However, calculating the interatomic force constant matrices using density functional theory for either method is a computationally expensive process. First, the unperturbed system be converged to a high degree of accuracy to avoid improper fitting to small error terms. More importantly, all density functional theory calculations assume a periodic cell, and a small displacement of “a single ion” will in fact be a periodic displacement of infinitely many ions throughout space. It is therefore necessary that a large enough supercell be taken to ensure that a given ion only interacts with a single image of another ion within the supercell¹⁴. As the dominant contributions to the interatomic force constant matrices die off exponentially as a function of distance past a nearest-neighbor-like distance, the supercell often does not need to be too large; for a cubic cell, a side length of $\approx 10 \text{ \AA}$ will often suffice, though this is system-dependent. Nevertheless, due to the $O(N^3)$ scaling of density functional

¹⁴These other ions can and often do reside in different primitive cells

theory and the large number of displacements to consider¹⁵, these calculations are computationally expensive at present and are only performed when absolutely necessary. It should also be noted that, in general, the interatomic force constants matrices are not transferable. Their similarity to distance-dependent pairwise interactions is deceptive; they in fact include all orders of interactions between all ions for the given system arising from the (small) displacement of two particular ions.

The phonons form decoupled harmonic oscillators with a total energy of

$$E = \sum_{i\mathbf{k}} \hbar(n_{i\mathbf{k}} + \frac{1}{2})\hbar\omega_{i\mathbf{k}}, \quad (2.53)$$

where $\omega_{i\mathbf{k}}$ is the frequency for the i^{th} vibrational mode at wavevector \mathbf{k} and $n_{i\mathbf{k}}$ is its occupation, an integer corresponding to excitation of motion of the lattice. The quantity $E_{zp} = \frac{1}{2} \sum_{i\mathbf{k}} \hbar\omega_{i\mathbf{k}}$ is known as the “zero-point energy”. A crystal lattice system can never be said to have zero momentum as this would imply complete uncertainty about the position of the ions via the Heisenberg uncertainty relation $\Delta x \Delta p \geq \hbar/2$. The zero-point energy is the minimum energy corresponding to motion about its equilibrium position that a quantum mechanical system must have to satisfy the Heisenberg uncertainty principle. The zero-point energy is often small relative to other energetic effects and is commonly neglected, except for systems containing hydrogen, as phonon frequencies scales as $1/\sqrt{M}$.

2.2 Phase Stability and Phase Diagrams

2.2.1 A Brief Review of Thermodynamics and Statistical Mechanics¹⁶

¹⁵Formally $3N-3$ displacements need to be considered for a solid system, where N is the number of atoms in the supercell and commonly $N \approx 100$ for suitable supercells, but symmetry considerations can substantially reduce the number of unique displacements.

¹⁶Excellent books on thermodynamics and equilibrium statistical mechanics include [34, 35, 36, 37, 38, 39, 40].

Here the main results of thermodynamics and statistical mechanics will be presented before moving on to discuss phase stability. In the interest of space, only topics necessary to understanding free energy modeling will be discussed.

2.2.2 Thermodynamic Quantities

The four laws of thermodynamics are as follows:

The Zeroth Law of Thermodynamics: There exists an intensive state variable known as “temperature” which has a universal and absolute scale, that is, the temperature of two isolated systems are comparable in absolute terms.

The First Law of Thermodynamics: There exists an extensive state variable known as “energy”. The sum of all systems’ energies over all space is conserved. When a system A interacts with a system B, it may perform a work W_A on the other subsystem and absorb a quantity of heat Q_A from the other system. The change in energy ΔU_A is then

$$\Delta U_A \equiv Q_A - W_A. \quad (2.54)$$

The Second Law of Thermodynamics: There exists an extensive state variable known as “entropy”, S . The infinitesimal heat flowing into a system, δQ under any process is related to the change in its entropy by the relation

$$\delta Q \equiv TdS \quad (2.55)$$

where the usage of δ to denote an infinitesimal stresses that Q is dependent on the process and cannot be defined by a potential. Entropy is not a conserved quantity, and under *any* process, the total entropy of the interacting systems cannot decrease,

$$\sum_i \Delta S_i \geq 0, \quad (2.56)$$

where ΔS_i is the change in entropy for system i .

The Third Law of Thermodynamics (Planck’s Form): The universal temperature scale is bounded below; there exists some minimum temperature. Without loss of

generality, this may be taken to be zero. All systems *in equilibrium* at this minimum temperature have an identical value for entropy per volume; this may also be taken to be zero¹⁷.

2.2.3 Consequences of the Four Laws of Thermodynamics

The second law defines δQ , and

$$dU = TdS + \delta W. \quad (2.57)$$

There is no general form for the work portion, as any force (gravity, electromagnetism, etc.) will have associated with it a work. However, it is always assumed that a system has some volume V , and it will be assumed for this and future sections that the system is an aggregate of different species of particles with numbers $\{N_i\}$, where the total number of particles of a given species i over all systems remains fixed. Then two types of work may be defined, the mechanical work $-p dV$, where p is the pressure, and a “chemical work” $\mu_i dN_i$ consisting of the change in energy the system undergoes when exchanging particles with some other system. μ_i here functions as a potential for particle number and is accordingly referred to as the “chemical potential”. If only these two types of work are considered,

$$dU = TdS - pdV + \sum_i \mu_i dN_i, \quad (2.58)$$

and energy is expressible as a function of entropy, volume, and particle number. Furthermore, any differentiable multivariate function $F(x_1, x_2, \dots, x_m)$ has an exact differential of form

$$dF = \sum_{i=1}^m \frac{\partial F}{\partial x_i} dx_i. \quad (2.59)$$

¹⁷It is important to stress here that equilibrium must have been reached for the Third Law to apply. This will be discussed in detail later.

As dU is a total differential, this implies

$$T = \left. \frac{\partial U}{\partial S} \right|_{V, N_i} \quad (2.60)$$

$$p = - \left. \frac{\partial U}{\partial V} \right|_{S, N_i} \quad (2.61)$$

$$\mu_i = \left. \frac{\partial U}{\partial N_i} \right|_{V, S, \{N_j\}}, \quad (2.62)$$

where in the last line $\{N_j\}$ refers to all particle species other than i .

Given equations for T , p , and μ_i in terms of S , V , and N_i , dU may be integrated to obtain a “fundamental equation” $U = U(S, V, \{N_i\})$ from which all state variables for the system may be derived. Due to their ability to recover the energy, equations for T , p , and μ_i called “equations of state”. Equations of state describe the state of the system, but they cannot be used to find all state variables of the system. It must be stressed that the equations of state are partial derivatives of the fundamental equation *only* when expressed in terms of the proper constrained variables.

2.2.4 Entropy Maximization, Stability Conditions, and Equilibrium

But what if the equation for the energy of the system has additional variables? Suppose U is given as a function $U = U(S, V, \{N_i\}, X)$, where X does not correspond to some additional type of externally applied work. As $U = U(S, V, \{N_i\})$ is a fundamental equation, X must be some function of S , V , and $\{N_i\}$.

The second law of thermodynamics may be written in an alternative form, known as “the principle of entropy maximization”: “At a constant value for energy, in thermodynamic stability the entropy is maximized.” It is always possible to invert the equation for U to obtain $S = S(U, V, \{N_i\}, X)$. To be a maximum, it must be the case that $dS = 0$ and $d^2S \leq 0$. As U is held fixed, if V and $\{N_i\}$ are assumed given,

the equilibrium value of any unconstrained variable X must satisfy

$$\left. \frac{\partial S}{\partial X} \right|_{U,V,\{N_i\}} = 0 \quad (2.63)$$

$$\left. \frac{\partial^2 S}{\partial X^2} \right|_{U,V,\{N_i\}} \leq 0, \quad (2.64)$$

which will yield an equation $X = X(U, V, \{N_i\})$.

For entropy maximization to occur, it must be the case that

$$S(U, V, N) \geq \frac{1}{2} \left(S(U - \Delta U, V, N) + S(U + \Delta U, V, N) \right) \quad (2.65)$$

for all ΔU ; otherwise, the system could increase its entropy by segregating into two systems with $N/2$ particles and volume $V/2$, one with energy $(U + \Delta U)/2$ and the other with energy $(U - \Delta U)/2$.¹⁸ This condition leads to the weaker (but more commonly used) condition

$$\left. \frac{\partial^2 S}{\partial U^2} \right|_{V,\{N_i\}} \leq 0. \quad (2.66)$$

This argument is easily extended to N_i and V , and the entropy is a concave function of energy, volume, and particle number.¹⁹

It can be shown using properties of the differential that these equations may be reformulated to read

$$\left. \frac{\partial U}{\partial X} \right|_{S,V,\{N_i\}} = 0 \quad (2.67)$$

$$\left. \frac{\partial^2 U}{\partial X^2} \right|_{S,V,\{N_i\}} \geq 0, \quad (2.68)$$

where entropy is held fixed, and

$$U(S, V, N) \leq \frac{1}{2} \left(U(S - \Delta S, V, N) + U(S + \Delta S, V, N) \right), \quad (2.69)$$

¹⁸This is in fact an example of a tie-line construction of phase co-existence, which will be discussed later.

¹⁹There is no constraint on the first derivative, as there was for unconstrained variables, as U , V , and N_i are constrained variables, and therefore their differentials are 0 and automatically satisfy $dS = 0$.

implying

$$\left. \frac{\partial^2 U}{\partial S^2} \right|_{V, \{N_i\}} \geq 0, \quad (2.70)$$

with similar relations for V and $\{N_i\}$, and energy is convex in entropy, volume, and particle number.

2.2.5 Legendre Transforms and Free Energies

The energy expressed as a fundamental equation contains only extensive variables S , V , and $\{N_i\}$. However, if the system is in thermodynamic equilibrium, rescaling all variables by some parameter t must increase U by that same factor as well, as energy is extensive. Thus

$$U(\lambda S, \lambda V, \{\lambda N_i\}) = \lambda U(S, V, \{N_i\}). \quad (2.71)$$

Because the system is in thermodynamic equilibrium, this equation must hold for all λ , which gives it the property of being a “homogeneous function of the first order”. By Euler’s Homogeneous Function Theorem, the equality

$$U(S, V, \{N_i\}) = S \frac{\partial U}{\partial S} + V \frac{\partial U}{\partial V} + \sum_i N_i \frac{\partial U}{\partial N_i} \quad (2.72)$$

holds. Using Equation 2.62, the energy may be expressed as

$$U(S, V, \{N_i\}) = TS - pV + \sum_i \mu_i N_i. \quad (2.73)$$

This expression for energy is usually unsuitable for manipulation. Manipulation of entropy and volume are indirect processes; other quantities such as temperature and pressure are controlled to obtain a desired entropy or volume. Despite energy’s fundamental importance to building the framework of thermodynamics, other fundamental equations will be needed for practical applications and modeling. The generation of other fundamental equations suitable for a particular set of constrained variables is known as a “Legendre transform”, where the fundamental equation U is transformed

to a new fundamental equation U' depending on $a = \partial U / \partial A$, an intensive quantity, via

$$U' = U - aA. \quad (2.74)$$

Whether this quantity has any physical meaning depends on the problem in question. Suitable Legendre transforms are called “free energies”. What gave energy its thermodynamic significance is that its mathematical expression is a fundamental equation, from which all thermodynamic quantities may be derived. Free energies have the same significance, only for a more natural list of constrained variables known as their “ensembles”. To make this concept more concrete, two important examples follow.

The Helmholtz Free Energy A

The first troublesome quantity is entropy. There is no direct way to measure entropy, but its conjugate quantity, temperature, is relatively easy to control, at least conceptually. So we define the Helmholtz free energy

$$A(T, V, \{N_i\}) \equiv U - TS = -pV + \sum_i \mu_i N_i. \quad (2.75)$$

Its equations of state for p and μ_i are similar to U , but with different controlled variables:

$$p = - \left. \frac{\partial A}{\partial V} \right|_{T, \{N_i\}} \quad (2.76)$$

$$\mu_i = \left. \frac{\partial A}{\partial N_i} \right|_{T, V, \{N_j\}}. \quad (2.77)$$

But as temperature is now a controlled quantity, entropy becomes a partial derivative with a new equation of state,

$$S = - \left. \frac{\partial A}{\partial T} \right|_{V, \{N_i\}}. \quad (2.78)$$

When using the Helmholtz free energy, T , V , and $\{N_i\}$ define the ensemble.

The Gibbs Free Energy G

Transforming away both entropy and volume yields the Gibbs free energy

$$G(T, p, \{N_i\}) = U - TS + pV = \sum_i \mu_i N_i. \quad (2.79)$$

The partial derivatives are

$$V = \left. \frac{\partial G}{\partial p} \right|_{T, \{N_i\}} \quad (2.80)$$

$$\mu_i = \left. \frac{\partial G}{\partial N_i} \right|_{T, p, \{N_j\}} \quad (2.81)$$

$$S = - \left. \frac{\partial G}{\partial T} \right|_{p, \{N_i\}}. \quad (2.82)$$

Here T , p , and $\{N_i\}$ define the ensemble.

2.2.6 Stability of Free Energies and Additional Thermodynamic Quantities

For a free energy F , the condition of stability must be slightly amended, as it was generated from the energy using a Legendre transform. For an extensive variable X , the stability condition is identical to that of the energy,

$$\frac{\partial^2 F}{\partial X^2} \geq 0, \quad (2.83)$$

and the free energy is convex in X . However, for intensive variables x , the free energy is concave in x :

$$\frac{\partial^2 F}{\partial x^2} \leq 0. \quad (2.84)$$

The first derivatives of the free energies have been previously given a physical meaning. The second derivatives also have physical meaning for certain free energies, and in these contexts they are known as “susceptibilities”. Two important susceptibilities are the heat capacity C , an extensive measure of the heat flow necessary to change temperature,

$$C \equiv \frac{\delta Q}{dT} = T \frac{dS}{dT}, \quad (2.85)$$

and the bulk modulus K , an intensive measure of the change in pressure upon expansion/contraction of the system,

$$K \equiv -V \frac{dp}{dV}. \quad (2.86)$$

Both assume a particular process is being carried out, the former that temperature is changing and the later that volume is changing, but knowledge of the other constrained variable are necessary to convert these into proper thermodynamic quantities. It is usually assumed that particle number is fixed, so the heat capacity may be evaluated at fixed pressure C_p or fixed volume C_V , and the bulk modulus may be evaluated at fixed temperature K_T or fixed entropy K_S . Each quantity suggests a natural ensemble,

$$K_T = V \left. \frac{\partial^2 A}{\partial V^2} \right|_{T, \{N_i\}} \quad (2.87)$$

$$K_S = V \left. \frac{\partial^2 U}{\partial V^2} \right|_{S, \{N_i\}} \quad (2.88)$$

$$C_V = -T \left. \frac{\partial^2 A}{\partial T^2} \right|_{V, \{N_i\}} \quad (2.89)$$

$$C_p = -T \left. \frac{\partial^2 G}{\partial T^2} \right|_{p, \{N_i\}}. \quad (2.90)$$

The stability criteria requires all four of these quantities to be positive, and the specific heat and bulk modulus must always be non-negative.

2.2.7 Ensemble Averages, the Microcanonical Ensemble, and the Ideal Solution

Thermodynamics and statistical mechanics were founded to explain why macroscopic phenomena exhibits predictable behaviors, even though the microscopic phenomena are often chaotic at the atomic scale. The system will have at any given moment some instantaneous configuration, its “microstate”. Classically, the microstate is some function of the $3N$ position variables and $3N$ momentum variables, which combined

denote its position in “phase space”²⁰. The energy as a function of the microstate is usually straightforward to write down, but the large number of degrees of freedoms (scaling with number of particles) for a microstate makes this intractable for actual computation.

For an isolated system, all thermodynamic state variables, including the energy, remain constant. Though the microstate is continuously evolving, this evolution is restricted to the set of all microstates with the same thermodynamic constrained state variables, the “macrostate”. However, though the system is in a definite microstate at any given time, if the laws of thermodynamics are valid, it shouldn’t matter which microstate the system is in as long as it is consistent with the macrostate! This suggest an assumption: as a calculational tool, it may be assumed that the system is equally likely to be in any microstate consistent with the macrostate. The assumption that the time average of the system is equivalent to the average over microstates is known as “ergodicity”. Instead of working with a definite microstate, the system may be taken to be a “microcanonical ensemble average”, with all possible microstates associated with a given macrostate equally contributing.

The more possible microstates the system can be in, the more disordered it will appear to an observer, suggesting that the number of microstates $\Omega(U, V, \{N_i\})$ for the given macrostate is related to the entropy. This insight led Ludwig Boltzmann (1877) to propose that the entropy has a form

$$S(U, V, \{N_i\}) = k_B \ln \Omega(U, V, \{N_i\}), \quad (2.91)$$

where $k_B = 1.38 \times 10^{-23} J/K$ is the Boltzmann constant. For systems with quantized degrees of freedom (such as quantum mechanical systems or lattice models), the number of microstates can be explicitly enumerated (at least in theory). For continuum

²⁰Here the Heisenberg uncertainty relation may be neglected, as the quantities of interest for phase stability are ions, which under the Born-Oppenheimer approximation may be treated as classical particles.

models where the degrees of freedom are continuous, this becomes

$$\Omega(U, V, \{N_i\}) = \frac{\int d^{3N} \mathbf{r} d^{3N} \mathbf{p} \rho(\{\mathbf{r}\}, \{\mathbf{p}\})}{\omega_0}, \quad (2.92)$$

where

$$\rho(\{\mathbf{r}\}, \{\mathbf{p}\}) = \begin{cases} C & U - \frac{\Delta}{2} < H(\{\mathbf{r}\}, \{\mathbf{p}\}) < U + \frac{\Delta}{2} \\ 0 & \text{otherwise} \end{cases}, \quad (2.93)$$

ω_0 is some constant depending only on particle number, H is the Hamiltonian, C is some constant, and Δ is an arbitrarily small quantity whose dependence should cancel during the course of the calculation. Ω here is the volume of phase space occupied by a energy range of width Δ about U , renormalized by a “phase space volume per microstate” quantity ω_0 .

To demonstrate a simple example of how the entropy function may be generate from the number of microstates, take the simple concrete example of the binary ideal solution or binary “lattice gas” model. The binary ideal solution consists of two particle types A and B, with particle numbers N_A and N_B , constrained to lie on a lattice with $N = N_A + N_B$ sites. The particles are assumed to be non-interacting and all lattice sites are equivalent, so that any particle may occupy any site. The macrostate here corresponds to particle numbers N_A and N_B . The number of possible microstates for such a macrostate is the binomial coefficient

$$\Omega(U, V, N_A, N_B) = \frac{N!}{N_A! N_B!}, \quad (2.94)$$

yielding an entropy of

$$S(U, V, N_A, N_B) = k_B (\ln N! - \ln N_A! - \ln N_B!). \quad (2.95)$$

Ω should grow exponentially with number of particles for entropy to be an extensive quantity, but in this form it does not. It is necessary to go to the thermodynamic limit where $N \rightarrow \infty$ to achieve the proper scaling of quantities. Using the Stirling approximation $\ln N! \approx N \ln N - N$ (valid for large N), the entropy reduces to

$$S(U, V, N_A, N_B) = k_B \{N \ln N - N_A \ln N_A - N_B \ln N_B\} = -N k_B \{x_A \ln x_A + x_B \ln x_B\}, \quad (2.96)$$

where $x_i \equiv N_i/N$ is the concentration of species i . This form has the proper scaling with N . This entropy is known as the “ideal solution entropy”, the “ideal entropy of mixing”, or the “ideal entropy”. As it has a simple closed form, it is commonly used for modeling, and most experimental measurements of entropy report the entropy as the deviation from this ideal formula, known as the “excess entropy”. The ideal entropy is the upper limit for entropy in lattice based models. Introducing interactions between particles will cause particles to be either attracted or repelled from one another, which will order the system in some way. This decreases the number of possible microstates, decreasing the total entropy. This quantity is convex in $x_A = 1 - x_B$, is maximized at $x_A = x_B = 0.5$, and is zero at $x_A = 0$ or $x_B = 0$, with tangent lines having infinite slopes there. This also gives a measure of the scale of the entropy per particle for a (binary) system, as $s \leq k_B \ln 2 \approx 6 \times 10^{-5}$ eV/K.

Taking the derivative of entropy with respect to either N_A or N_B yields the relation

$$\mu_\alpha = k_B T \ln x_\alpha \quad (2.97)$$

for species $\alpha = A$ or B . As the ideal solution is the conceptual basis of much of practical thermodynamics, certain disciplines will generalize this relation for arbitrary systems, in form

$$\mu_\alpha = k_B T \ln a_\alpha = k_B T \ln \gamma_\alpha x_\alpha. \quad (2.98)$$

a is known as the “activity” and γ the “activity coefficient”, the later measuring deviation from ideality where $\gamma = 1$. For $\gamma > 1$, the system acts as if there are fewer particles of a given species than there actually are, and for $\gamma < 1$, the system acts as if there are more particles of a given species than there actually are, hence the nomenclature. For an ideal solution at $T > 0$, the chemical potential for α at $x_\alpha = 0$ will be negative infinity, signalling a strong free energetic preference for the system to absorb α if possible. If the system is brought into contact with any other system containing α , equilibration will necessarily leech some of α from the other system. At $x_\alpha = 1$, the opposite occurs. The chemical potential is 0²¹, and the energy may freely

²¹More generally, it goes to some constant which may be set to be the zero of energy.

remove small quantities of α at no free energetic cost.

The preceding discussion was in fact a restatement of the principle of entropic maximization and thus applies to arbitrary systems. To reach chemical equilibrium, the equilibrium concentration in either system is given by integrating the Gibbs-Durham relation $0 = \sum_i N_i d\mu_i$ (assuming fixed temperature and pressure) for that particular system combined with the constraint that the total particle number is fixed.

2.2.8 The Canonical Ensemble

Such explicit enumeration of the number of microstates will not be possible in general, and the microcanonical ensemble is rarely used in practice. Not only is it theoretically difficult to work with, but it is experimentally impractical. Only for thermally shielded systems might it be possible to say that energy is a fixed parameter. When two normal system are brought together, their temperatures will equilibrate. If one of the systems is sufficiently large, its intensive parameters should not be appreciably affected by the equilibration process, and it acquires the moniker “reservoir”. If a system is brought into contact with a reservoir, and the volumes and particle numbers of both systems are held fixed (using rigid, impermeable containers, for example), then one can use the reservoir to control the temperature of the system, as the system will equilibrate to the temperature of the reservoir. The controlled quantities are now T , V , and $\{N_i\}$ for the system, yielding the “canonical ensemble”.

Energy is no longer controlled, and will in fact fluctuate over time in both systems. In the microcanonical ensemble, it was argued that all microstates are equally likely, and thus the probability to be in a particular microstates is $\Omega(E, V, \{N_i\})^{-1}$. Via conservation of energy, additivity of the entropy, and the requirement that only heat be exchanged between the system and the reservoir, it can be shown that the probability for the system to be in a particular microstate with energy E_j in the canonical ensemble is

$$p_j = e^{\beta(U-TS(U))} e^{-\beta E_j}, \quad (2.99)$$

where U is the ensemble/time averaged energy of the system and $\beta \equiv 1/k_B T$. As probability must normalize to one and $A \equiv U - TS$,

$$e^{-\beta A} = \int dE g(E) e^{-\beta E} \equiv Z(T, V, N). \quad (2.100)$$

where $g(E)$ is the density of states of the system, and the second term becomes a discrete sum in the case of quantized degrees of freedom. The quantity Z is known as the “partition function”, and rewriting it yields the simple-yet-powerful relation

$$A(T, V, N) = -k_B T \ln Z(T, V, N). \quad (2.101)$$

2.2.9 The Partition Function in Detail

It cannot be stressed enough how important the partition function is for statistical mechanics. Though it may have a complicated closed form solution, in principle the partition function can always be written down for any given energy model, and the Helmholtz free energy can be calculated. For the values of pressure in most condensed matter applications, below 10 GPa, the pressure dependence of the Gibbs free energy is negligible, and the pressure may be safely taken to be zero. For zero pressure, the Helmholtz free energy is numerically equal to the Gibbs free energy, and

$$G(T, p \approx 0, \{N_i\}) = -k_B T \ln Z, \quad (2.102)$$

where the free energy is now expressed in terms of variables (relatively) easy to control experimentally. As the functional form of the Helmholtz (and Gibbs) free energies form a fundamental equation in the proper ensembles, it follows that *all thermodynamic quantities may be derived from the partition function*. For simplicity in the following discussion, it will be assumed the partition function is a sum over discrete states.

The energy spectrum of the system $\{E_j\}$ must be bounded below for the system to be stable. Thus there is some lowest energy E_0 , and it is common to factor this

out of the partition function,

$$Z = e^{-\beta E_0} \sum g(E_j) e^{-\beta(E_j - E_0)} \rightarrow e^{-\beta E_0} Z, \quad (2.103)$$

where $\beta \equiv 1/(k_B T)$, yielding a free energy of

$$A(T, p, \{N_i\}) = E_0 - k_B T \ln Z. \quad (2.104)$$

This redefinition of Z is equivalent to changing the zero of energy.

This new formalism gives the general behavior of any system with respect to temperature. The probability that a system will have an energy E_j is

$$p(E_j) = g(E_j) p_j = g(E_j) e^{-\beta E_j} / Z, \quad (2.105)$$

The quantity $g(E_j) e^{-\beta E_j}$ is known as the ‘‘Boltzmann factor’’, and it is proportional to the probability of occupation. The quantity $k_B T$ is an approximate measure of the energy scale for the entropic contribution to energy, and how likely a state is to be occupied is determined by its energy relative to $k_B T$. Microstates with lower energies will have a higher occupancy than states with higher energies, and the distribution occurs in an exponential fashion,

$$p_i / p_j = e^{-\beta(E_i - E_j)}. \quad (2.106)$$

In the $T \rightarrow 0$ limit, only the microstates with the lowest possible energy E_0 will be occupied, and

$$A(0, p, \{N_i\}) = E_0. \quad (2.107)$$

Furthermore, at $T = 0$, the partition function will be equal to the degeneracy of the ground state, $Z = g(E_0)$. At $T = 0$, the entropy is

$$S(0, p, \{N_i\}) = \frac{\partial A}{\partial T} = k_B \ln Z = k_B \ln g(E_0). \quad (2.108)$$

By the Third Law, $S(T = 0)/N = 0$, and the ground state of the system must have sub-extensive degeneracy, $\lim_{N \rightarrow \infty} g(E_0)/N = 0$. In this limit, the free energy of the system is dominated by energetic effects: $A \approx U$.

In recent years, this assertion has become controversial, as certain models for geometric frustrated systems have degenerate ground states while seeming to obey all other laws of physics and the first three Laws of Thermodynamics (including the Zeroth). In all reported cases, this has been solved by inclusion of additional interactions or different structures which break the degeneracies and restore agreement with the Third Law of Thermodynamics. One famous example is Pauling's model for ice [41], and a brief digression here is needed. In conventional ice, H_2O molecules reside on a hexagonal lattice, with the oxygen atoms occupying the vertices. It is optimal for the oxygen atoms to close their valence shell by bonding with two additional hydrogens from other H_2O molecules. However, due to geometric frustration, in the hexagonal lattice it is not possible to do this in a well-ordered structure, and it is relatively simple to show the resulting disordered structure has a residual entropy per molecule of $s = k_B \ln 3/2$ at 0 K, which was in line with experimentally observed values. It turns out, however, that the ice we humans know and love is actually ice Ih, one of the (at present) 14 different solid phases for H_2O . The true 0 K structure for ice is ice XI [42], a well-ordered orthorhombic variant of ice Ih with no residual entropy, and thus the Third Law of Thermodynamics is preserved. Why this was not observed is that ice Ih's geometric frustration makes it difficult to undergo the mechanism by which ice Ih transitions into ice XI, as each H_2O is locally in the most optimal state, and it is difficult to reach equilibration on experimental time scales. This only highlights the necessity of using theoretical methods to understand phase diagrams at low temperatures and not relying strictly on experimental results.

Nevertheless, this has caused some speculation that the Third Law of Thermodynamics is not a physical law. Supporting this is the Third Law of Thermodynamics's status as a newcomer: it is the newest of the Laws of Thermodynamics, only appearing in this form after quantum mechanics had already been formulated and the bulk of statistical mechanics had already been derived. However, without the Third Law of Thermodynamics, the universal tendency of materials to crystallize at low temper-

atures would be accidental rather than fundamental²², violating the main unspoken law of physics, “that which is not expressly prohibited will occur”.

As $T \rightarrow \infty$, if the energy spectrum $\{E_j\}$ is bound above, then

$$e^{-\beta E_j} \rightarrow 1, \quad (2.109)$$

which implies

$$Z \rightarrow \sum_i g(E_i) \equiv N_{micro}, \quad (2.110)$$

This suggest that the partition function has as a physical interpretation the number of states that are thermally accessible. At 0 K, only the ground state is occupied, but as temperature increases, more and more states become occupied, eventually reaching full saturation in the $T \rightarrow \infty$ limit. Indeed, in this limit all microstates are equally likely to be occupied,

$$p_j \rightarrow 1/N_{micro}, \quad (2.111)$$

That all microstates are equally occupied suggests that the entropy should be maximal in the high temperature limit. In this limit, the Helmholtz free energy becomes

$$U - TS = A \rightarrow -k_B T \ln N_{micro}. \quad (2.112)$$

As U is bounded above and S is strictly increasing in temperature, for sufficiently large T , U may be neglected, and $A \approx -TS$; the free energy is dominated by entropic effects. As this free energy is independent of U , the principle of entropic maximization ensures that the entropy attained in this limit must be the maximum value attainable for the system, which is

$$S = k_B \ln N_{micro}. \quad (2.113)$$

The partition function also allows for the calculation of various quantities. Suppose there is some physical quantity O that, for each microstate j , takes on a definite

²²An important exception is quantum liquids like He₄ which are the low temperature phases of the associated system, however, their low temperature states are special low entropy superfluids.

value O_j . If this observable is measured over a long enough time scale, by the principle of ergodicity, all states should be sampled according to the ensemble probability spectrum. Then the measurement of O is given by the weighted average of the O_j over the ensemble probability spectrum p_j ,

$$\langle O \rangle = \sum_j p_j O_j = \sum_j \frac{O_j e^{-\beta U_j}}{Z}. \quad (2.114)$$

In particular, the expectation value of energy is

$$\langle U \rangle = \sum_j \frac{U_j e^{-\beta U_j}}{Z} = -\frac{\partial(\ln Z)}{\partial\beta}. \quad (2.115)$$

The expectation value $\langle O \rangle$ for an observable may be fixed due to symmetry considerations. However, this does not imply that the observable must be fixed in time, as it may fluctuate about its expectation value. A measure of the strength of its fluctuations about $\langle O \rangle$ is its susceptibility, which generally has the form

$$\chi_O \propto \langle O - \langle O \rangle \rangle^2 = \langle O^2 \rangle - \langle O \rangle^2. \quad (2.116)$$

By the principle of ergodicity, the averages in Equation 2.116 can be taken to be either time or ensemble averages. An important example is C_V , which may be calculated using

$$C_V = T \frac{\partial^2}{\partial T^2} k_B T \ln Z = \frac{1}{k_B T^2} (\langle U^2 \rangle - \langle U \rangle^2). \quad (2.117)$$

If the free energy $F = -k_B T \ln Z$ is given, the first equality may be used, and if the time averages (obtainable from molecular dynamics simulations) or equivalently the ensemble averages (obtainable from Monte Carlo simulations), are given, the second equality may be used.

2.3 The (Classical) Theory of Phase Transitions and Free Energy Modeling²³

²³References specializing in both classical and modern approaches (discussed in the next section)

2.3.1 Phase Transitions: An Overview

The preceding implicitly assumed that the free energy is differentiable, as various measurable physical quantities were related to the derivatives of free energy. However, it is *not* the case that the free energy of the system is everywhere differentiable. For particular values of the constrained variables, some order of derivatives of the free energy can be discontinuous, and abrupt changes will be seen in thermodynamic quantities.

This leads to a formal definition of a phase. If there exists some chain of analytic continuations of the free energy linking two sets of values for ensemble variables, then the system is said to be in the same phase for both sets of ensemble variables. If no such chain of analytic continuations link two sets of values for ensemble variables, the system is said to be in different phases for those two sets of values. This would be rather difficult to prove, and thankfully there is an easier way. If no such chain of analytic continuations exist, there must be a “phase boundary” between two sets of variables where some order of derivatives of the free energy is undefined. If one finds the phase boundaries, one has found the phases as well, and it is only necessary to examine where the free energy of the system shows non-analytic behavior.²⁴

2.3.2 Phase Competition and Free Energy Minimization

To understand why this occurs, it is important to note that thermodynamic stability and thermodynamic equilibrium are not equivalent concepts. Returning to the example of bulk carbon, the thermodynamically stable free energy has discontinuities in derivatives when the graphite phase transitions to the diamond phase. However,

to phase transitions include [43, 44, 45, 46, 47], and a general treatment exists in all references mentioned in the thermodynamics and statistical mechanics sections.

²⁴It is not necessarily the case that discontinuities imply a phase transition, however. One example is near the critical point for water, where the “phase boundary” between “liquid” and “gaseous” phases abruptly ends, and an analytic continuation around the “phase boundary” endpoint can be done, showing that liquid and gaseous water are in fact the same “fluid” phase.

the free energy of graphite does not abruptly end where the free energy of diamond begins. As mentioned in the Introduction, a phase can be meta-stable and exist under conditions where formally it is unstable. It is still in thermodynamic equilibrium, the free energy can be written down, and the system can absorb heat and do work.

If more than one phase can be defined under the same set of conditions, which one is thermodynamically stable? By the Second Law of Thermodynamics, it will be the phase that maximizes entropy given constant energy or, equivalently, minimizes energy given constant entropy. Suppose there are multiple possible phases, indexed by α , and the system must be in one of these phases, which in the canonical ensemble have free energies of:

$$A(T, V, \{N_i\}, \alpha) = U(S, V, \{N_i\}, \alpha) - TS(S, V, \{N_i\}, \alpha). \quad (2.118)$$

These phases are said to be “competing”. The right hand side is written in terms of entropy and energy, and thus the principle of maximal entropy may be applied with respect to α . The principle of maximal entropy holds U fixed, and the value of α that maximizes S for this value of U also minimizes A . Therefore the stable phase at constant temperature, volume, and $\{N_i\}$ is the phase that minimizes the Helmholtz free energy. This may also be done for the enthalpy and the Gibbs free energy in their appropriate ensemble, yielding “the principle of free energy minimization”:

Given a set of competing phases, the thermodynamically stable phase is the phase that minimizes the free energy in the appropriate ensemble.

Under this formulation, where a phase transition occurs, the free energy of the two phases must be equal. As one moves away from the phase boundary in one direction, one phase has a lower free energy and is stable, and as one moves in another direction, another phase has a lower free energy and is stable.

This method seems different from finding discontinuities in some order of derivatives in the free energy of the system. It is in fact equivalent, if the free energies of each phase are assumed to be analytic functions²⁵. Where a phase transition occurs,

²⁵It is important to note that under this assumption the free energies of the *phases* are analytic,

the stable phase will switch from one phase to the other. By the theory of analytic functions, if at any point two functions have the same value for all orders of derivatives, they must be the same function. That the phase has changed means that while the free energies at the phase transition are identical, they are not the same function, and at a phase boundary, some order of some derivative of the free energy of the system must abruptly change, yielding discontinuities.

2.3.3 Phase Segregation, Coexistence, and the General Behavior of Phase Transitions

There is another possibility, that the system is in a state of “phase co-existence” or “phase segregation”. Which one occurs depends on the dynamics of the phase transition, and from the standpoint of free energy modeling they are equivalent²⁶. In either case, multiple phases i , each occupying a volume V_i with free energy F_i , may appear in the system²⁷. By extensivity, $V = \sum_i V_i$, where V is the total volume of the system, and the free energy F of the system becomes

$$F(V, \{V_i\}, X, \{X_i\}) = \sum_i F_i(V_i, X_i) \equiv \sum_i V_i f_i(x_i), \quad (2.119)$$

where for the sake of clarity only one other extensive variable X has been explicitly included in the ensemble, X_i is its value for phase i , $x_i \equiv X_i/V_i$, and $f_i \equiv F_i/V_i$ is the free energy density. It is necessary to include at least one extensive variable X in this definition, as if V were the only non-varying extensive variable, the system would

but the free energy of the *system*, the thermodynamically stable free energy, will not in general be analytic.

²⁶Formally, phase co-existence/segregation is considered its own phase separate from the phases forming the expansion of its free energy. However, it is common informally to describe it as a collection of multiple phases

²⁷It is also possible for the same phase to segregate into co-existence between two sets of values for ensemble variables if the free energy curve for the phase is not convex, but the formalism to calculate this type of co-existence is identical to the one described here.

always choose the phase with the lowest f_i . x_i here are unconstrained variables, and the principle of free energy minimization may be invoked to determine their values. As phase co-existence necessarily implies more than one phase, this system must have some characteristic length scale where it is no longer homogeneous. However, in the thermodynamic limit, this length scale has been washed out and the system is considered a homogeneous mixture of the constituent phases.

The determination of the x_i 's is accomplished using the process of “common tangent construction”. Consider the case where only two phases A and B are likely to co-exist, with free energies densities f_A and f_B . Assuming x is a conserved quantity (i.e. externally constrained), all possible phase co-existence free energies have the form

$$f_{A+B}(x, x_A, x_B) = \frac{1}{x_A - x_B}((x - x_B)f_A(x_A) + (x_A - x)f_B(x_B)), \quad (2.120)$$

where x_A and x_B are unconstrained, and without loss of generality it is assumed $x_A \leq x \leq x_B$. This physically corresponds to a system with some mixture of phase A at x_A and phase B at x_B , weighted to give the externally constrained value for x . At $x = x_A$, the system is completely in phase A, and at $x = x_B$ the system is completely in phase B. This free energy curve ties the two phases together, giving it the name “tie line” in the literature. The values of x_A and x_B that stabilize A and B co-existence must minimize f_{A+B} . A necessary condition is that $f_{A+B}(x)$ lies tangent to f_A at $x = x_A$ and f_B at $x = x_B$, as otherwise either x_A or x_B could be shifted to further minimize the free energy.

This construction gives three possible behaviors for phase transitions. The first is trivial: over the range of physically valid x , phase A always has a lower free energy than phase B . No phase transition is observed in this case. The second case is phase co-existence/segregation, where a tie line can be constructed between the two phases, and this tie line smoothly transitions the system from one phase to the other. The final case is the $x_A = x_B$ case. That is, the two phases meet at some value x_0 where both the free energy and the first derivatives are equal, but for $x > x_0$ the free energy

of A exceeds B, and for $x < x_0$ the free energy of B exceeds A. Here the phase transition is abrupt.

2.3.4 The Landau Formalism for Phase Transitions

The tie-line construction characterizes the general behavior of a “first-order phase transition”. One such example is melting ice in the Gibbs ensemble. As some constrained variable is changed (in this example, temperature), one or more first order derivatives must experience a jump discontinuity (here, entropy and volume). This does not imply that during the process the thermodynamic quantities are discontinuous, rather that there is some subprocess (in this example, adding heat) where various state variables smoothly vary while the values for the chosen ensemble variables remain fixed, and thus the free energy in that particular ensemble does not change. While the subprocess is occurring, phase co-existence/segregation occurs (water co-exists with ice), until eventually the entire system has converted from one phase to another. From the viewpoint of a different ensemble (say, the microcanonical ensemble whose “free energy” is entropy), the free energy will change during this subprocess, this subprocess traversing the tie line between the two phases. Some kind of work or heat is flowing into the system to cause it to change phase, even though from the standpoint of the original ensemble (the Gibbs ensemble), the process appeared to occur abruptly.

But not all phase transitions see jump discontinuities in first-order derivatives. There are phase transitions where no jump discontinuities are seen until the n^{th} derivative, with associated names “second-order”, “third-order”, etc. During the phase transition, discontinuities and peaks emerge only in the n^{th} derivative of the free energy. In particular, the internal energy and the entropy remain constant, earning the name “continuous phase transitions”. Unlike first-order transitions, there is no observed phase co-existence and no work or heat flow. But something must be happening to the system to cause it to undergo a phase transition.

This puzzled physicists for a considerable length of time until Landau (1937) devised his theory of symmetry breaking [48], which is now considered one of the cornerstones of condensed matter physics. Landau hypothesized that what was changing in the system was the symmetry, and he proposed a phenomenological method to model the phase transition. This type of phase transition is known as an “order-disorder transition” and occurs when a system goes from a low symmetry phase (order) to a high symmetry phase (disorder). It is usually the case that the high temperature phase is the high symmetry phase due to entropic enhancement, but this is not required by the laws of thermodynamics, and exceptions exist.

Landau proposed that the relevant quantity to study second-order and higher phase transition was the “density function” ρ . The density function depends on the system under consideration, and the only requirement is that its thermodynamic average ρ^0 obeys the symmetry operations of the system (and only those symmetry operations) and that the free energy of the system be expandable in terms of ρ near the phase transition point.

ρ^0 is not a fixed quantity and will change as the constrained variables are varied, but as long as it is in a particular phase, it will always obey that phase’s symmetry operations. In the language of group theory, ρ^0 belongs to the invariant irreducible representation (invariant irrep) of the space group. However, at any time the instantaneous density function $\rho = \rho^0 + \delta\rho$ differs from the thermodynamic average ρ^0 by an instantaneous fluctuation $\delta\rho$.

The low symmetry phase and high symmetry phases will have different equilibrium density functions, ρ_{LS}^0 and ρ_{HS}^0 . Landau’s insight was that at the phase transition, the system must belong to both space groups simultaneously, hence the low symmetry space group must be a proper subset of the high symmetry space group, known as the “compatibility criterion”. Thus ρ_{HS}^0 must satisfy all symmetry operations of the low symmetry group (ρ_{HS}^0 belongs to the invariant irrep of the low symmetry group) but ρ_{LS}^0 will only satisfy all symmetry operations of the high symmetry group at one

point, the phase transition point (ρ_{LS}^0 only belongs to the invariant irrep of the high symmetry group at the phase transition point).

Define $\rho^0 \equiv \rho_{HS}^0 + \delta\rho$. In the high symmetry phase, $\delta\rho = 0$, but as one transitions into the low symmetry phase, $\delta\rho$ will become non-zero, because if it did not, then the high-symmetry and low-symmetry phases would have the same symmetry operations, invalid by assumption. From the viewpoint of the high symmetry phase, $\delta\rho$ is a fluctuation away from the thermodynamic average ρ_{HS}^0 , as it will break some symmetry of the high symmetry phase, but in the low symmetry phase it is viewed as part of the thermodynamic average ρ_{LS}^0 . That is, what was an instantaneous fluctuation in the high symmetry phase has become part of the equilibrium density in the low symmetry phase. *The physical mechanism of a second-order (and higher) phase transition is stabilization of a particular instantaneous fluctuation in the density function that lowers the free energy.*

One may characterize this $\delta\rho$ function, and thus whether the system is in a state of order or disorder, using an “order parameter” η , a number related to $\delta\rho$ ’s magnitude. Assuming analyticity, the free energy can be expanded in a power series of η , from which Landau used group theoretic and symmetry arguments to derive the form (assuming here for concreteness that phase transition is temperature-driven, and taking the usual case where the high temperature phase is the high symmetry phase):

$$G = G_0 + \frac{A}{2}(T - T_C)\eta^2 + G_4\eta^4 + O(\eta^5). \quad (2.121)$$

where $A > 0$ and $G_4 > 0$. In particular, it is asserted that the η^3 term must vanish by symmetry, which in group theoretic language is the assertion that $(\delta\rho)^3$ does not contain the invariant irrep for the high symmetry group, the “stability or Landau criterion” [49]. This may be determined by usage of character tables and the appropriate orthogonality relations from group theory without any knowledge of the physics of the system. If this term is not excluded by symmetry, in all but the most pathological of instances, the phase transition associated with this symmetry transformation is first-order.

By construction, thermodynamic stability gives η a temperature dependence of

$$\eta = \begin{cases} \sqrt{\frac{-A(T-T_C)}{4G_4}} & T < T_C \\ 0 & T \geq T_C \end{cases}. \quad (2.122)$$

This leads to the well-known result that mean field modeling has a “critical exponent” $\beta = 1/2$ for the dependence of the order parameter on temperature near the critical point. Deviations away from this critical exponent are hallmarks of non-analytic behavior of the free energy. This non-analytic behavior only affects the free energy near the phase transition point, and the mean field formalism generally overestimates the critical temperature by 10-20%. Substituting this back into the free energy equation yields

$$G = \begin{cases} G_0 - \frac{A^2(T-T_C)^2}{16|G_4|} & T < T_C \\ G_0 & T \geq T_C \end{cases}. \quad (2.123)$$

This free energy does not exhibit a jump discontinuity in the first derivative with respect to temperature, the entropy, but it does experience a jump discontinuity of $A^2T_C/8|G_4|$ in the second derivative with respect to temperature, the heat capacity. Importantly, this jump discontinuity scales linearly with particle number, as A and G_4 (when expressed as extensive quantities) scale linearly with particle number. This jump discontinuity does not disappear in the thermodynamic limit.

This jump discontinuity in the second derivative arises because the first and third order terms are excluded by symmetry, and the second order term is linear in temperature. If the coefficients for the free energy were expanded in other ensemble variables p or $\{N_i\}$, it will still be the case that the third order terms must be excluded by symmetry as this arose solely from group theoretic considerations, but the expansion of the second order term may be constant or linear to lowest order depending on the shape of the phase boundary. Thus the first derivatives for the ensemble variables p and $\{N_i\}$ must also be continuous at the phase transition point, and this phase transition for this model is second order with the jump discontinuity in the “specific

heat”, the heat capacity per particle, and possible discontinuities in other higher-order derivatives.

2.3.5 Free Energy Modeling

So how are free energies obtained computationally? One way is through “free energy modeling”. The fundamental characteristic of free energy models is that they are *phenomenological* by nature. Formally, to derive the thermodynamically stable free energy of the system, one would write down the internal energy and entropy dependent on the $3N$ position variables and $3N$ momentum variables of the carbon atoms. The full partition function is

$$Z = \frac{1}{N!h^{dN}} \int d\mathbf{r}_1 \dots d\mathbf{r}_N d\mathbf{p}_1 \dots d\mathbf{p}_N e^{-\beta U(\mathbf{r}_1, \dots, \mathbf{r}_N; \mathbf{p}_1, \dots, \mathbf{p}_N)}, \quad (2.124)$$

where d is the dimensionality of space. Alternatively, one could write down M many equations linking these $6N$ variables to the M constrained ensemble variables, yielding a total of $6N - M$ unconstrained variables, and minimization of the appropriate free energy over the $6N - M$ unconstrained variables would obtain the thermodynamically stable free energy.

Not only is this method prohibitive as N is in general very large, but it is in many cases overkill, as for a solid phase, only a small portion of phase space will meaningfully contribute to the free energy for the phase. That is, the Boltzmann factor $g(E)e^{-\beta E}$ will be vanishingly small for all but a select regions of values for \mathbf{x}_i and \mathbf{p}_i . For carbon, the two phases of interest are graphite and diamond. Both graphite and diamond occupy a small portion of the configurational portion of phase space, as they are solids with definite equilibrium lattice structures. It is not necessary to know the behavior of the system at all possible locations in phase space, only the behavior of the system in the regions of phase space that are expected to contribute meaningfully to the partition function, due to the decaying exponential in the Boltzmann factor. In addition, it is the phase with the minimum free energy

that is thermodynamically stable. When determining stability, only the free energy *differences* between two phases are relevant, simplifying the necessary modeling. As the Gibbs free energy contains the ensemble variables most suitable for experiment, it will be considered here in the $p \approx 0$ limit, but free energy method applies for other ensembles as well.

The relevant portions of phase space consists of equilibrium lattice structures, the “configurational portion” of the free energy, and the shape of the free energy function near the equilibrium lattice structures, the “phonon portion”. In addition, by introducing temperature, thermal excitation of the electrons into higher energy states is possible, yielding an “electronic portion” for free energy. If the assumption is made that each of these contributions to the free energy are independent of the other, then the associated partition functions will factorize,

$$Z = Z_{config} Z_{phonon} Z_{elect}, \quad (2.125)$$

and the free energies will add linearly,

$$G = G_{config} + G_{phonon} + G_{elect}. \quad (2.126)$$

The free energy of each portion may be calculated separately.

The Configurational Free Energy and Common Solid Phase Models

The configurational portion of the free energy depends on the equilibrium position of the particle, and much of the art associated with free energy modeling comes from determination of the right model for the configurational portion of free energy. If the phase is a solid, the relevant portions of phase space can be expanded around a set of positions for particles, or “configurations”. Modeling the configurational contribution to free energy consists of determining what configurations are expected to contribute appreciably to the free energy, then deriving energy and entropy functions accordingly.

Some of the most common configurational free energy models will be summarized here. For the case of graphite or diamond, there is only one configuration in each case,

the observed equilibrium lattice. The energy is $U = uN$, where u is the energy per particle, and the entropy is zero, as a perfect lattice has no disorder. This is known as a “well-ordered phase” and has a configurational contribution to free energy of $G_c(T, p, N) = uN$. This type of free energy depends only on the total number of particles N even for multi-species phases, as the requirement that the lattice be fixed imposes constant ratios amongst the particle numbers of constituent species.

If a phase has multiple possible configurations, it is known as a “disordered phase”. One example of a disordered phase has already been given, the binary ideal solution model. For the more general ideal solution model where arbitrary number of species are allowed, each configuration is a particular placement of the N_i particles of species i on the lattice with $N = \sum_i N_i$ many sites. This formulation assumes the lattice is fully occupied, as lattice vacancies can be handled naturally by labelling them as a species. For this particular phase model, as there are no interactions, the energy also has form uN , but there is an ideal entropy of mixing $-Nk_B \sum_i x_i \ln x_i$, giving a configurational contribution to the free energy of

$$F_c(T, p, \{N_i\}) = uN + Nk_B T \sum_i x_i \ln x_i. \quad (2.127)$$

Yet another commonly used model is the regular solution model. This is an empirical model where the energy portion of the free energy is fit to the equation (for the binary case)

$$U_c(T, p, N_A, N_B) = N(a_{00} + a_{10}x_A + a_{01}x_B + \sum_{i,j>0} a_{i,j}x_A^i x_B^j), \quad (2.128)$$

where the constant and linear terms have been pulled out of the sum explicitly, and it is assumed that the energy function has weak explicit temperature dependence²⁸, and the pressure is fixed. The generalization to multi-component systems is done by including additional factors for each new specie into the sum. This form is commonly

²⁸This explicit energy dependence may come from, for example, lattice expansion as temperature increases moving particles farther apart. For fitting to experimental data, this constraint may be relaxed.

chosen to model a broad class of phases known as “solid solutions”. For solid solutions, over a large range of values for compositions x_i , particles occupy lattice sites like the ideal solution, but some interaction energy term exists, U . Excluding the constant and linear terms (which, as will be shown later, can be taken to zero), it is commonly observed that the energies of these phases are roughly symmetric about the “equiatomic composition” where all compositions are equal. One such function that displays this symmetry is $x_A x_B$, yielding the lowest order term in the sum. Higher order terms in the sum are used to fit asymmetries.

It is difficult to derive the entropy for such a model directly. However, the ideal entropy of mixing serves as an upper bound for the entropy of a regular solution. Furthermore, as the temperature increases, eventually the entropic contribution to the free energy will dominate the energetic contribution, as the energetic contribution is bounded. In this case, the ideal solution model will be recovered. This motivates rewriting the entropy in form

$$S_c(T, p, \{N_i\}) = S_x(T, p, \{N_i\}) - Nk_B \sum_i x_i \ln x_i, \quad (2.129)$$

where S_x is the excess entropy. For phases with small S_x , the assumption of “ideal entropy” is taken as a first approximation for modeling work, especially where no experimental data is available to determine the excess entropy. Under this assumption, the configurational free energy becomes

$$F_c(T, p, \{N_i\}) = N \sum_{ij} a_{ij} x_A^i x_B^j + Nk_B T \sum_i x_i \ln x_i, \quad (2.130)$$

where the constant and linear terms of the enthalpy have been set to zero. The final model considered is the substitutional solid solution model with sublattice filling. The ideal and regular solution models are effective for simple lattice types like face centered cubic (fcc) and body centered cubic (bcc) where all sites are equivalent. For more complicated crystal structures, different sites will not be equivalent. The crystal may be decomposed into disjoint “site classes”, where each site within a site class is

related by symmetry to every other site within that site class. One or more of these site classes may form different “sublattices” of the lattice. If a sublattice has only one species of particle, it is an ordered sublattice, and if it has more than one species of particles, it is disordered. Defining the number of particles of species i on sublattice j to be the unconstrained variables N_{ij} , the total number of particles in sublattice j to be the fixed quantity²⁹ N_j , and the composition of specie i on sublattice j to be $x_{ij} \equiv N_{ij}/N_j$, under the ideal entropy assumption the entropy S_j of sublattice j may be derived exactly as for the ideal solution, obtaining

$$S_j = -N_j k_B \sum_i x_{ij} \ln x_{ij}. \quad (2.131)$$

The total configurational entropy of the system will then be

$$S_c = \sum_j S_j = -k_B \sum_j N_j \sum_i x_{ij} \ln x_{ij}, \quad (2.132)$$

where many of the x_{ij} 's will be 0 or 1, as energetic considerations only allow a few site classes to exhibit disorder in a structure, if any. The energy of this system will have some general form $U(T, p, \{N_{ij}\})$, where again it is commonly assumed for computational modeling that the energy shows weak temperature dependence and $p \approx 0$. Then the free energy for the system is

$$F(T, p, \{N_{ij}\}) = U(T, p, \{N_{ij}\}) + k_B T \sum_j N_j \sum_i x_{ij} \ln x_{ij}. \quad (2.133)$$

However, this free energy depends on the unconstrained variables $\{N_{ij}\}$ (equivalently $\{x_{ij}\}$, as $\{N_j\}$ are held fixed), and by the principle of free energy minimization it must be minimized over all unconstrained variables

$$F(T, p, \{N_i\}) = \min_{N_{ij}} (U(T, p, \{N_{ij}\}) + k_B T \sum_j N_j \sum_i x_{ij} \ln x_{ij}), \quad (2.134)$$

subject to the constraint that every sublattice is fully occupied ($N_j = \sum_i N_{ij}$) and every particle must appear in one and only one sublattice ($N_i = \sum_j N_{ij}$).

²⁹More precisely, N_j/N is fixed.

A simple example of the substitutional solid solution model with sublattice filling is modeling entropic stabilization of substitutional defects onto a sublattice. Placing a defect, denoted as species i , onto a sublattice α will have an energy cost ΔE . If this “cost” is negative, it will be energetically stabilized and occur at $T = 0$. Even if this energy cost is positive, it is still possible to see this defect occurring via entropic stabilization. If ΔE is small enough that at observable temperatures the entropic energy associated with disordering sublattice α compensates for the energetic cost, free energy minimization will stabilize some number of defects. For a binary system with a sublattice with N' many sites and N_d many defects, the free energy will be

$$G = uN + N_d\Delta E + N'k_B T(x_d \ln x_d + (1 - x_d) \ln(1 - x_d)), \quad (2.135)$$

where $x_d = N_d/N'$ is the defect concentration of the sublattice. The entropy has an infinite slope at $x_d = 0$, and therefore at all non-zero temperatures, free energy minimization will stabilize some defects in such a system. For all finite temperatures a solubility range exists for the phase, and in the high entropy/infinite temperature limit, the phase will be perfectly disordered on this sublattice, with $x_d = 0.5$.

That being said, substitutional solid solution models with sublattice filling will not generally be stable at high temperatures, as they only reduce to the ideal solution model (the high temperature limit for all lattice models due to its maximal entropy) in this limit when no external constraints are put on any x_{ij} other than those imposed by the lattice.

Which configurational model should be used? In order to propose a configurational model for the free energy, one must know the behavior of the configurational energy. If one has a candidate list of configurations, first principles calculations may be used to generate configurational energies for the system. From these energies, one may propose a free energy model and fit the free energy model to these energies. Often some experimental data will exist to help guide selection of configurations, an example being a phase having a solubility range but no indication how that solubility range arises. Even in these cases, physical intuition is necessary to determine both the trial

configurations and the resulting free energy model.

But why can first principles calculations be used, when several approximations (truncated basis sets and functionals) have been used? Most quantities in physics depend on energy *differences*. At a fixed composition, various errors in the total energy introduced by the pseudopotentials for particular ions and the functional for the valence electrons will systematically cancel between two phases, and errors for differences in cohesive energies in first principles calculations are commonly less than 10 meV/atom. A back-of-the-envelope estimate $\Delta T \approx \Delta E/k_B$ yields error bars of 100 K in phase transition temperatures due to errors in cohesive energies. Though chemists may balk at these error bars, for material scientists looking for initial guesses and notoriously error-tolerant physicists, this is often sufficient to gain semi-quantitative insight into the behavior of a particular system.

The Phonon Contribution to Free Energy

The configurational portion of free energy depends only on the equilibrium configurations, the zeroth order term in the expansion of the free energy about equilibrium positions. If the energy is truncated to second order, the behavior of the particles near the equilibrium will be described by the phonon band structure, with a energy of

$$E = \int d\omega \rho(\omega) \hbar\omega \left(n(\omega) + \frac{1}{2} \right), \quad (2.136)$$

where $\rho(\omega)$ is the phonon density of states at frequency ω ³⁰. It may be shown via construction of the grand canonical partition function that the free energy for a single phonon mode is

$$f_\omega(T, p, \{N_i\}) = \frac{\hbar\omega}{2} + k_B T \ln(1 - e^{-\beta\hbar\omega}), \quad (2.137)$$

³⁰Here the continuum approximation for the density of states is used, which may be converted back to the discrete form previously given using delta functions, and equivalently may be approximated from the discrete form using some form of smearing, commonly Gaussian.

and, as in the harmonic approximation all phonons are decoupled, the total phonon contribution to free energy is

$$f_{\text{phonon}}(T, p, \{N_i\}) = \int d\omega \rho(\omega) \left(\frac{\hbar\omega}{2} + k_B T \ln(1 - e^{-\beta\hbar\omega}) \right). \quad (2.138)$$

The phonon contribution to free energy depends only on the phonon density of states, and this quantity may be calculated from density functional theory calculations using the supercell convergence method previously described.

For a well-ordered phase, the phonon contribution to free energy is straightforward to calculate, as there is only one set of phonons about one equilibrium configuration. For a disordered phase, even in the harmonic approximation, there are many possible equilibrium configurations, each with their own set of phonons, and no reliable general method exists to determine the phase’s phonon contribution to free energy. The crudest method is to take certain representative well-ordered equilibrium structures for the phase, calculate their phonon contributions to free energies, and then average and interpolate these free energies to estimate the phase’s total contribution. Another method, valid for simple phases like body-centered cubic, face-centered cubic, and hexagonal close-packed, is to use a set of representative structures known as “special quasirandom structures” (SQS) [50]. SQSs are formally well-ordered structures with relatively small unit cell size (some only eight atoms large) formed by decorations of the associated lattices, but whose pair correlations and chemical environments mimic those of random alloys, allowing them to be used as disordered phase “approximants” for fitting both configurational and vibrational free energies. Finally, one may calculate the interatomic force constants between certain chemical species, then perform computationally cheap (relatively to density functional theory) Monte Carlo or molecular dynamics to generate a vibrational free energy from the ensemble average. However, depending on the chemical system, the resulting fit for force constants can suffer from a lack of transferability between different lattice types or even different compositions.

The Electronic Contribution to Free Energy

The easiest portion of the free energy to model is also the most frequently neglected portion, the electronic portion. The Fermi exclusion principle applies to electrons, and energy minimization at $T = 0$ K occupies states up to the Fermi level, with states above the Fermi level unoccupied. The occupation of states at energy E obeys Fermi-Dirac statistics

$$f(E, T) = \frac{1}{e^{\beta(E-E_F)} + 1}, \quad (2.139)$$

where E_F is the Fermi energy for the system. For higher temperatures, the electronic states are partially occupied by electrons, and this partial occupancy is a disorder that yields an associated entropy. This entropy may be derived in an analogous way to the ideal solution entropy, yielding the equation

$$S_e(T, p, \{N_i\}) = -Nk_B \int dE \rho(E) \left(f(E, T) \ln f(E, T) + (1-f(E, T)) \ln(1-f(E, T)) \right), \quad (2.140)$$

where $\rho(E)$ is the density of states at energy E , where care must be taken to make sure it is properly normalized so that the electronic free energy properly scales with total number of particles N ³¹. The electronic energy is

$$U_e(T, p, \{N_i\}) = N \int dE \rho(E) f(E, T). \quad (2.141)$$

yielding a electronic contribution to free energy of

$$F_e(T, p, \{N_i\}) = U_e - TS_e. \quad (2.142)$$

However, the configurational contribution to free energy already contains the electronic energy at 0 K, so the electronic contribution should be amended to $F_e(T, p, \{N_i\}) - F_e(0, p, \{N_i\})$.

³¹Often experimental work will normalize per volume and computational per particle, which is the normalization assumed here.

Unlike the configurational and phonon contributions to free energy, the electronic contribution has formally exact equations³² that are simple to calculate computationally. However, for an insulator or semi-metal, the Fermi level lies in a band gap, and the temperatures necessary to see significant excitations across the band gap will be commonly be much larger than the melting temperature for the solid phase of interest; for (undoped) silicon’s relatively small band gap of 1.1 eV, the Fermi level being in the middle of the gap yields a characteristic excitation temperature around 6500 K. Even for metals, where no band gaps exist to suppress excitations, much of the density of states between two different phases will be similar due to similar bonding characteristics. The difference in the electronic contributions will be small, often on the order of $\Delta F_e/N$ being a few meV/atom. This is on the order of the error expected for first principles calculations, and the electronic free energy contributions are commonly ignored.

2.3.6 The Convex Hull

One important class of phase transitions is driven by “alloying”, where a set of chemical species are brought together, each with some number of particles N_i , and the thermodynamically stable phase is desired. The free energy should be expressed as a function of the relative chemical concentrations $\{x_i\}$, as all possible phases have identical scaling in total number of particles, $N = \sum_i N_i$. To eliminate the dependence on N , it is more natural to work with “Gibbs free energy per particle”,

$$g(T, p, \{x_i\}) = G(T, p, \{N_i\})/N. \quad (2.143)$$

For purposes of stability, $\{x_i\}$ functions like extensive constrained variables (as they were not obtained by performing Legendre transforms), and the Gibbs free energy per particle is convex in $\{x_i\}$. There is a freedom of choice of zero for free energy at every

³²Though it should be noted that for density functional theory, the Kohn-Sham eigenvalues are not the true electronic energy eigenvalues.

set of values of $\{x_i\}$ as long as this choice does not change free energy differences between phases or affect the stability criteria.

The choice of zero is commonly taken to be the tie line between the $T=0$ stable phases for the pure elements. For each species i , the $T=p=0$ stable phase has an energy per particle e_i , which is equivalent to the Gibbs free energy per particle under those conditions. The difference in energy per particle between a particular phase and phase co-existence between the pure species, one of its competing phases, at $T=p=0$ is

$$\Delta h(\{x_i\}) = g(0, 0, \{x_i\}) - \sum_i x_i e_i. \quad (2.144)$$

Δh is known as the ‘‘enthalpy of formation’’ and is the energetic portion of the configurational portion of the free energy. This quantity is important because it can be calculated explicitly by first principles methods and, as an energy difference, has physical meaning, unlike the total energies which depend on the zero of energy chosen by the pseudopotential used. When the enthalpy of formation is negative, free energy minimization will favor alloying into the new phase when the pure species are brought together at $T=p=0$ (assuming no other phase has a lower free energy), and when the quantity is positive, alloying into this particular phase at $T=p=0$ will not occur. It should be noted that for $T \neq 0$ and $p \neq 0$, the enthalpy of formation for the pure elements will not be 0, as the enthalpy of formation is measured relative to the $T = p = 0$ values for the pure elements.

The general form of the Gibbs free energy per particle is then

$$g(T, p, \{x_i\}) = \Delta h(\{x_i\}) - T s_{conf}(T, p, \{x_i\}) + g_{phonon}(T, p, \{x_i\}) + g_{elec}(T, p, \{x_i\}). \quad (2.145)$$

To determine what phases are stable, these Gibbs free energies per particle may be plotted and the common tangent construction used to determine phase co-existence/stability regions. As the Gibbs free energies per particle are convex in composition, the resulting free energy for the system will be convex, giving it the name ‘‘convex hull’’.

2.4 Ensemble Average Approaches: Monte Carlo and Molecular Dynamics

2.4.1 Ensemble Average Approaches for Phase Transitions: An Overview

The previous section was primarily concerned with free energy modeling. While free energy modeling is a useful tool for constructing phase diagrams and understanding the underlying physics, as has been repeatedly stressed it is encumbered with various approximations. Most important is the assumption that configurational entropies are either solid-solution-like or zero. These two assumptions are partially physically motivated, as the former is valid at high temperature when the internal energy scale is negligible to the entropic scale, and the latter is valid at low temperature when the internal energy scale dominates the entropic energy scale. Realistic systems at finite temperatures, of course, live somewhere in between, and the real reason these assumed forms are used is because they are simple and roughly “get the physics right”.

Additionally, the mean field approximation is commonly taken for free energy models. As shown in the section on the Landau formalism, this yields particular values for exponents for certain quantities as they approach the critical point, independent of the underlying physics of the system. For example, in a temperature-driven transition, the order parameter in the Landau formalism depends on temperature in a $|T_C - T|^{\frac{1}{2}}$ fashion as one approaches the critical temperature from one side (commonly the low-temperature side). In the language of critical exponents³³, $\beta = \frac{1}{2}$. The derivation of this relationship, as one will recall, was quite general, depending only on the assumed analyticity of the free energy with respect to the density function and some reasonable constraints on the coefficient expansions. If this result seems too simple,

³³That β is used both for the inverse temperature and the critical exponent for the order parameter is unfortunate, but in practice its meaning is clear from context.

that’s because it is. Most real systems have $\beta \neq \frac{1}{2}$.

There are other ways to model a phase transition, however. One underlying assumption for all equilibrium thermodynamics is ergodicity, that the ensemble average is equivalent to the time average, and it is ensemble averages that are the primary quantities of interest in statistical mechanics. Recall that the construction of the partition function was nothing but a formalism for taking the ensemble average in the canonical ensemble, from which one may derive the associated free energy. Free energy modeling skips directly to the final step, but with the partition function always lurking in the background, at least conceptually. However, one may also take the ensemble average of the system directly, or equivalently, the time average of its dynamics. The former is commonly done using “Monte Carlo” simulations, and the latter using molecular dynamics simulations. While these two methods require an assumed energy model, they make no assumption on the form of the entropy or the analyticity of the free energy, and non-ideal entropies and non-mean field critical exponents can be obtained from them. In particular, first principles calculations can be used to derive an energy model (or as an energy model) with a high degree of accuracy. The price one pays is that both of these methods are statistical in nature, and some statistical error is always present, though diminished as one runs the simulations longer³⁴. In this section, a brief discussion of the modern theory of phase transitions and critical exponents will be presented to motivate the usage of these methods, these two methods will be discussed, and finally finite size scaling will be presented.

³⁴This is the primary reason methods using energies taken directly from first principles do not yet dominate this field: such calculations are relatively slow compared to methods like cluster expansions the Embedded Atom Method (EAM), and one trades accuracy of the energy model with statistical error due to a limited sample set.

2.4.2 The “Modern” Theory of Phase Transitions and Critical Exponents

To understand why methods other than classical free energy modeling are necessary to explain the behavior of a second-order phase transition near the critical point, an (extremely brief) discussion of the “modern” theory of phase transitions is appropriate. As the Landau formalism is a mean field formalism, the failure to obtain the right critical exponents arises from the assumption that a macroscopic local quantity, the density function, is relevant. That is, the pairwise correlation function (a measure of deviation from locality) may be approximated as

$$G(r) = \langle \sigma(r)\sigma(0) \rangle - \langle \sigma \rangle^2 \approx 0, \quad (2.146)$$

where here we will use the example of spins σ in an Ising model in a temperature-driven phase transition, and it is assumed all spins are equivalent so only the magnitude of the displacement vector r contributes. Empirically, it is found that for large r , far from the critical temperature T_C , $G(r)$ takes the form

$$G(\mathbf{r}) \propto e^{-r/\zeta}, \quad (2.147)$$

where ζ is the “correlation length”. The correlation length defines a length scale for the system in the sense that if one is looking at large enough distances, this quantity is essentially zero, and the fluctuations in the system are negligible. As thermodynamics is only formally defined in the infinite length limit, were ζ to be constant, this relation would support the usage of a mean field approximation. More specifically, the true behavior of the system could be reached as a perturbation away from the mean field behavior, this perturbation incorporating the pair-correlation function with finite spacial extent.

But ζ is not constant. In particular, it is found empirically that the correlation length diverges near the critical temperature as

$$\zeta(T) \propto |T - T_C|^{-\nu}. \quad (2.148)$$

For any given length scale, there is some temperature near the critical temperature where fluctuations are non-negligible, and at the critical point, fluctuations appear on *all* length scales. At the critical temperature, for large r the pair correlation function converts from an exponential form to a power law form:

$$G(r) \propto \frac{1}{r^{d-2+\eta}}, \quad (2.149)$$

where d is the spacial dimension and η is another critical exponent. No fundamental length scale exists in this pair-correlation function, a phenomena known as “scale-invariance”³⁵. The existence of fluctuations at all length scales introduces essential non-analytic behaviors in the system, yielding differing critical exponents from the Landau formalism. Explicitly reintroducing these fluctuations to formally recover the true behavior of system requires renormalization group theory, field theoretic methods, and the associated Feynman diagrams. While these methods have been indispensable for understanding the behavior of the laws of physics near a phase transition, at present they remain too formal to understand the behavior of many real materials near a phase transition.

The critical exponents ζ , ν , and η are not defined in mean field/Landau formalism, as they all deal with the behavior of the correlation function, which is assumed negligible in the mean field/Landau formalism. Two other critical exponents more relevant to this work, α and β , relate to the specific heat C

$$C \propto |T - T_C|^{-\alpha}, \quad (2.150)$$

where $\alpha = 0$ in the Landau formalism (the specific heat from either side of the critical temperature approaches constant though differing values) and the order parameter M ³⁶

$$M \propto |T_C - T|^\beta, \quad (2.151)$$

³⁵However, there is always a lower length scale defined by the lattice.

³⁶The order parameter is here denoted as M instead of η as before to avoid confusion with the critical exponent for the pair correlation at the critical point.

where $\beta = \frac{1}{2}$ for mean field/Landau formalism.

Some comments are necessary before moving on. These critical exponents are easy to define but difficult to measure experimentally or computationally, as they require power law fitting in a small range around the critical temperature. This is difficult to do reliably, as large fluctuations are a feature of systems in the critical region. Furthermore, all critical exponents are defined for the asymptotic behavior near the critical points. The actual behavior includes “corrections-to-scaling” terms that may need to be accounted for, and it is possible for a fit to an assumed power law without correction-to-scaling terms to give faulty exponents.

Second, it may be shown via renormalization group theory that “universality classes” exist: classes of phase transitions with wildly differing physical implementations that nevertheless share identical critical exponents due to an underlying similarity in the free energy function. This may not seem especially noteworthy when considering the universality classes of the 2D Ising model and the mean field/Landau formalism, whose critical exponents have been derived exactly as simple fractions. It is the (epistemologically unjustified) basis of theoretical physics for differing systems to have the same underlying simple behavior given by simple fractions and physical constants, after all. It is more surprising for other models, such as the 3D Ising model, whose critical exponents have no known formal solution, and whose present estimates do not appear to be simple fractions. Such behavior is usually a hallmark of essential underlying physics, varying from system to system. Nevertheless, to the measured degree of accuracy, these “non-simple” critical exponents are the same for all system in the universality class³⁷. An extensive review article³⁸ on renormalization group theory for spin systems, including estimates for critical exponents for various universality class, may be found at [51].

³⁷This surprisingly agreement between different physical systems with “non-simple” critical exponents was one of the main driving forces behind formation of the modern theory of phase transitions.

³⁸As a personal aside to any starting graduate students reading this thesis, a good review article is worth its weight in rhodium.

2.4.3 Metropolis Monte Carlo and Molecular Dynamics

The most common method used for ensemble averaging is known as the Monte Carlo method. As its name suggests, in this method, phase space is sampled randomly, but in such a way that the relative likelihood for the system to be sampled in two (micro)states A, (p_A) and B (p_B) is the ratio of their Boltzmann factors (in the canonical ensemble):

$$\frac{p_A}{p_B} = e^{-\beta_A E_A + \beta_B E_B}, \quad (2.152)$$

where E_α and β_α are the energies and inverse temperatures for state α .

As is commonly done, it will be assumed here that it is a lattice model: the system consists of identical vertices on a lattice, these vertices may take on discrete values, i.e. “spins”, and the energy is any arbitrary function of these spins.³⁹

First, the system is initialized into some initial state, and its energy E_{old} is calculated. The initial state can be any state, but it is common to begin in a completely randomized state to reduce the probability of getting stuck in a local energy minimum, as will be discussed later. Next, a proposed configuration is chosen, and its energy E_{new} is calculated. For a lattice method, it is common to “flip” one of the spins, that is, change one of their values, but any proposed configuration will suffice as long as the method used to generate the choice satisfies ergodicity and detailed balance (discussed below). The proposed configuration is accepted with probability

$$p_{accept} = \begin{cases} 1 & E_{new} \leq E_{old} \\ e^{-\beta(E_{new}-E_{old})} & E_{new} \geq E_{old} \end{cases}. \quad (2.153)$$

Whether or not the proposed configuration is accepted, the new configuration is recorded. This process of choosing of proposed configurations, acceptance/rejection,

³⁹Though this is the canonical example of the Metropolis method, the method is no means restricted to lattice methods. In fact, the original Metropolis paper[52] was concerned with the motion of particles confined to a square under a two-body potential, and the “spin flips” were random displacements of said particles.

and updating of the configuration is repeated to satisfaction. The expectation value for any quantity Q is then given by

$$\langle Q \rangle = \sum_i p_i Q_i, \quad (2.154)$$

where the sum is taken over all configurations observed, $p_i = N_i/N$ is the probability of observing configuration i (where N_i is the number of times configuration i was observed and N is the total number of proposed configurations), and Q_i is the value of Q in configuration i . The error in this quantity is on the order $N^{-1/2}$, and one may obtain more accurate estimates by increasing the number of proposed configurations. An important exception is near critical points for second-order phase transition, as “critical slowdown” is caused by large-scale, long-lifetime fluctuations, and much longer runs or modified methods (such as Ferrenberg-Swendsen [53, 54] or Wang-Landau [55]) are necessary to accurately resolve the statistics.

Of particular importance for thermodynamics is the expectation value for the energy

$$\langle E \rangle = \sum_i p_i E_i, \quad (2.155)$$

which may be calculated at essentially no computational cost by storing the values for energy as they are calculated, and the specific heat⁴⁰, which is calculated via

$$C = \frac{1}{k_B T^2} (\langle E^2 \rangle - \langle E \rangle^2) = \frac{1}{k_B T^2} \sum_i p_i (E_i - \langle E \rangle)^2. \quad (2.156)$$

To recover the canonical ensemble, we must satisfy Equation 2.152. To prove this, note that the change in the frequency/probability of a state A at a given time using the Metropolis rule is given by a simple flux-like equation

$$\frac{dp_A}{dt} = \sum_{B, E_A < E_B} [p_B - p_A e^{-\beta(E_B - E_A)}] + \sum_{B, E_B < E_A} [p_B e^{-\beta(E_A - E_B)} - p_A], \quad (2.157)$$

⁴⁰Whether this quantity is C_V or C_p depends on the details of the simulation, but commonly the lattice is held fixed.

where B is the set of all other possible states of the system. When the statistics of the Monte Carlo simulation have suitably converged, the steady state has been reached and this quantity will be zero. Assuming “detailed balance”, each individual term may be taken to be zero, yielding Equation 2.152.

A second requirement of Monte Carlo methods is that it be ergodic, and in particular it must be possible to reach any configuration in phase space from any other configuration in phase space by the chosen method for generating candidate structures⁴¹. The previous example of taking one spin and flipping it obviously satisfies this condition, as one may move from one configuration to any other configuration by sequentially flipping all spins in the system to the values assumed by the second configuration. It is not necessary that this be likely, only that it be possible.

However, one important (practical) flaw with Monte Carlo is that it is possible to get stuck in “local energy minima”. That is, for particular configurations, the chosen method for generating new configurations gives small probabilities of accepting any new proposed configuration, and for finite times, the system will remain in the original configuration. The ensemble averaging will then assign the configuration an incorrectly large weight over all of phase space, though correctly assigning the configuration a higher relative weight than previously proposed configurations. In the previous example, it may be the case that flipping any individual spin gives extremely low probability to leave the present configuration, but flipping two or more spins simultaneously is energetically preferable and gives a higher probability of leaving the present configuration. This is not a formal issue with Monte Carlo, as in the infinite time limit where Monte Carlo is formally defined, eventually the system will leave any configuration, and ergodicity ensures that the proper ensemble average will be obtained. However, no professor (that I know of) has funding for a graduate student for an infinitely long project. One way to get around problems with local

⁴¹This last condition is commonly referred to as “ergodicity”, but strictly speaking this is only a necessary condition of ergodicity.

energy minimums is to try different types of spin flips, for example, alternate between flipping one spin and flipping multiple spins. As long as sampling of all of phase space is possible via *any* of the types of the spin flips, sampling of all of phase space will be possible by the collection of spin flips in any combination of relative frequencies, and it is often the case that a smart choice of infrequent “auxiliary” spin flips can break the system out of a local energy minimum.

The second common method to generate ensemble averages is molecular dynamics ensemble averaging. The assumption of ergodicity demands that time and ensemble averages be equivalent. As long as molecular dynamics is properly implemented in a suitable ensemble, one may simply run a molecular dynamics simulation, generate configurations in this manner, then use the same ensemble averaging equations as the Monte Carlo case to find thermodynamic quantities. This can be more efficient than continuum Monte Carlo because it intrinsically favors low energy phonon modes. Additionally, it can be efficient for first principle methods using wavefunction prediction. Molecular dynamics averaging works well for well-ordered structures where particles are expected to oscillate around the unique well-ordered equilibrium structure. However, for disordered structures, molecular dynamics ensemble averaging has the difficulty that it is easy to get stuck in particular energy minimums, as the energy landscape is riddled with energy barriers; even relatively simple events like atomic species swaps require a coordinated motion of two particles moving through the potential generated by other particles. By occasionally interspersing Monte Carlo steps between molecular dynamics steps, “hybrid Monte Carlo/molecular dynamics”, one may overcome these energy barriers via the Monte Carlo steps while incorporating the phononic contributions to free energy via the molecular dynamics steps.

2.4.4 Finite Size Effects

While Monte Carlo and molecular dynamics methods allow a greater degree of accuracy over free energy models, primarily due to a lack of assumed form for the entropy

function, these two methods suffer from the imposition of a finite size cell. From free energy models, which are defined in thermodynamic limit, one may recover non-analytic behaviors in the thermodynamically stable free energy, as has already been seen in the Landau formalism. However, for finite sized systems, only a finite number of degrees of freedom exist, and the full partition function (Equation 2.124), as an integral of an analytic function over a finite number of variables, must itself be an analytic function for all parameters (except for the extremal values of T and V). That is, *every finite system exists in only one phase for finite temperatures and volumes.*

So why use such methods in the first place? Recall that the primary mechanism for a phase transition in the classical theory of phase transitions is the nucleation of a phase via a particular fluctuation that grows to destabilizes the entire system, and the growth of scale invariant fluctuations in the modern theory of phase transitions. This partially explains why a finite system cannot undergo a phase transition, as its finiteness only allows for a finite size fluctuation. Increasing the size of the cell increases the size of the possible fluctuations, bringing the system closer to the infinite size limit. This phenomenon goes under the name of “finite size effects”.

One particularly important class of finite size effects is “peak scaling”. The most common method to determine the existence of a (temperature-driven) phase transition is to find a discontinuity in the specific heat. For any finite size system, the specific heat will always be continuous and finite. One cannot determine whether a phase transition occurs in such systems from a single cell size, as it is possible for the specific heat to have a *finite* peak with no phase transition occurring at that peak. The hallmark of the phase transition is an essential discontinuity in the specific heat peak. Where a phase transition occurs, the peak will approach the infinite size limit as the cell size increases, that is, the peak height will increase in height as a function of the cell size. Assuming a cell with uniform side length L in dimensionality d , in a second order phase transition, a relatively simple scaling argument may be used to show that the peak grows like $L^{\alpha/\nu}$, where the factor of ν arises from the limited

cell size reducing the correlation length [47]. In a first order phase transition, a more complicated argument shows that the peak grows like L^d , the number of particles.

For the case of second-order phase transitions, this also gives a hint as to the universality class of the phase transition. If one is unclear as to what type of phase transition the system is undergoing, one may use the peak scaling to find α/ν to suggest a universality class. Finding the universality class suggests a type of broken symmetry (Ising: inversion, Potts: n-fold rotation, etc.) for the unknown order parameter, which combined with the physics of the system under consideration may lead to candidate order parameters.

Chapter 3

On the Structure of Boron Carbide¹

3.1 What is Boron Carbide?

Boron carbide is a mundane material at first glance. It was discovered accidentally in 1864 and was assigned the chemical formula “B₄C” in 1934 [58]. It is one of the hardest materials known to man and has a low density, as boron and carbon are second row elements, with applications as diverse as padlocks and tank armor. It is not a particularly rare material, producible by chemical reactions



or



with production exceeding 500 tons per year in 1990 [59]. It can be used as a neutron absorber and has been used in control rods and shielding for nuclear reactors. Even its associated phase diagram, reproduced in Fig. 3.1, is mundane at first glance,

¹Much of this chapter has been adapted from my papers “Prediction of Orientational Phase Transition in Boron Carbide” [56] and “A Free Energy Model of Boron Carbide” [57].

containing a single phase labeled “B₄C” with a nearly constant solubility range from 8.6% to 18.8% C [5, 60] from the lowest listed temperature of 1000 K to 2075 K, the solid phase transitioning to liquid by 2450 K. Such an ordinary mass-produced material cannot be nearly as interesting as, say, graphene².

In fact, the structure of boron carbide is a 150-year-old puzzle. X-ray and neutron diffraction experiments in the 1940s [61, 62] showed that boron carbide, being boron rich, inherits boron’s complicated crystallographic structure, constructed out of building blocks of icosahedra³ with additional three atom chains. Icosahedra are one of

²There, I said it.

³It should be noted that due to the Jahn-Teller effect and crystalline packing, the icosahedron

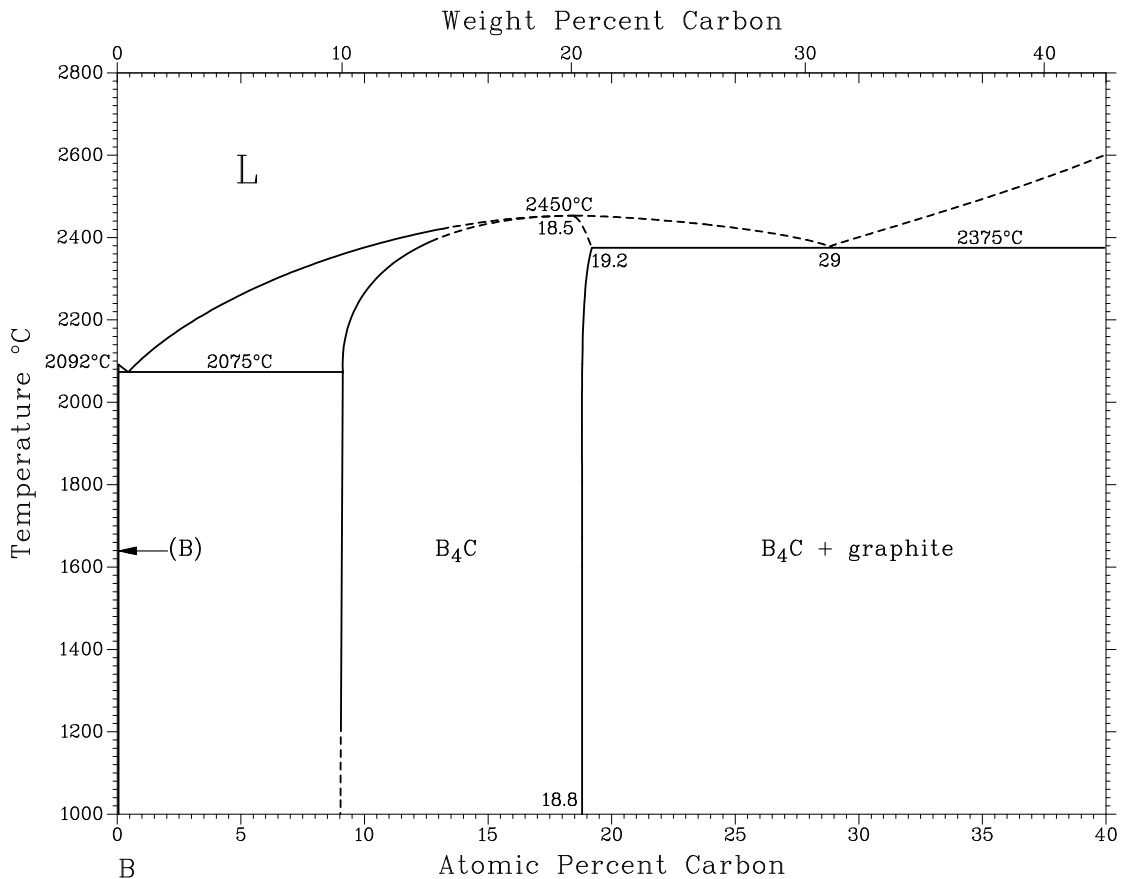


Figure 3.1: Assessed phase diagram of the boron carbide system [5].

the structural motifs possible for close-packed structures (along with octahedra and tetrahedra), however, due to their forbidden five-fold symmetry, they generally do not appear in 3D periodic structures, and when they do, the resulting structure cannot achieve close packing⁴. As boron is a covalent valence 3 element, its electron deficiency is so strong that it sacrifices global close-packing to maximize the number of local neighbors, favoring icosahedral ordering and forming unique non-directional “three-atom-two-electron” bonds [63]. These unique bonds share two electrons amongst the three borons forming the vertices of triangular faces of the icosahedron. Longuet-Higgins and de V. Roberts [64] showed that such an icosahedron require 38 electrons to optimize bonding, 26 to satisfy the icosahedron’s internal bonding orbitals and 12 to bond covalently outside the icosahedron. As each icosahedron has 36 valence electrons, two orbitals are left unoccupied. Attempting to occupy these orbitals gives rise to pure elemental boron’s complicated crystallographic structure, which is still a matter of active debate [65, 66, 67].

The icosahedra in boron carbide are arranged on the corners of a rhombohedral cell, with covalent bonds between the icosahedron (filling the 12 external covalent bonds on each icosahedron) and with the three atom chain in the center of the cell, this chain aligned with the (111) axis. Shown in Figure 3.2 are the primitive cells for two chemical orderings on this lattice. Although it is useful to decompose boron carbide into these structural elements to conceptualize the material and to identify particular types of ordering, it is still unknown whether inter-icosahedral or intra-icosahedral bonds are stronger. Some variant structures exist, in particular a proposed structure [68] for a boron-rich structure where the three atom chain is replaced by a four atom chain with a significant amount of disorder on the center of the chain,

are distorted, but as this distortion remains consistent with the space group this will not affect this discussion in any way.

⁴When either the constraint that space be flat 3-dimensional or the structure be periodic is relaxed, it becomes the dominant structural motif for all close-packed systems, appearing in quasi-crystals, amorphous materials, and liquids.

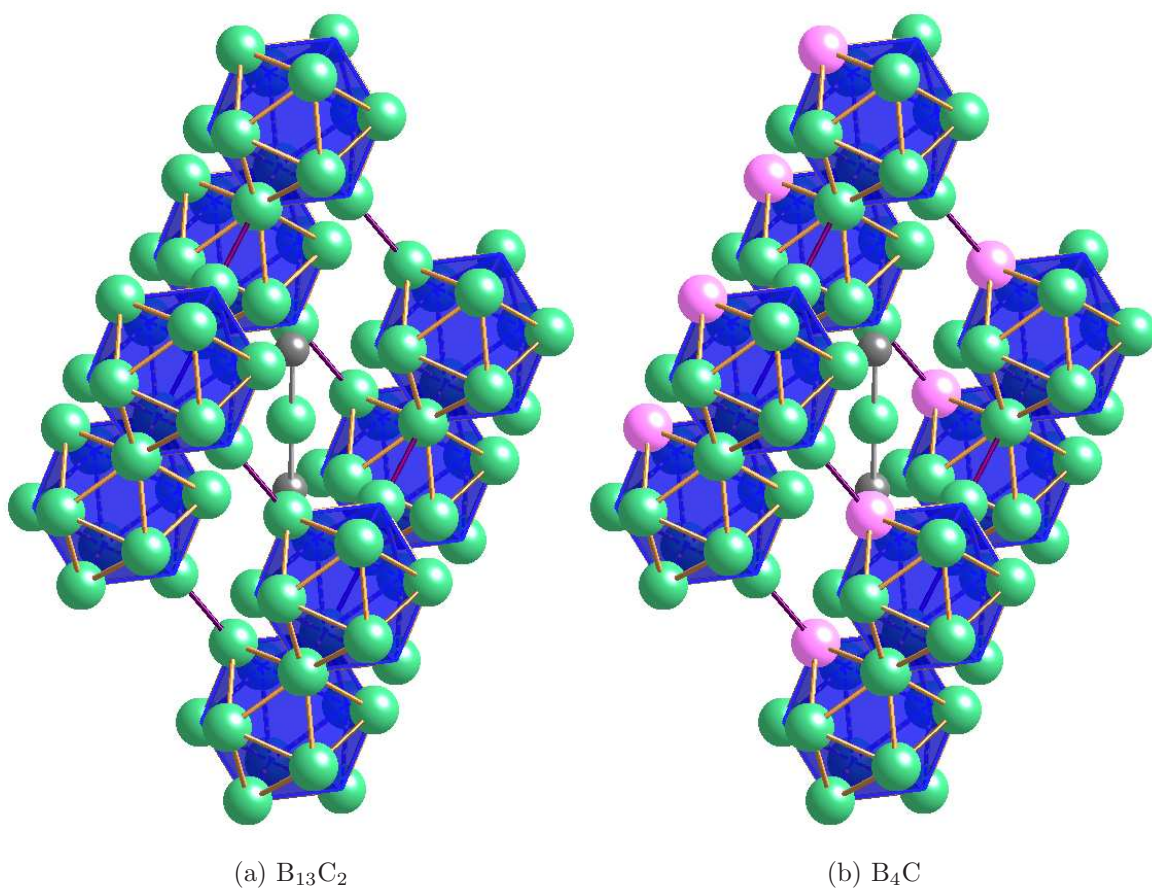


Figure 3.2: The two predicted 0 K structures. Green denotes borons, grey denotes carbons on the chain terminator sites, and pink denotes carbons on polar sites.

containing two boron in a plane perpendicular to the chain, but this basic structural motif of icosahedron+chain has been accepted in the literature for over 70 years.

This only defines the lattice; it is still necessary to decide where the carbon and boron reside. The two usual ways to identify ordering on a lattice are X-ray and neutron diffraction. However, boron and carbon have similar atomic numbers, 5 and 6 accordingly, and it is difficult to distinguish the two reliably from X-ray diffraction. As for neutron diffraction [69], two stable isotopes of boron exist, ^{10}B and ^{11}B . The later, more common (80%) isotope has a (bound coherent) scattering length of 6.65, nearly identical to that of ^{12}C , 6.6511. The former, less plentiful (20%) isotope is the

neutron absorber previously mentioned (-0.1-1.066i), and hence neutron diffraction is difficult to observe.

It is still possible to determine the symmetry of the structure from the diffraction patterns, and “B₄C”⁵ is observed to have the maximum symmetry possible for a rhombohedral cell: space group $R\bar{3}m$ (#166) and a Pearson symbol hR15 [61, 70, 71]. This structure has four site classes in the primitive cell: six polar sites on the icosahedron that link the icosahedron together, six equatorial sites on the icosahedron that link the icosahedron to the chains, two terminator sites on the chain that lie on the ends and bind to the equatorial sites of the icosahedron, and one chain center site that lies at the center. Inversion centers exist both at the chain center and the center of the icosahedron. As this “B₄C” phase is nominally 20% carbon, it should have three carbons per primitive cell. There is only one such well-ordered placement of three carbons that preserves the full rhombohedral symmetry: putting all three carbons on the chain [61, 62]. It was proposed that part of the observed solubility range below 20% carbon of the phase was replacement of the chain center carbons with boron, again preserving rhombohedral symmetry [72]. However, this proposal does not explain the full phase behavior, as full substitution on the chain center yields a structure with 13.3% carbon, and the carbon-poor phase boundary resides at 8.6% carbon.

Nuclear magnetic resonance studies casts doubt onto this ordering, as they reported that up to 60% of the chain centers were occupied by boron in the “B₄C” structure [73]. It has been subsequently confirmed that the C-C-C chains are energetically unfavorable, and after a considerable amount of argument back and forth in the literature (including a model proposed by Emin, where the phase is stabilized by bipolarons [74]), the general consensus of the community is that the dominant chain configuration for the high-carbon limit of the “B₄C” phase is C-B-C, that the excess carbon resides on the icosahedron and prefers the polar to the equatorial site, and the

⁵The reason for the scare quotes will become obvious later.

system preferentially replaces the icosahedral carbon with boron as one moves away from 20% carbon.

But here again we run into a problem. The well-ordered structure where two carbons occupy the chain centers and one occupies the polar site has monoclinic symmetry: space group Cm (#8) and Pearson symbol mC30. While at temperatures above 0 K one may recover a rhombohedral symmetry by occupying all six polar sites with equal probability, if the Third Law of Thermodynamics is correct, this disordered rhombohedral structure cannot be the 0 K structure, as the disordering of the carbons on polar sites yields an extensive entropy. Furthermore, as the third law of thermodynamics prohibits a solubility range at 0 K [75, 9], the phase at 20% carbon must reduce to a single well-ordered phase at 0 K. Due to the change in symmetry, one cannot go from the observed rhombohedral phase to this well-ordered monoclinic phase without going through a phase transition. In addition, the stability region for “ B_4C ”, amusingly, never actually reaches 20% carbon [5, 60]. However, there is a second well-ordered structure [76] that has full rhombohedral symmetry and lies almost directly in the middle of the solubility range, $B_{13}C_2$. This phase lies at 13.3% carbon with the two carbons per unit cell lying on the chain terminator sites. It is tempting (as some have done [77]) to simply declare that this is the proper well-ordered phase, ignore the monoclinic variant, and declare the problem finished.

However, simple electron counting arguments show that $B_{13}C_2$ still has an unoccupied bonding molecular orbital on the icosahedron, as the C-B-C chain only has one excess electron to contribute to the icosahedron’s two unoccupied bonding orbitals. It is energetically favorable to dope the structure with one additional carbon to fill the molecular orbital, yielding the monoclinic B_4C structure. As will be shown, density functional theory also supports this assertion, with a lower enthalpy of formation of the monoclinic B_4C structure than the rhombohedral $B_{13}C_2$ structure, both lying on the convex hull [78, 79, 80, 81], and with structures containing vacancies (a proposed alternative stabilizing mechanism [77]) having energies far off the convex hull. Both

structures are shown in Figure 3.2.

We believe that solid boron carbide is out of thermodynamic equilibrium at all but the very highest temperatures. In this case, conventional experimentation cannot easily determine the equilibrium phase diagram, and theoretical approaches are needed to resolve the fundamental character of the stable state(s) at low temperature. There is an experimentally observed rhombohedral phase [77] with a composition-dependent mixture of B_{12} and $B_{11}C_1$ icosahedra and C-B-C, C-B-B and B-V-B chains (where V denotes vacancies), but clear theoretical support for a more stable monoclinic phase. Here, we propose that these are not incompatible. The observed phase on the currently assessed phase diagram *is* the rhombohedral $B_{13}C_2$ phase, which has considerable disorder. However, a second low temperature phase, the monoclinic B_4C phase, also exists. This phase is a well-ordered structure, and at some temperature, the monoclinic phase segregates into a coexistence between the rhombohedral phase and graphite.⁶

We will show this in two different ways. The first is explicit enumeration of states from which we compute the partition function. We explore the ensemble of higher energy structures obtained by varying the placement of carbon atoms among the sites, both of the 15 atom primitive cell and of various supercells. We then calculate the configurational partition function to obtain the finite temperature free energy. We do this at two carbon concentrations, 13.3% and 20%, finding evidence of a phase transition in the later but not in the former.

The second is construction of a simplified thermodynamic model that elucidates the probable evolution of the equilibrium boron carbide phase field at low temperatures. In the monoclinic phase, all of the carbons lie on equivalent polar sites of the icosahedra, forming a well-ordered structure. Although there is an entropic term

⁶We presently believe there is a third phase that “polarizes” the polar carbons onto one pole of the icosahedra while preserving disorder within that pole, but at present this research is very much in flux and will not be presented in this section. It will be addressed in the Summary section of this thesis.

corresponding to the choice of this site, it is non-extensive and thus vanishes in the thermodynamic limit. In the absence of substitutional disorder the monoclinic phase is a line compound. Landau theory [48] predicts no such transition occurs in the rhombohedral phase, as the symmetry already matches the high T limit. Here, we construct an analytic model to interpret our previous explicit enumeration results, from which we can derive an actual phase diagram.

Both methods predict that the B_4C phase is unstable above 500-600 K. The principle excitation that destabilizes the B_4C phase corresponds to independent rotations⁷ of the $B_{11}C$ icosahedra in adjoining primitive cells, resulting in a restoration of full rhombohedral symmetry. A secondary effect is the replacement of polar carbons with boron, causing a slight reduction in the carbon content below the ideal B_4C stoichiometry. Because the $B_{13}C_2$ phase already has rhombohedral symmetry, it suffers no phase change as temperature rises, until melting around 2800 K.

3.2 What Does Density Functional Theory Predict for Boron Carbide?

3.3 Method 1: Partition Function Enumeration

3.3.1 First Principles Total Energy Calculations

First principles total energy calculations yield the enthalpy of formation of specific trial structures. Enthalpy minima, i.e. the convex hull of $H(x)$ where x is composition, correspond to predicted low temperature stable phases. Structures lying above the convex hull are unstable to decomposition into competing stable phases at low temperature, but they can contribute significantly to the free energy at elevated temperatures as outlined in the following section.

⁷These are not physical rotations but rather hypothetical rotations.

Our total energy calculations are based on electronic density functional theory, the highest level of theory presently available for extended structures. We utilize projector augmented wave (PAW) potentials [27], an all electron generalization of pseudopotentials, as implemented in the plane wave code VASP [82, 83]. For our exchange correlation potential we choose the PW91 generalized gradient approximation (GGA) [24]. All structures are fully relaxed in both atomic and cell coordinates, yielding enthalpy H_i for structure i at $T = P = 0$. Default energy cutoffs of 400 eV were used for plane wave calculations. Brillouin zone integrations were performed using Monkhorst-Pack k-point meshes [84] sufficiently dense that energies had converged to within 0.001 eV/atom. We subtract all enthalpies from the tie-line connecting elemental boron (β -boron, Pearson hR141 optimized with 107 atoms [65]) with elemental carbon (graphite, Pearson hP4), yielding the enthalpy of formation ΔH_i . We also define the energy of instability, ΔE_i , as the energy of an unstable structure above the tie-lines joining competing stable phases on the convex hull of $H(x)$.

In order to fully explore configuration space we carry out calculations both in the primitive cell and in super cells, including a $2 \times 1 \times 1$ cell doubled along the rhombohedral a axis, the hexagonal unit cell formed from three primitive cells, and a $2 \times 2 \times 1$ super cell doubled along both the a and b rhombohedral axes containing four primitive cells. We concentrate our efforts on structures expected to be low in energy based on results from the primitive cell calculations. For the primitive cell, we used all possible symmetry independent primitive cell configurations up to 27% carbon concentration. In supercells we explored many (but not all) of the possible combinations of primitive cell configurations. The vast majority of combinations yield high energy. Configurations containing the well-known structure elements of B_{12} , $B_{11}C_1$, and $B_{10}C_2$ icosahedra, and containing C-B-C and C-B-B chains prove reasonably low in energy. The combination of a $B_{10}C_2$ icosahedron with a B_{12} icosahedron forms the bipolar defect [85]. All possible positions of carbon atoms within each icosahedron and chain are considered. Structures are grouped into symmetry-equivalent classes

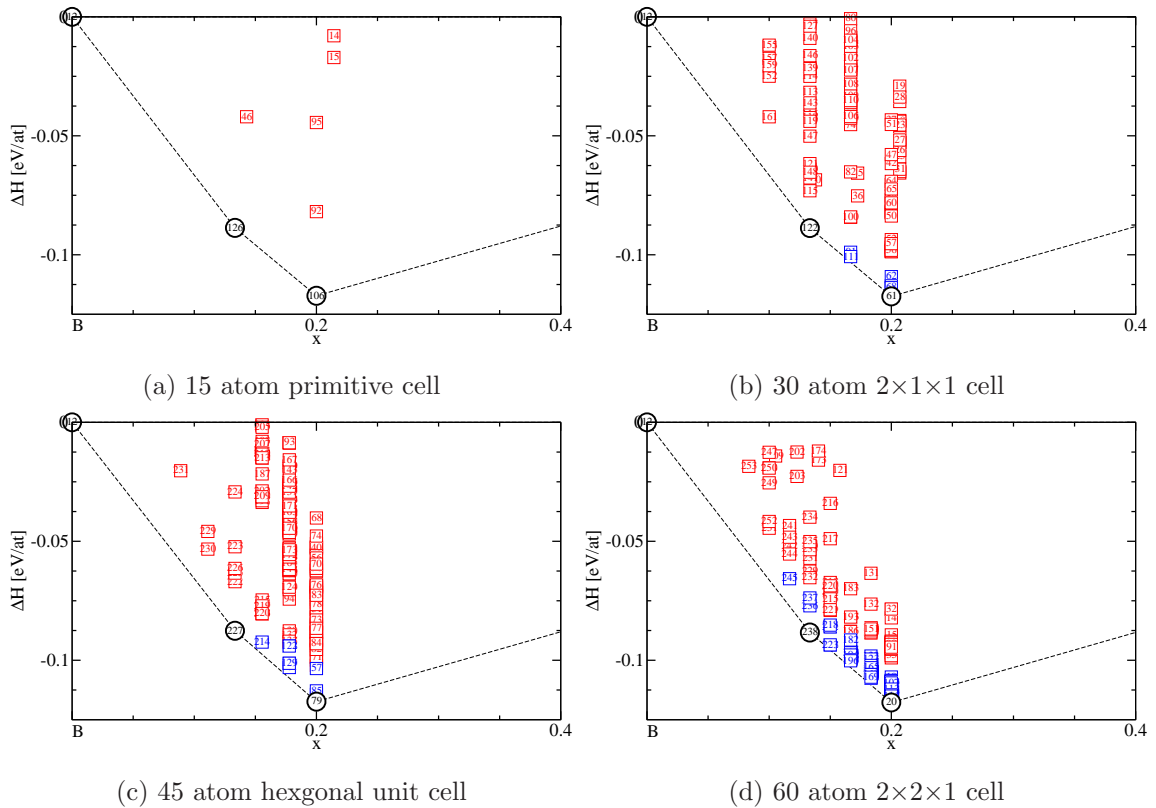


Figure 3.3: Cohesive energies of boron carbide structures. Heavy black circles at $x_C = 0.133$ and 0.20 , respectively, correspond to the ideal $B_{13}C_2$ and B_4C structures displayed in Figure 3.2. Data points in blue have $0 < \Delta E < 0.015$ eV/atom, while red has 0.015 eV/atom $< \Delta E$.

and we record their multiplicities, that is, the number of distinct symmetry-equivalent structures. Enthalpies of selected structures are shown in Figure 3.3 for each cell size considered, and listed in Table 3.1 for the hexagonal unit cell.

3.3.2 Configurational Free Energy via the Partition Function

To go from total energy of a configuration of $N = N_B + N_C$ atoms $E(\{r_j\})$ in volume V to free energy, we must calculate the statistical mechanical partition function

| Name | ΔE (meV/atom) | ΔH (meV/atom) | x_C | Cell Content | Ω | Description |
|------------------------|--------------------------|--------------------------|--------|--------------------------------|----------|---|
| C.hP4 | 0 | 0 | 1 | C ₄ | 1 | Graphite |
| B.hR141 | 0 | 0 | 0 | B ₁₀₇ | 1 | β Boron |
| (p0tt')(p0tt')(p0tt') | 0 | -117.4 | 0.2 | B ₃₆ C ₉ | 6 | B ₄ C (monoclinic) |
| (tt')(tt')(tt') | 0 | -87.6 | 0.1333 | B ₃₉ C ₆ | 1 | B ₁₃ C ₂ (rhombohedral) |
| (p0tt')(p0tt')(p1tt') | 3.0 | -114.4 | 0.2 | B ₃₆ C ₉ | 36 | Rotation |
| (p0tt')(p0tt')(tt') | 4.4 | -103.1 | 0.1778 | B ₃₇ C ₈ | 18 | Mixed icosahedra |
| (p0tt')(p1tt')(p2tt') | 4.5 | -112.9 | 0.2 | B ₃₆ C ₉ | 12 | Rotation |
| (p0tt')(tt')(tt') | 5.2 | -92.4 | 0.1556 | B ₃₈ C ₇ | 18 | Mixed icosahedra |
| (p0tt')(p1tt')(tt') | 6.2 | -101.3 | 0.1778 | B ₃₇ C ₈ | 36 | Mixed icosahedra |
| (p1p1'tt')(tt')(p0tt') | 10.6 | -106.8 | 0.2 | B ₃₆ C ₉ | 36 | Bipolar defect |
| (p0tt')(p1'tt')(tt') | 13.4 | -94.0 | 0.1778 | B ₃₇ C ₈ | 18 | Mixed icosahedra |
| (e0tt')(p0'tt')(p0tt') | 13.9 | -103.5 | 0.2 | B ₃₆ C ₉ | 18 | One equatorial, rotation |

Table 3.1: Table of low ΔE structures for pure elements and the hexagonal boron carbide cell. In our naming scheme, adapted from the primitive cell, sites listed are those containing carbons. t and t' denotes the two ends of the chain (so that tt' denotes a C-B-C chain), p{0,1,2} denotes the polar atoms on the "north" side of the icosahedra, p'{0,1,2} denotes the polar atoms on the opposite ("south") side of the icosahedra. Likewise e{0,1,2} and e'{0,1,2} denotes the atoms just to the north and south of the equator. Ω is the multiplicity.

$$Z(N_B, N_C, V, T) = \int_V \Pi_j d\mathbf{r}_j e^{-\beta E(\{r_j\})}$$

However, we prefer to work at fixed pressure, hence we switch to the Gibbs (N, P, T) ensemble,

$$Q(N_B, N_C, P, T) = \int dV e^{-\beta PV} Z(N_B, N_C, V, T)$$

Since the dominant contributions to the partition function arise at relatively low energies, we can replace the integral over positions $\{r_j\}$ and volumes V with a sum over local energy minima i of a Boltzmann-like factor $e^{-F_{vib}^{(i)}/(k_B T)}$ related to the vibrational free energy of the local minimum i ,

$$Q(N_B, N_C, P, T) \approx \sum_i e^{-\beta F_{vib}^{(i)}}$$

. As a further approximation, we replace $F_{vib}^{(i)}$ with the enthalpy ΔH_i . While this assumption is certainly not valid, the result should affect our conclusions only quantitatively, not qualitatively, provided the vibrational properties of different relaxed configurations differ only slightly. Taking the logarithm, we obtain the Gibbs free energy

$$G(N_B, N_C, P, T) = -k_B T \ln Q(N_B, N_C, P, T) = \mu_B N_B + \mu_C N_C$$

. Since the total number of atoms $N = N_B + N_C$ is fixed, for a given primitive cell or super cell, it is convenient to re-express $G(N_B, N_C, T) = \mu_B N + \delta\mu N_C$, where $\delta\mu = \mu_C - \mu_B$. In fact, we can change to a semi-grand canonical potential

$$\Sigma(N, \delta\mu, T) = \sum_{N_C} e^{\beta\delta\mu N_C} Q(N - N_C, N_C, T)$$

and use the chemical potential difference to control the composition $x_C = N_C/(N_B + N_C)$. The free energy in this ensemble is simply $Y(N, \delta\mu, T) = -k_B T \ln \Sigma = \mu_B N$. Inspecting the enthalpies shown in Fig. 2 we see that choosing $\delta\mu = 0$ at low temperature places us in the B_4C phase at $x_C = 0.200$, while $\delta\mu = -0.55$ corresponds to $B_{13}C_2$ at $x_C = 0.133$.

Results and Discussion

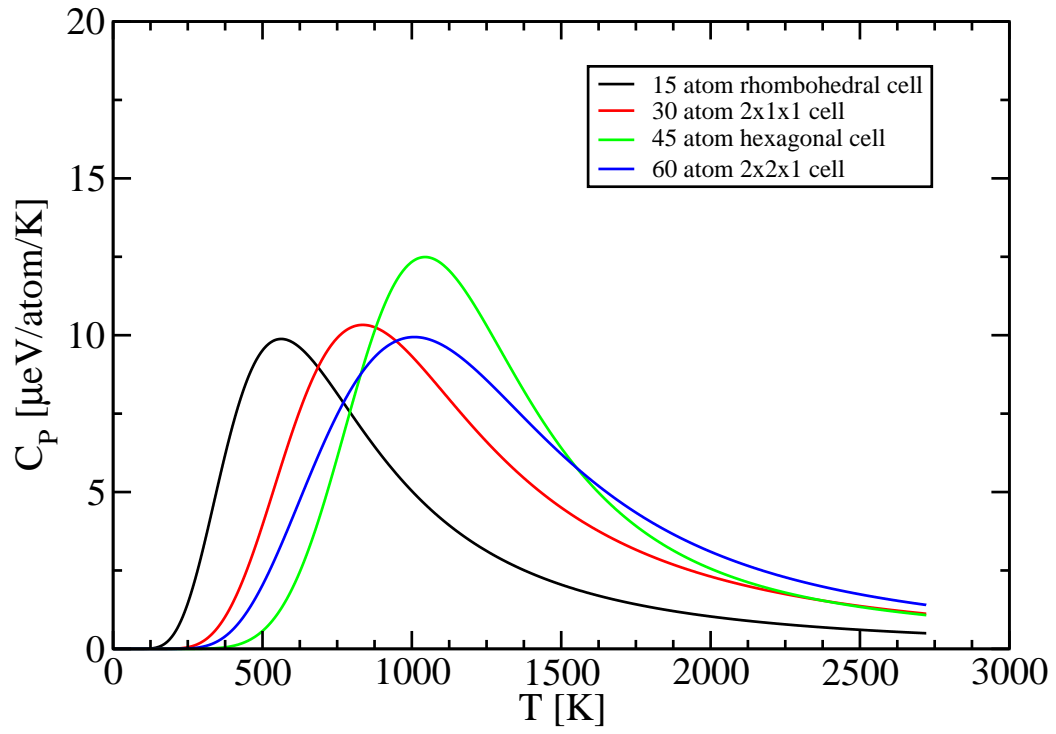
Differentiating Y with respect to $\delta\mu$ gives the number of carbon atoms N_C , while two derivatives with respect to T give the heat capacity

$$C_P(N, \delta\mu, T) = T \frac{d^2 Y}{dT^2} = -k_B T \frac{d^2 (T \ln Z)}{dT^2} = \frac{\langle H^2 \rangle - \langle H \rangle^2}{k_B T^2}$$

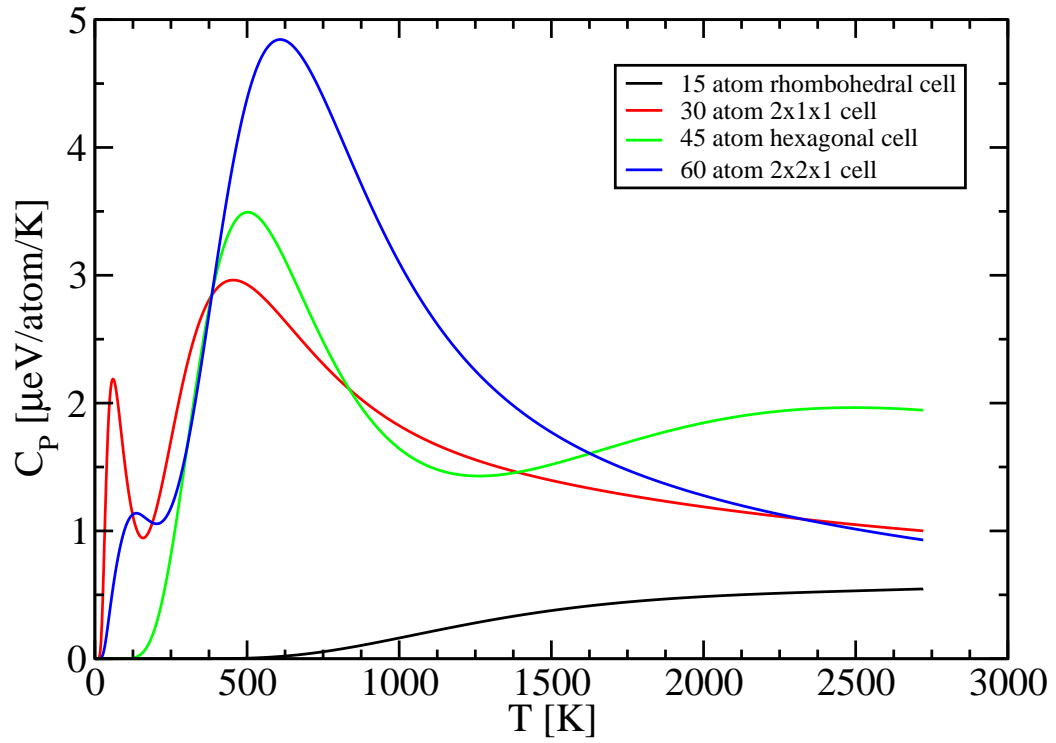
Where angle brackets indicate the configurational ensemble average, and H is the enthalpy of formation. Results for C_P are shown in Figure 3.4, using the energies displayed in Figure 3.3. Note that we only use subsets of the possible energies (those in black and blue), chosen to accurately reflect the thermodynamics up to 1000 K but omitting higher energy states that would cause the heat capacity to rise again as T increases. These states were omitted for reasons of limitations in computer time when dealing with larger cells and have no impact on the curves shown in Figure 3.4.

A phase transition is clearly indicated at $\delta\mu = 0$ by the peak in heat capacity around 500-600 K. The peak is growing in strength as system size increases, indicating a divergence in the infinite size limit. The peak is entirely absent in the case of the single primitive cell because the relevant excitation, rotations of C among polar B sites, is an exact symmetry of the primitive cell. In fact, there is a 6-fold degeneracy of the ground state. This degeneracy has no consequence in the thermodynamic limit as it is non-extensive. A weak peak is observed around 100-200 K in the two even super cells (30 and 60 atoms). These are due to a loss of inversion symmetry but with non-extensive multiplicity, so that the peak height tends to zero in the thermodynamic limit. For super cells of two or more primitive cells, the primary peak corresponds to rotation of the carbon atoms among icosahedral polar sites. The relevant excitations are rotational degrees of freedom in the selection of polar site on which to place carbon atoms. Because this phase transition corresponds to unlocking the orientations of polar carbons, rhombohedral symmetry is restored in the high temperature phase.

Although there is a heat capacity peak at $\delta\mu = -0.55$, this peak diminishes in



(a) $\delta\mu = -0.55$



(b) $\delta\mu = 0$

Figure 3.4: Heat capacities for $\delta\mu$'s of interest.

magnitude as system size increases, and thus is not evidence of a phase transition. It is caused by excitation of $B_{11}C_1$ icosahedra, while only B_{12} exist in the ground state at this chemical potential. Thus the $B_{13}C_2$ phase persists to high temperature with no change in thermodynamic state. The presence of polar carbons as low energy excitations allows this phase to exhibit a broad composition range. Owing to orientational disorder, full rhombohedral symmetry is present throughout the entire temperature and composition range.

By varying the chemical potential $\delta\mu$ we may vary the compositions of the B_4C and $B_{13}C_2$ phases. We find that the composition of B_4C remains nearly fixed at $x_C = 1/5 = 0.200$ at low temperatures. $B_{13}C_2$ shows some variability around the value $x_C = 2/15 = 0.133$ at low temperature, and high variability at high temperatures, reaching a low value of $x_C = 0.070$ a high value of $x_C = 0.198$. We do not expect our low carbon limit to be accurate because we have not extensively studied boron-rich structures. The carbon content decreases at high temperature owing to the entropy of selecting icosahedra on which to replace polar carbon atoms with boron. The high temperature limit at $\delta\mu = 0$ is precisely the same thermodynamic phase as was obtained at $\delta\mu = -0.55$.

3.4 Method 2: Analytic Free Energy Models

3.4.1 The Free Energy Models

Four solid phases compete for stability: elemental boron (β -rhombohedral), elemental carbon (graphite), and monoclinic and rhombohedral boron carbide. The first three phases are modeled as line compounds throughout the entire temperature range, but rhombohedral boron carbide will be allowed a carbon composition ranging from $B_{14}C_1$ ($x = 1/15 = 0.067$) to $B_{12}C_3$ ($x = 3/15 = 0.200$). The stable $T = 0$ K composition for the rhombohedral phase is $B_{13}C_2$ ($x = 2/15 = 0.133$). According to our previous first principles calculations, the most stable $B_{14}C_1$ structure consists of B_{12} icosahedra

with B-B-C chains. At composition $B_{12}C_3$ the most stable structure is monoclinic (i.e., not rhombohedral). Rhombohedral structures at this composition correspond to $B_{11}C$ icosahedra with C-B-C chains, but the placement of the carbon atom on the polar sites is randomly oriented among different primitive cells, unlike the monoclinic structure where all polar carbons are uniquely aligned throughout space. Thus our model for the rhombohedral phase allows as structural units B_{12} and $B_{11}C$ icosahedra, and C-B-C and B-B-C chains. Let y_C be the fraction of icosahedra containing a polar carbon, and y_B the fraction of chains containing a terminal B. Note that y_B and y_C are bounded between 0 and 1, and that the carbon fraction

$$x = \frac{1}{15}(y_C - y_B + 2). \quad (3.3)$$

The enthalpies of formation of β -rhombohedral boron and graphite vanish by definition, while we denote the 0 K enthalpies of the stable rhombohedral and monoclinic boron carbide phases, respectively, as h_R^0 and h_M^0 . Our first principles calculations yielded $h_R^0 = -0.087$ and $h_M^0 = -0.117$ eV/atom (see Fig. 3.5). Notice that the monoclinic phase is more stable, at $x = 0.200$, than the rhombohedral phase is at $x = 0.133$. We extend the rhombohedral phase entropy beyond its ideal composition by assigning an enthalpic penalty $\beta > 0^8$ for each excess chain boron and an enthalpic benefit $\gamma < 0$ for each icosahedral polar carbon. Thus $h(y_B) = h_R^0 + \beta y_B$ provided $y_C = 0$ and similarly $h(y_C) = h_R^0 + \gamma y_C$ provided $y_B = 0$, as illustrated in Fig. 3.5. In general, y_B and y_C are both nonzero, so that

$$h_R(x) = h_R^0 + \beta y_B + \gamma y_C. \quad (3.4)$$

To complete the free energy model we assign an entropy based on random substitution disorder. Specifically, an ideal site substitution entropy $-k_B(y \ln y + (1 - y) \ln(1 - y))$ for selecting the fraction y of structural units on which to substitute,

⁸To avoid confusion with this parameter, in this section we will explicitly write $1/k_B T$ instead of β .

together with an intrinsic rotational entropy $k_B \ln 6$ for the orientation of the icosahedral polar carbon, and an intrinsic reflection entropy $k_B \ln 2$ for the choice of terminal chain position, as there are six polar sites per icosahedron and two terminal sites per chain. Thus,

$$s_R(x) = \frac{k_B}{15}(y_B \ln 2 - y_B \ln y_B - (1 - y_B) \ln(1 - y_B)) + \frac{k_B}{15}(y_C \ln 6 - y_C \ln y_C - (1 - y_C) \ln(1 - y_C)) \quad (3.5)$$

combined with Equation 3.4 yielding the free energy

$$g_R(x, T) = h_R(x) - T s_R(x). \quad (3.6)$$

A similar free energy model was proposed by Emin [74], although he supplemented the free energy with an additional bipolaron density that is no longer considered as relevant. As the monoclinic phase is a line compound, no composition dependence is required for its enthalpy, and because the rotational degree of freedom is locked, it lacks entropy.

Fig. 3.5 illustrates components of the free energy. Black circles denote the enthalpies h_R^0 and h_M^0 , while the black line segments are the convex hull of free energy $g(x)$ at $T = 0$ K. Red lines and green curves illustrate enthalpy and 2000 K free energy under the constraint that either y_B or y_C vanishes, taking parameter values $\beta=0.05$ and $\gamma = -0.024$. The blue curve illustrates the 2000 K free energy $g_R(x)$ (Equation 3.6) with the constraint relaxed, while the dashed pink line is the full convex hull of free energy $g(x)$.

The free energy $g_R(x)$ in Equation 3.6 is to be regarded as a Landau-type free energy, as the order parameters y_B and y_C must still be determined as a function of composition x and temperature T . Note the two order parameters are not independent, as the composition Equation 3.3 implies $(dy_C/dy_B)|_x = 1$. Now, minimizing g_R with respect to y_C yields

$$0 = \left. \frac{dg_{rhom}}{dy_C} \right|_x = \beta + \gamma + \frac{k_B T}{15} \left(-\ln 12 + \ln \left(\frac{y_B}{1 - y_B} \frac{y_C}{1 - y_C} \right) \right) \quad (3.7)$$

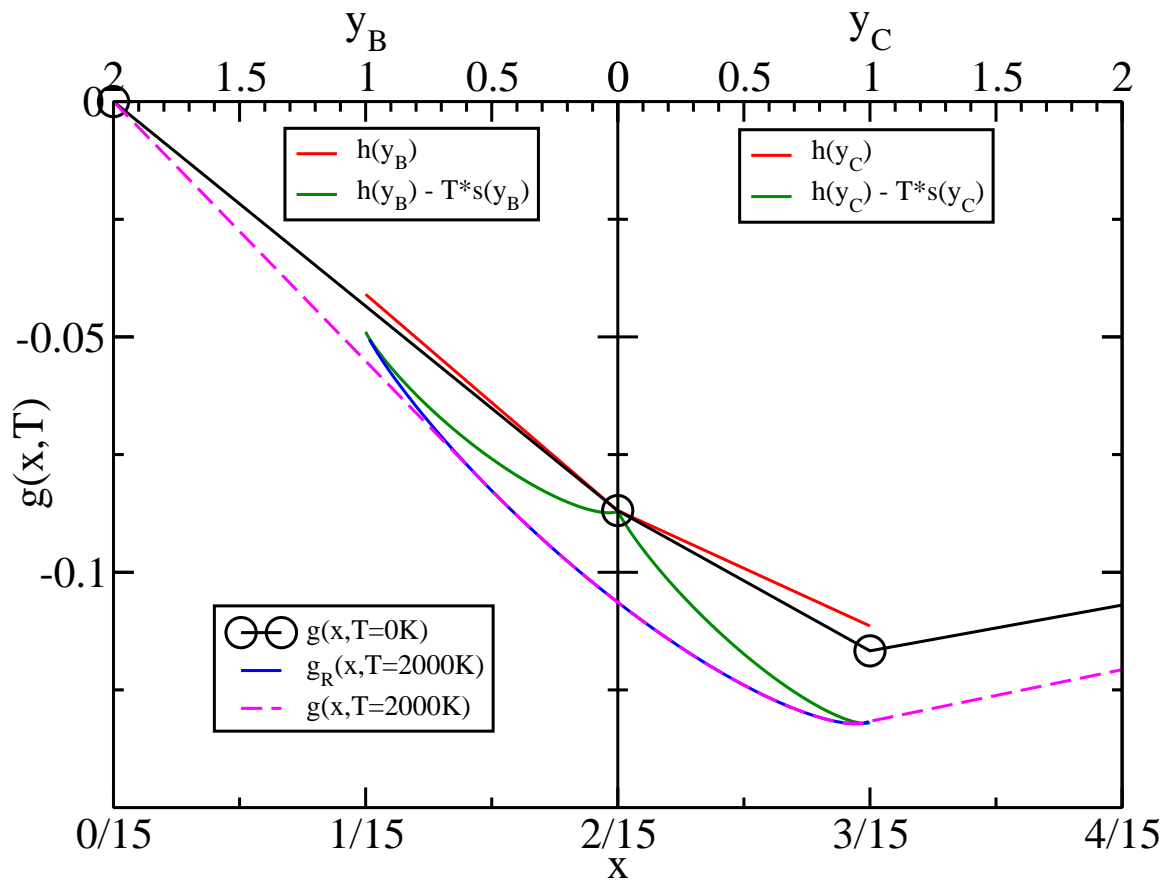


Figure 3.5: Components of free energy model. Details in text.

Substituting for the parameter y_B and rearranging yields a quadratic equation for y_C ,

$$y_C^2(1 - \kappa) + (2 - 15x(1 - \kappa))y_C + \kappa(1 - 15x) = 0, \quad (3.8)$$

where we define

$$\kappa(T) \equiv 12e^{-15(\beta+\gamma)/k_B T} \quad (3.9)$$

as a measure of the extent to which polar boron atoms can swap positions with chain terminal carbons, which constitutes the fundamental excitation of the ideal rhombohedral structure.

3.4.2 T \rightarrow 0 K Limit

We require that the enthalpy parameters $\beta + \gamma > 0$ to ensure that the ideal rhombohedral structure with $y_B = y_C = 0$ minimize the free energy at $x = 2/15$ in the limit $T = 0$. Hence,

$$\lim_{T \rightarrow 0} \kappa(T) = 0, \quad (3.10)$$

reduces Equation 3.8) to the equation $y_C^2 + (2 - 15x)y_C = 0$ with two solutions: either $y_C = 0$ (and then $y_B = 2 - 15x$), or else $y_C = 15x - 2$ (and then $y_B = 0$). That is, either boron substitutes on chain terminal carbon sites, in which case $y_C = 0$ and $x < 2/15$, or else carbon substitutes on icosahedral polar boron sites in which case $y_B = 0$ and $x > 2/15$. As a function of composition we have

$$y_B = (2 - 15x)\theta(2/15 - x), \quad y_C = (15x - 2)\theta(x - 2/15) \quad (3.11)$$

where θ is the Heaviside step function.

Although exact only at 0 K, the essential singularity in κ makes this an excellent approximation over a wide range of temperature, up to 1000K and sometimes even higher in the examples discussed later. The approximation represented by Equation 3.11 separates the free energy into two branches, an $x < 2/15$ branch where only y_B terms contribute, and an $x > 2/15$ piece where only y_C terms contribute, as illustrated in Fig. 3.5. In each case, one branch of this piecewise-analytic free energy

competes with a line compound, so we next derive a general equation for the phase boundary in this scenario.

Substitutional Disorder Coexisting with a Line Compound

To find the phase boundaries of rhombohedral boron carbide we must locate the coexistence of our substitutional disordered phase with the competing phases. Depending on composition and temperature the coexisting phase might be β -rhombohedral boron, monoclinic boron carbide, or graphite. In every case the coexisting phase is treated as a line compound whose free energy is simply its enthalpy. In this section we solve the coexistence equations generally, then apply this solution to specific phase boundaries in the following sections.

Consider the free energy model for substituting on a fraction y of structural units, each with intrinsic multiplicity Ω and enthalpic penalty δ ,

$$g(y, T) = h_R^0 + \delta y - \frac{k_B T}{15} (y \ln \Omega - y \ln y - (1 - y) \ln(1 - y)). \quad (3.12)$$

Such a free energy represents one of the two branches of our rhombohedral free energy Equation 3.6 at low temperature. Let this phase coexist with an ordered line compound of free energy $g^* = h^*$ and “composition” y^* . We now wish to find the composition, y' , of the disordered phase that coexists with the ordered phase at y^* .

Coexistence is determined by a double tangent condition, at y' and y^* . Specifically, there exists a straight line $f(y) = f_0 + f_1 y$ that is tangent to g^* at $y = y^*$ and to $g(y, T)$ at $y = y'$. For the line compound, tangency at y^* is the simple condition $f(y^*) = h^*$. For the disordered phase, tangency requires both that $f(y') = g(y', T)$ and that $f' = f_1 = g'(y', T)$, where

$$g'(y, T) = \delta - \frac{k_B T}{15} \left(\ln \Omega - \ln \frac{y}{1 - y} \right). \quad (3.13)$$

Solving, we find

$$\Omega^{y^*} e^{15(h^* - h_R^0 - \delta y^*)/k_B T} = (y')^{y^*} (1 - y')^{1 - y^*}. \quad (3.14)$$

In the case where $y' \approx 0$, this equation simplifies to

$$y' \approx \Omega e^{15(h^* - h_R^0 - \delta y^*)/y^* k_B T}, \quad (3.15)$$

while for $y' \approx 1$, we have

$$y' \approx 1 - \left(\Omega e^{15(h^* - h_R^0 - \delta y^*)/k_B T} \right)^{\frac{1}{1-y^*}}. \quad (3.16)$$

Boron-rich phase boundary

We apply this general solution to the specific case of rhombohedral boron carbide coexisting with β -rhombohedral boron. In the notation of the preceding section, $h^* = 0$. There are two cases to consider depending on whether the phase boundary lies to the left or to the right of $x = 2/15$.

Case 1. If the boundary lies at $x \leq 2/15$, so that $y_C = 0$, then we identify $y = y_B$, $\delta = \beta$ and $\Omega = 2$, as the disorder corresponds to substitution of boron onto the terminal chain carbon sites. Also, $y^* = 2$ corresponds to the composition $x = 0$. The requirement that β -rhombohedral boron be stable at $x = 0$ against the boron carbide phase at $y_B = 2$ implies a constraint that $2\beta > -h_R^0$. The phase boundary occurs in the limit of small y , and from Equation 3.15 we have

$$y'_B = 2e^{-15(h_R^0 + 2\beta)/2k_B T}. \quad (3.17)$$

Case 2. If the boundary lies at $x \geq 2/15$, so that $y_B = 0$, then we identify $y = y_C$, $\delta = \gamma$ and $\Omega = 6$, as the disorder corresponds to substitution of carbon onto the icosahedral polar sites. Also, $y^* = -2$ corresponds to the composition $x = 0$. The requirement that free energy be convex at $x = 2/15$ implies a constraint that $2\gamma > h_R^0$. The phase boundary occurs in the limit of small y , and from Equation 3.15 we have

$$y'_C = 6e^{+15(h_R^0 - 2\gamma)/2k_B T}. \quad (3.18)$$

To determine if case 1 or 2 occurs, consider the ratio

$$y'_C/y'_B = 3e^{-15(\gamma - \beta - h_R^0)/k_B T}. \quad (3.19)$$

If $\gamma - \beta - h_R^0$ is positive, then the ratio vanishes at low temperature and the requirement of convexity places us in case 1. If instead it is negative, then the ratio diverges and we have case 2.

Carbon rich phase boundaries

Next we apply our general solution to the specific case of rhombohedral boron carbide coexisting with monoclinic boron carbide. Now, in the general notation, $h^* = h_M^0$. As in the case of coexistence with elemental boron, two specific cases are possible. However, the fact that carbon substitution is known to be energetically favorable (i.e. $\gamma < 0$) implies that only the case of $y_B = 0$ and $y = y_C$ is relevant. Thus we identify $\delta = \gamma$ and $\Omega = 6$. Noting that the condition for low temperature stability of monoclinic B_4C against disordered rhombohedral at $x = 3/15$ is $h_R^0 + \gamma > h_M^0$, the phase boundary occurs in the limit of small y' , and from Equation 3.15 we have

$$y'_C = 6e^{-15(h_R^0 - h_M^0 + \gamma)/k_B T} \quad (3.20)$$

as the phase boundary in coexistence with the monoclinic phase.

However, above a certain temperature T_0 the rhombohedral phase coexists with graphite. We assume T_0 lies in the low temperature limit, and find the general form for the phase boundary due to coexistence between graphite and the rhombohedral phase. In our general notation, $y^* = 13$, $y = y_C$, $\delta = \gamma$ and $\Omega = 6$. In contrast to the preceding cases, the phase boundary occurs in the limit of $y \approx 1$, and from Equation 3.16 we have

$$y'_C = 1 - 6^{-\frac{13}{12}} e^{15(h_R^0 + 13\beta)/12k_B T} \quad (3.21)$$

as the phase boundary in coexistence with graphite. The two carbon-rich boundaries cross at a certain temperature T_0 that can be determined by setting the values of y'_C equal in Equation 3.20 and 3.21. For realistic parameters, the crossing occurs at $y_C \approx 1$. Then from Equation 3.20 we find

$$T_0 \approx \frac{15(h_R^0 - h_M^0 + \gamma)}{k_B \ln 6}. \quad (3.22)$$

3.4.3 Analytic $T=\infty$ Limit

We now examine the high temperature limit for the free energy model. For all possible values of β and γ we have $\lim_{T \rightarrow \infty} \kappa(T) = 12$ giving the quadratic equation $-11y_C^2 + (2 + 165x)y_C + 12(1 - 15x) = 0$, only one of whose roots is physical: $y_C = \frac{1}{22}(2 + 165x - \sqrt{532 - 7260x + 27225x^2})$. Notice that only the multiplicities enter into this equation. Although this equation is more complicated than the one obtained for the low temperature limit, it is defined across the composition range from $x = 1/15$ to $x = 3/15$. The phase boundary on the boron rich side, x'_{boron} , is given by

$$\left. \frac{dg_R}{dx} \right|_{x=x'_{boron}} = \frac{h_{\beta-boron} - g_R(x'_{boron}, T)}{0 - x'_{boron}} \quad (3.23)$$

and the phase boundary on the carbon rich side x'_{carbon} is given by

$$\left. \frac{dg_R}{dx} \right|_{x=x'_{carbon}} = \frac{h_{graphite} - g_R(x'_{carbon}, T)}{1 - x'_{carbon}}. \quad (3.24)$$

The high temperature limits are dominated by the entropic terms, yielding nonlinear implicit equations for x' . Using a numeric equation solver we find $x'_{boron} = 0.1095$ and $x'_{carbon} = 0.1515$. However these values are reached only at extreme high temperatures, while our model is intended only for use below the melting temperature.

3.4.4 Results of the Free Energy Models

Our simple model depends on just four parameters, h_R^0 , h_M^0 , β and γ . Of these, the values of $h_{R,M}^0$ are easily determined from first principles calculations with simple idealized models. Estimated values of β and γ may be obtained by inserting a single B or C substitutional defect into a hexagonal supercell of the ideal rhombohedral $B_{13}C_2$ structure. Resulting values are listed in Table 3.2. These parameters obey the constraints discussed in previous sections. Because $\gamma - \beta - h_R^0 = -0.0406$ is negative, we are in case 2 as discussed in Section 3.4.2 where $x'_{Boron} > 2/15$ at low temperature, although it eventually goes to $x'_{Boron} < 2/15$ at very high temperatures.

| Parameter | Value (eV/atom) |
|-----------|-----------------|
| h_R^0 | -0.0869 |
| h_M^0 | -0.1167 |
| β | 0.1031 |
| γ | -0.0244 |

Table 3.2: Parameters for the rhombohedral phase obtained from first principles calculations.

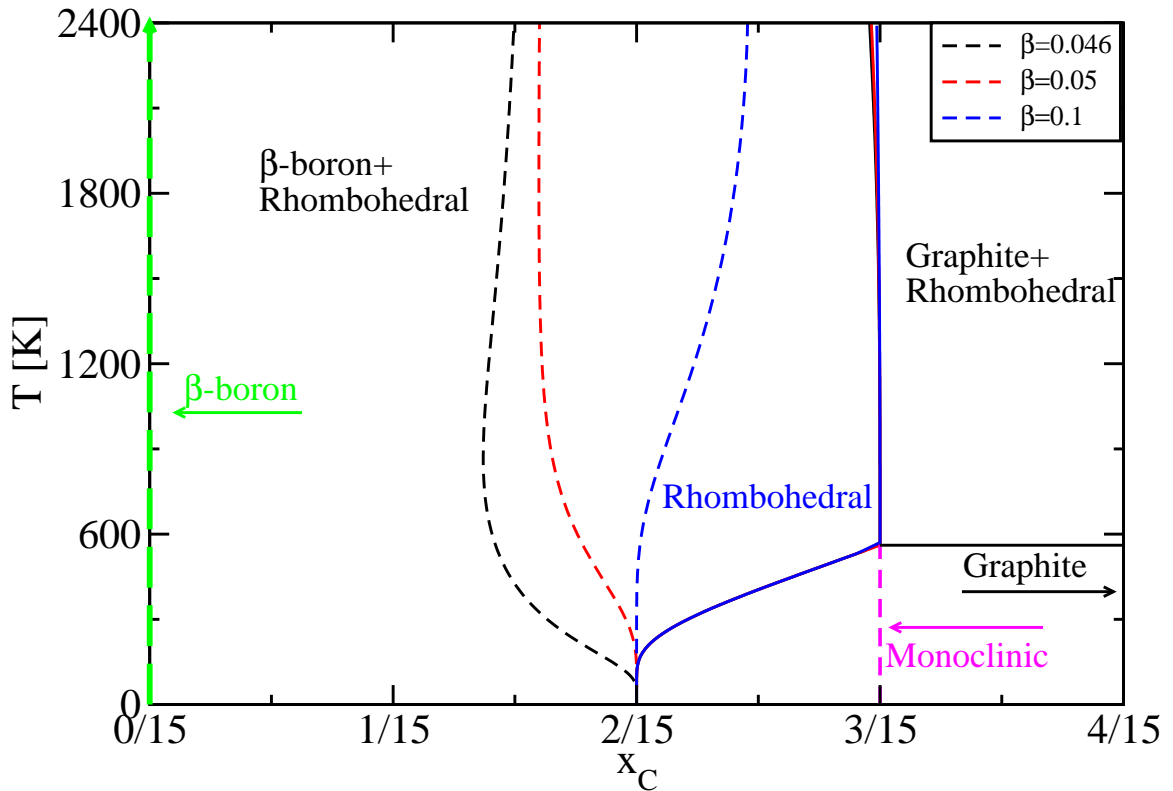


Figure 3.6: Predicted phase boundaries for our model using calculated parameters as listed in Table 3.2 and a selection of values of β . Line compounds are β -boron at $x = 0$, graphite (not shown) at $x = 1$ and monoclinic boron carbide at $x = 3/15$. Carbon-rich phase boundaries of rhombohedral boron carbide are shown as solid lines, while boron-rich phase boundaries are shown as dashed lines.

There is some question whether our structural model is complete in the B-rich limit, as alternate structure models contain additional sites in the chain region, some only partially occupied [68, 86, 71]. To take into account a possible influence of these additional sites, we investigate the effect of reducing the value of β , in order to model the effect of lower boron-rich enthalpies. Note that increased multiplicity Ω would also enter the free energy linearly in y_B , though with an added factor of temperature T .

Results for a selection of values of β are shown in Fig. 3.6. As expected, the monoclinic phase is destabilized above a temperature ≈ 600 K, at which it decomposes into a coexistence of carbon-rich rhombohedral phase together with graphite. This value of T_0 is surprisingly consistent with the location of the heat capacity peak obtained from enumeration of the partition function. The maximum carbon content of the rhombohedral phase is bounded below 20%, owing to the logarithmic singularity in $s(y)$ at $y_c = 1$ creating an infinite slope in $g(x, T)$ (too weak to be visible in Fig. 3.5). Note that the Gibbs phase rule [9] implies that rhombohedral and monoclinic boron carbide must have differing compositions while in coexistence with graphite, hence $x'_C = 0.2000$ is forbidden in principle.

At temperature 2400 K (around the melting point) the maximum carbon content depends on the value of β , and ranges from 19.9% down to 19.7% in our model for the given range of β considered, whereas the experimentally assessed limit is 19.2%. The phase boundary in coexistence with boron depends strongly on the value of β , as can be seen in Fig. 3.6. The experimentally assessed limit is 9% carbon, but over the range of β values studied here, the limit ranges from 10-16% carbon, strictly above the assessed value. This is a further indication of inadequacy of our model in the boron-rich limit.

Chapter 4

On the Stability of the High-Entropy Alloy Mo-Nb-Ta-W¹

4.1 The High-Entropy Alloy Mo-Nb-Ta-W: A Vague Phase Diagram

Over the past 30 years, a new paradigm has emerged for materials design. Instead of stumbling on new materials accidentally, then finding uses for them, one starts with a list of properties then creates a material from multiple species with the desired properties. This is in theory possible because various “averaging schemes” or “rules of mixtures” exist in materials design, where one can roughly estimate a property for an alloy given its constituent species and their relative number/mass/volume concentrations². Designing a material from scratch may seem rather obvious, and it is indeed

¹Much of this chapter has been adapted from my papers “Hybrid Monte Carlo/Molecular Dynamics Simulation of a Refractory Metal High Entropy Alloy” [87] and “Prediction of A2 to B2 Phase Transition in the High Entropy Alloy Mo-Nb-Ta-W” [88]

²This is not exactly true, as most interesting materials are useful because they deviate favorably from averaging schemes. Nevertheless, averaging schemes are a useful first step towards materials design

not a particularly new idea, but it was impeded by thermodynamic considerations in most cases. Even if the materials researcher succeeds in creating a material, it will likely be metastable. He can only hope that the material he creates is thermodynamically stable, which is the “miracle material” approach all over again³.

So how can stability be enhanced? Viewed from the standpoint of equilibrium statistical mechanics, there are two primary mechanisms for stabilization (at $p \approx 0$), energetic and entropic. The former dominates the low temperature regime and is based off favorable bonding. This is the stabilization that is primarily (though not exclusively) responsible for the “miracle materials” approach. The latter dominates the high temperature regime and is based off disorder. Usually, entropy is the difficult part of free energy modeling, and designing materials with a favorable entropic contribution is difficult for most materials. There is one exception: the ideal solution, for which the entropy becomes $-Nk_B \sum_i x_i \ln(x_i)$. It is trivial to show that this is maximal when all x_i are equivalent, and for a system with d many species, this quantity becomes $N k_B \ln(d)$.

Alloying more species together in an ideal solution enhances the entropy and thus the temperature range over which the ideal solution is stable. This is the idea behind “high-entropy alloys” (HEAs) [89], where four or more species are alloyed together in equal parts to form solid solutions in relatively simple lattice structures (bcc, fcc, hcp). Due to the flatness of the configurational entropy near equiatomic compositions, some deviation from perfect equiatomic composition is possible while still maintaining the strong entropic stabilization. Properties of the HEA may be tuned using alloying species with the desired properties via a rule-of-mixtures approach [90]. The resulting phase forms a solid solution on the simple lattice structures, and its stability should be enhanced due to the increase in configurational entropy and *only* the increase in

³Alternatively, one may make peace with metastability and to try to make the energy barriers realistically insurmountable. This is the concept behind amorphous materials, which will be discussed in the next chapter.

configurational entropy. Importantly, unlike their close cousin bulk metallic glasses, their stability is *enhanced* as temperature increases.

It is always possible that undesired complex metastable intermetallic phases may appear when growing any material. Fortunately, it is a commonly reported feature of HEA growth that, with relatively little processing, either a single disordered phase exists across the entire sample or small regions with some ordering (for example, regions of B2/CsCl ordering existing in an A2/bcc phase) [89, 91]. This is not always the case, as some HEA families do exhibit multiple phases at high temperature due to residual energetic considerations [92, 93, 94], but these families are the exception rather than the rule, and it can be argued that they should not be classified as HEAs.

Furthermore, because the stability of HEAs is entropy dominated, which is independent of the species chosen, the materials researcher has a degree of freedom in his design. It must be stressed that many combinations of species will have significant enough interactions (atomic size mismatches, enthalpies of formations, etc.) to impede formation of the ideal solution [95, 96, 97, 98, 99], and determining exactly which elements form HEAs is an active field of research at present.

One common class of HEAs are those containing “refractory metals”, with high melting temperatures (2750 K for Nb and 3695 K for W) and high hardness at room temperature, yielding possible application in the aerospace industry. Even at lower temperatures, their high melting temperatures are useful as they impede the phenomena of “alloy softening”, where alloys’ mechanical properties degrade at around 50% to 60% of the melting temperature due to temperature activation of diffusion events. Here we are concerned with one such HEA, Mo-Nb-Ta-W [100, 101] with an estimated rule-of-mixtures melting temperature of 3160 K. Its measured density and lattice parameters of 13.75 g/cm³ and 3.2134 Å agree well with the rule-of-mixtures estimate of 13.64 g/cm³ and 3.2230 Å, respectively. Where the rule-of-mixtures approximation fails is the hardness, with a sample expected to have a Vickers hardness of 1788 MPa exhibiting an average microhardness of 4455 MPa, likely due to solid

solution strengthening induced by atomic size mismatches locally distorting the underlying lattice [89, 102]. However, its practical application has been impeded by it being brittle.

These high melting temperatures combined with large temperature ranges for phase stability makes experimental study of the thermodynamic properties of alloys involving refractory metals problematic, as it is unlikely that thermodynamic equilibrium can be achieved on experimental time scales. Accordingly, only high temperature (>2000 K) phase diagrams exist for the refractory metal binaries, all of which present a single A2 phase across the entire composition range, with liquidus and solidus lines nearly coincident. Due to lack of equilibration, experimental values for thermodynamic properties at low temperatures are of doubtful accuracy. To study phase stability of such alloys, first principles calculations are the most accurate method currently available.

In this section we will calculate stability of the Mo-Nb-Ta-W HEA from first principle calculations. This is an uncommon usage of first principles calculations, which are commonly used for well-ordered structures, as no known crystal structure for any combination of Mo, Nb, Ta, or W exists, and HEAs are by definition disordered phases. We will extend first principles calculations in two ways. The first is to calculate the ensemble average of the HEA using a hybrid MC/MD method on a bcc lattice, where molecular dynamics steps are alternated with Monte Carlo swaps. Pair correlations functions can be determined from ensemble averaging, showing tendency towards ordering at various temperatures. Our results show that atomic size differences (e.g. Nb and Ta being larger than Mo and W) favor chemical ordering at low temperature, and a surprising degree of disorder among atoms of similar size (e.g. Nb with Ta, and Mo with W) persists even below 300 K. This points towards a strong tendency towards cP2 ordering in a pseudobinary model.

The second method uses an effective Hamiltonian fit to first principles data. As no known structure exists in these binary families, we use a cluster expansion method

known as the Alloy Theoretic Automated Toolkit to generate candidate convex hulls for the various binaries. Using both a mean field model and Monte Carlo simulations, we predict an order/disorder A2 to B2 transition at 1280 K due to energetic preference of Mo-Ta bonding, upholding the basic results of the pseudobinary model previously proposed but with some deviations. That the HEA phase is stable over a temperature of 1900 K due solely to textbook thermodynamics only highlights the versatility of this new paradigm.

4.2 A Pairwise Bond Model

The four elements belong to a 2×2 square block of the periodic table, and hence their physical properties will bear specific relationships to each other. The present study considers elements from the chromium group (group 5, here Ta and Nb) and from the vanadium group (group 6, here W and Mo) located in the fourth row (here Nb and Mo) and in the fifth row (here Ta and W). Atomic size drops as group number increases, and to a lesser as row number increases. Hence, we understand the sequence of atomic volumes (in units of $\text{\AA}^3/\text{atom}$): Ta (18.10) \gtrsim Nb (18.05) \gg W (15.82) \gtrsim Mo (15.61). Trends in electronegativity (Pauling scale) are nearly (but not perfectly) opposite to atomic volume, hence: Ta (1.5) \lesssim Nb (1.6) \ll Mo (2.16) \lesssim W (2.36). Various combinations of size and electronegativity differences have been linked to structure formation, and the present compounds lie close to a predicted cP2-forming region [103, 104]. Here we will mainly refer to atomic size, but in fact both size and electronegativity play mutually reinforcing roles.

Owing to these volume and electronegativity contrasts we anticipate relatively strong binding between elements from different transition metal groups of the periodic table (here Nb-Mo, Nb-W, Ta-Mo and Ta-W), and relatively weak binding between elements from the same group (Nb-Ta and Mo-W). Among the inter-group formation enthalpies, we expect the pair Nb-W, with intermediate sizes and electronegativities,

| | Group 5 | | Group 6 | |
|----|------------|------------|------------|------------|
| | Ta | Nb | W | Mo |
| Ta | cI2 (0) | hR8 (4) | oA12 (103) | oA12 (186) |
| Nb | hR8 (4) | cI2 (0) | cF16 (47) | oA12 (103) |
| W | oA12 (103) | cF16 (47) | cI2 (0) | cP2 (9) |
| Mo | oA12 (186) | oA12 (103) | cP2 (9) | cI2 (0) |

Table 4.1: Optimal structures and enthalpies for pairwise interactions at 50-50% composition. Elements are ordered in decreasing atomic volume. Pearson symbol of stable compound followed by negative enthalpy of formation (units meV/atom).

to be the weakest interaction, and this expectation is reflected in the strong negative deviation of the Nb-W solidus temperature relative to Vegard’s rule.

The results at equiatomic concentrations are summarized in Table 4.1, based on the VASP [83] calculations using projector augmented wave potentials [28] with the PBE [25] exchange correlation functional. The enthalpies of formation increase away from the diagonal in this table, reflecting the greater tendency towards compound formation associated with greater atomic size contrast. The most common energy minimizing structure is Pearson type oA12 (Strukturbericht B₂₃) which is cP2-like but with antiphase boundaries. On average the perfectly ordered cP2 structure is about 8 meV/atom (i.e. $k_B T$ at about 100 K) above the energy minimizing structure.

Consequently, in our four element compound, we anticipate low energy structures will exhibit chemical order dominated by cP2-like alternation of (Nb,Ta) atoms on one sublattice (e.g. cube vertices) and (Mo,W) atoms on the other sublattice (e.g. cube body centers). The absolute ground state may in fact separate into binaries or ternaries of various compositions, but owing to the strong interactions across groups, and the weak interactions within groups, we expect to achieve cP2-like order even at relatively low temperatures.

4.3 A Search for the T=0 K States

To generate ground state structures, we use the Alloy Theoretic Automated Toolkit (ATAT) [105, 106, 107, 108], a framework that iteratively generates a cluster expansion, based on ab-initio total energies, to suggest new candidate ground state structures for a given lattice type. We applied ATAT to all six binary combinations of Mo, Nb, Ta, and W on a BCC lattice. Between 60 and 100 structures were generated per binary. The K-Point Per Reciprocal Atom (KPPRA) density was fixed to 9000 for all binaries. All binaries finished with crossvalidation scores less than 0.0063. Subsequent relaxation and convergence of predicted ground state and metastable structures in k-point density was then performed. To calculate total energies, we use VASP (the Vienna Ab-Initio Simulation Package) [82, 83], a plane wave ab-initio package implementing PAW pseudopotentials [27]. We use the PBE density functional [25], with default energy cutoffs for total energy calculations. Relaxation was performed at P=0. To our knowledge, no examinations of refractory metal binaries have been performed using this functional.

We identify structures by the notation [chemical formula].[Pearson symbol], using only the Pearson symbol when the chemical formula is implicitly understood. Common candidate structures for these binaries include cP2 at 50% composition (Strukturbericht B2, prototype CsCl), oA12 at 50% composition (Strukturbericht B2₃), tI6 at 33.3% and 66.7% composition (Strukturbericht C11_b, prototype MoSi₂), and cF16 at 25% and 75% composition (Strukturbericht D0₃, prototype BiF₃). oA12, a variant of cP2 with antiphase boundaries, is of special importance as it has been identified by previous work [109, 110] using cluster expansion methods as a potential ground state structure in Mo-Nb, Nb-W, and Ta-W.

Our results for binaries may be summarized as follows. Mo-Ta shows strongest bonding, with strongest enthalpy of formation of -186 meV/atom. Mo-Nb and Ta-W have nearly equal bonding at -103 meV/atom and -110 meV/atom respectively, with Nb-W the weakest of the intergroup binaries at -53 meV/atom. The intragroup bi-

naries Mo-W and Nb-Ta are essentially ideal (i.e. vanishing enthalpy). This ordering is consistent with electronegativity and atomic radii differences. Mo-Ta and Mo-Nb have roughly symmetric convex hulls about equiatomic concentration, whereas Nb-W and Ta-W are biased towards high W concentrations with minima at 66.7% W. Both sets of observations are consistent with experimental observations that intergroup alloys Mo-Ta, Mo-Nb, Nb-W, and Ta-W exhibit cleavage near equiatomic concentrations, while Mo-W and Nb-Ta exhibit flow [111]. We confirm that in these systems cP2 is not the stable structure at equiatomic concentration, with the exception of Mo-W where enthalpies of formation deviate negligibly from ideality, and that oA12 is stable for many of the binaries. However, with the exception of Nb-W, cP2 is within 10 meV/atom of the convex hull. This suggests that a B2 phase could be stabilized at intermediate temperature through the entropy of intragroup mixing. Below we compare our predictions for individual binaries with prior literature.

4.3.1 Mo-Nb

Previous first principles calculations on this system have been performed by Curtarolo *et al.* [112] and Blum and Zunger [110]. While both observe the cP2, Mo-rich cF16, and Mo-rich and Nb-rich tI6 structures stable using the LDA functional, Blum and Zunger contend that their mixed-basis cluster expansion (MBCE) fit indicates that the cP2 and Nb-rich tI6 are not stable and that at equiatomic concentration oA12 is stable (although LDA predicts this structure to be unstable). Our PBE study predicts oA12 is stable and minimizes the enthalpy of formation at -102.9 meV/atom, while cP2 lies 4.3 meV/atom above. We find both Mo-rich and Nb-rich tI6 lie on the convex hull. Mo-rich cF16 lies 1.0 meV/atom off the convex hull, well within margin of error, but Ta-rich cF16 lies substantially above at 18.9 meV/atom. The Mo-rich side of the convex hull is more detailed than the Nb-rich side, though the convex hull is generally symmetric about equiatomic concentration.

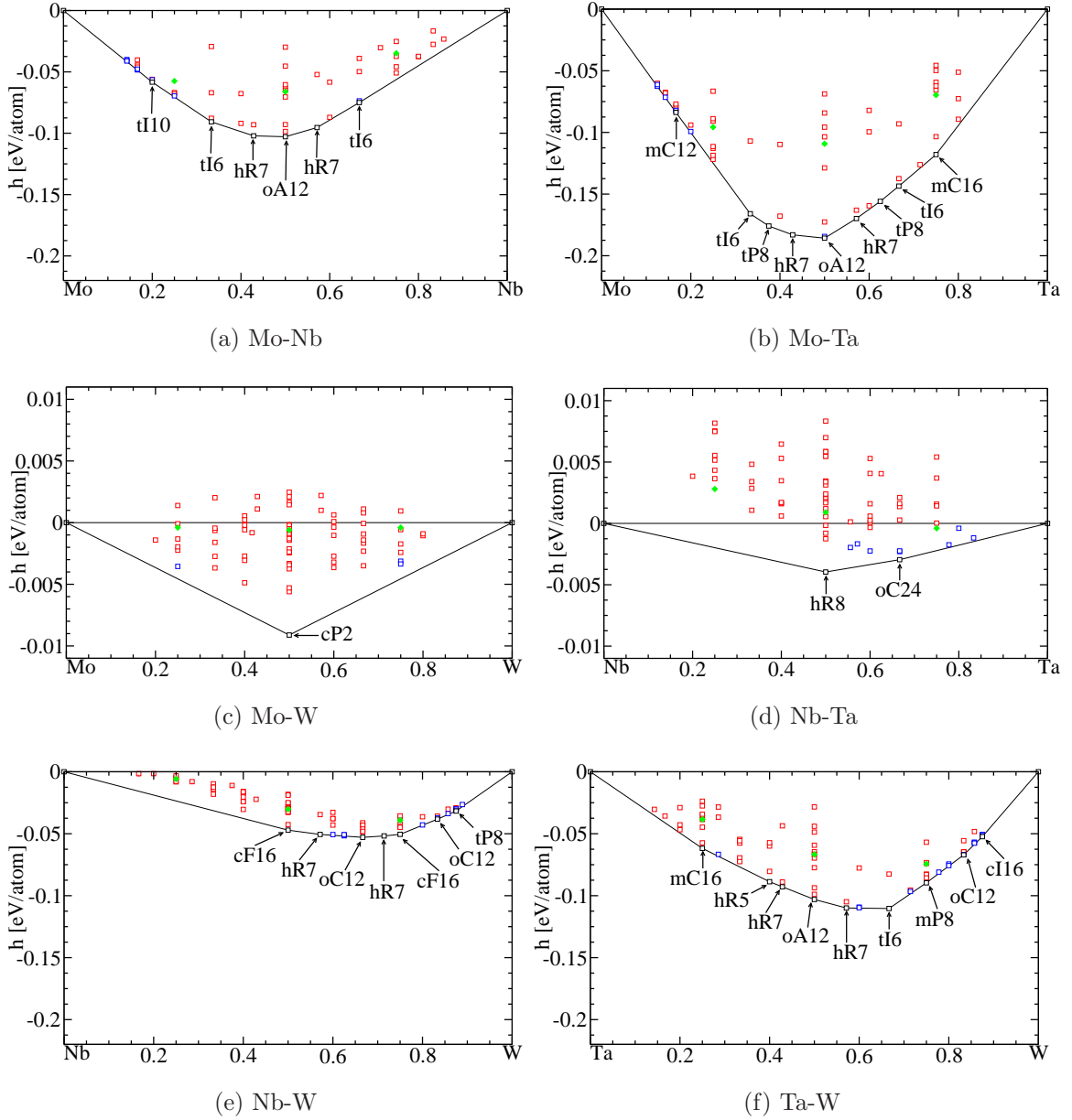


Figure 4.1: First principles enthalpies of formation for binaries. Black squares denotes structures on the convex hull, blue squares denotes structures within 2 meV/atom of the convex hull, and red squares above 2 meV/atom. Filled green diamonds denote 16 atom BCC SQS structures [6]. The scales of Mo-W and Nb-Ta differ from the scales from the other four binaries.

4.3.2 Mo-Ta

Previous first principles work on this system has been performed on this system by Blum and Zunger [113, 110] and Turchi *et al.* [114]. While Blum and Zunger observe the cP2 and Mo-rich and Ta-rich tI6 to be stable using the LDA functional, their MBCE states that the Ta-rich tI6 is not stable. Turchi *et al.*, using a cluster variation method approach combined with first principles calculations, find an A2 to B2 transition at 1772K and 47% Ta. oA12 minimizes enthalpy of formation for the system at -185.8 meV/atom, with cP2 1.4 meV/atom above. We find Mo-rich and Ta-rich tI6 to both be stable, in agreement with LDA results but not Blum and Zunger's MBCE. van Torne and Thomas [111] observed non-ideal behavior in Mo-Ta BCC solid solutions at 273 K, in line with the tendency towards chemical ordering, though they attribute this to concentration gradients in their sample which were likely not in equilibrium.

4.3.3 Mo-W and Nb-Ta

For binaries Mo-W and Nb-Ta, at 2000K and 2600K, respectively, experimental enthalpies of mixing are low for all compositions and activities perfectly follow Raoult's Law, suggesting an ideal solution with no chemical bonding. This is in agreement with our first principles calculations, which have a minimum enthalpy of formation of -10 meV/atom and -3 meV/atom for Mo-W and Nb-Ta, respectively, indicating nearly perfect mixing of atomic species. This is in agreement with Villar's empirical criteria [103], as both binaries consist of BCC metals with similar electronegativity and atomic radius. To our knowledge, no other first principles results for these binaries exist in the literature.

4.3.4 Nb-W

For Nb-W significant deviations from symmetry in the convex hull are observed, with no stable structures found on the Nb-rich side of the convex hull. The equiatomic concentration stable structure is cF16 (prototype NaTl), with cP2 28.2 meV/atom above. However, the minimum enthalpy of formation structure is an oC12 structure at 66.7% W with enthalpy of formation at -52.9 meV/atom. Blum and Zunger [110] also found a detailed W-rich side of the convex hull, and a Nb-rich side containing only one structure that negligibly affects the shape of the convex hull. In particular, our PBE predicts W-rich tI6 is unstable by 6.6 meV/atom, which does not agree with LDA results, but does agree with Blum and Zunger’s MBCE.

4.3.5 Ta-W

Of all binaries considered, Ta-W is the most studied. Experimental work [115] indicates negative deviation from Vegard’s law for lattice constants, asymmetry of the enthalpy of mixing towards the Ta-rich side, and significant deviation from ideality of activities at 1200K, suggesting the presence of short range order. Early work by Turchi *et al.* [116] focused only on cP2 and cF16, both Ta- and W-rich, finding all three structures stable. Order-disorder transitions were studied by Masuda-Jindo *et al.* [117] using a cluster expansion fitted from first principles calculations on random alloys, finding a second order A2 to B2 phase transition first appearing around 1000K near equiatomic concentration. We find oA12 to be stable at equiatomic concentration at an enthalpy of formation of -103.1 meV/atom, with cP2 9.4 meV/atom above, but W-rich tI6 minimizes enthalpy of formation at -110.3 meV/atom. That the convex hull leans W-rich is supported by the cluster expansions of Blum and Zunger *et al.* [110] and Hart *et al.* [109], both of whose cluster expansions have W-rich tI6 on the convex hull and nearly minimizing the enthalpy of formation. While the convex hull leaning W-rich disagrees with experimental evidence, this is in line with other theoretical results and at 1200K it is unlikely experimental results can be properly

equilibrated.

4.3.6 T=0 K Mo-Nb-Ta-W

By the Third Law of Thermodynamics, at 0 K we expect Mo-Nb-Ta-W to chemically order or to phase segregate into well-ordered structures. Considering only the convex hull formed by binary structures⁴, we find at the equiatomic concentration for Mo-Nb-Ta-W, the stable coexisting phases are Mo-Ta.oA12, Nb-W.cF16, Ta-W₂.tI6, and Mo₃Nb₄.hR7, with an average enthalpy of formation of -117 meV/atom. That the first 3 are stabilized in the quaternary is not surprising as they are the enthalpy minimizing structures in their respective binaries. Mo-Ta.oA12 in particular is stabilized as it has enthalpy of formation a factor of two or more larger than all other binaries. While Mo-Nb.oA12 is the enthalpy of formation minimizing structure for Mo-Nb, the convex hull for the Mo-Nb system is shallow near equiatomic concentration and thus little enthalpy is lost segregating out Mo₃Nb₄.hR7 instead. This allows Ta-W₂.tI6 and Nb-W.cF16 to be stabilized while maintaining the proper stoichiometry.

4.4 Hybrid Monte Carlo/Molecular Dynamics

Molecular dynamics is well suited to reproduce the small amplitude oscillations of atoms in the vicinity of crystal lattice sites. At low temperatures the probability for an atom crossing the barrier from one lattice site to another is prohibitively low and will rarely occur on the time scale of a molecular dynamics run. In contrast, Monte Carlo swaps of atomic species on different sites occurs with a probability $P = \exp(-\beta\Delta E)$ related to the net energy difference $\Delta E = E_{swap} - E_{ini}$ of swapped and initial configurations. In particular, it is independent of the energy barrier separating the states. Since some of the pairwise interactions presented in Table 4.1 are quite low, we expect that some Monte Carlo species swaps will be accepted even at temperatures

⁴Work is currently underway to incorporate ternaries and quaternaries.

below 300 K.

We implement this computationally by alternating molecular dynamics with Monte Carlo swaps, each performed from first principles using VASP. In the runs described below we perform 10 MD steps, with a 1 fs time step, between each attempted species swap. We prepare an initial configurations starting with a 16-atom $2 \times 2 \times 2$ BCC supercell with a random distribution of atomic species which we thoroughly anneal under MC/MD at a given temperature. We use annealed structures to create successively larger supercells, of size 32, 64 and eventually 128-atoms, thoroughly annealing at each size. Following the annealing, run durations for data collection are 10 ps, and include 1000 attempted species swaps. The volume is held at $16.9 \text{ \AA}^3/\text{atom}$ throughout, a value obtained consistently when fully relaxing samples equilibrated at 300 K.

The feasibility of the MC/MD method depends on adequate acceptance rates for attempted species swaps. As illustrated in Fig. 4.2, it is evident that many swaps are accepted with reasonably high probability at all temperatures studied (200 K and above). These high acceptance rates indicate that the Monte Carlo achieves our intended goal of sampling the full configurational ensemble in the solid state. The acceleration of sampling relative to conventional molecular dynamics is effectively infinite, as the same species swap will almost never be observed via molecular dynamics at low temperatures. The utility of various hybrid MC/MD methods has been reviewed recently [118] although these are more often applied in conjunction with empirical interaction potentials.

Swaps with the greatest size contrast (e.g. Ta-Mo and Nb-Mo) occur most infrequently, and are nearly absent at low temperatures, while the intermediate size swaps (Nb-W) occur occasionally and the most similar size swaps (e.g. Ta-Nb and W-Mo) occur with high probability even at the lowest temperatures. We conclude that at low temperature the system behaves nearly as a pseudobinary, consisting of the chromium group (group 5, here Ta and Nb) and the vanadium group (group 6,

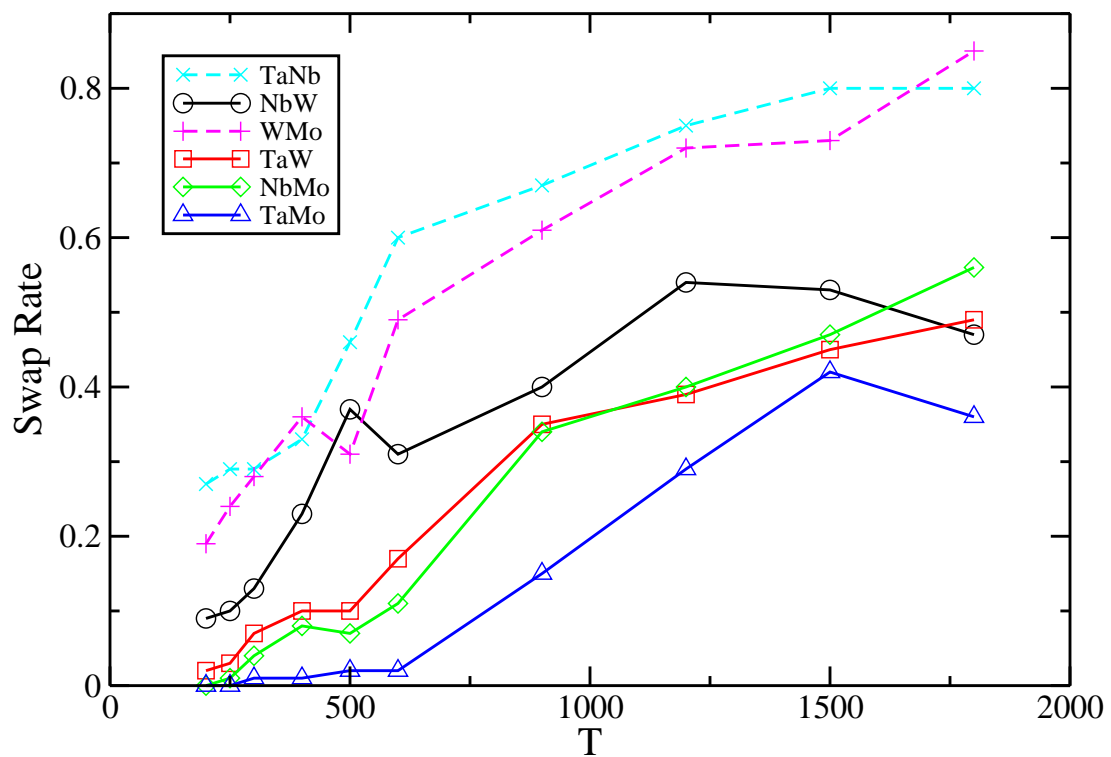


Figure 4.2: Monte Carlo acceptance rates (ratio of accepted to attempted species swaps) for each species pair vs. temperature.

here W and Mo) as two effective species.

Given a thoroughly sampled ensemble of configurations, we can analyze a great many properties. Of special interest are structural characterizations such as pair correlation functions and their reciprocal space equivalents, structure factors. Fig. 4.3 illustrates the partial pair correlation functions $g_{\alpha\beta}(r)$ which give the spatial distribution of atoms of species β as a function of distance from an atom of species α , normalized by their respective densities. On a body centered lattice of conventional lattice constant a , the nearest neighbor (NN) separation $\sqrt{3}a/2$ corresponds to the cube vertex-to-body center distance, while the lattice constant a itself corresponds to the next nearest neighbor (NNN) distance, vertex-to-vertex or center-to-center. For our structures the conventional cubic lattice constant $a = 3.23 \text{ \AA}$ while the nearest neighbor distance $\sqrt{3}a/2 = 2.80 \text{ \AA}$.

The nearest neighbor partial distribution functions (NN-PDF) at 300 K in Figure 4.3 generally agree with the magnitudes of enthalpies obtained from the previous section, though deviations exist. Mo-Ta has the largest enthalpy of formation, and indeed the NN-PDF for Mo-Ta shows the strongest peak, suggesting enthalpic stabilization and energetic preference towards maximization of Mo-Ta bonds. Next comes Nb-Mo and Ta-W, which are nearly degenerate in enthalpy, and their NN-PDF are nearly equal, although their peak positions reflect the smaller size of fourth transition metals (Nb and Mo) relative to fifth row (Ta and W). Nb-Nb and W-W come next, which anomalously deviate from pseudobinary behavior, as they are intragroup peaks. Nb-W is the weakest of the intergroup bonds and has the smallest NN peak, though it is still significant. The intragroup correlations, WMo and TaNb are both quite weak and strongly reveal the size difference between group 5 and group 6 pairs. Among the pair correlations of like species, TaTa and MoMo are weak, as expected, however the intermediate size NbNb and WW correlations show surprising strength indicating the pseudobinary model is not perfect, suggesting the presence of some more subtle and complex order than cP2, perhaps including phase separation that

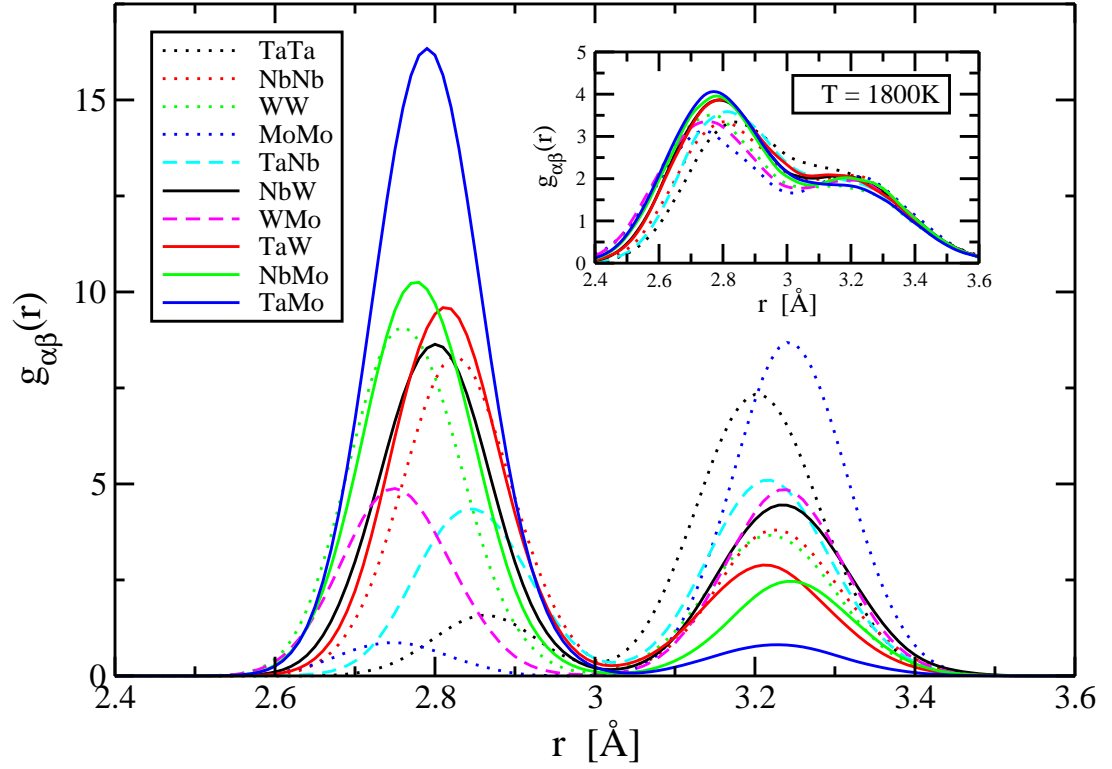


Figure 4.3: Partial density functions obtained from MC/MD for the Mo-Nb-Ta-W BCC phase, showing first and second nearest neighbors. Solid lines denote PDFs between species from differing groups, dashed lines between differing species from the same group, and dotted lines between the same species. The main figure shows results for 300 K, and the inset for 1800 K.

cannot be fully realized in these small system sizes. As a possible explanation for the presence of W-W and Nb-Nb NN bonds, note that at 0 K two of the stable structures near this stoichiometry, Ta-W₂tI6 and Mo₃Nb₄hR7, are respectively W-rich and Nb-rich, yielding W-W and Nb-Nb bonds. The anomalous NN peaks may indicate the tendency of the system to undergo partial phase segregation at this temperature. The next-nearest neighbor partial distribution functions (NNN-PDF) at 300 K show exactly opposite ordering, with Mo-Mo and Ta-Ta showing strong peaks and Mo-Ta essentially zero, characteristic of cP2-like ordering.

For 1800 K, shown in the inset of Figure 4.3, all NN peaks have similar magnitude, as do NNN peaks. By 1800 K, ordering has apparently been lost and the system is a random BCC solid solution. We propose the following temperature evolution. At high temperature, the system is a nearly ideal disordered BCC solution, as shown by the 1800 K PDF. As the temperature of the system decreases, the system undergoes an order/disorder phase transition, most likely to cP2-like alternation with the pattern of chemical order reflecting preferred bonding types amongst species. As the temperature further decreases, additional phase transitions are possible, culminating in phase segregation into the 0 K coexisting phases.

Analogous neighbor correlations were obtained previously [119] by a group using the Bozzolo, Ferrante and Smith [120] empirical interaction model. Owing to their interactions, the precise details of favored and disfavored neighbor pairs differ from our present results. Interestingly, they obtain order-disorder transitions around 600-800 K, consistent with our finding. An order-disorder transition in Ta-W has been predicted near 1000 K [121].

4.5 A Proposed Nearest Neighbor Model and Its Mean Field Reduction

To calculate qualitative details of the order-disorder transition in Mo-Nb-Ta-W, we derive a mean field free energy model for chemical ordering within the BCC phase. Previous work on phase stability using Monte Carlo methods has been performed by del Grosso *et al.* [122, 123], however their empirical interaction model predicts Mo and Ta avoid NN bonding at 0 K. This yields different low-temperature phase segregation behavior than what first principles unambiguously predicts. As we are using a mean field model, local elastic distortion of the crystal lattice due to atomic radius mismatch, a known strong effect in HEAs [124], is incorporated in our study only in so far as it affects the binary enthalpies of formation.

We work in the Gibbs ensemble at fixed temperature, pressure, and chemical composition in a system with N atoms and d chemical species, all of which have the same number of atoms N/d . We consider only nearest neighbor interactions, which for a BCC lattice exist between cell center and cell vertex sites, yielding an enthalpy in the form of an effective Hamiltonian

$$H = \sum_{\langle ij \rangle} \sum_{\alpha\beta} \sigma_{\alpha}(i) b_{\alpha\beta} \sigma_{\beta}(j), \quad (4.1)$$

where i and j denotes all possible sites, summation over $\langle ij \rangle$ denotes summation over all nearest neighbor bonds, summation over α and β denotes summation over all possible species, $b_{\alpha\beta}$ denotes the nearest neighbor bond strength between species α and β , and $\sigma_{\alpha}(i)$ is 1 if site i contains species α and 0 otherwise.

Anticipating cP2-like ordering, we now define the quantities

$$e_{\alpha} = \frac{2}{N} \sum_{i \in \text{vertices}} \sigma_{\alpha}(i) \quad (4.2)$$

and

$$o_{\alpha} = \frac{2}{N} \sum_{i \in \text{centers}} \sigma_{\alpha}(i), \quad (4.3)$$

which are, respectively, the concentration of species α on cell vertex (“even”) sites and the concentration of species α on cell center (“odd”) sites. Inverting Equations 4.2 and 4.3, we rewrite $\sigma_\alpha(i)$ as

$$\sigma_\alpha(i) = (e_\alpha, o_\alpha) + \delta\sigma_\alpha(i), \quad (4.4)$$

where the first term is e_α if i is a cell vertex and o_α if i is a cell center. As all NN bonds are between cell centers and vertices, we may rewrite Equation 4.1 as

$$H = \sum_{i \in \text{centers}} \sum_{j \in \text{NN}(i)} \sum_{\alpha\beta} (o_\alpha + \delta\sigma_\alpha(i)) b_{\alpha\beta} (e_\beta + \delta\sigma_\beta(j)). \quad (4.5)$$

In a mean field approximation, terms in $\delta\sigma$ vanish. The remaining term is independent of i and j and thus scales as the total number of bonds $4N$, giving an enthalpy per atom of

$$h = H/N = \sum_{\alpha\beta} o_\alpha \Omega_{\alpha\beta} e_\beta, \quad (4.6)$$

where $\Omega_{\alpha\beta} = 4b_{\alpha\beta}$.

We now introduce the ideal entropy approximation, assigning an entropy per atom of

$$s = -\frac{k_B}{2} \sum_{\alpha} (e_\alpha \ln e_\alpha + o_\alpha \ln o_\alpha). \quad (4.7)$$

As e_α and o_α are bounded between 0 and $2/d$ and sum to 1, this entropy can only vanish in the case where $d = 2$, whereas we will apply this free energy to HEAs with $d \geq 4$. Hence this entropy violates the third law of thermodynamics were we to naïvely extrapolate it to 0 K. This is a natural consequence of B2 ordering, with 2 unique sites occupied by $d > 2$ chemical species, requiring disorder on the sites and creating entropy of mixing. To predict phase transitions at lower temperatures, both a unit cell with number of unique sites divisible by 4, and more interaction terms, must be included. Including the entropic contribution $-Ts$, we obtain a free energy per atom of

$$g = \sum_{\alpha\beta} o_\alpha \Omega_{\alpha\beta} e_\beta + \frac{k_B T}{2} \sum_{\alpha} (e_\alpha \ln e_\alpha + o_\alpha \ln o_\alpha). \quad (4.8)$$

We now examine ordering tendencies driven by the energetics of the system. Suppose we have an enthalpy of general quadratic form

$$h = \boldsymbol{\psi}^T \Omega \boldsymbol{\psi}, \quad (4.9)$$

where $\boldsymbol{\psi}$ is a vector containing $n+r$ variables, where n of the variables are independent and r are dependent, and Ω is an $(n+r) \times (n+r)$ dimensional symmetric matrix. We rewrite this enthalpy in terms of only independent variables. Define $\boldsymbol{\psi}$ with the first n entries independent, so that it may be decomposed into an n -dimensional vector $\boldsymbol{\psi}_i$ containing independent variables and an r -dimensional vector $\boldsymbol{\psi}_d$ containing dependent variables. Rewrite Eq. (4.9) in block diagonal form

$$h = \begin{bmatrix} \boldsymbol{\psi}_i^T & \boldsymbol{\psi}_d^T \end{bmatrix} \begin{bmatrix} \Omega^{ii} & \Omega^{id} \\ (\Omega^{id})^T & \Omega^{dd} \end{bmatrix} \begin{bmatrix} \boldsymbol{\psi}_i \\ \boldsymbol{\psi}_d \end{bmatrix}, \quad (4.10)$$

where Ω^{ii} is an $n \times n$ dimensional matrix, Ω^{id} an $n \times r$ matrix, and Ω^{dd} and $r \times r$ matrix. Assume that $\boldsymbol{\psi}_d$ depends linearly on $\boldsymbol{\psi}_i$, so the constraints on the system may be written in form

$$\boldsymbol{\psi}_d = \mathbf{k} + D\boldsymbol{\psi}_i, \quad (4.11)$$

with \mathbf{k} an r -dimensional vector and D an $r \times n$ dimensional matrix. Imposing this on Eq. (4.10) yields

$$h = \boldsymbol{\psi}_i^T \theta \boldsymbol{\psi}_i + B\boldsymbol{\psi}_i + C, \quad (4.12)$$

where $\theta = \Omega^{ii} + \Omega^{id}D + D^T(\Omega^{id})^T + D^T\Omega^{dd}D$ is an $n \times n$ matrix, $B = 2\mathbf{k}^T((\Omega^{id})^T + \Omega^{dd}D)$ a n -dimensional row vector, and $C = \mathbf{k}^T\Omega^{dd}\mathbf{k}$. If θ is invertible, h has a unique extremum at

$$\boldsymbol{\psi}_0 = -\frac{1}{2}\theta^{-1}B^T, \quad (4.13)$$

so Eq. (4.12) may be rewritten with a coordinate redefinition of $\boldsymbol{\psi}' \equiv \boldsymbol{\psi} - \boldsymbol{\psi}_0$ as

$$h = \boldsymbol{\psi}'^T \theta \boldsymbol{\psi}' + C - \boldsymbol{\psi}_0^T \theta \boldsymbol{\psi}_0. \quad (4.14)$$

As Ω^{ii} and Ω^{dd} are symmetric, θ must be a real symmetric matrix and is therefore diagonalizable with orthogonal eigenvectors. Its eigenvalues and eigenvectors yield information about preferential ordering in the system.

Returning to the special case of cP2 symmetry, there are d constraints of the form

$$e_\alpha + o_\alpha = \frac{2}{d}, \quad (4.15)$$

one for each α , and two constraints imposing that each site class must be completely occupied,

$$\sum_\alpha e_\alpha = \sum_\alpha o_\alpha = 1. \quad (4.16)$$

However the two constraints of Eq. (4.16) are redundant, as required by Eq. (4.15). It follows that only $d - 1$ of the original $2d$ variables are independent. Here we take all o_α and one of the e_α to be dependent. For cP2 ordering, translational symmetry and equiatomic composition require all components of ψ_0 equal $1/d$. This yields an enthalpy of the form

$$h = \sum_{\alpha'\beta'} (e_{\alpha'} - \frac{1}{d}) \theta_{\alpha'\beta'} (e_{\beta'} - \frac{1}{d}) + \frac{1}{d^2} \sum_{\alpha\beta} \Omega_{\alpha\beta}, \quad (4.17)$$

where primed indices denote summation over independent species and unprimed indices denote summation over all species. The enthalpy is invariant under the body centering operation $e_\alpha \rightarrow 2/d - e_\alpha$. This enthalpy has the natural form expected for an order-disorder transition. In particular, for the binary ($d=2$) system A-B, $h = \Omega_{AB}(e_A - \frac{1}{2})^2$ up to a constant, with $e_A - \frac{1}{2}$ the well known order parameter for the order/disorder phase transition in the cP2 structure.

We diagonalize θ , obtaining its eigenvectors \mathbf{v}_i with associated eigenvalues λ_i . Any point in composition space may be written as $\psi' = \sum_i \chi_i \mathbf{v}_i$, where χ_i is the associated normal coordinate for eigenvector \mathbf{v}_i . Each normal coordinate is a linear combination of e_α 's, with $\chi_i = 0 \forall i$ corresponding to $e_\alpha = \frac{1}{d} \forall \alpha$. Normalizing the eigenvectors with a magnitude of unity, the enthalpy becomes

$$h = \sum_i \lambda_i \chi_i^2 + \frac{1}{d^2} \sum_{\alpha\beta} \Omega_{\alpha\beta}. \quad (4.18)$$

There are two cases for the temperature evolution of the system, depending on the spectrum of θ . In the first case, θ has only positive or zero eigenvalues. In this case, the enthalpy-minimizing configuration is $\chi_i = 0 \forall i$. As this is also the entropy maximizing configuration, the system remains disordered at $e_\alpha = 1/d \forall T$. No order/disorder phase transition occurs if θ has only non-negative eigenvalues.

In the second case, θ has negative eigenvalues leading to solutions with enthalpy less than the disordered solution. Were it not for the constraint $0 \leq e_\alpha \leq 2/d$, the enthalpy would be unbounded below. The $T = 0$ K enthalpy-minimizing solution must lie on the boundary of configuration space, i.e. $e_\alpha = 0$ or $e_\alpha = 2/d$ (which are physically equivalent due to body centering symmetry) for at least one species α , corresponding to at least one species showing perfect ordering at 0 K. At any point in configuration space not on the boundary, we may always increase the normal coordinate corresponding to any negative eigenvalue to lower the enthalpy until the boundary is reached. In general, multiple normal coordinates contribute to the solution. Non-zero normal coordinates for positive eigenvalues may exist, as increasing the normal coordinates for positive eigenvalues may move the system in configuration space away from the boundary. Subsequently increasing the normal coordinate for negative eigenvectors moves the system in configuration space back to the boundary, possibly with lower enthalpy than before. As the enthalpy is independent of temperature, there must be a finite temperature where the entropic contribution to free energy (which grows proportionate to) dominates the enthalpic contribution. An order/disorder phase transition must occur if θ has at least one negative eigenvalue.

4.6 Results of the Mean Field Model

To determine if an order-disorder phase transition exists in Mo-Nb-Ta-W, we compute the NN bond strengths $b_{\alpha\beta}$. Using the structures previously obtained from ATAT, we reran the cluster expansion, restricting it to a single two body term, which yields the

| | Group 5 | | Group 6 | |
|----|---------|-----|---------|-----|
| | Ta | Nb | W | Mo |
| Ta | 0 | 1 | -34 | -53 |
| Nb | 1 | 0 | -14 | -30 |
| W | -34 | -14 | 0 | -1 |
| Mo | -53 | -30 | -1 | 0 |

Table 4.2: Nearest neighbor bond strengths $b_{\alpha\beta}$ used in modeling the Mo-Nb-Ta-W BCC phase, in units of meV/atom.

| λ | $e_{Ta} - 1/4$ | $e_{Nb} - 1/4$ | $e_W - 1/4$ | $e_{Mo} - 1/4$ |
|-----------|----------------|----------------|-------------|----------------|
| -701 | 0.786 | 0.600 | 0.152 | -1.537 |
| 8 | 0.321 | -0.186 | -0.929 | 0.793 |
| 18 | -0.529 | 0.778 | -0.339 | 0.089 |

Table 4.3: The eigenvalues and associated eigenvectors of θ using bond strengths given in Table 4.2. λ is in units of meV/atom. The final column is the selected dependent species and is not part of the associated eigenvector; it is shown here to give physical intuition to how the particular mode is ordering the system.

NN bond strengths between differing species given in Table 4.2. Shown in Table 4.3 are the eigenvalues of the θ matrix, the eigenvectors, and the associated dependent composition $e_{Mo} - 1/d = \sum_{\alpha'} (e_{\alpha'} - 1/d)$. Positive signs for eigenvector components denote ordering on cell vertices and negative signs denote ordering on cell centers (only the relative sign between components are relevant). Of the three possible modes, one has a negative eigenvalue, so an order/disorder phase transition must exist. The lowest enthalpy mode ordering the system ($\lambda = -701$ meV/atom) indeed has strong ordering with opposite signs for Mo and Ta, supporting the assertion that Mo-Ta NN bonds drive the ordering of the system. This mode also has strong ordering with opposite signs on Mo and Nb, in agreement with Mo-Nb as the second strongest bonding type.

Shown in Figure 4.4 is the temperature evolution of the species concentration on cell vertices, obtained by minimizing the free energy at a given temperature over all independent variables $e_{\alpha'}$ subject to the bounds. Monte Carlo simulations using the same enthalpy model were subsequently performed to verify our mean field results, and they show excellent qualitative agreement. Here the system achieves perfect sublattice occupancies for all species at low temperature, with Ta and Nb on the cell vertices and W and Mo on the cell centers. This agrees with our pseudobinary model where group 5 (Ta,Nb) and group 6 (W,Mo) form pseudobinary species. As

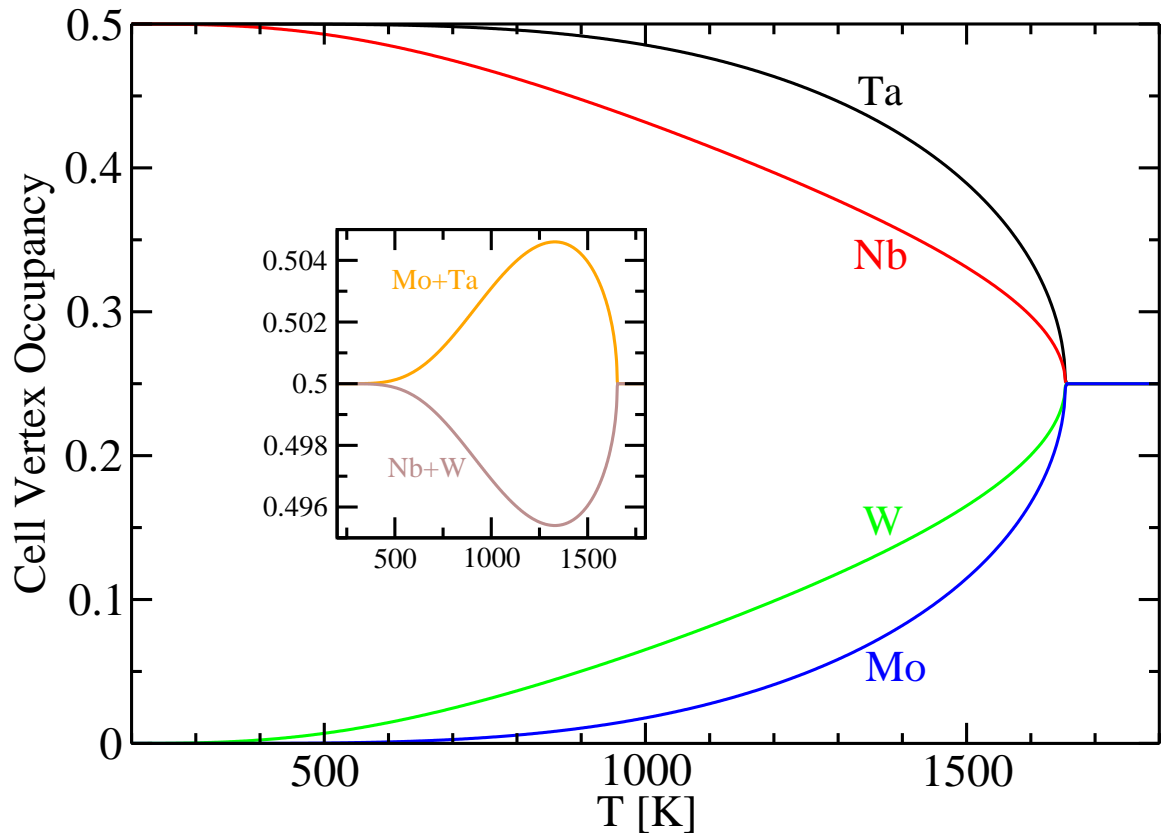


Figure 4.4: The vertex sublattice occupancy as a function of temperature for the mean field model. See text for information on inset.

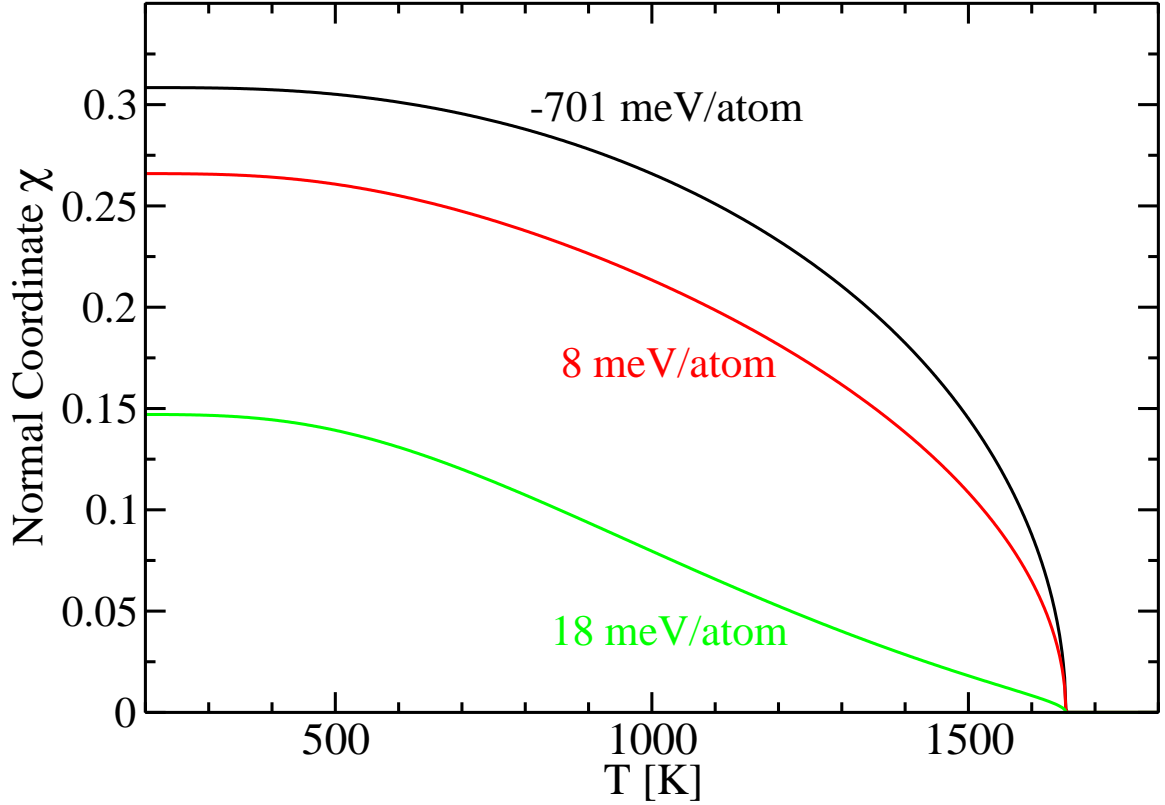


Figure 4.5: The normal coordinates of the system as function of temperature.

temperature rises, the system begins picking up some disorder, with Nb and W more strongly affected than Mo and Ta, finally reaching complete disorder at $T_C = 1654K$.

The inset shows the temperature evolution of the quantities $e_{Ta} + e_{Mo}$ and $e_{Nb} + e_W$, both quantities remaining close to $1/2$ for all temperatures, explaining the mirror-image-like relation of Mo to Ta and Nb to W. This arises from Mo-Ta's strong binding, pinning the configuration close to the boundary $e_{Ta} \approx e_{Nb} \lesssim \frac{1}{2}$, with $e_W \approx e_{Mo} \gtrsim 0$ at low temperatures. Even at $T \approx 1000K$, where e_{Nb} and e_W differ appreciably from their boundary values, e_{Ta} and e_{Mo} remain close to their extremes, requiring that $e_{Nb} + e_W = 1 - (e_{Ta} + e_{Mo}) \approx \frac{1}{2}$. By the time T reaches T_C , $e_\alpha = \frac{1}{4} \forall \alpha$, so the values of $e_{Ta} + e_{Mo}$ and $e_{Nb} + e_W$ never deviate significantly from $1/2$.

Figure 4.5 shows the temperature evolution of the normal coordinates of the system. At low temperatures, all modes contribute to the thermodynamic equilibrium of

the system, though the -701 meV/atom mode dominates the enthalpy of the system. All three normal coordinates vanish at $T_C = 1654K$, yielding the disordered solution where entropy is maximized in configuration space. The square root singularity as $T \rightarrow T_C$ matches the well known mean field classical critical exponent $\beta = \frac{1}{2}$.

The system strongly prefers the -701 meV/atom mode at 0 K due to its substantially low enthalpy. This places Ta, Nb, and W on cell vertices and Mo on cell centers. To maintain overall concentration 1/4 for each species, the other two modes are needed to compensate. The 8 meV/atom mode replaces some Mo at cell centers with W, while further strengthening the ordering of Ta on cell vertices. Finally, the least favored 18 meV/atom mode is the only mode that orders Nb and W onto different sublattices, giving the observed disordering of Nb and W in Figure 4.4. The large contribution of Mo-Ta ordering in the -701 meV/atom mode presents compelling evidence of ordering dominated by Mo-Ta bonding.

4.7 Results of Monte Carlo Simulations

It is well known that mean field models systematically overestimate transition temperatures due to lack of correlations. To confirm the validity of our mean field model (in particular, our assumption of an entropy function corresponding to sublattice ordering) and to obtain a more precise estimate for the transition temperature, we perform Metropolis Monte Carlo using as the energy function Equation 4.1 at 10 K intervals from 100 K to 2000 K for supercells of the bcc unit cell, ranging from size $2 \times 2 \times 2$ to $20 \times 20 \times 20$, each simulations consisting of 10^6 initialization steps followed by 2×10^6 collection steps. Temperatures less than 400 K were thrown out due to probable lack of equilibration at these low temperature. Using these configurations, we may calculate not only the cell vertex occupancy as in the mean field theory, but also the specific heat and possible order parameters. Shown in Figure 4.6 are our results for cell vertex occupancies for supercell size $16 \times 16 \times 16$. We see strong

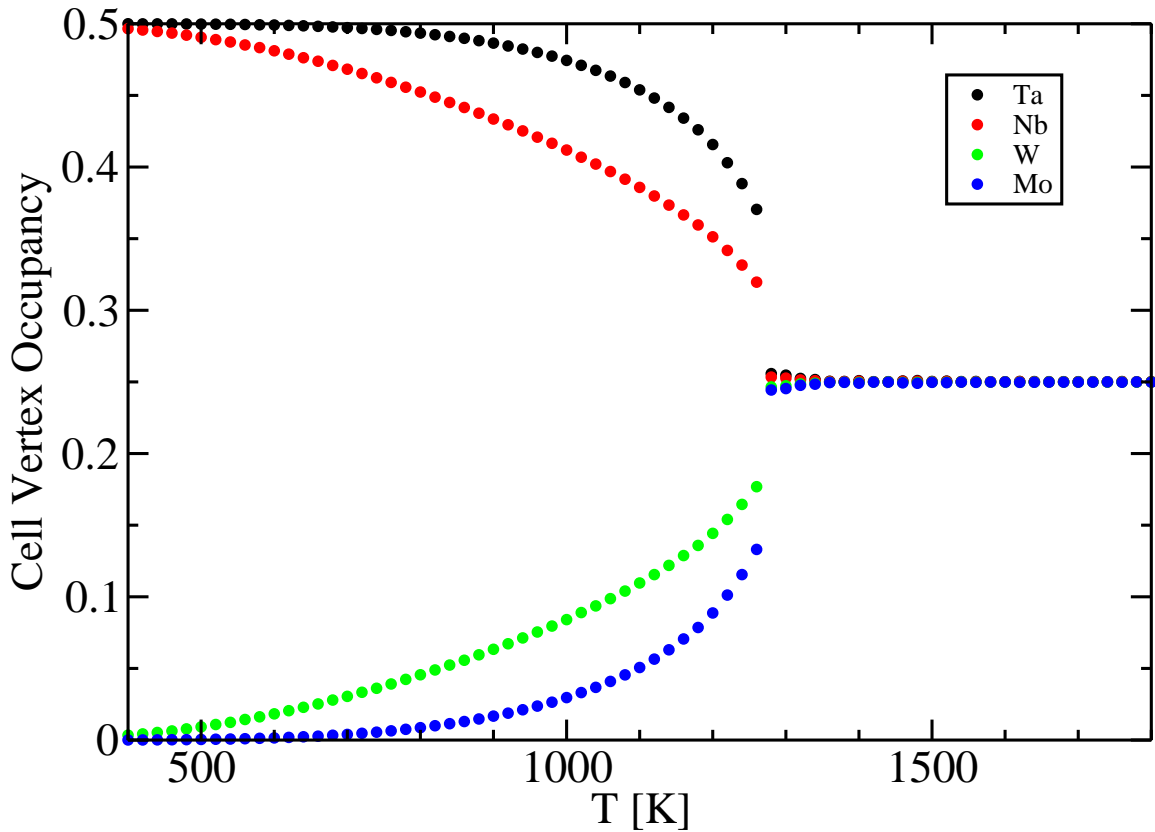


Figure 4.6: The vertex sublattice occupancy as a function of temperature for our Monte Carlo simulations.

qualitative agreement with Figure 4.4. The only differing features are the transition temperature occurring near 1280 K and the scaling of the various species occupancies near the critical point. However, near the critical point there is likely some residual error due to critical slowdown. Shown in Figure 4.8 are is a plot of the specific heat as a function of temperature. We here see a growing specific heat peak at 1280 K characteristic of a phase transition, though it is relatively slow-growing and has some noise for supercell sizes larger than $14 \times 14 \times 14$.

Sublattice ordering for a bcc lattice in a binary system belongs to the 3D Ising universality class. Although our system is a quaternary, it exhibits a pseudo-binary behavior. For the 3D Ising class, the critical exponent for order parameter scaling near the critical temperature is $\beta = 0.327$, and the critical exponent for finite size

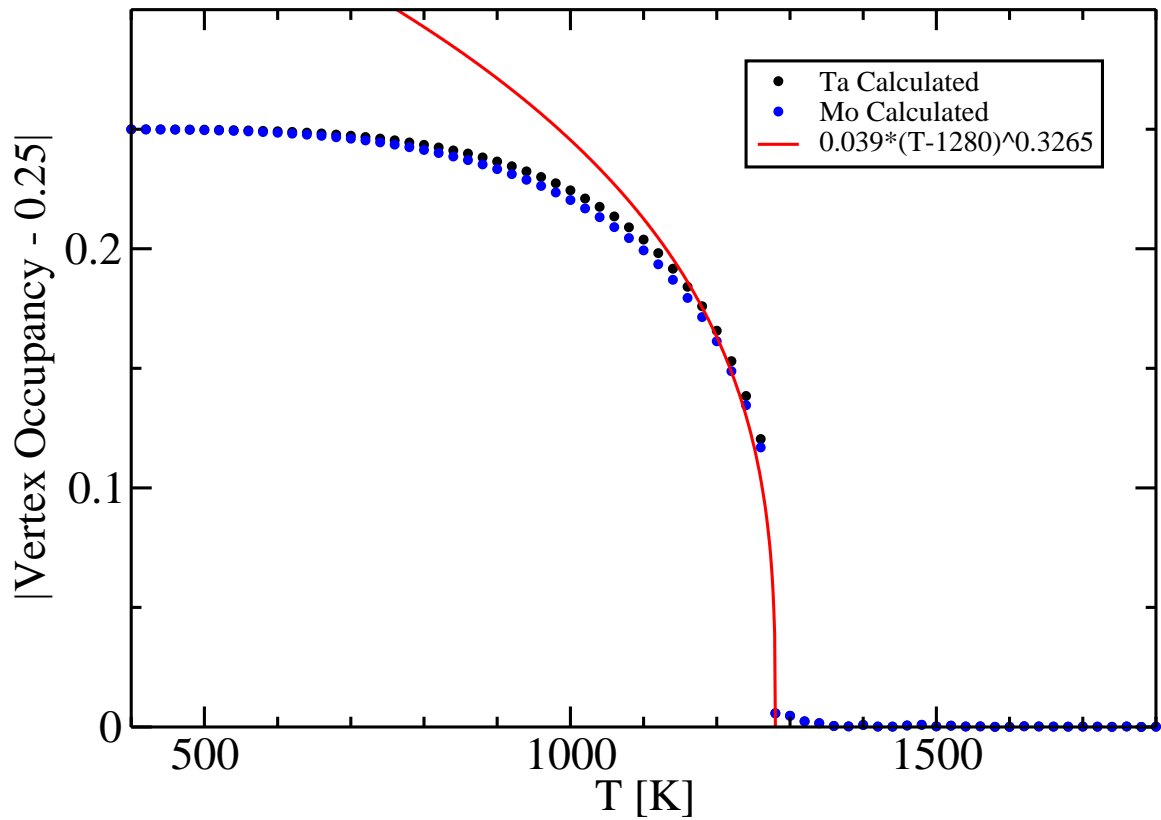


Figure 4.7: Comparison of Mo and Ta vertex occupancies to the expected form for the order parameter in a 3D Ising model. The red line denotes an estimate for the behavior of the order parameter at critical temperature 1280 K with the expected 3D Ising critical exponent $\beta = 0.327$.

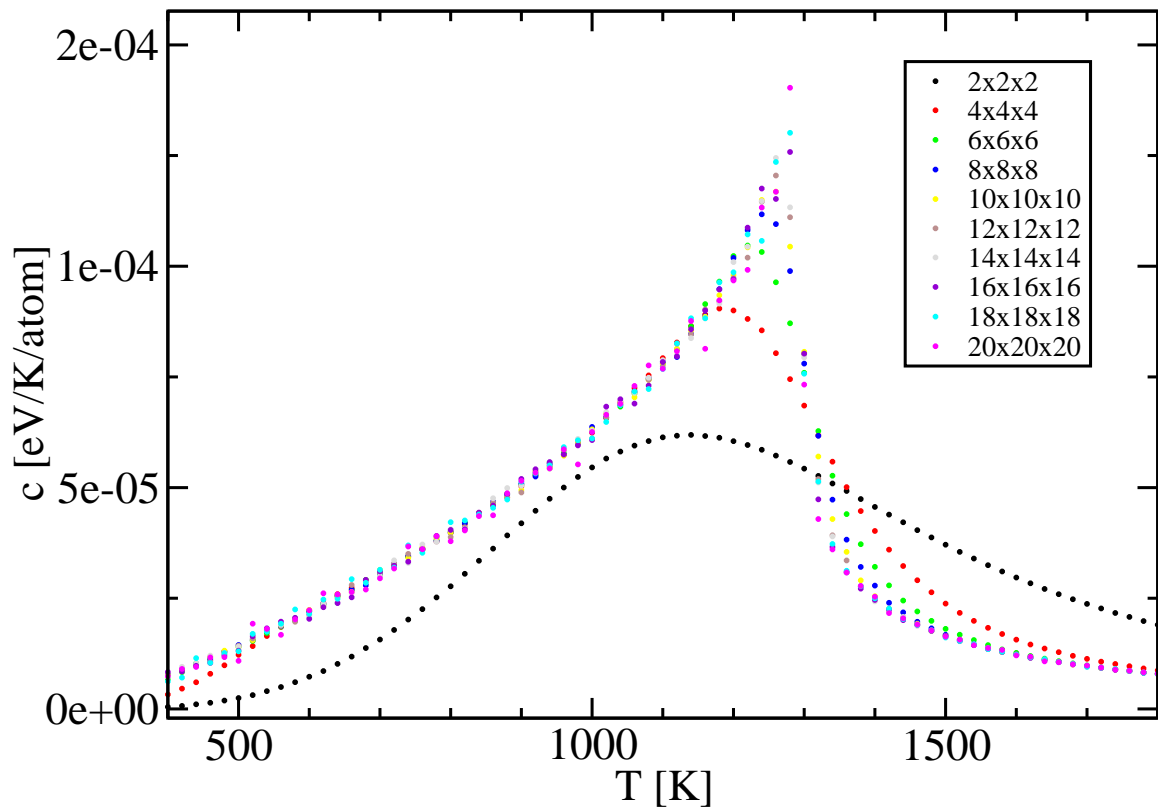


Figure 4.8: Specific heat as a function of temperature for various supercell sizes.

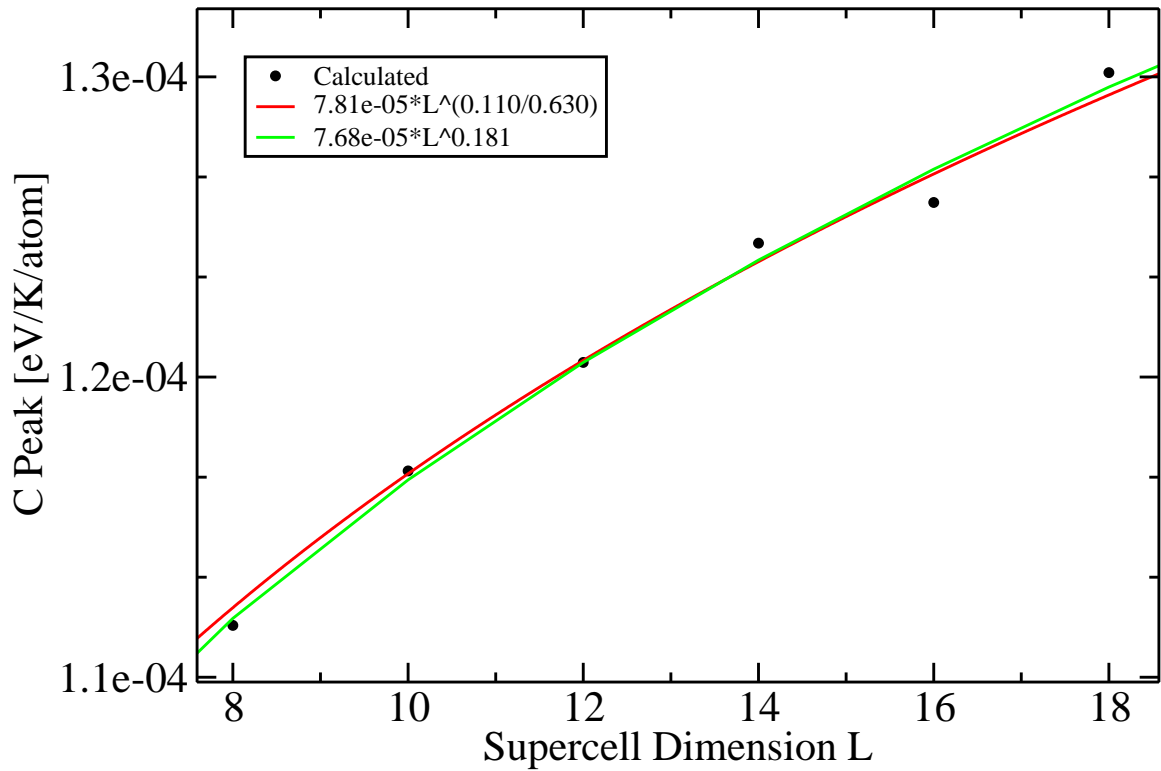


Figure 4.9: The specific heat peak height as a function of supercell dimension. The green line denotes a fit to an exponential scaling law with both the prefactor and exponent free to vary, and red a fit imposing the expected 3D Ising critical exponent $\alpha/\nu = 0.175$.

scaling of the specific heat peak height is $\alpha/\nu = 0.110/0.630 = 0.175$ [51]. Shown in Figure 4.7 are the vertex occupancies for Mo and Ta for supercell size $16 \times 16 \times 16$, which we expect to be order parameter-like, and shown in Figure 4.9 are the peak heights for the specific heat as a function of supercell dimension. We restrict to supercell dimensions 8 through 18, as it is this dimension range that is likely close to equilibration and outside the corrections-to-scaling regime. Residual error due to critical slowdown and uncertainty in the precise transition temperature complicates fitting the order parameter near the critical point, and we can only definitively say from this figure that, by comparison with an estimate for the functional form of the order parameter, it is plausible that our Mo and Ta vertex occupancies act as the order parameter near the critical point, though the strong observed Mo-Ta bonding from the mean field model strengthens this assertion. Our finite size scaling for the specific heat peak shows basic agreement between expected and predicted values, with a critical exponent of 0.181 observed, the difference likely due to the noise for supercell sizes greater than $14 \times 14 \times 14$ previously noted. We therefore believe that our free energy model belongs in the 3D Ising universality class, with a second-order phase transition driven by an order parameter involving Mo or Ta vertex occupancies.

Chapter 5

On the Elasticity of Transition Metal Alloys¹

5.1 Elasticity of Transition Metal Alloys: Too Many Phase Diagrams

The field of metallic glasses began in 1960 when Klement et al. [126] created a ribbon of amorphous Au-Si with a thickness of 10 μm using splat cooling, quenching the liquid rapidly enough that atoms were “frozen” in space. While formally any metallic glass can be formed by cooling the associated liquid rapidly enough, even the rapid cooling rate of 10^7 K/s achievable in splat quenching [127] is glacial on the characteristic time scales of atomic motion (1 fs) and the average time scale for atoms to switch places (10 ps) [128], and only systems with relatively large free energy and kinetic barriers retarding nucleation of crystal phases could be created [129]. Even for metals where glass formation using splat cooling was possible, rapid quenching only allows for relatively thin samples.

¹Much of this chapter has been adapted from my paper “First Principles Calculation of Elastic Moduli of Early-Late Transition Metal Alloys” [125].

In the early 1990's [130, 131], it was discovered that by using multiple (4+) alloying species with mismatched atomic radii and favorable interspecies bonding, "geometric frustration" could be induced, where the natural tendency towards crystallization is frustrated via size mismatches and conflicting chemical ordering. These new "bulk metallic glasses" (BMGs) could be grown with cooling rates as low as 1 K/s. These lower cooling rates allows equilibration in bulk quantities, with critical casting thicknesses on the order of centimeters obtainable [129]. BMGs are generally nearly close-packed, giving them excellent corrosion resistance, as atoms are unable to rearrange to form reactants and diffusion is inhibited. They also show excellent mechanical properties, with yield strength of 1.5-2.5 GPa and elastic strain limits of 2% typically reported, higher than steels' 0.5-2 GPa and 0.5%, respectively [132]. Sportsgear and personal electronics devices incorporating BMGs are already on the consumer-grade market.

But there's a catch. In practice, there is a trade off between strength and ductility. Strong materials have high energy costs for various micro- and mesoscopic defects forming. However, ductility usually occurs *because* a material can support the creation and movement of certain low-energy defects (usually dislocations) which cause plastic flow. Strong materials will resist small deformations, but once enough energy has been put into the deformation, cleavage occurs.

Amorphous materials are even worse in this regard. As amorphous materials have no regular lattice, the very concept of a dislocation defect is ill-defined. This gives amorphous materials their high yield strength, but once that yield strength is exceeded, they will fail spectacularly, as witnessed by the common example of conventional soda-lime glass (not a BMG) shattering. In amorphous materials, the defects that are triggered are known as "shear transformation zones" [133, 134, 135, 136], point-like regions where externally applied global stress causes localized regions of shearing. Upon reaching the yield strength, these regions combine to form "shear bands". Plastic flow is associated with many such bands forming, diffusing the strain

throughout the material, and brittle fracture with few bands forming, focusing the strain into small regions. While this process is well-accepted in the literature, there is considerable disagreement at present on the exact mechanism by which STZs lead to shear banding, and no formalism exists to aid design in inhibiting the growth of solitary shear bands responsible for brittle fracture.

While the trade-off between strength and ductility is empirically observed, it is not required by the laws of physics, and ductile BMGs able to support plastic strains as high as 22% have been reported in the literature [137]. A correlation between Poisson's ratio and ductility [138, 139, 140] exists, including an empirical threshold of $\nu = 0.32$ past which amorphous materials may be ductile, and below which they will be brittle. This suggests, as a first approximation, a rule-of-mixtures approach: to further enhance the ductility of BMGs, species with high Poisson's ratios should be alloyed together to create amorphous materials. This is too crude a measure, however, as it fails to consider interspecies bonding, one of the primary mechanism (meta)stabilizing most amorphous materials. In addition, the large number of alloying species gives unfavorable combinatorial growth in the number of possible combinations, and it still remains to determine the composition that maximizes ductility. An exhaustive search for BMGs with favorable elastic properties is out of the question experimentally.

But it is not out of the question computationally. First principles computational methods prove fruitful, owing to their chemical specificity and absence of adjustable parameters, as well as the insight they yield into electronic structure. While technically possible, amorphous metals pose computational difficulties, as they lack both spatial periodicity and a unique structure. While the first problem can be practically overcome by imposing suitably large periodic boundary conditions, this requires hundreds of atoms per computational cell², straining computational resources, and

²It should be noted that this cell size is likely too small to observe more interesting effects like shear band formation.

requiring averaging over multiple samples to remove sample dependence. The second problem can be partially overcome by running molecular dynamics on a liquid sample then rapidly quenching. However the requirement for equilibration further increases the computational time necessary, and the question remains whether the unphysical rapid cooling rates (on the order of 10^{15} K/S) seen in these computational quenches give structures representative of realistically quenched materials.

Hence we adopt a different strategy. We propose that, in order to understand the ductility of amorphous materials based upon their constituent species, one should examine the Poisson's ratio for the known intermetallics formed by those species. We will focus mostly on transition metals, in particular early-late transition metal alloys, as these combinations are favorable toward BMG formation. As Poisson's ratio is known to depend on the nature of chemical bonding [141], species that systematically show enhancement of Poisson's ratio upon alloying into crystalline phases should also show enhancement of Poisson's ratio when alloyed into amorphous phases, as amorphous materials have similar short-range order with the associated crystalline phases. To propose these candidate combinations, we will calculate the bulk modulus K and the shear modulus G for a variety of binaries using first principles calculations, the isotropic Poisson's ratio being a function of G/K . This gives not only a list of proposed alloying species but initial guesses for approximate compositions for alloying to achieve maximum ductility.

As we are computing the properties of crystalline phases but wish to extend our results to amorphous phases, it is necessary to understand how these moduli depend on the chemical bonding between species (which should transfer to amorphous materials with similar relative concentrations of the two species) and how they depend on the particular structure (which will not be transferable). To quantify this dependence, comparison to a well-known effective field theory known as the Coherent Phase Approximation (CPA) and various physical measures of chemical bonding strength will be used. Though our primary concern here is ductility, this work has wide appli-

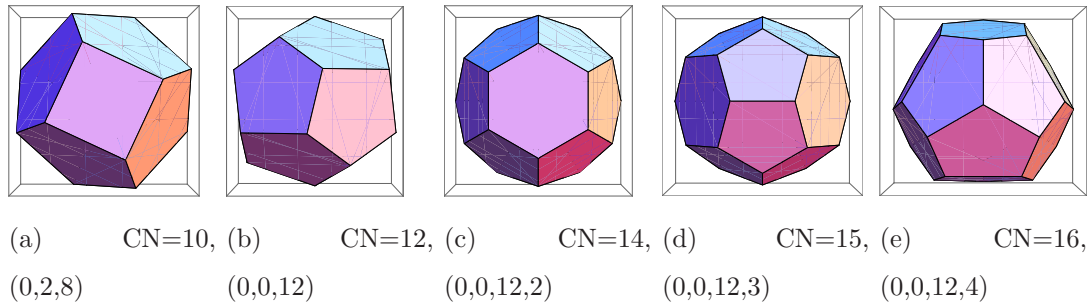


Figure 5.1: Frank-Kasper Voronoi polyhedra, listing coordination numbers and polyhedron codes.

capability for diverse properties of amorphous materials, as bulk moduli, shear moduli, and their ratio correlates to glass transition temperature [142, 143], glass forming ability [144], Grüneisen parameters [145], maximum resolved shear stress at yielding [146], chemical bonding type [141], and possibly fragility [141]. It is not too much of an exaggeration to say that nearly every material property of amorphous materials depends in some way on their elastic moduli.

We will also highlight two crystalline phases that have similar structures to amorphous materials, which we propose may be viewed as “amorphous approximants”, (motivated by the “quasi-crystalline approximants” found in the related field of quasicrystallography). These phases, known as Frank-Kasper phases [147, 148, 149] are complex but otherwise ordinary crystalline phases. Due to their topological close packing they exhibit local icosahedral ordering similar to that found in many amorphous metals. Fig. 5.1 shows the standard Voronoi polyhedra of Frank-Kasper structures. We expect that the similar local chemical environments of the Frank-Kasper phases can be used to mimic amorphous metals, yielding “amorphous approximants”, similar in concept to “quasicrystal approximants”. These crystalline phases will be used to understand trends in the elastic properties of amorphous metals. Such “amorphous approximants” are useful for computational work as they typically have small unit cells compared to system sizes required to reproduce amorphous structures.

5.2 The Basics: Elasticity

The fundamental equation of linearized elasticity is $\sigma_i = C_{ij}\epsilon_j$, where σ is the stress tensor, ϵ is the strain tensor, and C the stiffness tensor relating the two. Here we employ Voigt notation, converting the tensors σ and ϵ into vectors with six components $\{xx, yy, zz, xy, xz, yz\}$. For crystals C depends on the symmetry of the material in question [150] and contains at least three independent parameters. For the special case of isotropic materials C has only two independent parameters, the bulk modulus K and the shear modulus G . The non-vanishing elements are $C_{11} = C_{22} = C_{33} = K + 4G/3$, $C_{12} = C_{13} = C_{23} = K - 2G/3$, and $C_{44} = C_{55} = C_{66} = G$. An additional elastic quantity of interest is the Poisson ratio ν , defined to be the negative of the ratio of axial strain to transverse strain. For crystals ν depends on the direction of applied stress, but in the isotropic case it reduces to

$$\nu = \frac{3 - 2G/K}{6 + 2G/K}. \quad (5.1)$$

Notice that ν is a function of the shear to bulk modulus ratio G/K , also known as the Pugh ratio [151].

Ductility and Poisson's ratio are positively correlated in both polycrystalline [151] and amorphous [138] solids, with $\nu \geq 0.32$ (equivalently $G/K \leq 0.41$) proposed as an empirical criterion for good ductility [152]. Seeking simultaneously high strength and ductility, it is natural to choose chemical species which in elemental form have large K . The species chosen must also be known good glass formers. Early-late transition metal alloys fit both criteria, as the transition metals from Group IV to XI all have $K \geq 100$ GPa, and they are one of the most frequently examined classes of amorphous metals. Size mismatch criteria favor using transition metals from different rows and columns of the periodic table, e.g. Ta and W for early transition metals (ETMs), and Co and Ni as late transition metals (LTMs). Co and W are of particular interest for materials design as Co-based glasses exhibit ultrahigh fracture strength, W-based

glasses have the highest known glass transition temperature for BMGs, and both have high Young’s modulus [153, 141, 154].

Ordinary crystalline materials contain randomly oriented microscopic grains and appear macroscopically isotropic. To compute the elastic properties for these “polycrystals”, orientational averaging is required. Each grain is described microscopically by the same stiffness matrix, which contains between three (cubic) and 21 (triclinic) independent parameters [155], but macroscopically the crystal is isotropic with only two independent parameters K and G . In the Voigt average, the stiffness matrix C is averaged over orientations [156], which is exact if stress is uniform throughout space. In the Reuss average, the compliance matrix $S = C^{-1}$ is averaged over orientations, which is exact if strain is uniform throughout space. The Voigt average systematically overestimates the isotropic moduli, while the Reuss average systematically underestimates the moduli. Empirically, the arithmetic mean of the two, known as the Hill average [157], gives improved agreement with experiment, and this is what we will report.

The polycrystalline average assumes the stiffness matrices of various grains are identical to the perfect crystal, differing only by relative orientation. To obtain macroscopic elastic moduli in materials where chemical environment spatially varies, in particular in materials containing chemically distinct grains, it is necessary to include effects arising from fluctuations in the local stiffness matrices. A general class of approximation schemes known as “effective medium theories” exists where each grain with its local stiffness matrix interacts with an effective medium characterized by a background stiffness matrix incorporating the interactions of all other grains. A popular effective medium theory is the coherent potential approximation (CPA) [158], a self-consistent formalism in which the background stiffness matrix is taken as the macroscopic average itself. The self-consistent interaction of grains yields a pair of coupled non-linear equations,

$$\sum_i \phi_i \frac{K_i - K}{3K_i + 4G} = 0 \tag{5.2}$$

and

$$\sum_i \phi_i \frac{G_i - G}{5G(3K + 4G) + 6(K + 2G)(G_i - G)} = 0, \quad (5.3)$$

which can be solved numerically for the effective K and G , where ϕ_i denotes the volume fraction of grain type i in the material. K_i and G_i denote the bulk and shear modulus of grain type i , respectively.

Although intended for mixtures of crystalline grains, we will apply CPA in the limit where each grain shrinks to a single atom, to estimate the elastic moduli of compounds using the self-consistent average of properties of the constituent pure elements. Our usage of CPA may be viewed as a higher-order correction to the well-known but highly empirical “rule of mixtures” paradigm common in materials design, which has already been applied to bulk metallic glasses [159]. CPA takes into account the pure elemental properties but lacks information about interspecies bonding and specific alloy crystal structure. Thus we take CPA as a convenient, physically motivated interpolation to establish a baseline for comparison with the computed alloy moduli revealing the specific contributions of structure and bonding, though we note that metallic glasses exist where trace changes in composition yield relatively large changes in K and G due to alteration of chemical bonding type [160].

5.3 The Raw Data

Our first principles calculations use the Vienna Ab-Initio Simulation Package (VASP) [82, 83], a plane wave *ab-initio* package implementing PAW pseudopotentials [27] in the PW91 [24] generalized gradient approximation to density functional theory (DFT). VASP calculates total energies, forces, elastic moduli, and electronic structure. All structures are relaxed until the maximum ionic force is below 0.01 eV/Å, and the k-point density is subsequently increased until total energy per atom has converged to within 0.1 meV/atom. Default plane wave energy cutoffs are used for total energy calculations. In structures containing Co and Ni, spin polarization has been included.

However, we do not include spin-orbit coupling despite the presence of 5d elements Ta and W. Total energies are converted to enthalpies of formation by subtracting from the tie-line joining the total energies of pure elements in their stable crystalline forms [161].

We perform elastic calculations using a finite difference method internal to VASP. To ensure proper convergence of elastic moduli, we increase the k-point density until the all polycrystalline averages converge to within 2%, then increase the energy cutoff until the polycrystalline averages converge. Convergence in energy cutoff occurs at 360 eV, with the exception of Ni₂Ta and Ni₄W where 400 eV and 440 eV respectively were required. All structures were tested for mechanical stability, and elastic constants were not calculated for structures that were found to be mechanically unstable, though they were included in the enthalpy of formation plots, as it is possible for the stabilizing distortions to affect the calculated total energy only weakly.

To quantify bond strength between individual atoms in structures, we calculate interatomic force constants and the Crystal Overlap Hamilton Population (COHP). To calculate the force constant $k_{\alpha\beta}$ between atoms α, β at position $\mathbf{r}_{\alpha,\beta}$, separated by a bond in the direction $\hat{\gamma}_{\alpha\beta}$, we calculate the Hessian matrix $\mathbf{H}_{\alpha\beta} = d^2E/d\delta\mathbf{r}_\alpha d\delta\mathbf{r}_\beta$. We use density functional perturbation theory internal to VASP to calculate \mathbf{H} within a supercell of sufficient size that atoms lie at least 4.2 Å away from their own repeated images. Restricting our attention to longitudinal (bond stretching) interactions and assuming central forces, we define

$$k_{\alpha\beta} \equiv \hat{\gamma}_{\alpha\beta} \cdot \mathbf{H}_{\alpha\beta} \cdot \hat{\gamma}_{\alpha\beta} \quad (5.4)$$

as the projection of the Hessian along $\hat{\gamma}_{\alpha\beta}$. $k_{\alpha\beta}$ must be positive for the force to be stabilizing.

The COHP provides an electronic structure-based characterization of interatomic bond strength [162]. One calculates matrix elements $\langle \alpha L | H | \beta L' \rangle$ of the density functional theory Hamiltonian between localized atomic orbitals L and L' on a pair of atoms α and β , then multiplies by the density of states $N_{\alpha L, \beta L'}$ projected onto the two

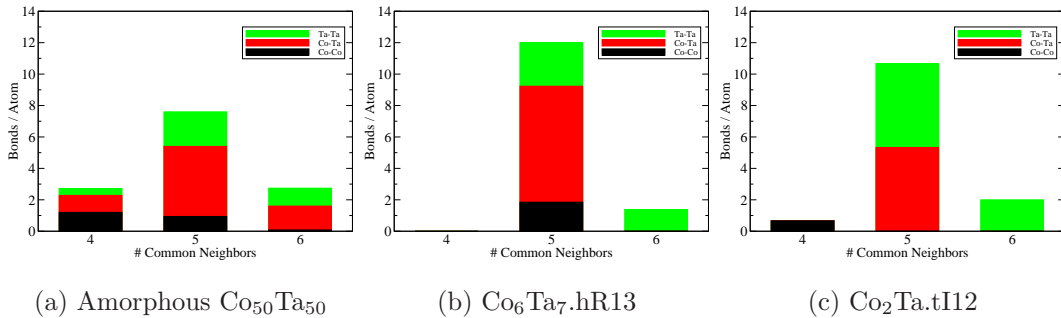


Figure 5.2: Stacked bar chart of Honeycutt-Andersen common neighbor statistics [7, 8].

orbitals. We calculate wave functions using a TB-LMTO method [163] then calculate an *integrated* COHP (iCOHP) for a pair of atoms $\alpha\beta$, summing over atomic orbitals and integrating over energies up to the Fermi energy.

5.3.1 Structures

Because we consider a large number of specific structures, we establish a numbering scheme to unambiguously identify them (see Table 5.1). In the text we refer to a given crystalline material using the notation Compound.Pearson (e.g. Co₂Ta.cF24). Of particular interest are the Frank-Kasper structures, which we take as amorphous approximants owing to the prevalence of their coordination polyhedra in many metallic glasses [3, 164]. Canonical Frank-Kasper polyhedra have coordination numbers CN=12, 14, 15 and 16. However, we include the Bernal holes [1, 2], notably CN=10, as tetrahedral but non-canonical Frank-Kasper polyhedra [3] suitable for smaller atoms. Also, the tetrahedral close-packing of the Frank-Kasper phases matches the packing properties expected in bulk metallic glasses [165].

To justify use of crystalline phases as amorphous approximants, we compare Honeycutt-Andersen common neighbor statistics [7, 8], of crystalline and amorphous structures. Amorphous structures were simulated by quenching 100 atom liquid structures in NPT ensembles from $T = 2500$ K down to 300 K over runs of more than

| Ref. | Prototype | Strukt. | Pearson | FK? | CN |
|------|--------------------------------|------------------|---------|----------|----------------|
| 1 | Cu | A1 | cF4 | NA | 12 |
| 2 | W | A2 | cI2 | NA | 14 |
| 3 | Mg | A3 | hP2 | NA | 12 |
| 4 | Fe ₆ W ₇ | D8 ₅ | hR13 | μ | 12, 14, 15, 16 |
| 5 | Al ₂ Cu | C ₁₆ | tI12 | non-FK | 10, 15 |
| 6 | AuCu ₃ | L1 ₂ | cP4 | NA | 12, 18 |
| 7 | BaPb ₃ | | hR12 | NA | 12, 18 |
| 8 | MgNi ₂ | C36 | hP24 | Laves | 12, 16 |
| 9 | MgZn ₂ | C14 | hP12 | Laves | 12, 16 |
| 10 | MgCu ₂ | C15 | cF24 | Laves* | 12, 16 |
| 11 | Ni ₃ Sn | D0 ₁₉ | hP8 | NA | 12, 18 |
| 12 | Al ₃ Ti | D0 ₂₂ | tI8 | NA | 12, 14, 16 |
| 13 | Cu ₃ Ti | D0 ₈ | oP8 | NA | 12, 14, 16 |
| 14 | NbPt ₃ | | mP16 | NA | 12, 14, 16 |
| 15 | MoSi ₂ | C11 _b | tI6 | NA | 14 |
| 16 | MoNi ₄ | D1 _a | tI10 | NA | 13, 14 |
| 17 | Pt ₈ Ti | | tI18 | NA | 13, 14 |
| 18 | MoNi | | oP56 | δ | 12, 14, 15, 16 |

Table 5.1: Structure types considered listing common prototype, and Strukturbericht and Pearson notations. Frank-Kasper phases list common names. * indicates symmetry-breaking distortion. “Non-FK” indicates non-canonical Frank-Kasper phase containing CN=10 Bernal Hole. The final column contains a list of coordination numbers from Voronoi polyhedra appearing in the structure [1, 2, 3].

15ps. All simulations were performed at the gamma point with default energy cutoffs. Shown in Figure 5.2 is the number of common neighbors between two bonded atoms of given types. We show results for Co-Ta, but Ni-Ta, Ni-W, and Co-W were also simulated and generated similar results, with the exception of one Ni-W amorphous sample which was likely out of equilibrium.

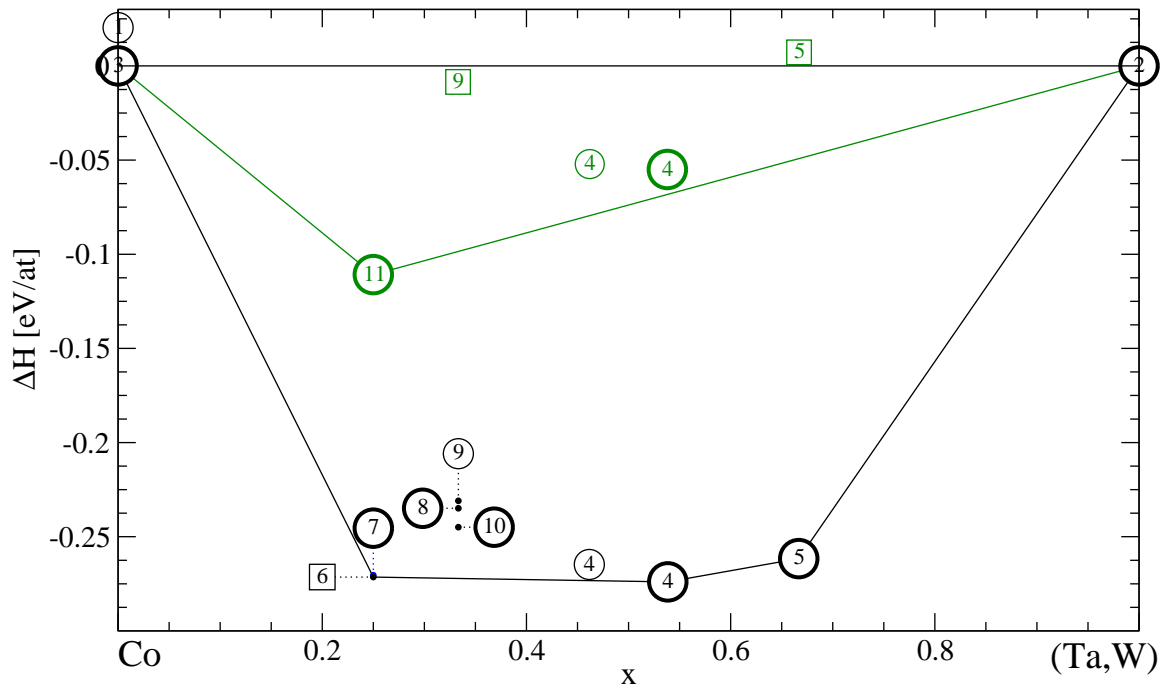
All structures have many bonds with $n = 5$ common neighbors, especially between unlike atomic species, reflecting the prevalence of icosahedral ordering in Frank-Kasper phases and amorphous materials. Very few Co-Co bonds have $n = 6$ common neighbors, and very few Ta-Ta bonds have $n = 4$ common neighbors, reflecting the relative sizes of Co and Ta atoms. Because hR13 is a canonical Frank-Kasper phase with no bonds sharing $n = 4$ common neighbors, we utilize tI12 to capture the role of $n = 4$ Co-Co bonds.

5.3.2 Convex Hulls

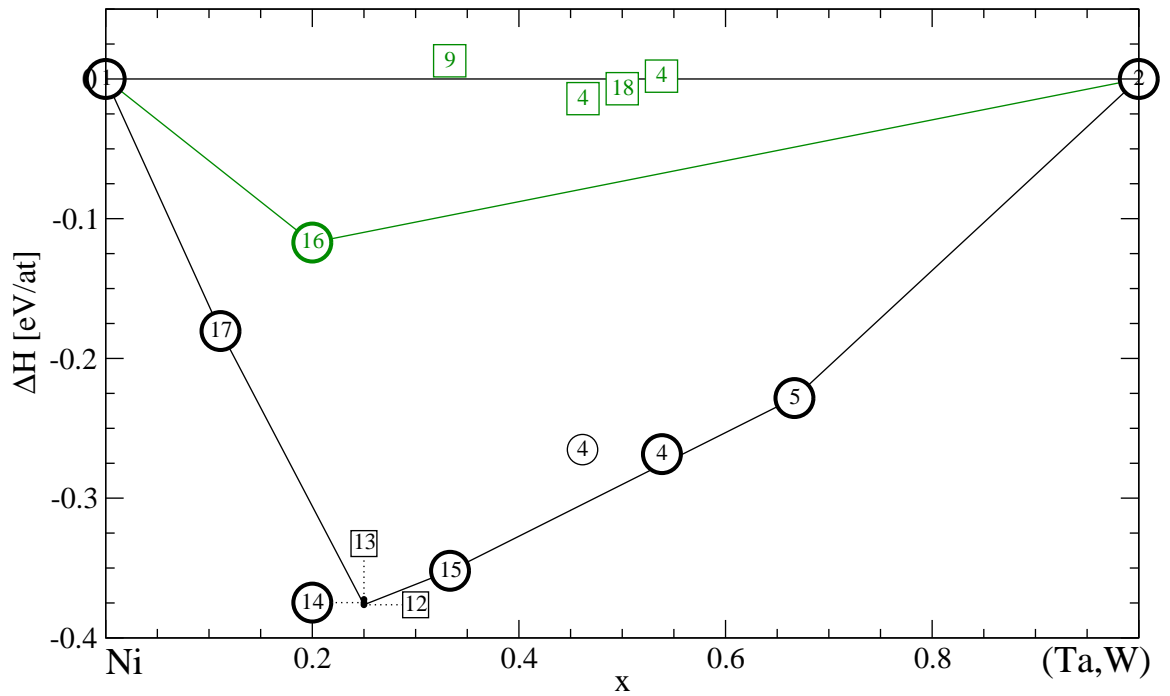
Figure 5.3 summarizes our calculated enthalpies of formation. Vertices of the convex hull of enthalpy as a function of composition are predicted to be stable phases at low temperature [161]. We employ special plotting symbols to indicate phases claimed experimentally to be stable at low temperature (heavy circles) and high temperature (light circles). Phases whose stability or existence is in question are shown as squares. From the prevalence of heavy circles on or near the convex hull we see general (though imperfect) agreement with the experimentally reported phase diagrams. We briefly summarize our findings for the four alloy systems of primary interest.

Co-Ta

For Co-Ta (Fig. 5.3a), at $x = 0.25$, we find that cP4 and hR12 (reference numbers 6 and 7) are nearly degenerate, with cP4 (stability not reported experimentally) favored by 1 meV/atom, which is closer than DFT can reliably distinguish. At $x = 0.33$, three different Laves phases have been reported (reference numbers 8-10), with conflicting



(a) Co-(Ta,W)



(b) Ni-(Ta,W)

Figure 5.3: Enthalpies of formation for (Co,Ni)-(Ta,W) alloys. Values for Ta shown in black, for W shown in green. Plotting symbols explained in text.

claims of stability and uncertain composition. We find that none of these phases lie on the convex hull. Further, all of their structures are mechanically unstable to deformation, casting doubt on the reported structure and stability of this phase. In our plot, we show the energy of a distorted cF24 structure which is mechanically stable, for comparison with the undistorted hP12 and hP24. In the vicinity of $x = 0.5$ lies the Frank-Kasper μ phase. This phase is common to many alloy systems containing fourth and fifth row early transition metals with third row late transition metals. In most cases the phase shows a broad composition range at high temperature but favors an ETM-rich low temperature limit (i.e. with the mixed occupancy $3a$ site occupied by an ETM). This feature is correctly reproduced by our calculation. At $x = 0.67$, the tI12 phase (reference number 5) is a non-canonical Frank-Kasper phase, as it contains a CN=10 Bernal Hole, in addition to a canonical CN=15 Kasper polyhedron.

Ni-Ta

For Ni-Ta (Figure 5.3b) at $x = 0.11$ we find $\text{Ni}_8\text{Ta.tI18}$ to be low-temperature stable. The experimental phase diagram has a tI36 structure stable, however no crystallographic refinement exists, so we use the known tI18 phase instead. There is disagreement on recent phase diagrams concerning the stable structure at $x = 0.25$, and we find three different structures have nearly identical enthalpies (tI8 is the lowest). The main source of disagreement between our $T = 0$ K phase diagram and experimental phase diagrams is the stability of NiTa.hR13 , with even the ETM-rich variant lying 7 meV/atom above the convex hull.

(Co,Ni)-W

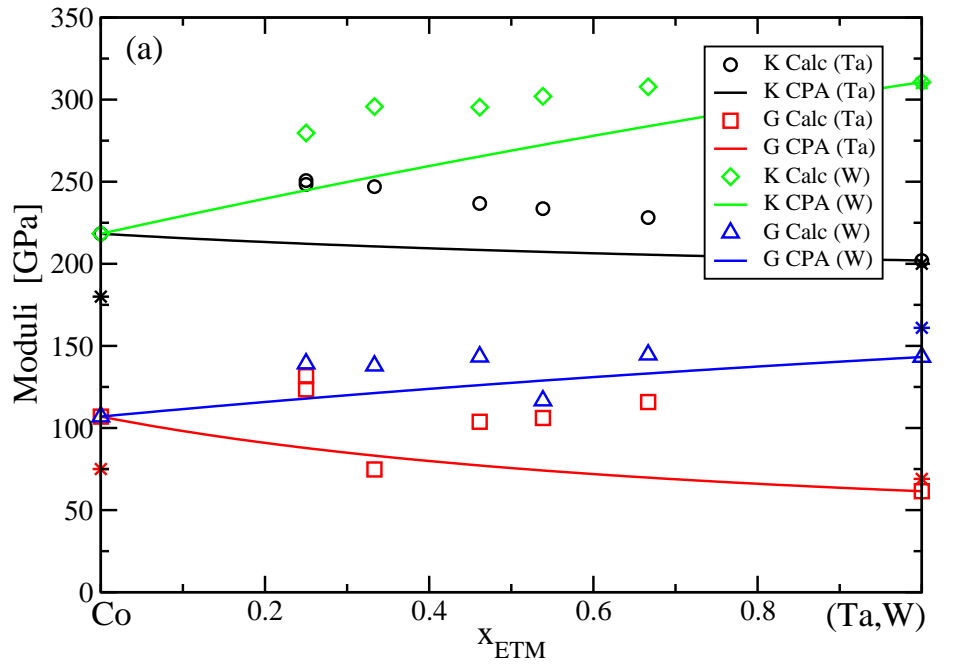
Our calculations verify the known Co_3W and Ni_3W phase stabilities. However, the reported Co_7W_6 phase lies above the convex hull, and additionally favors the ETM-rich limit contrary to experimental report. This phase has not been reported in the

Ni-W alloy system, and we indeed find it lies well above the convex hull. However, we will study the electronic and elastic properties of this hypothetical phase in order to elucidate trends with respect to composition. Notice that enthalpies of formation for alloys with W are lower than enthalpies with Ta. This does not necessarily reflect lower mechanical stability or melting points for the compounds, as the greater cohesive energy of tungsten compared to tantalum contributes to a reduction of the alloy formation enthalpies. An equiatomic Ni-W phase with orthorhombic symmetry has been observed low temperature stable [166], however no atomic structural data exists. Owing to similar chemical identity and Bravais lattice, we attempted to use the Frank-Kasper phase MoNi.oP56 with Mo substituted for W, but found that this structure lies 66 meV/atom above the convex hull and likely is not the correct phase. It was also too computationally expensive to compute elastic moduli for this phase.

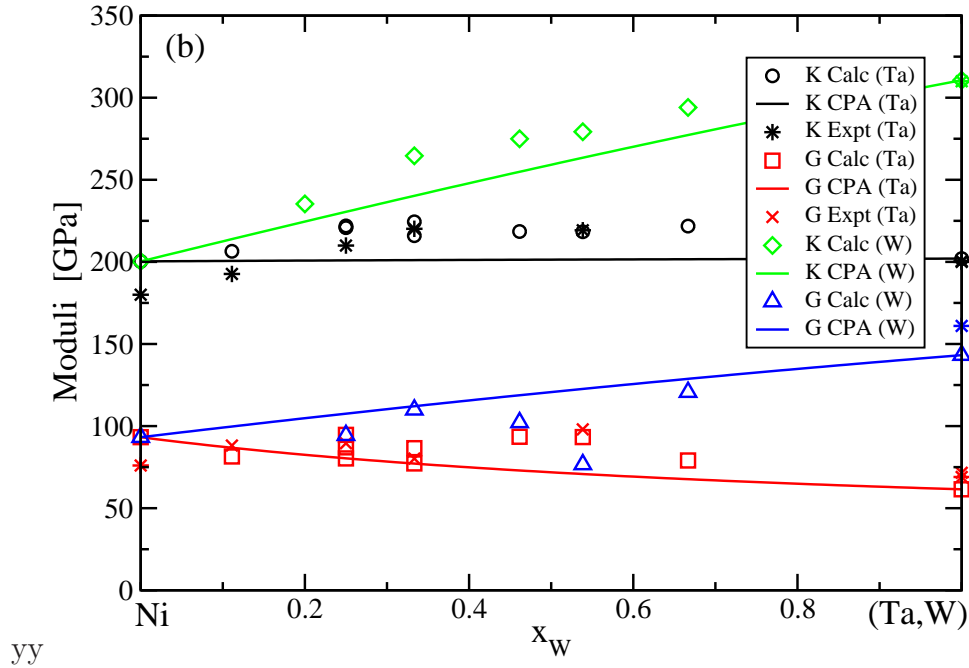
5.3.3 Binary Elastic Moduli

We examine the effect of alloying on the elastic moduli by using CPA to approximate a hypothetical alloy where no interspecies interactions exist. That is, for a well-ordered phase with stoichiometry A_xB_{1-x} , we compare its elastic moduli to a hypothetical solution of pure specie A and pure specie B with a stoichiometric ratio $x:(1-x)$ in the CPA approximation. As input for CPA, we use our computed elemental elastic moduli. These agree closely with experimental moduli for Ta and W but are relatively high for Co and Ni. Note that our calculation are valid at 0 K, while the experimental values are room temperature, so it is expected that our values should be high, especially for non-refractory elements. As the CPA approximation only incorporates elemental elastic moduli with no atomic environmental details, the deviation of computed polycrystalline moduli from the CPA approximation yields a measure of the relative importance of atomic environment and alloying species for elastic moduli.

All crystal structures are elastically anisotropic, and it is of interest to characterize the anisotropy of our amorphous approximants. We define three anisotropies [155,



(a) Co-Ta



(b) Ni-Ta

Figure 5.4: Elastic moduli for (Co,Ni)-(Ta,W) compounds. Lines show CPA estimates. Data points are our DFT calculations. Asterisks are experimental values from our experiments on Ni-Ta alloys and from the literature for pure elements.

167]: A_Z (Zener), A_G (shear) and A_E (Young's) as

$$A_Z = \frac{2C_{44}}{C_{11} - C_{12}},$$

$$A_G = \frac{S_{44} + S_{66}}{2S_{44}},$$

and

$$A_E = \frac{S_{11}}{S_{33}},$$

all of which are 1 for isotropic structures, where S_{ij} are elements of the compliance matrix. Table 5.2 compares calculated anisotropies of our hR13 and tI12 structures with the four pure elements. Our anisotropies are close to one, similar to those seen in the pure metals, with hR13 exhibiting less anisotropy than tI12. These anisotropies can be taken as estimates of the local anisotropy expected at the atomic level in actual amorphous structures. Recall that the polycrystalline averages are expected to reflect the globally isotropic properties of the bulk amorphous structures.

5.4 Trends in the Data

Shown in Figure 5.4 are our calculated K values, compared with CPA estimates. All CPA estimates are indicated by lines, all calculated moduli by individual data points, and for Ni-Ta asterisks indicate experimental results. Our calculated Ni-Ta bulk moduli show excellent agreement with our experimental results. For all four chemical families, CPA gives reasonable estimates for bulk moduli, with at most a 16% deviation between estimated and calculated bulk moduli. However, in all alloy systems and for all structures examined, CPA underestimates the bulk modulus. This suggests the dominant correction to the bulk moduli is chemical bonding and not atomic environmental details such as the prevalence of tetrahedra. Shear moduli show relatively larger and less regular deviations from CPA, suggesting that bond topology plays a significant role. Nonetheless, our calculated Ni-Ta shear moduli are in good agreement with experiment (crosses).

| Composition | Structure | A_Z | A_G | A_E |
|-------------|-----------|-------|-------|-------|
| Co-Ta | hR13 | 0.70 | 0.85 | 1.13 |
| Ni-Ta | hR13 | 0.81 | 0.91 | 1.14 |
| Co-W | hR13 | 0.76 | 0.88 | 1.18 |
| Ni-W | hR13 | 1.12 | 1.06 | 1.45 |
| Co-Ta | tI12 | 0.90 | 1.17 | 1.27 |
| Ni-Ta | tI12 | 1.32 | 1.24 | 1.50 |
| Co-W | tI12 | 1.24 | 1.12 | 1.20 |
| Ni-W | tI12 | 1.42 | 1.16 | 1.07 |
| Co | hP2 | 1.01 | 1.00 | 1.31 |
| Ni | cF4 | 2.18 | 1 | 1 |
| Ta | cI2 | 1.16 | 1 | 1 |
| W | cI2 | 0.83 | 1 | 1 |

Table 5.2: Measures of anisotropy for materials of interest. $A_G = A_E = 1$ for cubic structures.

| | Δv | Δh | ΔK | ΔG |
|------------|------------|------------|------------|------------|
| Δv | | 0.20 | -0.83 | -0.66 |
| Δh | 0.20 | | 0.06 | -0.47 |
| ΔK | -0.83 | 0.06 | | 0.60 |
| ΔG | -0.66 | -0.47 | 0.60 | |

Table 5.3: Correlation coefficients for linear regressions involving elastic moduli and thermodynamic quantities of interest, where rows denote independent variables and columns dependent variables for a given regression.

Shown in Table 5.3 are the correlation coefficient for various linear regressions across all calculated CoTa, CoW, NiTa, and NiW alloys, where the sign of the correlation coefficient denotes the sign of the slope. Here ΔK and ΔG (units GPa) are deviations of calculated bulk and shear moduli from CPA estimates, Δv (units \AA^3 per atom) the deviation of volume per atom from a linear interpolation of pure elements, and Δh (units eV per atom) the enthalpy of formation per atom as illustrated in Fig. 5.3. Correlations of elastic moduli with Δv and Δh reflect structure and bonding effects that are missing from CPA. There is only a weak correlation between Δh and Δv , though the associated slope is positive, expected as increased bond strength (more negative Δh) draws atoms closer together (more negative Δv). ΔG and ΔK are both correlated to Δv , with ΔK in particular strongly correlated. This is line with other work that shows that K and G correlate with V and that the correlation for K is particularly strong [141]. This is also true for individual chemical families, and for ΔK all chemical families' regressions have similar slopes. This strong correlation of ΔK with Δv explains why all structures have CPA underestimating the bulk moduli (positive ΔK), as all structures were also observed to have negative Δv , as expected. The slopes of ΔG and ΔK are both negative, as decreasing Δv draws atoms closer together, shortening bonds and enhancing interatomic force constants. The observed correlation of ΔG with ΔK is likely due to the underlying correlation of each with Δv .

A goal of metallic glass design is to predict glass-forming compounds with high ductility. Thus, as a guide, we plot the Poisson ratio's of the various alloys under discussion. Our computed $T = 0$ K crystalline Poisson ratios are expected to be systematically low relative to the corresponding glasses, as G decreases more rapidly than K as temperature increases [168], and amorphous G and K are lower relative to crystalline values by around 30% and 10%, respectively. Here we see no systematic trend in the choice of Ta versus W (empty versus filled plotting symbols) but Ni generally has higher Poisson's ratio than Co (red versus blue). Empirically, it has

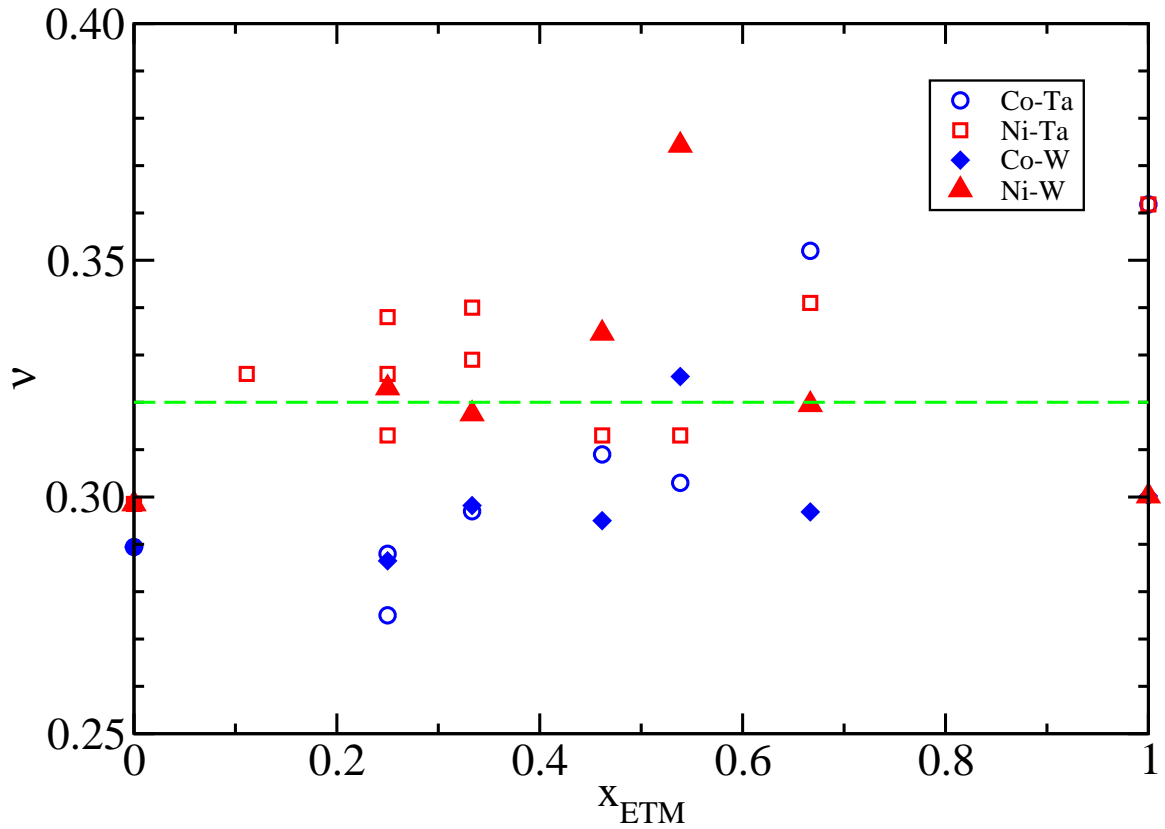


Figure 5.5: Calculated Poisson ratios. Dashed line at $\nu=0.32$ is putative threshold for ductility.

been observed that $\nu = 0.32$ serves as a rough criterion for separating ductile and brittle behavior in amorphous materials [140]. The majority of our Ni alloys lie above this criterion and Co alloy below. In particular, all Ni-W alloys satisfy this criterion, and Ni-W in the amorphous approximant structure hR13 shows particularly large Poisson's ratios. Combined with the large bulk modulus due to the presence of tungsten, we propose that Ni-W is a candidate system for future research into strong amorphous materials with high ductility.

To understand trends in elastic constants of these alloys we now look into the interatomic interactions. Within a first principles approach there is no unique decomposition of interactions into pairwise and many-body forces, and no simple notion of a chemical bond, especially for metals. However some heuristic measures are available.

| Compound | ETM-ETM (44x) | | | ETM-LTM (32x) | | | LTM-LTM (4x) | | | mean | mean | | |
|-------------------|---------------|------|-----|----------------------|------|-----|----------------------|------|-----|----------------------|------|----------------------|-----|
| | tI12 | R | k | ρ_{COHP} | R | k | ρ_{COHP} | R | k | ρ_{COHP} | k | ρ_{COHP} | K |
| NiTa ₂ | | 3.12 | 4.2 | 0.31 | 2.63 | 4.7 | 0.25 | 2.43 | 4.2 | 0.025 | 30.7 | 0.27 | 222 |
| CoTa ₂ | | 3.11 | 5.2 | 0.31 | 2.61 | 3.7 | 0.30 | 2.48 | 4.0 | 0.030 | 32.0 | 0.29 | 228 |
| NiW ₂ | | 3.02 | 4.0 | 0.31 | 2.55 | 7.6 | 0.34 | 2.38 | 4.3 | 0.041 | 37.7 | 0.31 | 294 |
| CoW ₂ | | 3.02 | 5.1 | 0.37 | 2.54 | 6.7 | 0.36 | 2.38 | 4.8 | 0.037 | 39.9 | 0.35 | 308 |

Table 5.4: Data for tI12. R are average bond lengths for nearest neighbors under 4 Å. k are averaged over atoms (i.e. weighted by the number of bonds per atom) in units $\text{eV}/\text{\AA}^2$, ρ_{COHP} is iCOHP volume density in units $\text{eV}/\text{\AA}^3$, and K is the calculated bulk moduli in units GPa.

Here we examine the interatomic force constants, which can be regarded as springs connecting the atoms, and the crystal overlap Hamilton populations (COHPs) which are a measure of the covalency of electronic wave functions.

5.4.1 Force Constants and COHP

To compare different ETM and LTM substitutions, Table 5.4 shows k , the mean force constants for the near neighbor bonds of a given species combination, ρ_{COHP} , the total iCOHP per unit volume for bonds of a given species combination up to 4 Å, and K , the bulk moduli in the structural prototype tI12. To calculate the mean force constant, we sum force constants for all bonds up to 4 Å for a given cell then divide by the number of atoms.

Both the mean force constant and ρ_{COHP} correlate with the bulk moduli. This is especially notable in the mean force constant, where there is a large increase in mean force constant performing a Ta \rightarrow W substitution and a relatively small increase performing a Ni \rightarrow Co substitution, but the effect is also present in ρ_{COHP} . As a force constant gives a measure of the stiffness of an individual bond, this mean

force constant gives a measure of the total stiffness of all bonds, and bulk modulus is increased under chemical substitution by an overall increase in the interatomic force constant. We also see in Table 5.4 that performing a Ni \rightarrow Co or a Ta \rightarrow W substitution enhances ρ_{COHP} . Thus these substitutions have enhanced the bonding nature of the electronic states.

To further understand the enhancement of bonding, we calculate electronic densities of state (Fig. 5.6). The low-energy peak near -4 or -5 eV consists of *sd*-hybrid orbitals, followed by a series of higher-energy peaks consisting solely of *d* orbitals, with the Fermi level lying in the middle of the ETM *d*-band and at or above the top of the LTM *d*-band. For Co-W, the Co and W *d* bands are closely aligned, inducing strong hybridization of Co and W *d* orbitals. This effect is present in all structures we have examined. Performing a W \rightarrow Ta substitution shifts the ETM *d*-band up relative to the LTM *d*-band, decreasing the *d*-band overlap and diminishing hybridization. Performing a Co \rightarrow Ni substitution shifts the LTM *d*-band down relative to the ETM *d*-band, also decreasing the *d*-band overlap. Both of these induce a decrease in the hybridization of the ETM-LTM *d*-bands. As hybridization generally creates bonding states below the Fermi level, this reduction in hybridization going from W \rightarrow Ta and Co \rightarrow Ni decreases the overall bonding characteristic of the occupied states, leading to the observed trends in ρ_{COHP} , and hence in bulk modulus.

5.4.2 Microstructural Details: Ternaries and Quaternaries

Elemental properties provide the dominant contribution to the elasticity of these ETM-LTM intermetallic compounds, as can be seen in the qualitative agreement of calculated alloy moduli with the CPA predictions shown in Fig. 5.4. In Table 5.5 we see that the small decreases in modulus from Co to Ni, and the large increases from Ta to W, are echoed in the moduli of the hR13 Frank-Kasper structure.

While binary amorphous metals exist, size mismatch criteria and material property tuning favor the usage of multiple constituent species in amorphous metals for

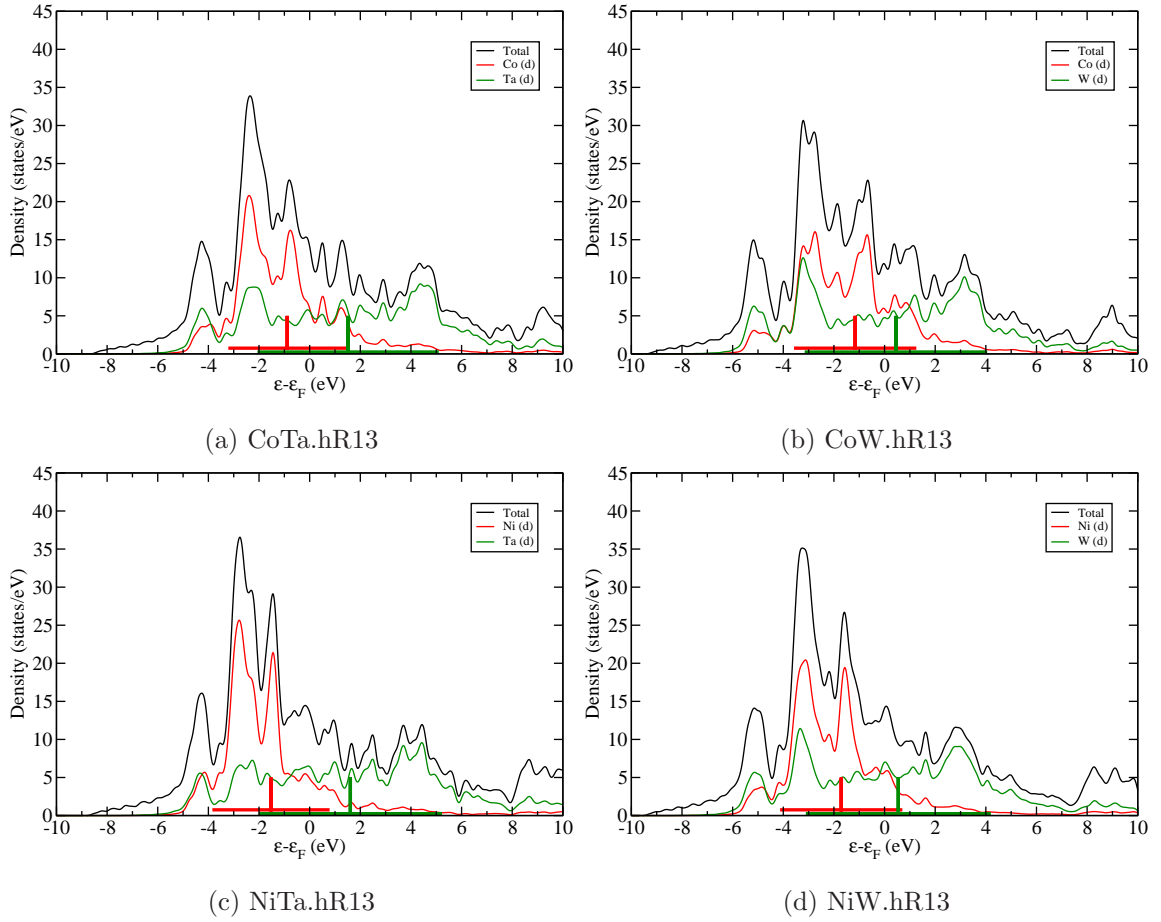


Figure 5.6: Electronic densities of states for hR13 structures. Line segments indicate the mean and standard deviations of the element projected d -bands.

| | | K | G | | K | G |
|-------------------------|---------------------------------|-----|-----|---------------------------------|-----|-----|
| | Co | 218 | 107 | Ni | 200 | 93 |
| Nb ($K=173$, $G=22$) | Co ₆ Nb ₇ | 213 | 92 | Ni ₆ Nb ₇ | 198 | 81 |
| Ta ($K=202$, $G=61$) | Co ₆ Ta ₇ | 234 | 106 | Ni ₆ Ta ₇ | 218 | 93 |
| W ($K=331$, $G=143$) | Co ₆ W ₇ | 302 | 117 | Ni ₆ W ₇ | 279 | 77 |

Table 5.5: Elastic moduli for pure elements and binary hR13 structures.

practical applications, and thus the question of transferability of binary results to structures with three or more constituent species must be addressed. In addition, there is still the lingering need to quantify how atomic environment affects the elastic moduli. To answer both these questions, we perform chemical substitutions in a binary structure to yields ternaries and quaternary structures. This changes the chemical identities of formerly equivalent sites, altering local chemical ordering.

Shown in Table 5.6 is a comparison of binary hR13 structures (including also alloys with Nb, an ETM) with nearly equiatomic composition quaternary variants of hR13 and six associated ternaries. Site occupancies in the quaternary has been chosen to maintain the ETM/LTM nature of sites and minimize energy, and the ternaries were formed by keeping the early/late site identity fixed.

To compare our binary results to ternaries and quaternaries, we here use a simple chemical environment averaging scheme between ETM and LTM, with a equiatomic ABCD mixture with A and B LTM and C and D ETM approximated by $1/4*(AC+AD+BC+BD)$, and an ABC mixture (with C having near 50% concentration) approximated by $1/2*(AC+BC)$. Here AC, AD, BC and BD refer to the relevant binary hR13 structure with the associated chemical formula. As an example, the predicted bulk moduli of $\text{Co}_6\text{Ta}_3\text{W}_4$ would be the average bulk modulus of Co_6Ta_7 and Co_6W_7 . While this ignores interspecies ETM-ETM and LTM-LTM bonds present (i.e. AB and CD), binary enthalpies of formation for ETM-ETM and LTM-LTM families are weak compared to ETM-LTM families, suggesting that as a first approximation we may assume the differences in interspecies ETM-ETM and LTM-LTM bond strength average out.

Differences between our predicted interpolated elastic moduli and computed elastic moduli follow the trends previously reported for CPA. Again we see bulk moduli negligibly affected by atomic environment and predominately determined by the alloying species, with deviations in bulk moduli below 2.6% for all structures. For shear moduli, the structures can be placed into two categories: those structures that have only one ETM species or else two ETM species from the same group (here Nb and

| Chemical Formula | Calculated K, G | Averaged K, G | Deviation |
|--|-------------------|-----------------|-----------|
| $\text{Co}_3\text{Ni}_3\text{Nb}_7$ | 205, 87 | 205, 87 | 0.3, 0.5 |
| $\text{Co}_3\text{Nb}_3\text{Ta}_7$ | 225, 100 | 223, 99 | 0.7, 1.4 |
| $\text{Co}_3\text{Ni}_3\text{Ta}_7$ | 225, 102 | 226, 100 | 0.4, 2.2 |
| $\text{Ni}_6\text{Nb}_3\text{Ta}_4$ | 210, 89 | 208, 87 | 0.9, 2.2 |
| $\text{Co}_3\text{Ni}_3\text{W}_7$ | 290, 94 | 291, 97 | 0.3, 2.4 |
| $\text{Co}_3\text{Ni}_3\text{Nb}_3\text{Ta}_4$ | 217, 97 | 216, 93 | 0.1, 3.7 |
| $\text{Co}_6\text{Ta}_4\text{W}_3$ | 261, 123 | 268, 111 | 2.5, 10.0 |
| $\text{Co}_3\text{Ni}_3\text{Ta}_3\text{W}_4$ | 253, 115 | 258, 98 | 2.1, 14.6 |
| $\text{Co}_6\text{Nb}_3\text{W}_4$ | 261, 121 | 257, 104 | 1.5, 16.4 |
| $\text{Ni}_6\text{Nb}_3\text{W}_4$ | 241, 92 | 239, 79 | 0.8, 16.8 |
| $\text{Ni}_6\text{Ta}_4\text{W}_3$ | 242, 100 | 249, 85 | 2.6, 17.8 |
| $\text{Co}_3\text{Nb}_3\text{Ni}_3\text{W}_4$ | 248, 109 | 248, 92 | 0.2, 18.7 |

Table 5.6: Comparison of calculated ternary and quaternary hR13 moduli with averaged values of binaries. Moduli are given in GPa, and deviations in percentages.

Ta belong to group IV) which have deviations in shear moduli below 3.7%, and those that have ETM species from different groups (here W from group V together with Nb or Ta from group IV) which have deviations in shear moduli between 10.0% and 18.7%. In all cases where predicted shear moduli deviate significantly from calculated shear moduli, the computed shear moduli have been enhanced.

That mixing Co and Ni or Nb and Ta causes little deviation in shear modulus, but mixing Ta and W does, is further evidence for the dependence of shear modulus on atomic environment. Co and Ni have similar atomic radii and electronegativity, as do Nb and Ta. For a topologically close packed structure like hR13, substitution of these chemical species should not noticeably affect bond lengths and ionic charges, yielding similar calculated and averaged results. However, Nb and Ta have larger

atomic radii and lower electronegativity than W, leading to larger charge transfers and changes in bond length, reducing the accuracy of our averaging scheme while generally increasing bonding strength.

Chapter 6

On Bulk Sulfidization of the Cu-Pd System¹

6.1 Sulfidization of Copper-Palladium Membranes: What Do These Numbers Mean?

Every human is familiar with the corrosion process of oxidation, where oxygen atoms strongly bond to materials via electron transfer to form oxides, whose properties strongly differ from the unreacted materials'. Sulfur may also bond to materials to form sulfides in a similar corrosion process known as "sulfidization"². Unlike oxygen, sulfur is not present in standard atmosphere conditions, and the process of sulfidization is not nearly as prevalent as oxidation. This is quite fortunate, as the rate of sulfidization is generally 10^4 - 10^6 times higher than the oxidation rate

¹This chapter is adapted from my manuscript "First Principles Modeling of the Temperature Dependent Ternary Phase Diagram for the Cu-Pd-S System", currently under review for Comp. Mat. Sci.

²The literature has not converged on a single term, and the process may be known as "sulfidation" or "sulfidization", not to mention the alternative spellings involving "sulphur". We here choose "sulfidization" as the standard term.

under similar circumstances [169]. One of the primary design considerations for any material that comes into contact with sulfur in its multitude of forms is its resistance to sulfidization.

One class of materials that will come into contact with sulfur are palladium-based catalytic membranes for hydrogen separation [170, 171, 172], of potential application in clean energy technology. Such membranes are used to separate out pure H₂ gas from a “feed gas” containing a mixture of gases, commonly produced from coal gasification. Molecules containing hydrogen in the gas (including H₂) bind to the upstream side of the membrane, and a chemical reaction resulting in dissociation of hydrogen is catalyzed. Due to hydrogen’s small size, if the bulk of the membrane has favorable binding sites for hydrogen, the hydrogen will be absorbed into the bulk and individual hydrogen atoms will diffuse through the membrane via interstitial hopping, forming a metal/hydrogen solid solution. When the hydrogen reaches the downstream side of the membrane, it will combine with another hydrogen atom on the surface to reform H₂. Assuming the hydrogen partial pressure of the downstream side is small, free energy minimization will prevent H₂ from re-absorbing into the bulk. Over time, pure H₂ gas can be captured and stored via various hydrogen storage methods [173, 174]. The performance of the membrane is given by a material property “permeability” derivable from Sievert’s Law³,

$$k = \frac{N_{H_2} X_m}{\sqrt{P_{up}} - \sqrt{P_{down}}}, \quad (6.1)$$

where k is the permeability, N_{H_2} is the downstream H₂ flux, P_{up} and P_{down} the upstream and downstream hydrogen partial pressures respectively, and X_m the membrane thickness.

While conceptually very pretty, from the viewpoint of phase stability there are two major problems with this approach⁴. The first is the formation of hydrides within the

³Only valid past some critical thickness where diffusion becomes the rate-limiting step.

⁴Additional problems involving the membrane include, but are not limited to, the proper temperature to run the absorption/desorption cycling, grain boundaries, phase stability of the membrane

membrane caused by hydrogen-hydrogen interactions at high hydrogen concentration. These hydrides reduce output flux and embrittle the membrane [174]. The more serious problem, and the subject of this chapter, is the reaction with molecules other than H_2 . All practical feed gases contain trace amounts of hydrogen sulfide (H_2S), and all known catalytic membranes that show favorable catalysis of H_2 also show favorable catalysis of H_2S . When H_2S binds to the feed side of the membrane, the dissociation $H_2S \rightarrow 2H + S$ occurs, and $2H$ diffuses into the bulk as in the case of H_2 . The lone sulfur remains on the surface, and it can either bind to the surface or diffuse into the bulk to form a sulfide, rendering the local region catalytically inert. Even a trace amount of H_2S will rapidly sulfidize a membrane, owing to its concentration at the surface.

It has been known since the 19th century that palladium serves as an excellent material for hydrogen separation. However, a high susceptibility to sulfidization (as much as an 85% decrease in permeability after only 100 minutes of exposure to a gas with 50 ppm H_2S), possibly irreversible growth of a Pd_4S phase with greatly diminished permeability, embrittlement of the membrane after several absorption/desorption cycles due to lattice expansion by the hydrogen atoms, and palladium's high cost make pure palladium a poor choice for industrial application [175, 171, 176, 177, 178]. Commercial viability for fuel cells and the semiconductor industry was only possible when it was discovered that alloying Pd with 25% Ag by weight in a solid solution eliminates embrittlement (as the lattice is already expanded due to the presence of Ag atoms), increases hardness due to solid solution hardening, improves permeability, and lowers cost. Most importantly, sulfidization has been observed to be reversible in Ag-Pd alloys using a process where the sulfidized membrane is alternatively exposed to air and pure H_2 and the temperature is increased over three days [179, 180, 181, 182].

Examining the periodic table, the natural next choice is the current leading can-

during cycling, supporting the membrane to withstand a large difference in pressure between the upstream and downstream sides, and corrosion by other elements such as Cl and O.

didate for hydrogen segregation membranes, copper-palladium alloys with 40% Cu by weight [183, 184, 185, 176, 186]. While Cu-Pd membranes show reduction in permeability relative to Ag-Pd, and the existence of two Cu-Pd phases (fcc and bcc) makes membrane growth and stability problematic, they are resistant to embrittlement, and some samples have permeability similar to bulk Pd at standard operating temperatures (~ 650 K) at an even lower price. A considerable variance in reported permeabilities and sulfidization tolerances for Cu-Pd membranes at identical compositions exists in the literature. This is likely due to samples being in differing phases at differing temperatures, with samples in the fcc phase having permeability an order of magnitude smaller than the bcc phase [187, 184]. This confusion only highlights the necessity of the phase diagram for material design.

The fcc phase is much more resilient to sulfidization, with as little as a 10% drop in steady state permeability for 1000 ppm H_2S reported for some samples [187]. It was observed in another study [188] that while a Cu-Pd membrane with 40% Cu by weight sulfidizes more rapidly than a pure Pd membranes at 623 K (where the membrane is in bcc-fcc phase coexistence), reaching 6% of its initial diffusion rate after one day of exposure of a feed gas with 4.5 ppm of H_2S at 623 K, upon switching to a feed gas containing no H_2 , the membrane recovered to 91% of its initial permeability after only one day of exposure. After five days of treatment, its pre-exposure permeability after five days was recovered, a dramatic recovery not seen in either Pd or Ag-Pd membranes. This suggests that although the bcc phase of Cu-Pd is affected by sulfidization, bulk sulfidization of Cu-Pd at 40% Cu is impeded, and the observed sulfidization of Cu-Pd is primarily a surface phenomena, though some studies dispute this claim [185]. While Cu-Pd and Ag-Pd membranes have shown small-scale production success due to their superior mechanical properties and lower cost, sulfidization still occurs for both, and new candidate materials are necessary before industrial-scale production of hydrogen via membrane separation is economically feasible on the scale necessary for energy storage.

In this chapter we show how first principles calculations can be used to calculate various thermodynamic quantities useful for the design of new hydrogen separation membranes, such as free energies, activities, predominance diagrams, and, of course, phase diagrams. It should be mentioned this is only one part of the over-arching design process : kinetic barriers to sulfide formation may retard their formation [169], and successful prediction of new membranes will likely involve both thermodynamic and kinetic factors. We will only focus on bulk sulfidization of the Cu-Pd system interacting with an S_2 gas, as previous studies of surface sulfidization [189] and hydrogen diffusion through the bulk [190, 191] exist in the literature. While some experimental results for Cu-Pd-S already exist in the literature [192], our results highlight the underlying physics of this system with relatively simple models and semi-quantitative accuracy. This stands in stark contrast to complicated models such as the CALPHAD method with many fitting parameters that yield close agreement with experiment at the cost of obscuring the underlying physics. This work may be extended to predict the behavior of candidate sulfidization-resistant systems with no previous experimental data.

6.2 What Does Density Functional Theory Predict?

In order to calculate a phase diagram using first principles methods, all plausible crystal structures must be considered, in principle. In the case of Cu-Pd-S, a wealth of experimental crystallographic data gives an excellent starting point, especially for the binary compounds. We generalize these binaries to ternary structures formed from substitutions of the ternary species into either lattice sites or interstitial sites. Once the 0 K total energies for all likely crystalline structures have been calculated, it is straightforward to generate a 0 K phase diagram by creating the convex hull of total energies.

Subramanian and Laughlin [193] determined the phase diagram for Cu-Pd experimentally, and Li *et al.* created a CALPHAD model [194]. Above 871 K, the entire composition range of solid Cu-Pd exists in fcc solid solution. Below this temperature other solid phases are present. β -CuPd has a CsCl structure and exhibits a Cu-rich composition range extending to a composition of 58% Cu. At copper concentrations near 75%, phases based on 1D and 2D long period superstructures (LPS) compete. Studies using ab initio methods to examine this region of the phase diagram have already been performed [195, 196]. As we are primarily concerned with the palladium-rich side of the phase diagram, we only calculate the ideal 1D LPS, Cu₃Pd.tP28, (using a notation of [chemical formula].Pearson symbol) and ignore the 2D LPS and phase solubility ranges in the 1D LPS.

Determination of the phase diagram for Cu-S [197] using first principles calculations is problematic, as it contains an abundance of phases, many of which are non-stoichiometric or have large unit cells. We include only Cu-S structures with well-defined crystallographic refinements, as we do not expect this discrepancy to affect our results on the palladium-rich side of the phase diagram. The Pd-S phase diagram [198] is relatively simple, containing Pd₁₆S₇, Pd₄S, PdS, and PdS₂ phases as line compounds at low temperature, with Pd₃S stabilized at 829 K. We summarize the phase diagrams here only for comparison; our method does not require pre-existing knowledge of the phase diagrams.

In order to add temperature dependence to the phase diagrams, we introduce free energy models for select phases of interest, all of which are based on substitutional solid solution models with sublattice filling (where for some structures, the "sublattice" is the entire lattice). When calculating the ternary phase diagram and the activities, we work in the Gibbs ensemble, where we specify temperature, pressure, and chemical concentration. We neglect pressure dependence in the solid phases' free energies, as solid compressibilities are low. Phonon free energies are included, in the

harmonic approximation, giving free energies of form

$$G_{tot} = G_{config} + G_{phonon}. \quad (6.2)$$

Based on our results, we chose to model only substitutional defects and not interstitials. We here summarize the configurational free energy G_{config} of a simple substitutional solid solution model, valid in the dilute limit. In a substitutional solid solution, we have a set of site classes i , each with N_i sites, an associated enthalpic cost of performing a chemical substitution of species α into site class i , $\Delta E_{i,\alpha}$, and a substitution concentration of $x_{i,\alpha}$. In the substitutional solid solution model, it is assumed that each substitution is uncorrelated with all other chemical substitutions, and all spatial configurations have identical energies. This implies a linear dependence of ΔH with respect to composition, giving an enthalpic contribution of

$$\Delta H = \Delta H_0 + \sum_{i,\alpha} x_{i,\alpha} N_i \Delta E_{i,\alpha}, \quad (6.3)$$

where ΔH_0 denotes the enthalpy of the base structure with no substitutions. Including an ideal entropy of mixing

$$\Delta S = -k_B \sum_{i,\alpha} N_i [x_{i,\alpha} \ln x_{i,\alpha} + (1 - x_{i,\alpha}) \ln(1 - x_{i,\alpha})], \quad (6.4)$$

leads to a Gibbs free energy $\Delta G = \Delta H - T\Delta S$. Here, ΔH_0 and $\Delta E_{i,\alpha}$ can be determined from first-principles calculations. However, we control only the total impurity concentration for a species α , x_α , not the number of substitutions in a given site class $x_{i,\alpha}$. Since we work with a fixed number of sites, we fix the total concentration of substitutions, and thus minimize the free energy over all $x_{i,\alpha}$ subject to the constraint of species number conservation.

To better elucidate the model, we restrict to the special case of where only one type of substitution (with an enthalpic cost of ΔE) is allowed in only one sublattice containing N_0 sites. A case with two sublattices will be considered later. The configurational free energy takes the form

$$\Delta G(N', T) = \Delta H_0 + \Delta E * N' + kTN_0(x' \ln x' + (1 - x') \ln(1 - x')), \quad (6.5)$$

where N' is the number of substitutions performed and $x' = N'/N_0$ is the concentration of substitutions in the sublattice. The appropriate quantity to consider for thermodynamics is the free energy per atom (that is, the total number of atoms N), $\Delta g = \Delta G/N$, expressed in terms of the $x = N'/N$, which can be shown to be

$$\Delta g(x, T) = \Delta h_0 + \Delta E * x - T\Delta S, \quad (6.6)$$

where $\Delta h_0 = \Delta H_0/N$, and $\gamma = N_0/N$ is a measure of the number density of sublattice sites. Of particular importance is the entropic contribution to the free energy,

$$-T\Delta S = k_B T \gamma (x \ln x + (\gamma - x) \ln(\gamma - x) - \gamma \ln \gamma), \quad (6.7)$$

which we use for all phases modeled throughout this paper.

In order for a given substitution type to appreciably affect the free energy, the two necessary features are large γ values, corresponding to a sublattice dense in the total lattice and thus a significant entropic contribution from the sublattice, and small positive (or any negative) enthalpic cost Δh_0 for the substitutions, such that at a given temperature the entropic portion of the free energy can overcome the enthalpic cost (or reinforce the enthalpic gain).

We use VASP (the Vienna Ab-Initio Simulation Package) [82, 83] a plane wave ab-initio package implementing PAW potentials [27] to determine total energies. Previous work by Hu et al. [199] compared the accuracy of different pseudopotentials in the Pd-S system, and recommended PBEsol [200] as most suitable for calculations involving sulfur. The total energy calculations were performed by fully relaxing atomic positions and lattice parameters until energies converged to within 0.1 meV/atom. Subsequent convergence in k-point density was performed. A common energy cutoff of 273 eV was used. In order to model solubility ranges, calculations were performed both in unit cells and larger supercells. All phonon calculations were done using density functional perturbation theory, and were performed in at least a $2 \times 2 \times 2$ supercell of the unit cell, with the exception of Pd₁₆S₇.cI46, where due to its large size only a $2 \times 2 \times 2$

supercell of the primitive cell was used. Table 6.1 shows a list of structures and their total energies.

Given total energies, we calculate the enthalpy of formation for our structures at $T = 0$ K,

$$\Delta h = \Delta h_0 - \sum_i x_i \Delta h_i, \quad (6.8)$$

where Δh_0 is the calculated 0 K total energy for the base structure, x_i is the composition of a given species i in the structure, and Δh_i is the 0 K total energy for pure species i in a chosen reference structure. By convention, this reference structure is chosen to be the equilibrium structure at 0 K, so that at 0 K all enthalpies of formation for the pure species vanish. In the Cu-Pd-S system, the standard reference structures would be Cu.cF4 for copper, Pd.cF4 for palladium, and S.mP48 for sulfur.

As we are interested in interaction of gaseous sulfur with copper-palladium membranes, we have chosen to use gaseous sulfur dimers rather than the standard S.mP48 when calculating phase diagrams. In the case of the ternary phase diagram, all structures of interest have relatively low sulfur composition, so the mismatch in reference phase compared to experimental phase diagrams is negligible.

The quantity of importance for constructing temperature dependent phase diagrams is

$$dE = \Delta h - [\Delta h], \quad (6.9)$$

where $[\Delta h]$ is the enthalpy of formation of the convex hull at a structure's stoichiometry. By definition, this quantity is non-negative, and it vanishes only when the structure lies on the convex hull. This quantity is a measure of how far above the convex hull a particular structure lies at 0 K. Structures with large dE 's require large entropic contributions to free energy in order to overcome enthalpic costs.

Figure 6.1 shows the 0 K binary enthalpies of formation. Observe that palladium and sulfur react strongly, as can be seen by the maximum enthalpy of formation of

| Phase | Pearson Symbol | Prototype | Group # | Space Group | ΔH | dE |
|--|----------------|---|---------|----------------------------------|------------|------|
| Cu [201] | cF4 | Cu | 225 | Fm $\bar{3}m$ | 0 | 0 |
| Pd [202] | cF4 | Cu | 225 | Fm $\bar{3}m$ | 0 | 0 |
| S ₂ Dimer | N/A | N/A | N/A | N/A | 0 | 0 |
| Cu ₃ Pd [203] | tP28 | Cu ₃ Pd | 99 | P4mm | -103.0 | 0 |
| CuPd | cP2 | ClCs | 221 | Pm $\bar{3}m$ | -116.9 | 0 |
| Cu ₂ S [204, 205] | mP144 | Cu ₂ S | 14 | P2 ₁ /c | -496.4 | 0 |
| CuS [206] | oC24 | CuS | 63 | Cmcm | -715.4 | 0 |
| CuS ₂ [207] | cP12 | FeS ₂ | 205 | Pa $\bar{3}$ | -821.5 | 0 |
| Pd ₄ S [208] | tP10 | Pd ₄ Se | 114 | P $\bar{4}2_1C$ | -418.9 | 0 |
| Pd ₁₆ S ₇ [209] | cI46 | Pd ₁₆ S ₇ | 217 | I $\bar{4}3m$ | -589.7 | 0 |
| PdS [210] | tP16 | PdS | 84 | P4 ₂ /m | -892.8 | 0 |
| PdS ₂ [211] | oP12 | PdSe ₂ | 61 | Pbca | -952.4 | 0 |
| CuS [206] | hP12 | CuS | 120 | I $\bar{4}c2$ | -712.9 | 2.5 |
| Cu ₂ S [212] | tP12 | Cu ₂ S | 96 | P4 ₃ 2 ₁ 2 | -479.3 | 3.3 |
| Cu ₄ Pd [213] | cP4 | AuCu ₃ | 221 | Pm $\bar{3}m$ | -99.7 | 3.4 |
| Pd ₃ S [214] | oC16 | Pd ₃ S | 40 | Ama2 | -492.8 | 8 |
| Cu ₅₀ Pd ₅₀ [215] | cF4 | Cu | 225 | Fm $\bar{3}m$ | -106.9 | 10 |
| Cu ₄ Pd [216] | tP20 | Cu ₄ Pd | 84 | P4 ₂ /m | -69.6 | 12.8 |
| Cu ₂ Pd ₃ S ₄ | mP18 | Cu ₂ Pd ₃ Se ₄ | 14 | P2 ₁ /c | -743.0 | 13.2 |
| Cu ₂ S [217] | cF12 | CaF ₂ | 225 | Fm $\bar{3}m$ | -503.1 | 20.6 |
| Cu | cI2 | W | 229 | Im $\bar{3}m$ | 36.3 | 36.3 |

Table 6.1: A partial list of calculated structures, focusing on "base" structures with no substitutions. All energetic quantities are given in units of meV/atom. Cu₂Pd₃S₄ is a hypothetical structure based on Cu₂Pd₃Se₄.mP18 [4]. Cu.cI2 and CuPd.cP2 are hypothetical structures used to model the β -CuPd phase. ΔH and dE are defined in eqs. 6.8 and 6.9

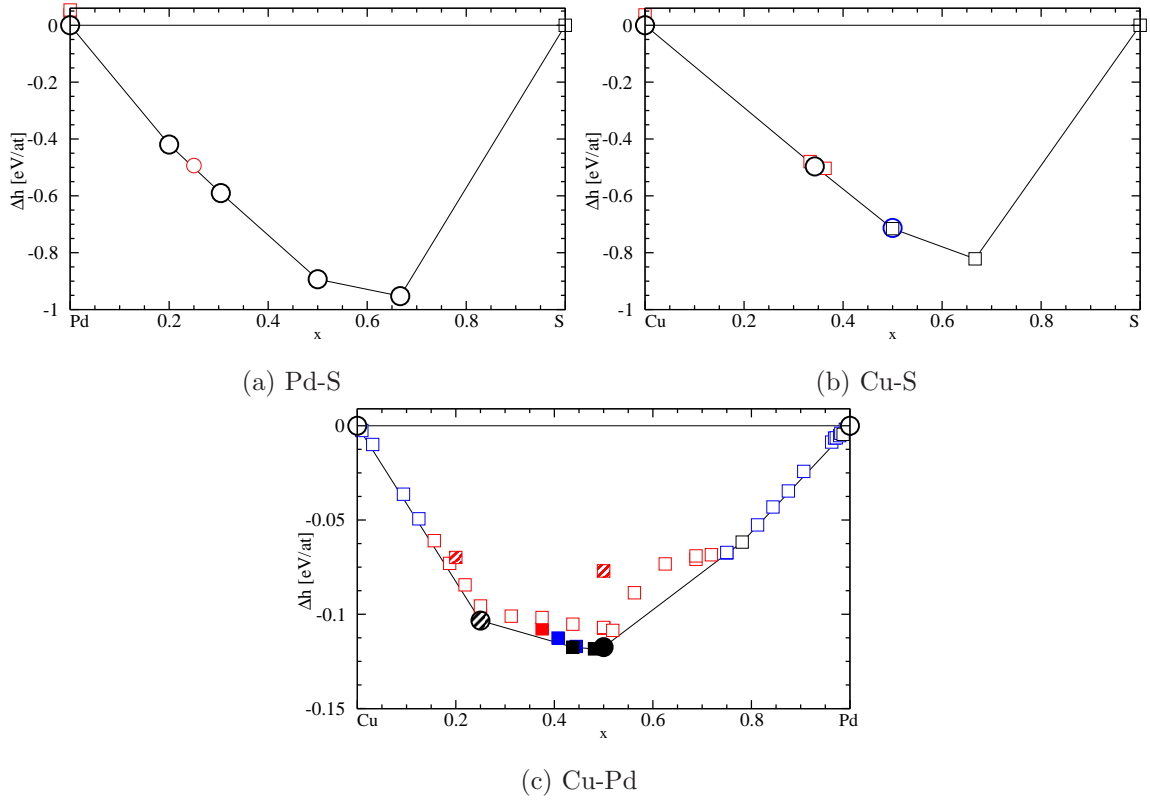


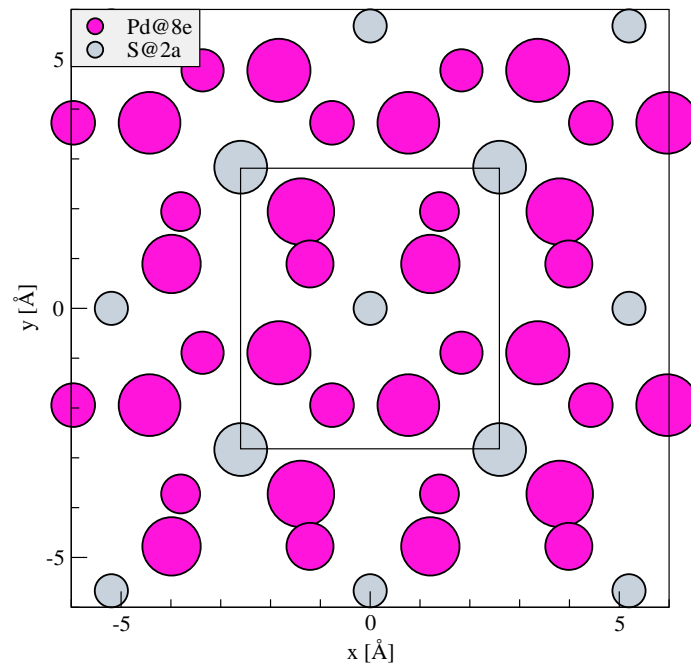
Figure 6.1: Binary enthalpies of formation for Pd-S, Cu-S, and Cu-Pd. The x axis corresponds to concentration, and y axis corresponds to enthalpy of formation. Black symbols denote stable structures, blue correspond to structures within 3 meV of the convex hull, and red to structures above 3 meV. Circles with thick borders are known low temperature stable structures, circles with thin borders are known high temperature stable structures, and squares denotes all other cases (including hypothetical structures). For Cu-Pd, to better distinguish phases, filled symbols corresponding to bcc structures, empty symbols to fcc, and dashed for the three other structures ($\text{Cu}_3\text{Pd.tP28}$, $\text{Cu}_4\text{Pd.tP20}$, and the SQS configuration for fcc at 50% Pd).

0.95 eV/atom. This strong enthalpy of formation reflects the tendency of pure palladium membranes to sulfidize. Next, copper and sulfur react almost as strongly, with a maximum enthalpy of formation of 0.82 eV/atom. Finally, copper and palladium have a maximum enthalpy of formation of only 0.12 eV/atom, indicating that the interspecies binding between copper and palladium is relatively weak. This is expected from the Cu-Pd phase diagram, as all known phases are variants of fcc (the $T=0$, $p=0$ structure for both Cu and Pd) or bcc (which is reached from fcc by a martensitic transition [218]). We find that the known structure CuS.oC24 is mechanically unstable, with an imaginary phonon mode that stabilizes a slight monoclinic distortion, and this distorted monoclinic structure, CuS.mC24, is the true ground state structure according to DFT. The stable phases predicted correspond to known low temperature stable phases, with the exception of CuS₂.tP12, which is not observed stable at temperatures as low as 300 K (its stability is mostly likely due to the use of S₂ as a reference structure), and CuS.mC24, the experimentally observed stable structure being CuS.hP12.

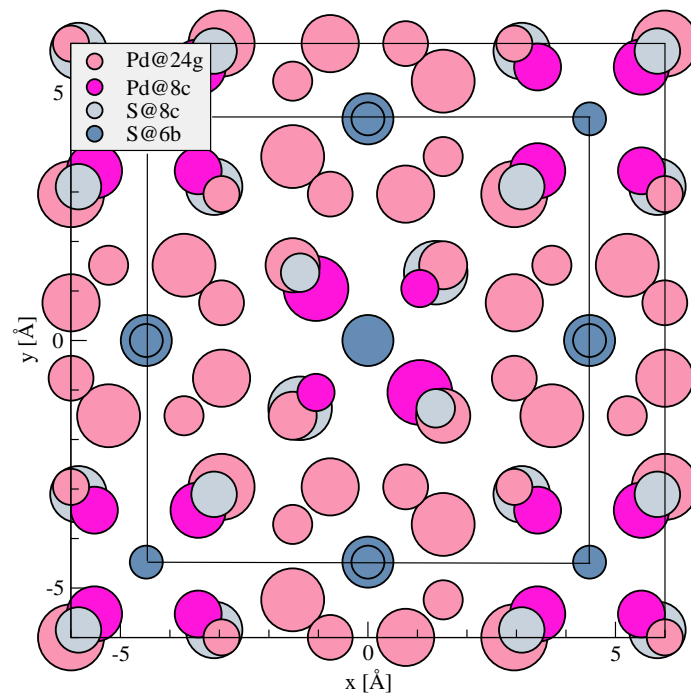
Experimental results [192] show Pd₁₆S₇.cI46 and Pd₄S.tP10 having solubility ranges for copper, which implies the existence of substitutional or interstitial defects. Pd₁₆S₇.cI46 contains four Wyckoff site classes: 8c and 24g sites containing palladium and 8c and 6b sites containing sulfur (see Fig. 6.2). For Pd₄S.tP10 there are only two site classes, an 8g containing palladium and 2a containing sulfur.

6.3 Proposed Ternary Phase Diagrams

Shown in Figure 6.3 is our calculated $T = 0$ K phase diagram for the Cu-Pd-S system (supporting data is in Table 6.2). We find the 8c site class in Pd₁₆S₇ is favorable to copper substitution. At 0 K it is enthalpically favorable to occupy six of the eight possible lattice sites, with a sudden upturn for further filling of the 8c site class. The only other substitutions that are found favorable are S and Cu in β -CuPd,



(a) $P_4S.tP10$



(b) $P_{16}S_7.cI46$

Figure 6.2: Crystal structures for $P_4S.tP10$ and $P_{16}S_7.cI46$. The unit cells are outlined. Atomic sizes indicate vertical height.

Cu in Pd.cF4, and Pd in CuS₂. Substitutions of Cu in the β -CuPd phase have a solubility range from 50% Cu to 55.5% at 0 K. We find the β -CuPd phase is only favorable to Cu substitutions on the Pd sublattice, and not Pd substitutions on the Cu sublattice, which is experimentally supported by observations that the palladium content of β -CuPd never exceeds 50%. As none of the Cu- and Pd- rich structures are in competition with CuS₂.tP12, and the entropic contribution is small, we ignore substitutions in CuS₂.tP12. We also find a small sulfur solubility range in the Cu sublattice of β -CuPd at 0 K, which is supported by experimental phase diagrams at 673 K and 823 K.

While these are the only stable 0 K substitutions, we expect that at higher temperatures, substitutions into other sites that had suitably low enthalpic cost will be stabilized by entropy: PdS.tP16 (2c), Pd₁₆S₇.cI46 (24g), and Pd₄S.tP10 (8e) sites being possible candidates (see Table 6.2). However, we chose to exclude modeling the PdS.tP16 2c substitution range, as due to the small concentration of 2c sites in PdS.tP16, combined with competition with other phases with strong entropic effects, we expect the concentration range to be negligible.

To determine solubility ranges more precisely, we model phases analytically (see Table 6.3), using first principles calculation data to suggest suitable enthalpic models. We choose the models to smooth out small fluctuations in the first principles calculated energies while still keeping the essential trends seen intact. The phases modeled are Pd₄S, Pd₁₆S₇, β -CuPd, and the CuPd-FCC phase. In all cases we use the ideal entropy (Eq. 6.7) for sublattice filling. For Pd₁₆S₇, we use a piecewise linear function (see Fig. 6.6) for the enthalpic part of the free energy, because the enthalpic contribution to the free energy is increasingly favorable up to 6 substitutions ($x=0.13$) on the 8c sublattice, but from six to eight substitutions ($x=0.174$) the favorability is reduced. Previous crystallographic work by Matkovic [209] observed a crystalline phase of Pd₁₆S₇ with 14% Cu concentration, the Cu occupying 8c sites. However this work was performed at 853 K and did not suggest any mechanism by which these

substitutions are stabilized. For Pd_4S , it was necessary to add a quadratic term to the free energy to accurately fit our first principle results. Both CuPd-FCC and β -CuPd were fit using a first-order regular solution model, with CuPd-FCC having the entire lattice available for substitution and β -CuPd having only the Pd sublattice available for substitution by Cu. We also compute a SQS configuration for fcc at 50 Pd% [219] with purely random correlations until the 8th nearest neighbor and find it lies above the convex hull by 40 meV/atom.

Experimental phase diagrams show a sulfur solubility range near $\text{Cu}_{0.5}\text{Pd}_{0.5}$ trending in the palladium-rich direction. We find dilute S substitutions onto the Cu sublattice in β -CuPd, creating a phase trending in the palladium-rich direction, are stable at 0 K. Subsequent substitutions become rapidly unfavorable. From this, we expect limited entropic stabilization of additional substitutions of S in β -CuPd at higher temperatures, leading to a roughly constant solubility range.

To include phonon free energy in solid solution phases, we calculate phonon free energies in the harmonic approximation at well-ordered configurations at select compositions and linearly interpolate between these compositions across the phase region. To model the free energy of gaseous sulfur, we use empirical data taken from the NIST-JANAF tables, as explained later in the paper.

Figures 6.4 and 6.5 compare our calculated phase diagrams with experiment for $T = 673$ K and 823 K, respectively. Our 673 K phase diagram matches the experimental results qualitatively. Note, however, that the " Cu_{2-x}S " region of the experimental phase diagram contains multiple structures, many of which are non-stoichiometric, whereas ours contains only one structure. The phase labeled " Cu_3Pd " (or 1D LPS)

| Base Structure | Site Class | Chemical Specie Change | Enthalpic Cost (meV/atom) | Maximum Impurity Concentration in Site Class |
|---------------------------------------|------------|---------------------------|------------------------------|--|
| β -CuPd | 2a | Pd to Cu | 0 | 12.5 |
| β -CuPd | 2a | Cu to S | 0 | 3.8 |
| β -CuPd | 2a | Pd to S | 0 | 3.8 |
| Pd.cF4 | 4a | Cu to Pd | 0 | 21.9 |
| Pd ₁₆ S ₇ .cI46 | 8c | Pd to Cu | 0 | 12.5 |
| Pd ₁₆ S ₇ .cI46 | 24g | Pd to Cu | 12.9 | 8.33 |
| Pd ₄ S.tP10 | 8e | Pd to Cu | 4.7 | 3.13 |
| CuS ₂ .cP12 | 4a | Cu to Pd | 0 | 6.25 |
| PdS.tP16 | 2c | Pd to Cu | 5.3 | 50.00 |

Table 6.2: A list of substitutions into binary structures to produce ternary structures. Only low enthalpic cost substitutions are shown. Impurity concentration denotes the concentration in the appropriate sublattice, not concentration in the structure as a whole.

| Phase | Substitution Type (Cu Composition Range) | γ | Phonon Concentrations | h_{config} (eV/atom) |
|---------------------------------|---|----------|--------------------------|--|
| Pd ₄ S | Cu@Pd8e (0-0.8) | 8/10 | 0, 0.8, | $-5.350 + 1.612x + 0.225x^2$ |
| Pd ₁₆ S ₇ | Cu@Pd8c (0-0.175) | 8/46 | 0, 0.175 | $-5.237 + 1.445x$ ($x < 6/46$) $-5.251 + 1.554x$ ($x \geq 6/46$) |
| β -CuPd | Cu@Pd2a (0.5 - 1) | 1/2 | 0.5, 1 | $-5.744 + 1.773x$ $+(x - 0.5)(1 - x)(-0.206(x - 0.5) - 1.526(1 - x))$ |
| CuPd-FCC | Cu@Pd4a (0-1) | 1 | 0, 0.50, 0.75, 1 | $-5.477 + 1.469x$ $+x(1 - x)(-0.529x - 0.267(1 - x))$ |

Table 6.3: Description of our phase models. γ denotes the number concentration of the sublattice in the total lattice and is used for scaling the entropic contribution to energy (see equation 6.7). "Phonon concentrations" denotes the concentrations for which phonon free energies were calculated. x denotes the copper composition.

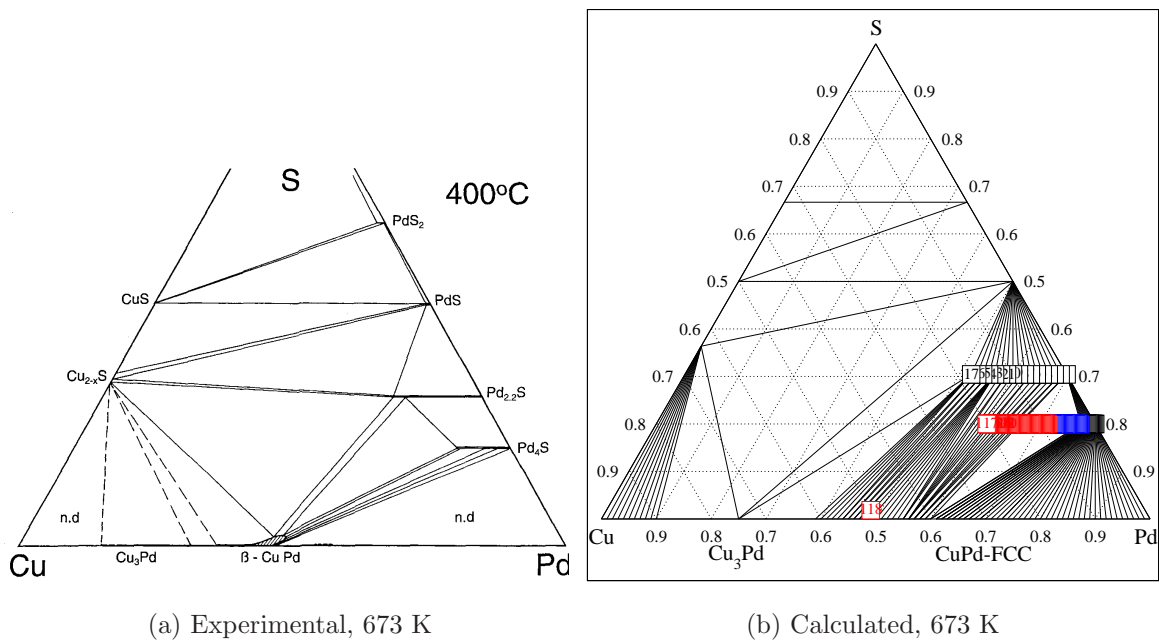


Figure 6.4: The experimental phase diagram for the Cu-Pd-S system at $T = 673$ K, and our calculated phase diagram.

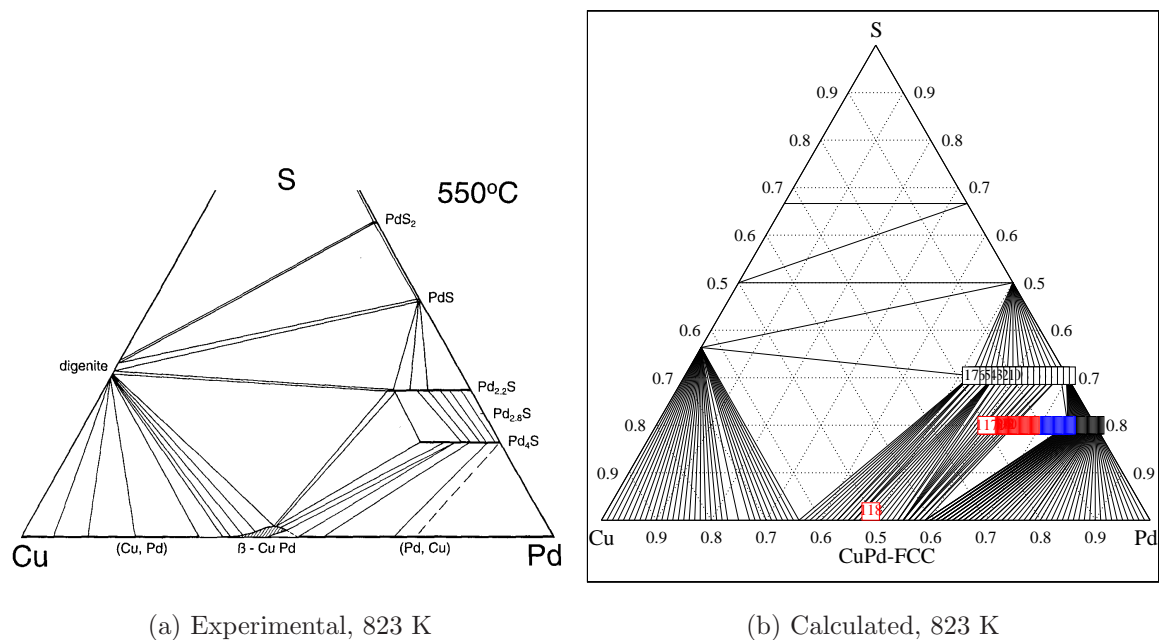


Figure 6.5: The experimental phase diagram for the Cu-Pd-S system at $T = 823$ K, and our calculated phase diagram.

has a slight solubility range experimentally whereas we model it as a well-ordered line compound. Our 823 K diagrams show more disagreement, as there is only one Cu-S structure that is stable and a Pd₃S structure is stabilized at this temperature. More recent phase diagrams have Pd₃S being stabilized at 829 K, however. This is likely due to entropic effects other than configurational and phononic (in the harmonic approximation) that were not included. As can be seen, Pd₃S is part of our collection of calculated structures but is not a stable low-temperature phase. At both temperatures we attempt to model sulfur solubility in the β -CuPd phase but find sulfur solubility to be unstable at temperatures of interest. This is surprising, as our 0 K phase diagram has a sulfur solubility range in β -CuPd similar in shape to what is experimentally observed at higher temperatures, and the enthalpic behavior of our sulfur substitutions supports the observed temperature independence of the sulfur solubility range.

6.4 Two Phases of Interest: Pd₄S and Pd₁₆S₇

The Pd₁₆S₇.cI46 copper solubility range is not appreciably affected by the temperature, as it is dominated by enthalpy rather than entropy. The 24g site is unfavorable for copper substitution. The high multiplicity of the 24g site class gives a large entropic contribution to the free energy at high temperature relative to the 8c site class. However, we find that the enthalpic cost (see Figure 6.6) associated with occupying 24g sites is too high relative to the entropic contributions at the given temperatures and only affects the solubility range by 1% to 2%. Thus the solubility range consists almost completely of 8c sites and is unappreciably affected by temperature. For this reason, our model (Table 6.3) only includes 8c sites and not 24g sites. For Pd₁₆S₇.cI46, at both measured temperatures the experimental copper solubility limit is 20%, and our calculated value is 17.5%, the mismatch likely due to Cu occupation of 24g sites. Our results explain why this solubility range appears to be independent of temper-

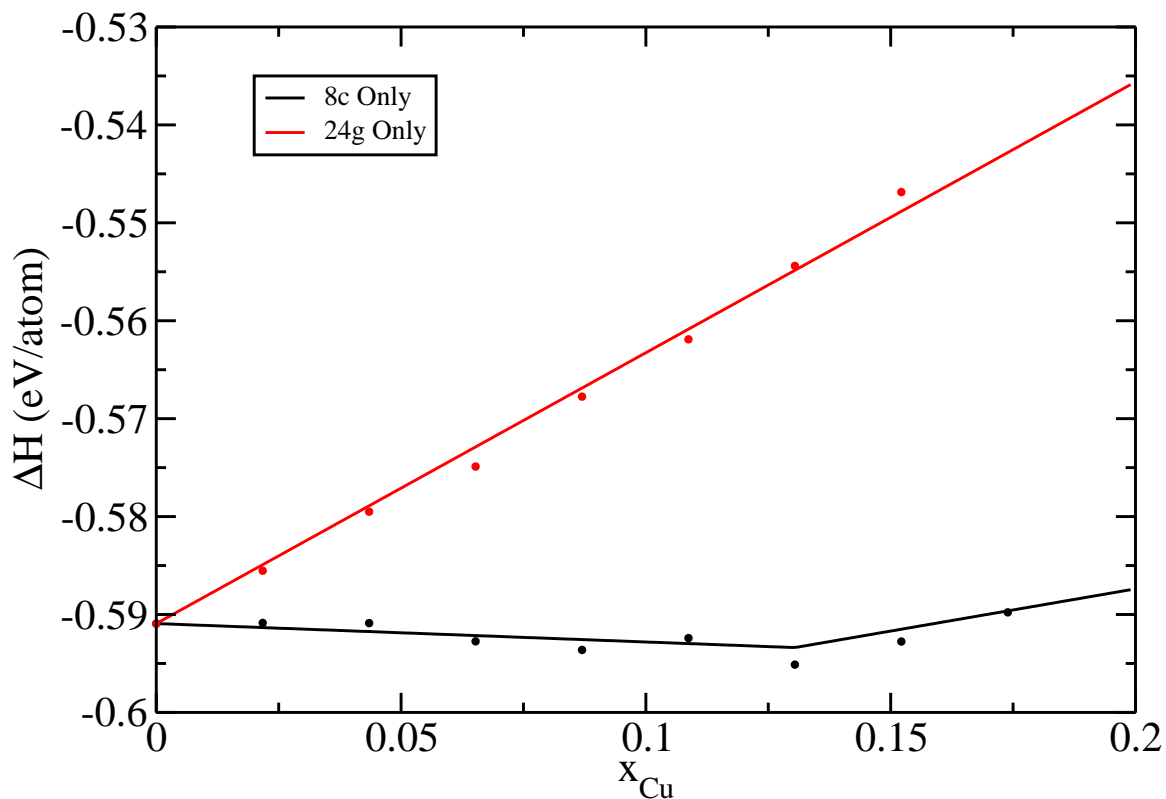


Figure 6.6: Comparison for the enthalpy of formations for filling 8c sites versus filling 24g sites in $\text{Pd}_{16}\text{S}_7.\text{cI46}$.

ature; it is not stabilized due to entropic contributions but due to enthalpy arising from details of the electronic structure (see subsection 6.4.1).

In contrast, Cu substitutions in $\text{Pd}_4\text{S.tP10}$ are not enthalpically favorable at 0 K but are entropically stabilized at higher temperature. As can be seen in the above phase diagrams, the copper solubility for $\text{Pd}_4\text{S.tP10}$ is temperature-dependent in both the calculated and experimental work. While our results agree qualitatively with experimental results, there is still a discrepancy in the copper solubility range. For $\text{Pd}_4\text{S.tP10}$, at 673 K the experimental value is 12.7% and ours is 2.5%, and for 823 K the values are 18.6% and 5% respectively. Solid solution models overestimate the configurational entropy, as including correlations between substitutions will alter the energies of distinct configurations with the same composition and reduce the multi-

plicity. We have thus overestimated the entropy of the Pd_{16}S_7 phase, whose solubility range extends to almost complete filling of the 8c site, relative to the Pd_4S phase, whose filling in the 8e sublattice is sparse. Thus we would expect more accurate free energy models will lead to decreased entropy in the Pd_{16}S_7 phase with comparatively small changes in Pd_4S , increasing the solubility range of Pd_4S . This will not affect the stability of Pd_{16}S_7 as it is primarily enthalpically stabilized.

The large solubility range in the palladium rich side of the CuPd-FCC phase at 0 K is also a factor in the incorrect solubility ranges for $\text{Pd}_4\text{S.tP10}$, as we have found that altering the fitting parameters for the CuPd-FCC phase appreciably affects the solubility range for $\text{Pd}_4\text{S.tP10}$. As we also encountered an issue with sulfur solubility in β -CuPd, with the sulfur solubility range destabilizing relative to CuPd-FCC at temperature below temperatures of interest, and we have a large solubility range on the Pd-rich side at 0 K for the CuPd-FCC phase, it appears that one major source of error is inaccurate modeling of the CuPd-FCC phase. We will return to this issue in the activities portion of this paper.

For our Cu-Pd binary at high temperatures, we find that $\text{Cu}_3\text{Pd.tP28}$ becomes unstable relative to the CuPd-FCC phase at 827 K, and β -CuPd becomes unstable relative to CuPd-FCC and $\text{Cu}_3\text{Pd.tP28}$ at 536 K and a composition of 59.5%, significantly below the experimentally observed temperature of 871 K but close to the experimental composition of 58%. This relative instability of β -CuPd at temperatures of interest is responsible for the observed instability of any sulfur solubility in β -CuPd in our 673 K and 823 K phase diagrams.

But even with these discrepancies, it is clear that we have predicted major details of the Cu-Pd-S ternary phase diagram, specifically the mechanism for stabilization of the solubility ranges of $\text{Pd}_4\text{S.tP10}$ and Pd_{16}S_7 as well as details about the stability of the β -CuPd system, using only first principles calculations with no empirical fitting.

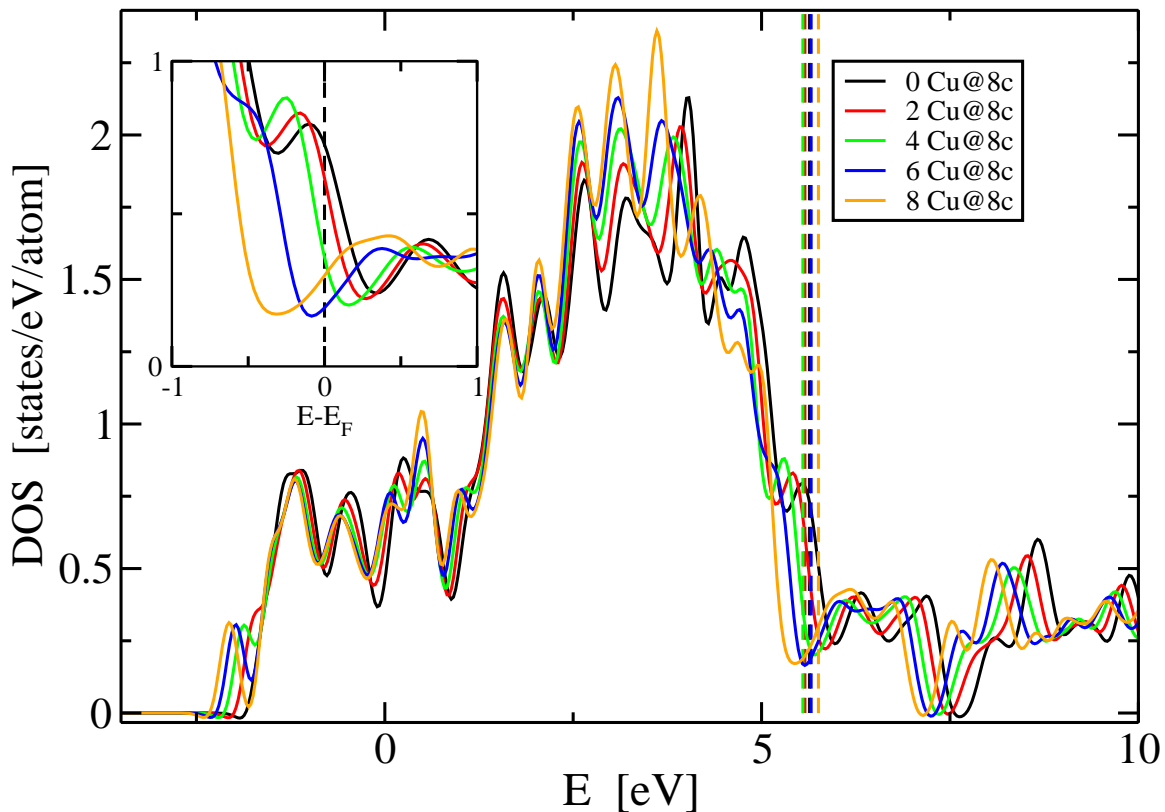


Figure 6.7: Calculated electronic densities of states for $\text{Pd}_{16}\text{S}_7.\text{cI46}$ with copper substitutions at the palladium 8c sites. Dashed lines indicate the Fermi level E_F . The inset shows the DOS relative to E_F and enlarges the pseudogap region.

6.4.1 Electronic Structure

The question remains why the $\text{Pd}_{16}\text{S}_7.\text{cI46}$ 8c site class favors copper in the first six substitutions, but substitution in the final two 8c sites are unfavorable. Consider the constituent binaries: copper binds less strongly with sulfur than palladium, and copper binding with palladium is relatively weak, so we would expect copper substitution into Pd-S binaries to be slightly unfavorable. If it were to turn out to be favored, then we would expect Cu to fully occupy the 8c class. First-principles methods provide electronic structure information that can resolve this issue.

Figure 6.7 shows the electronic densities of states for substitutions in $\text{Pd}_{16}\text{S}_7.\text{cI46}$.

Each colored solid line corresponds to the electronic density of states for a different number of substitutions in the 8c site class of Pd_{16}S_7 .cI46, and the colored dashed lines correspond to the associated Fermi levels. It can be seen that the densities of states follow a rigid band model. Here copper is being substituted for palladium, and copper has one more electron in its valence shell than palladium. Under a rigid band model, performing a substitution adds one electron per unit cell without appreciably changing the valence electronic eigenstates, increasing the Fermi level relative to the fixed band structure.

In all cases, a pseudogap lies near the Fermi level. In the case of no substitutions, the pseudogap lies to the right of the Fermi level. As the number of copper substitutions increases, the increased electron count drive the pseudogap to the left, towards the Fermi level. The inset shows the densities of states relative to the Fermi levels. At six substitutions the Fermi level lies almost directly at the minimum of the pseudogap. This is a well-known stabilization mechanism for alloys [220]. As the number of substitutions increases above six, the Fermi level is driven away from the pseudogap, destabilizing the structure and leading to the sudden increase in the enthalpy of formation (see Fig. 6.6). This pseudogap stabilization mechanism at 0 K, combined with large enthalpic cost of 24g substitutions, explains the temperature independence of the Pd_{16}S_7 solubility range.

6.5 Sulfidization Thresholds and Predominance Diagrams

We now calculate the predominance diagram for the Pd-S₂ system. We work with a fixed quantity of palladium interacting with a reservoir of gaseous S₂, with temperature and pressure being free parameters. For an ideal gas, this implies that we control the chemical potential of the gas, and thus we work in the semi-grand

canonical ensemble,

$$\Sigma(T, p, x) = G(T, p, x) - \mu_{S_2} N_{S_2}, \quad (6.10)$$

where G is the previously defined Gibbs free energy, μ_{S_2} is the chemical potential for the sulfur dimers, and $N_{S_2} = N_S/2$ is the half the number of sulfur atoms in a given phase (as the chemical potential is for sulfur dimers). To determine sulfidization thresholds, we calculate the semi-grand canonical free energy for all phases of interest, Pd.cF4, Pd₄S.tP10, Pd₁₆S₇.cI46, Pd₃S.oC16, and PdS.tP16. The phase with the lowest free energy will be stable. All Pd-containing phases of interest are line compounds, containing only total energy and phonon contributions.

The chemical potential for S₂ complicates the calculation, as it is a gaseous phase. We incorporate empirical results into our method, in a manner consistent with the results obtained from first principles calculations. For the free energy of the gas, we have

$$\mu(T, p) = \mu^0(T) + kT \ln \frac{p}{p_0}. \quad (6.11)$$

Here μ is the chemical potential per molecule, p_0 is a reference pressure (by convention taken to be 1 bar, as will be done here), and μ^0 is the chemical potential per molecule measured at the reference pressure,

$$\mu^0(T) = h - Ts|_{p=1}, \quad (6.12)$$

where H and S are obtained from the NIST-JANAF tables [221]. μ^0 obtained from the JANAF tables has a physically unrealistic infinite value at 0 K due to the presence of $1/T$ terms in both the H and TS contributions. As shown in Figure 6.8, μ^0 is nearly linear for temperatures of interest, so we fit to a linear equation using the 770 K < T < 1430 K region to eliminate the 0 K pole. There is still an issue of constant offsets to energy; the JANAF tabulated values are relative to the enthalpy at 298 K, and whereas all our calculated values are computed at 0 K. In order to incorporate the empirical data into our method, we must shift its zero of energy. In particular, at 0 K, we set the empirical data to match what first principles calculations would

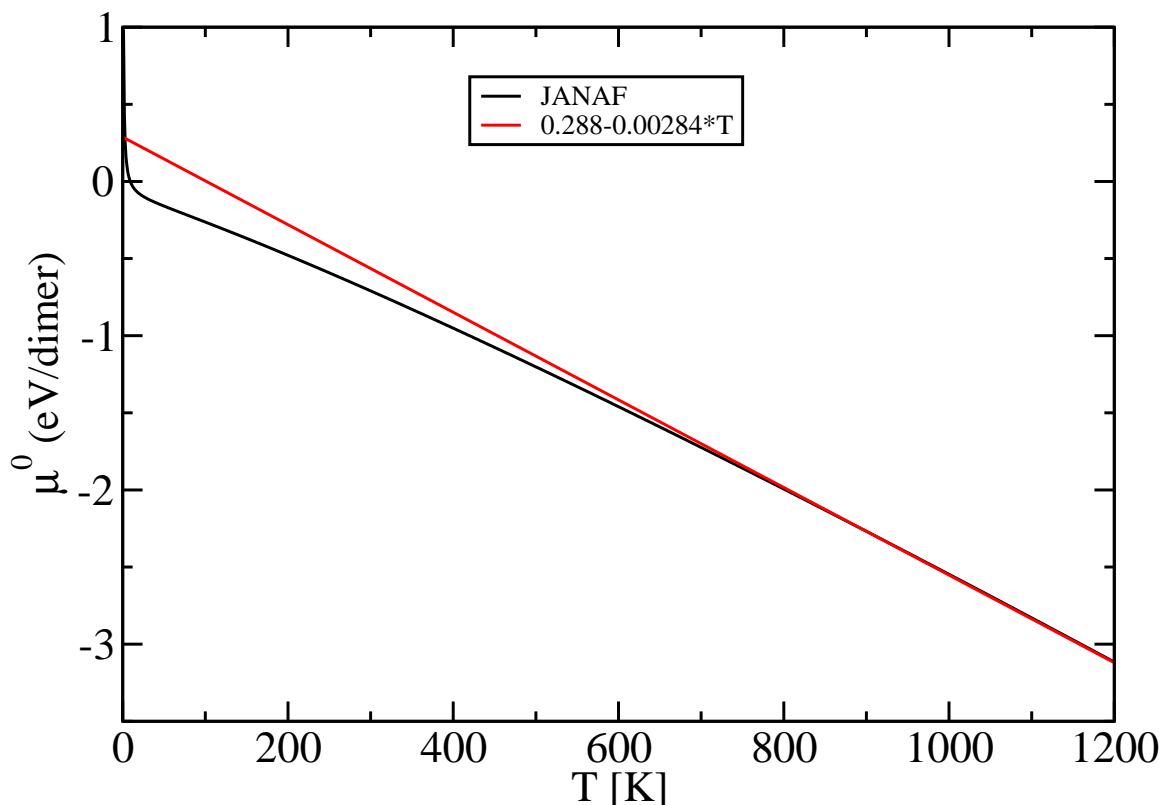


Figure 6.8: The chemical potential of S_2 dimers. Black is NIST-JANAF, and red is our linear fit.

have predicted,

$$g_{S_2} |_{0K} = e_{config} + e_{phonon} |_{0K} . \quad (6.13)$$

As we have measured all energies relative to the tie-plane between pure elements, $e_{config} \equiv 0$, and so the zero-point energy e_{phonon} is the only contribution at 0 K taken from first principles calculations.

Shown in Table 6.4 are our predicted sulfidization thresholds relative to experimental predominance diagrams obtained by Taylor [222]. Predictions with and without phonon free energies are shown. It is necessary to include phonons to obtain reasonable agreement with experimental results, as when phonon free energies are excluded, the relative errors in pressure are as large as four orders of magnitude. When including phonon free energies, in all cases our pressure estimates are within a

| T (K) | Transition | $\log_{10} \sqrt{P}$ Calculated Without Phonons | $\log_{10} \sqrt{P}$ Calculated With Phonons | $\log_{10} \sqrt{P}$ Experimental [222] |
|-------|--|--|---|--|
| 1000 | PdS to Pd ₁₆ S ₇ | -1.1 | -1.8 | -2.2* |
| 1000 | Pd ₁₆ S ₇ to Pd ₄ S | -1.4 | -2.6 | -2.4* |
| 1000 | Pd ₄ S to Pd | -3.3 | -5.3 | -5.2 |
| 800 | PdS to Pd ₁₆ S ₇ | -3.1 | -3.5 | -3.7 |
| 800 | Pd ₁₆ S ₇ to Pd ₄ S | -3.5 | -4.5 | -4.7 |
| 800 | Pd ₄ S to Pd | -5.9 | -7.6 | ** |

Table 6.4: Sulfidization threshold pressures for the Pd-S₂ system. Calculated values with and without phonon contributions are separately shown. Values * are liquid experimentally, but were extrapolated from the solid region of the predominance diagram for comparison purposes. ** not indicated in experimental results.

factor of six of experimental results. It should also be noted that Taylor's phase boundaries are themselves based on fits from experimental enthalpy data. One difficulty is that Taylor has a liquid region in the high-temperature, low pressure region of the predominance diagram, whereas we are only interested in solid phases, so experimental thresholds from the solid regions were extrapolated to liquid regions to give numbers suitable for comparison. This extrapolation is valid as Taylor's thresholds in the solid regions were found to be extremely linear. Another difficulty is that Pd₃S is stable for a small pressure range in between temperatures of 830 K and 920 K, and it would likely be stable for higher temperatures if not for the liquid phase, but our calculations do not predict it stable in this region. This is most likely due to errors in the phonon free energy, which as already shown appreciably affects results.

6.6 Activity Calculations

In this last section, the activities of species in binary Cu-Pd are calculated, as these can be used to predict sulfidization thresholds for Cu-Pd in the presence of S. We wish here to find the activities across the entire composition range with multiple phases.

The definition for the activity of a species A as a function of composition x_A , pressure P, and temperature T is [39]

$$\ln a_A(x_A, P, T) = \frac{\mu_A(x_A, P, T) - \mu_A^0(P, T)}{k_B T},$$

where a_A is the activity for species A, $\mu_A(x_A)$ is the chemical potential for species A, and μ_A^0 is a reference chemical potential for species A. As we are specifying x_A , P, and T, the natural choice of thermodynamic potential is the Gibbs free energy,

$$G = G(N_A, N_B, p, T) = \mu_A N_A + \mu_B N_B,$$

where N_A and N_B are the total number of A and B atoms, respectively, and the thermodynamic derivative giving the chemical potential is

$$\mu_A(N_A, N_B, P, T) = \left. \frac{\partial G}{\partial N_A} \right|_{N_B, P, T}.$$

However, the quantity of importance for phase transitions is the Gibbs free energy per atom,

$$g = g(x_A, P, T) = \frac{G(N_A, N_B, P, T)}{N_A + N_B}.$$

We may express the chemical potential in terms of intensive quantities as

$$\mu_A(x_A, P, T) = g + (1 - x_A) \left. \frac{\partial g}{\partial x_A} \right|_{P, T},$$

where x_i is the composition of species i, and we have chosen to parameterize the free energy by the composition for A. Similarly,

$$\mu_B(x_A, P, T) = g + (1 - x_B) \left. \frac{\partial g}{\partial x_B} \right|_{P, T} = g - x_A \left. \frac{\partial g}{\partial x_A} \right|_{P, T}.$$

These activities depend only on the free energy and the derivative of the free energy at a given composition. They are piecewise analytic functions across the composition range, completely determined by the thermodynamically stable phase at that composition. The activities can therefore be viewed as alternative representation of the underlying phase diagram for the system. They are discontinuous only when the derivative of the free energy changes (the free energy itself must always be continuous, due to the requirement of convexity).

As mentioned before, we believe the magnitude of the calculated free energy of our fcc phase is artificially large, destabilizing the β phase, and thus any calculated activities would be flawed near the 50% Cu region of the phase diagram. To support this assertion, here we refit the fcc phase using only low-solubility first principles data on either side of the composition range. This reduces the magnitude of the free energy of the fcc phase while still using first principles derived calculations. This should not be viewed as abandoning our pure first principles phase diagram as shown before, but rather a correction inspired by known experimental results presented in an alternative-but-equivalent format. The SQS estimate for fcc at 50% Pd lies almost directly on this free energy curve, further supporting its usage for quantitative estimates. We also neglect phonon free energy for activity calculations, as for ordered fcc and bcc at 50% Pd, the difference in phonon free energy per atom is only 2 meV at 1000 K.

Shown below in Figure 6.9 in solid lines are our calculated activities for palladium in the Cu-Pd binary, using the free energy models from Table 6.3, the modified fcc phase, and our calculated data for Cu_3Pd . The β phase is the sharply increasing region in the center of the graph. This sharp behavior is due to the entropic portion of the free energy, which has a logarithmic singularity at $x=0.5$ and sharply varying derivative near this singularity. The smooth curves on the left and right sides of the graph for $T < 1000$ K denote the fcc phase. Linear free energy functions give constant activities as a function of composition, and thus phase coexistence regimes appear as plateaus in activities, at a fixed temperature. Two sets of plateaus are

present. The set of plateaus on the left side are coexistence regimes between the bcc and fcc phases. There are three types of plateaus on the right side. For $T < 900$ K, the plateaus are due to coexistence with the line compound Cu_3Pd , where the plateaus in the region $0.6 < x < 0.8$ indicate coexistence with bcc and the plateaus at $0.8 < x < 0.9$ indicate coexistence with fcc. The plateau on the right side of the plot for 900 K is a special case. Our free energy models predict that the Cu_3Pd phase becomes thermodynamically unstable at 899 K and fcc becomes stable, so the plateau at 900 K indicates coexistence between bcc and fcc. At a temperature of 960 K, our model predicts that the bcc phase becomes unstable relative to the fcc phase, disappearing at a composition of $x = 0.576$. By decreasing the fcc free energy magnitude we have properly stabilized the β phase at temperatures of interest and brought the transition temperature to within 90 K of the expected value. The 1000 K and 1350 K plots are pure fcc throughout the entire composition range.

The activities of Pd at various temperatures were also calculated using CALPHAD (acronym of CALculation of PHase Diagrams) method. The thermodynamic database developed by Li et al [194] was used. Our activities are systematically low compared to the CALPHAD activities (shown in dashed lines on Figure 6.9), most likely due to our ideal entropy approximation. As the true entropy in solid solutions is reduced relative to the ideal entropy, the true free energy will be greater, leading to the true activities being greater than our calculated activities. This is especially true for fcc, where the refitted free energy still overestimates the magnitude of the free energy and leads to qualitatively different behavior in the high Pd limit. CALPHAD results give activities that exceed Raoult's Law in the high Pd limit, which would require positive enthalpies of formation for Cu substitution in Pd using a solid substitution model in the dilute limit. This contradicts first principle calculations which unambiguously predict Cu substitutions in bulk Pd having negative enthalpies of formation (see Figure 6.1). Clearly more precise models are needed to understand the binary in the high Pd limit. However, for the β phase and associated coexistence

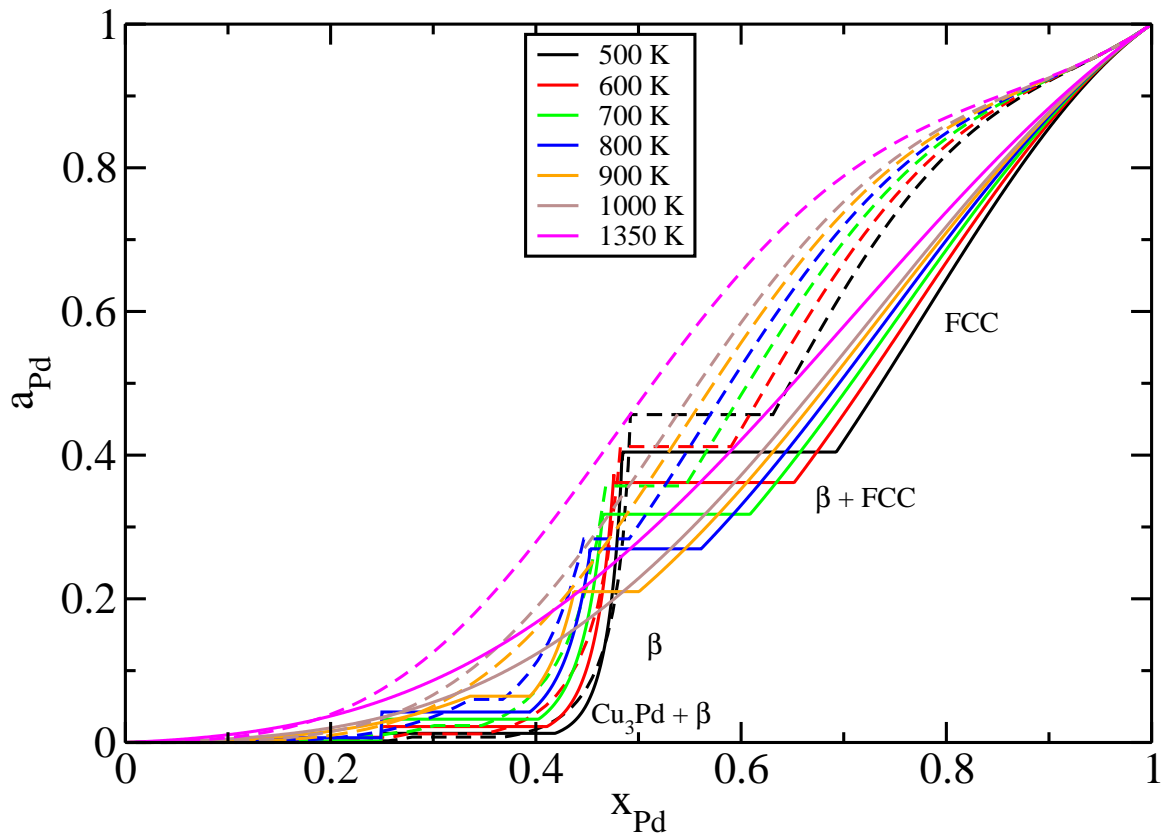


Figure 6.9: Activities of Pd in the Cu-Pd binary. First principles results are denoted with solid lines, and CALPHAD with dashed lines.

regimes, the first principles and CALPHAD results are in close agreement, and if one is interested in regions outside the single-phase fcc region, first principles calculations gives reasonably accurate results even with simple models.

Chapter 7

Summary, Difficulties, And Future Outlook

7.1 The Structure of Boron Carbide

We believe we have resolved the underlying physics of the observed “boron carbide” phase in the high carbon limit. The arguments over the nature of the experimentally observed phase are (partially) resolved once one realizes that there are multiple phases of boron carbide that need to be considered. Our enumeration of the partition function predicts the existence of two distinct boron carbide phases with differing symmetries at low temperatures. One has stoichiometry $B_{13}C_2$ at 0 K and rhombohedral symmetry. The other has precise stoichiometry B_4C at low temperatures and monoclinic symmetry. At high temperatures the monoclinic phase undergoes an orientational disordering transition and becomes thermodynamically indistinct from the rhombohedral phase. We also proposed a simple free energy model for boron carbide, where the rhombohedral phase has a temperature dependent solubility range, and the monoclinic phase has a line compound of exact stoichiometry 20% C. Despite its favorable low enthalpy, this phase is predicted to be stable only below 600 K, a temperature so low that it might not be possible to form experimentally in thermo-

dynamic equilibrium. Various limiting behaviors of the model phase boundaries were derived analytically, including the key fact that $x'_{Carbon} < 0.200$ in the rhombohedral phase. A quantitative discrepancy in the boron-rich limit reveals the need for further enhancement of our model.

Previous investigators have noticed that density functional theory predicted two T=0 K structures for the system, however they were quick to dismiss this result as being a “fluke of DFT”, as only one phase is observed experimentally, proceeding to declare one or the other as the true “boron carbide” phase. Not only have we shown that these two phases are equally physically valid, but we have also shown how density functional theory subsequently predicts that only one phase should appear in the regions of the phase diagram that have been experimentally examined. The controversial “B₄C” phase undergoes an order-disorder transition into the rhombohedral phase at 20% C and is subsequently destabilized at that composition by coexistence with the graphite phases at temperatures below what is seen by the phase diagram. In fact, here we have not buried the experimentally assessed phase diagram but praised it; our results only *strengthen* the claim that the experimentally assessed phase diagram is correct on the high carbon limit. We were able to do this in two different ways, each time reaching a critical temperature of ≈ 600 K, only strengthening our argument.

However, this is a description of the high carbon side of the phase. A reasonable start, given that this is the location of the B₄C/monoclinic phase that has caused issues in the literature. There is still the boron-rich side of the phase diagram, however. Experimentally a plethora of defects are claimed on this side of the phase diagram, however, no two groups agree on what these defects are, and all their claims are based on relatively shaky grounds (such as fitting results to one particular set of experimental observations, such as infrared or Raman modes, and ignoring all other experimental observation). Our own results predicted that only a few defects (B-B-C and C-V-C) have energy costs that are even plausible for entropic stabilization, but

they are still too high in energy cost to yield the currently assessed phase diagram. It is possible that a detailed analysis of the vibrational contribution to free energy [223] is needed, that there are defects spanning multiple cells with more favorable energy cost responsible for the stability, or that here we must bury the phase diagram and claim lack of equilibration. We also note that the predicted phase transition between the rhombohedral and monoclinic phases remains to be seen. The best hope of finding evidence for this transition will be the observation of residual polar carbon-polar carbon correlations, which may be possible computationally using the hybrid MC/MD method we used for our high-entropy alloy project.

7.1.1 A New Phase?

As was alluded to in the introductory section of the boron carbide chapter, we currently believe that the work presented in that chapter is slightly out-of-date and that there are at least three different phases in the boron carbide system. Because this work is still very much in flux, and because a significant portion of this work was done by a new graduate student in our group (Sanxi Yao), I have chosen not to include it in the main body of my thesis. Nevertheless, we are reasonably certain that it exists, and a brief discussion of it is warranted.

The possibility of this new phase became apparent when we began to question the order of the phase transition we were proposing. Our previous models state that upon undergoing a phase transition, the monoclinic phase gains a six-fold $\bar{3}$ symmetry to become the rhombohedral phase. However, the $\bar{3}$ symmetry is in fact a compound symmetry of inversion and 3-fold rotation. While it is certain possible for a system to gain multiple symmetries while undergoing a phase transition¹, it is rather unusual for multiple symmetries to be gained at once when undergoing a solid-solid phase transition, as gaining a symmetry has a particular energy cost, and we expect a phase

¹The obvious example being the solid-liquid transition, where an infinite number of symmetries are gained.

transition associated to this energy cost being overcoming by entropic gain. If one grinds the group theoretic machinery on the two space groups, $R\bar{3}m$ for rhombohedral and Cm for monoclinic, one sees that there are in fact two possible intermediate phase transitions, one in which inversion symmetry is gained, and one in which 3-fold symmetry is gained. Gaining inversion symmetry corresponds to a second-order phase transition (i.e. a third order term in the expansion of the free energy is forbidden by symmetry), but a first-order phase transition is expected when gaining the 3-fold symmetry (a third order term is not excluded by symmetry). If our predicted phase transition did occur, and both symmetries were gained simultaneously, the presence of an invariant corresponding to the gain of 3-fold symmetry would induce a third-order term, and thus the phase transition would be expected to be first-order.

We realized it was possible that our partition function approach failed to detect the intermediate phase, as our supercell sizes were too small. To detect this intermediate phase, we needed an efficient way to calculate reasonably accurate energies, and so we fit DFT-calculated energies for structures at 20% C for two different potentials, a simple Yukawa-like potential and a more detailed bond-fitting model. We then performed Metropolis Monte Carlo at select temperatures combined with a Ferrenberg-Swendsen multiple histograms approach to fill in the intervening temperatures. We discovered that there is an intermediate “polarized” phase between the well-ordered monoclinic phase and disordered rhombohedral phase. This polarized phase places all polar carbons on one “pole” of the icosahedron, i.e. all polar sites that are related by three fold-rotation about the (111) axis, breaking inversion symmetry, while disordering within the pole preserves the three-fold symmetry. Its formation is primary driven by a strong energetic preference to avoid placing carbons in close proximity on adjacent polar sites of neighboring icosahedra.

The finite-size scaling of specific heat peaks suggest that the monoclinic-to-polarized phase transition is first-order and the polarized-to-rhombohedral phase transition belongs to the 3D Ising universality class (and thus is second-order), as expected from

group theoretic arguments. The peak in the specific heat from our partition function approach that we identified as belonging to the monoclinic-to-rhombohedral phase transition is actually the peak in specific heat associated with the monoclinic-to-polarized phase transition, as this phase transition occurs at near 720 K for the bond fitting model and grows more rapidly. The polarized-to-rhombohedral phase transition occurs nears 790 K and grows very slowly, only appreciable for cell sizes larger than 6x6x6. That these phase transitions occurs at similar temperatures and that the polarized-to-rhombohedral phase transition peak grows quite slowly explains why our partition function approach was unable to detect this peak and instead combined them into one feature. Our free energy models will need to be altered to incorporate this new phase; however, we expect many of the major features will be preserved. On the high carbon side, we will still see an essentially flat phase boundary above 790 K, as here the polarized phase has been destabilized into the rhombohedral phase. The essential shape of the low carbon side will be preserved as it is primarily driven by the energy associated with chain boron defects.

7.2 The Stability of the High-Entropy Alloys Mo-Nb-Ta-W

The distinguishing feature of high-entropy alloys is their increased stability due to enhancement of the entropy. In Mo-Nb-Ta-W, we have shown how this effect may be directly observed using first principles calculations. We have shown how this may be done in two different ways: by performing hybrid MC/MD sampling of phase space and observing the emergence of correlations, and by fitting low temperature structures to a pairwise model and using a mean field model and Monte Carlo simulations. The observed temperature of a possible order/disorder A2 to B2 transition from the Monte Carlo simulations, 1280 K, is 1470 K less than the melting temperature of Nb, the lowest melting point of the four species, and 1880 K less than the rule-of-mixtures es-

timate for the melting temperatures. We also propose a physical mechanism by which the high-entropy alloy is destabilized, favorable binding between Mo and Ta. It is unlikely that such a mechanism could have ever been reliably observed experimentally due to the high melting temperature of the constituent species.

That being said, there are still lower temperatures to be considered. The B2 phase cannot be the 0 K thermodynamically stable phase due to residual entropy imposed by sublattice disorder of Mo-W and Nb-Ta. In fact, technically we have not shown that the A2 to B2 phase transition does occur, as there are other well-ordered structures that are in competition with the A2 and B2 phases and could be stabilized before B2. However, it is extremely unlikely that these structures are stabilized before the B2 phase, as we have clear evidence using the MC/MD correlations, the pairwise fitting, and the mean field model and Monte Carlo simulations that the onset of ordering is driven by relatively strong Mo-Ta bonding which favors cP2-like ordering (noting that oA12 is a weak distortion of cP2 both energetically and structurally). In terms of free energies, the B2 phase is the best of both worlds at these temperatures, as it has both the strong Mo-Ta bonding and the residual sublattice entropy. Still, eventually this phase must become unstable due to the Third Law, and the energetic portion of the free energy will dominate. While we have proposed the 0 K convex hulls for the binaries as well as possible competing phase for Mo-Nb-Ta-W, we do not yet have any notion precisely *when* these structures are stabilized. Currently MC/MD runs in an NPT ensemble are underway to look for thermodynamic signatures of these low temperature phase transitions using thermodynamic integration coupled with a multiple histograms method. Though we may be able to surmise when additional structures are stabilized, and perhaps some correlations suggesting possible stabilized structures, it is unlikely that we will be able to definitively prove which structures are stabilized, as computational cells suitable for density functional theory calculations will generally be too small to support phase segregation.

7.3 Elasticity of Transition Metal Alloys

The hunt for strong materials with good elastic properties is a difficult one, and we have only scratched the surface². In this chapter we examined the elasticity of various early-late transition metal alloys using first principles calculations and comparison with various averaging schemes. Calculated bulk moduli were reasonably close to CPA estimates using pure elemental species, but CPA predictions were systematically low. This deviation correlates strongly with change in volume per atom. As CPA contains no structural information, we surmise that bulk moduli is controlled almost completely by the strength of chemical bonding in transition metal alloys. Larger and less regular deviations were observed for shear moduli, suggesting structural distortion being responsible for the deviation, though there is still a moderate correlation with the change in volume per atom. Select ternary and quaternary structures were examined and confirmed these trends. To highlight the dependence of chemical bonding on elastic moduli, force constants and electronic densities of state were calculated, and it was found early transition metals are responsible for the strongest bonding, which agrees with observed trends in the bulk moduli. We find that Ni-W alloys have the largest Poisson ratios among the compositions studied and hence hold promise as the basis for design of ductile metallic glasses.

The list of things still left to examine are legion. The scheme we used for estimation, CPA, is at its heart an averaging scheme. A relatively sophisticated averaging scheme, far more mathematically rigorous than the usual ad hoc arithmetic sum found in the materials literature, but an averaging scheme nevertheless. However, it is already known that not all amorphous metals follow an averaging law for their elastic moduli. In particular, it has been observed [224] that introducing a trace amount of Al ($< 5\%$) into a $\text{Cu}_{50}\text{Zr}_{50}$ *increases* K by up to 12% while negligibly affecting G , despite Al's *lower* elastic moduli compared to Cu and Zr. Such a trend is likely due to changes in the nature of chemical bonding upon alloying, which an averaging

²Pun unintended.

scheme will not include.

But we do not need to go to these exceptions to find evidence of averaging schemes failing. Our shear moduli are a prime example of the CPA averaging scheme failing. This is actually a blessing in disguise, as the Poisson's ratio in the relevant parameter ranges are strongly affected by the shear modulus, and finding abnormally low shear moduli compared to bulk moduli (while still large in absolute terms) is the key to finding simultaneously large Poisson's ratios *and* elastic moduli. Though we have surmised that this is partially due to the shear moduli having a reliance on structural effects, our prime example being the size mismatches in the disordered hR13 samples, we are still only at the beginning of understanding the chemical origins of the shear modulus.

Having examined the elastic moduli for crystalline alloys, the next step is to calculate the elastic moduli of BMGs, which we have done for select ETM-LTM BMGs. Preliminary results suggest that bulk moduli of ETM-LTM glasses computed using first principles calculations do agree with the estimates given by CPA (and correspondingly the crystalline alloys). However, we found that all our calculated first principles shear moduli for ETM-LTM BMGs deviate by roughly a factor of two from CPA and experimental results³. There is the possibility that our results regarding the shear moduli for crystalline alloys holds here as well, and local structural effects are responsible. Indeed, we did see a greater deviation amongst the shear moduli in ETM-LTM bulk metallic glasses for various samples at identical stoichiometries than the bulk moduli, which were essentially constant. However, this deviation was on the order of $\pm 10\%$, too small to explain the observed effect. It is also possible that our density functionals are incorrectly predicting the structural motifs. This explanation is also not entirely satisfying as we do see a predominance in the icosahedral ordering expected for bulk metallic glasses, and this effect persists across multiple families. The more likely explanation is that the shear modulus is being enhanced by

³This factor of two is not the conversion factor between physical to "engineering" strain.

microstructural effects, the capture of which would require computational cells too large for current density functional theory methods. This is probable as our computational cells contain 100 atoms, whereas individual STZs size estimates can vary from 20-200 atoms [225]. Whether or not this is relevant to the observed mismatch of the shear moduli remains to be seen, but it is clear that more work needs to be done into the roots of this discrepancy.

7.4 Bulk Sulfidization of the Cu-Pd System

Our work was able to semi-quantitatively predict the behavior of four distinct phases on the phase diagram (β -CuPd, Pd₁₆S₇, Pd₄S, and to a lesser degree fcc-CuPd), without any fitting parameters, achieving first principles estimates for the temperature-dependent phase diagram over a range of 1000 K. This was possible using only simple solid solution models. The results most directly related to the process of sulfidization, the predominance diagram of the Pd-S₂ system, in particular show excellent agreement with experimental results once vibrational contributions were considered. Our results brings context to the existing experimental results. As an example, the experimental report of the copper solubility range of Pd₁₆S₇ has no explanation *why* this is the case, only that it is. We were able to show not only is this an energetic effect, but that it is driven by pseudogap stabilization, without any fitting parameters. Our work reveals the essential physics underlying the phase behavior.

Less impressive were our activities calculations for Cu-Pd, which shows deviation from CALPHAD, particularly ugly in the Pd-rich side above 800 K. This is a real physical effect and cannot be explained away by going to a more detailed free energy model or sampling more configurations. CALPHAD has a positive deviation from Raoult's law on the Pd-rich side. This implies that Cu substitutions in Pd should be energetically unfavorable in the low-solubility limit and are stabilized by entropic contributions. Our first principles unambiguously show that these substitutions are

energetically favorable, which will yield a negative deviation from Raoult's law for all choices of free energy model. Fortunately for us, the high Pd limit is of less interest due to Pd's high cost, and our activities in the more relevant region near β -CuPd are in semi-quantitative agreement with CALPHAD, with the exception of the location of the Pd-rich side of the β /fcc coexistence phase, again due to inaccurate modeling of the fcc phase.

Bibliography

- [1] J. D. Bernal. The Bakerian Lecture, 1962. The structure of liquids. *Proc. R. Soc. Lond. A*, 280:299–322, 1964.
- [2] David R. Nelson. Order, frustration, and defects in liquids and glasses. *Phys. Rev. B*, 28:5515–5535, Nov 1983.
- [3] H. W. Sheng, W. K. Luo, F. M. Alamgir, J. M. Bai, and E. Ma. Atomic packing and short-to-medium-range order in metallic glasses. *Nature*, 439:419–25, 2006.
- [4] D. Topa, E. Makovicky, and T. Balić-Žunić. The crystal structures of jauéite, $\text{Cu}_2\text{Pd}_3\text{Se}_4$, and chrisstanleyite, $\text{Ag}_2\text{Pd}_3\text{Se}_4$. *Can. Mineral.*, 44(2):497–505, April 2006.
- [5] H. Okamoto. B-C (boron-carbon). *J. Phase. Equilibria*, 13:436, 1992.
- [6] C. Jiang, C. Wolverton, J. Sofo, L.-Q. Chen, and Z.-K. Liu. First-principles study of binary bcc alloys using special quasirandom structures. *Phys. Rev. B*, 69:214202, 2004.
- [7] J. D. Honeycutt and H. C. Andersen. Molecular dynamics study of melting and freezing of small Lennard-Jones clusters. *J. Phys. Chem.*, 91:4950–63, 1987.
- [8] P. Ganesh and M. Widom. Ab initio simulations of geometrical frustration in supercooled liquid Fe and Fe-based metallic glass. *Phys. Rev. B*, 77:014205, 2008.

- [9] H. Okamoto and T. B. Massalski. Thermodynamically improbable phase diagrams. *J. Phase Equilib*, 12(2):148–168, 1991.
- [10] R. G. Parr and W. Yang. *Density-Functional Theory of Atoms and Molecules*. Oxford University Press, Inc., 1989.
- [11] R. O. Jones and O. Gunnarsson. The density functional formalism, its applications and prospects. *Rev. Mod. Phys.*, 61(3):689–746, July 1989.
- [12] W. Kohn. Nobel Lecture: Electronic structure of matter - wave functions and density functionals. *Rev. Mod. Phys.*, 71(5):1253–1266, October 1999.
- [13] D. S. Sholl and J. A. Steckel. *Density Functional Theory: A Practical Introduction*. John Wiley & Sons, Inc., 2009.
- [14] R. M. Martin. *Electronic Structure: Basic Theory and Practical Methods*. Cambridge University Press, 2004.
- [15] N. W. Ashcroft and N. D. Mermin. *Solid State Physics*. Harcourt College Publishers, 1976.
- [16] C. Kittel. *Introduction to Solid State Physics*. John Wiley & Sons, Inc., 7th edition, 1996.
- [17] P. Hohenburg and W. Kohn. Inhomogeneous electron gas. *Phys. Rev.*, 136(3B):864–871, November 1964.
- [18] M. Levy. Universal variational functionals of electron densities, first-order density matrices, and natural spin-orbitals and solution of the v-representability problem. *Proc. Natl. Acad. Sci. USA*, 76(12):6062–6065, December 1979.
- [19] M. Levy. Electron densities in search of Hamiltonians. *Phys. Rev. A*, 26(3):1200–1208, September 1982.

- [20] W. Kohn and L. J. Sham. Self-consistent equations including exchange and correlation effects. *Phys. Rev.*, 140(4A):1133–1138, November 1965.
- [21] R. Feynman. *Statistical Mechanics: A Series of Lectures*. W. A. Benjamin, Inc., 1972.
- [22] J. Harris. Adiabatic-connection approach to Kohn-Sham theory. *Phys. Rev. A*, 29(4):1648–1659, April 1984.
- [23] S. Kurth, J. P. Perdew, and P. Blaha. Molecular and solid-state tests of density functional approximations: LSD, GGAs, and meta-GGAs. *Int. J. Quantum Chem.*, 75(4):889–909, 1999.
- [24] J. P. Perdew and Y. Wang. Accurate and simple analytic representation of the electron-gas correlation energy. *Phys. Rev. B*, 45(23):13244–13249, June 1992.
- [25] J. P. Perdew, K. Burke, and M. Ernzerhof. Generalized Gradient Approximation made simple. *Phys. Rev. Lett.*, 77(18):3865–3868, October 1996.
- [26] A. D. Becke. A new mixing of Hartree-Fock and local density-functional theories. *J. Chem. Phys.*, 98(2):1372–1377, January 1993.
- [27] P. E. Blöchl. Projector augmented-wave method. *Phys. Rev. B*, 50(24):17953–17979, December 1994.
- [28] G. Kresse and D. Joubert. From ultrasoft pseudopotentials to the projector augmented-wave method. *Phys. Rev. B*, 59:1758–75, 1999.
- [29] R. Car and M. Parrinello. Unified approach for molecular dynamics and density-functional theory. *Phys. Rev. Lett.*, 55(22):2471–2474, November 1985.
- [30] S. A. Adelman and J. D. Doll. Generalized Langevin equation approach for atom/solid surface scattering: General formulation for classical scattering off harmonic solids. *J. Chem. Phys.*, 64(6):2375–2388, March 1976.

- [31] S. Nose. A unified formulation of the constant temperature molecular dynamics methods. *J. Chem. Phys.*, 81(1):511–519, July 1984.
- [32] W. G. Hoover. Canonical dynamics: Equilibrium phase-space distributions. *Phys. Rev. A*, 31(3):1695–1697, March 1985.
- [33] M. Parrinello and A. Rahman. Polymorphic transitions in single crystals: A new molecular dynamics methods. *J. Appl. Phys.*, 52(12):7182–7190, December 1981.
- [34] C. Kittel and H. Kroemer. *Thermal Physics*. W. H. Freeman and Company, 2nd edition, 1980.
- [35] L. D. Landau and E. M. Lifshitz. *Statistical Physics, Part 1*. Pergamon Press Ltd., 3rd edition, 1980.
- [36] D. L. Goodstein. *States of Matter*. Dover Publications, 1985.
- [37] K. Huang. *Statistical Mechanics*. John Wiley & Sons, Inc., 2nd edition, 1987.
- [38] R. K. Pathria. *Statistical Mechanics*. Butterworth-Heinemann, 2nd edition, 1996.
- [39] R. deHoff. *Thermodynamics in Materials Science*. CRC Press, 2nd edition, 2006.
- [40] H. B. Callen. *Thermodynamics and an Introduction to Thermostatistics*. John Wiley & Sons, Inc., 2nd edition, 1985.
- [41] L. Pauling. The structure and entropy of ice and of other crystals with some randomness of atomic arrangement. *J. Am. Chem. Soc.*, 57:2680–2684, December 1935.
- [42] V. F. Petrenko and R. W. Whitworth. *Physics of Ice*. Oxford University Press, 1999.

- [43] H. E. Stanley. *Introduction to Phase Transitions and Critical Phenomena*. Oxford University Press, 1971.
- [44] N. Goldenfeld. *Lectures on Phase Transitions and the Renormalization Group*. Perseus Books Publishing, L.L.C., 1992.
- [45] P. M. Chaikin and T. C. Lubensky. *Principles of Condensed Matter Physics*. Cambridge University Press, 1995.
- [46] W. D. McComb. *Renormalization Methods: A Guide for Beginners*. Clarendon Press, 2004.
- [47] D. P. Landau and K. Binder. *A Guide to Monte Carlo Simulations in Statistical Physics*. Cambridge University Press, 3rd edition, 2009.
- [48] L. D. Landau. *The Collected Papers of L. D. Landau*, chapter On the theory of phase transitions. Pergamon, 1965.
- [49] M. El-Batanouny and F. Wooten. *Symmetry and Condensed Matter Physics: A Computational Approach*. Cambridge University Press, 2008.
- [50] A. Zunger, S.-H. Wei, G. Ferreira, and J. E. Bernard. Special quasirandom structures. *Phys. Rev. Lett.*, 65(3):353–356, July 1990.
- [51] A. Pelissetto and E. Vicari. Critical phenomena and renormalization-group theory. *Phys. Reports*, 368:549–727, 2002.
- [52] N. M. Metropolis, A. W. Rosenbluth, M. N. Rosenbluth, A. H. Teller, and E. Teller. Equation of state calculations by fast computing machines. *J. Chem. Phys.*, 21(6):1087–1092, June 1953.
- [53] A. M. Ferrenberg and R. H. Swendsen. New Monte Carlo technique for studying phase transitions. *Phys. Rev. Lett.*, 61(23):2635–2638, December 1988.

- [54] A. M. Ferrenberg and R. H. Swendsen. Optimized Monte Carlo data analysis. *Phys. Rev. Lett.*, 63(12):1195–1198, September 1989.
- [55] F. Wang and D. P. Landau. Efficient, multiple-range random walk algorithm to calculate the density of states. *Phys. Rev. Lett.*, 86(10):2050–2053, March 2001.
- [56] M. Widom and W. P. Huhn. Prediction of orientational phase transition in boron carbide. *Solid State Sciences*, 14(11-12):1648–1652, November 2012.
- [57] W. P. Huhn and M. Widom. A free energy model of boron carbide. *J. Stat. Phys.*, 150(3):432–441, February 2013.
- [58] R. R. Rigdway. Boron carbide. A new crystalline abrasive and wear-resisting product. *Trans. Am. Electrochem. Soc.*, 66:117–133, 1934.
- [59] F. Thévenot. Boron carbide - a comprehensive review. *J. Eur. Ceram. Soc.*, 6:205–225, 1990.
- [60] K. A. Schwetz and P. Karduck. Investigations in the boron-carbon system with the aid of electron probe microanalysis. *J. Less-Common Met.*, 175(1):1–11, September 1991.
- [61] H. K. Clark and J. L. Hoard. The crystal structure of boron carbide. *J. Am. Chem. Soc.*, 65:2115–2119, 1943.
- [62] G. S. Zhdanov and N. G. Sevastyanov. *Compt. Rend. Acad. Sci. URSS*, 32:432, 1941.
- [63] W. H. Eberhardt, B. Crawford Jr., and W. N. Lipscomb. The valence structure of the boron hydrides. *J. Chem. Phys.*, 22(6):989–1001, June 1954.
- [64] H. C. Longuet-Higgins and M. de V. Roberts. The electronic structure of an icosahedron of boron atoms. *Proc. R. Soc. Lond. A*, 230:110–119, 1955.

- [65] M. Widom and M. Mihalkovič. Symmetry-broken crystal structure of elemental boron at low temperature. *Phys. Rev. B*, 77(6):064113, February 2008.
- [66] B. Albert and H. Hillebrecht. Boron: Elementary challenge for experimenters and theoreticians. *Angew. Chem. Int. Ed.*, 48:8640–8668, 2009.
- [67] T. Ogitsu, E. Schwegler, and G. Galli. β -rhombohedral boron: At the crossroads of the chemistry of boron and the physics of frustration. *Chem. Rev.*, 113:3425–3449, March 2013.
- [68] H. L. Yakel. The crystal structure of a boron-rich boron carbide. *Acta Cryst.*, 31:1797–806, 1975.
- [69] V. F. Sears. Neutron scattering lengths and cross sections. *Neutron News*, 3(3):26–37, 1992.
- [70] G. Will and K. H. Kossobutzki. An x-ray structure analysis of boron carbide, $B_{13}C_2$. *J. Less-Common Met.*, 44:87–97, 1976.
- [71] G. H. Kwei and B. Morosin. Structures of the boron-rich boron carbides from neutron powder diffraction: implications for the nature of the inter-icosahedral chains. *J. Phys. Chem.*, 100:8031–9, 1996.
- [72] V. I. Matkovich. Interstitial compounds of boron. *J. Am. Chem. Soc.*, 83(8):1804–1806, April 1961.
- [73] A. H. Silver and P. J. Bray. Nuclear magnetic resonance study of boron carbide. *J. Chem. Phys.*, 31(1):247–253, July 1959.
- [74] D. Emin. Structure and single-phase regime of boron carbides. *Phys. Rev. B*, 38(9):6041–6055, September 1988.
- [75] J. P. Abriata and D. E. Laughlin. The third law of thermodynamics and low temperature phase stability. *Prog. Mater. Sci.*, 49:367–87, 2004.

- [76] G. Will, A. Kirfel, A. Gupta, and E. Amberger. Electron density and bonding in $B_{13}C_2$. *J. Less-Common Met.*, 67(1):19–29, September 1979.
- [77] R. Schmechel and H. Werheit. Structural defects of some icosahedral boron-rich solids and their correlation with the electronic properties. *J. Solid State Chem.*, 154:61–67, 2000.
- [78] D. M. Bylander and L. Kleinman. Structure of $B_{13}C_2$. *Phys. Rev. B*, 43(2):1487–1491, January 1991.
- [79] F. Mauri, N. Vast, and C. J. Pickard. Atomic structure of icosahedral B_4C boron carbide from a first principles analysis of nmr spectra. *Phys. Rev. Lett.*, 87:085506, 2001.
- [80] J. Saal, S. Shang, and Z. K. Liu. The structural evolution of boron carbide via ab initio calculations. *Appl. Phys. Lett.*, 91:231915, 2007.
- [81] N. Vast, J. Sjakaste, and E. Betranhandy. Boron carbide from first principles. *J. Phys., Conf. Ser.*, 176:012002, 2009.
- [82] G. Kresse and J. Hafner. Ab initio molecular dynamics for liquid metals. *Phys. Rev. B*, 47(1):558–561, 1993.
- [83] G. Kresse and J. Furthmüller. Efficient iterative schemes for ab initio total-energy calculations using a plane-wave basis set. *Phys. Rev. B*, 54(16):11169–11186, October 1996.
- [84] H. J. Monkhorst and J. D. Pack. Special points for Brillouin-zone integrations. *Phys. Rev. B*, 13(12):5188–5192, June 1976.
- [85] R. Raucoules, N. Vast, E. Betranhandy, and J. Sjakste. Mechanical properties of icosahedral boron carbide explained from first principles. *Phys. Rev. B*, 84(1):014112, July 2011.

- [86] B. Morosin, G. H. Kwei, A. C. Lawson, T. L. Aselage, and D. Emin. Neutron powder diffraction refinement of boron carbides. Nature of icosahedral chains. *J. Alloys Compd.*, 226:121–5, 1995.
- [87] M. Widom, W. P. Huhn, S. Maiti, and W. Steurer. Hybrid Monte Carlo/molecular dynamics simulation of a refractory metal high entropy alloy. *Metall. Mater. Trans. A*, 45(1):196–200, January 2014.
- [88] W. P. Huhn and M. Widom. Prediction of A2 to B2 phase transition in the high entropy alloy MoNbTaW. *JOM*, 65(12):1772–1779, December 2013.
- [89] J.-W. Yeh, S.-K. Chen, S.-J. Lin, J.-Y. Gan, T.-S. Chin, T.-T. Shun, C.-H. Tsau, and S.-Y. Chang. Nanostructured high-entropy alloys with multiple principal elements: Novel alloy design concepts and outcomes. *Adv. Eng. Mater.*, 6(5):299–303, May 2004.
- [90] R. Kozak and W. Steurer. High-entropy alloys - a critical review. *Intermetallics*, submitted, 2013.
- [91] J.-W. Yeh, S.-K. Chen, J.Y. Gan, S.-J. Lin, T.-S. Chin, T.-T. Shun, C.-H. Tsau, and S.-Y. Chang. Formation of simple crystal structures in Cu-Co-Ni-Cr-Al-Fe-Ti-V alloys with multiprincipal metallic elements. *Metall. Mater. Trans. A*, 35A:2533–2536, August 2004.
- [92] S. Singh, N. Wanderka, B. S. Murty, U. Glatzel, and J. Banhart. Decomposition in multi-component AlCoCrCuFeNi high-entropy alloy. *Acta Mater.*, 59:182–90, 2011.
- [93] M. R. Chen, S. J. Lin, J. W. Yeh, S. K. Chen, Y. S. Huang, and C. P. Tu. Microstructure and properties of Al_{0.5}CoCrCuFeNiTi_x (x=0-2.0) high-entropy alloys. *Mat. Trans*, 47:1395–401, 2006.

- [94] Y. Zhang, T. T. Zuo, Y. Q. Cheng, and P. K. Liaw. High-entropy alloys with high saturation magnetization, electrical resistivity, and malleability. *Sci. Rep.*, 3:1455, 2013.
- [95] S. Guo, C. Ng, J. Lu, and C. T. Liu. Effect of valence electron concentration on stability of fcc or bcc phase in high entropy alloys. *J. Appl. Phys.*, 109:103505, 2011.
- [96] X. Yang and Y. Zhang. Prediction of high-entropy stabilized solid-solution in multi-component alloys. *Mat. Chem. and Phys.*, 132:233–8, 2012.
- [97] Y. Zhang, X. Yang, and P. K. Liaw. Alloy design and properties optimization of high-entropy alloys. *JOM*, 64:830–8, 2012.
- [98] F. Otto, Y. Yang, H. Bei, and E. P. George. Relative effects of enthalpy and entropy on the phase stability of equiatomic high-entropy alloys. *Acta Mater.*, 61:2628–38, 2013.
- [99] F. Y. Tian, L. K. Varga, N. Chen, L. Delczeg, and L. Vitos. Ab initio investigation of high-entropy alloys of 3d elements. *Phys. Rev. B*, 87:075144, 2013.
- [100] O. N. Senkov, G. B. Wilks, D. B. Miracle, C. P. Chuang, and P. K. Liaw. Refractory high-entropy alloys. *Intermetallics*, 18(9):17581765, September 2010.
- [101] O. N. Senkov, G. B. Wilks, J. M. Scott, and D. B. Miracle. Mechanical properties of $\text{Nb}_{25}\text{Mo}_{25}\text{Ta}_{25}\text{W}_{25}$ and $\text{V}_{20}\text{Nb}_{20}\text{Mo}_{20}\text{Ta}_{20}\text{W}_{20}$ refractory high entropy alloys. *Intermetallics*, 19(5):698–706, May 2011.
- [102] Y. J. Zhou, Y. Zhang, Y. L. Wang, and G. L. Chen. Solid solution alloys of AlCoCrFeNiTi with excellent room-temperature mechanical properties. *Appl. Phys. Lett.*, 90(18):181904, 2007.
- [103] P. Villars. A three-dimensional structural stability diagram for 998 binary AB intermetallic compounds. *J. Less-Common Met.*, 92(2):215–238, August 1983.

- [104] D. G. Pettifor. Structure maps for pseudobinary and ternary phases. *Materials Science and Technology*, 4:675–91, 1988.
- [105] A. van de Walle and G. Ceder. Automating first-principles phase diagram calculations. *J. Phase Equilib.*, 23(4):348–359, 2002.
- [106] A. van de Walle and M. Asta. Self-driven lattice-model Monte Carlo simulations of alloy thermodynamic properties and phase diagrams. *Model. Simul. Mater. Sc.*, 10(5):521–538, 2002.
- [107] A. van de Walle, M. Asta, and G. Ceder. The alloy theoretic automated toolkit: A user guide. *CALPHAD*, 26(4):539–553, December 2002.
- [108] A. van de Walle. Multicomponent multisublattice alloys, nonconfigurational entropy and other additions to the Alloy Theoretic Automated Toolkit. *CALPHAD*, 33(2):266–278, June 2009.
- [109] G. L. W. Hart, V. Blum, M. J. Malorski, and A. Zunger. Evolutionary approach for determining first-principles Hamiltonians. *Nat. Mater.*, 4:391–394, 2005.
- [110] V. Blum and A. Zunger. Prediction of ordered structures in the bcc binary systems of Mo, Nb, Ta, and W from first-principles search of approximately 3,000,000 possible configurations. *Phys. Rev. B*, 72:020104, July 2005.
- [111] L. I. van Torne and G. Thomas. Structure and mechanical properties of Ta-Mo alloy single crystals. *Acta Metall. Mater.*, 14:621–635, May 1966.
- [112] S. Curtarolo, D. Morgan, and G. Ceder. Accuracy of ab initio methods in predicting the crystal structures of metals: A review of 80 binary alloys. *CALPHAD*, 29(3):163–211, September 2005.
- [113] V. Blum and A. Zunger. Structural complexity in binary bcc ground states: The case of bcc Mo-Ta. *Phys. Rev. B*, 69:020103, January 2004.

- [114] P. E. A. Turchi, V. Drchal, J. Kudrnovsky, C. Colinet, L. Kaufman, and Z-K. Liu. Application of ab initio and CALPHAD thermodynamics to Mo-Ta-W alloys. *Phys. Rev. B.*, 71(9):094206, March 2005.
- [115] S. C. Singhal and W. L. Worrell. High temperature thermodynamic properties of solid Ta-W alloys. *Metall. Trans.*, 4:895–898, April 1973.
- [116] P. E. A. Turchi, A. Gonis, V. Drchal, and J. Kudrnovský. First-principles study of stability and local order in substitutional Ta-W alloys. *Phys. Rev. B*, 64:085112, August 2001.
- [117] K. Masuda-Jindo, V. V. Hung, N. T. Hoa, and P. E. A. Turchi. First principles calculations of thermodynamic and mechanical properties of high temperature bcc Ta-W and Mo-Ta alloys. *J. Alloy. Compd.*, 452(1):127–132, March 2008.
- [118] E. C. Neyts and A. Bogaerts. Combining molecular dynamics with Monte Carlo simulations: implementations and applications. *Theor. Chem. Acc.*, 132:1–12, 2013.
- [119] M. F. de Grosso, G. Bozzolo, and H. O. Mosca. Modeling of high entropy alloys of refractory elements. *Physica B*, 407:3285–7, 2012.
- [120] G. Bozzolo, J. Ferrante, and J. R. Smith. Method for calculating alloy energetics. *Phys. Rev. B*, 45:493–6, 1992.
- [121] K. Masuda-Jindo, V. V. Hung, and P. E. A. Turchi. Thermodynamic properties and phase diagram by the statistical moment and cluster variation methods: Application to pure metals and Ta-W alloys. *Met. Mat. Trans. A*, 37:3403–9, 2006.
- [122] M. F. del Grosso, G. Bozzolo, and H. O. Mosca. Modeling of high entropy alloys of refractory elements. *Physica B*, 407:3285–3287, 2012.

- [123] M. F. del Grosso, G. Bozzolo, and H. O. Mosca. Determination of the transition to the high entropy regime for alloys of refractory elements. *J. Alloy. Compd.*, 534:25–31, 2012.
- [124] Y. Zhang, Y. J. Zhou, J. P. Lin, G. L. Chen, and P. K. Liaw. Solid-solution phase formation rules for multi-component alloys. *Adv. Eng. Mater.*, 10(6):534–538, 2008.
- [125] W. P. Huhn, M. Widom, A. M. Cheung, G. J. Shiflet, S. J. Poon, and J. Lewandowski. First principles calculation of elastic moduli of early-late transition metal alloys. *Phys. Rev. B*, 2014, in press.
- [126] W. Klement Jr, R. H. Willens, and P. Duwez. Non-crystalline structure in solidified gold-silicon alloys. *Nature*, 187:869–870, September 1960.
- [127] D. C. Hofmann. Bulk metallic glasses and their composites: A brief history of diverging fields. *J. Mater.*, 2013:517904, 2013.
- [128] D. Turnbull. Under what conditions can a glass be formed? *Contemp. Phys.*, 10(5):473–488, 1969.
- [129] Jörg F. Löffler. Bulk metallic glasses. *Intermetallics*, 11:529–540, 2003.
- [130] T. Zhang, A. Inoue, and T. Masumoto. Amorphous Zr-Al-TM (TM=Co,Ni,Cu) alloys with significant supercooled liquid region of over 100 K. *Mater. Trans., JIM*, 32(11):1005–1010, 1991.
- [131] A. Peker and W. L. Johnson. A highly processable metallic glass: $Zr_{41.2}Ti_{13.8}Cu_{12.5}Ni_{10.0}Be_{22.5}$. *Appl. Phys. Lett*, 63(17):2342–2344, October 1993.
- [132] M. Telford. The case for bulk metallic glass. *Materials Today*, 7(3):36 – 43, 2004.

- [133] F. Spaepen. A microscopic mechanism for steady state inhomogeneous flow in metallic glasses. *Acta Metall.*, 25:407–415, 1977.
- [134] A. S. Argon. Plastic deformation in metallic glasses. *Acta Metall.*, 27:47–58, 1979.
- [135] P. Scahl, D. A. Weitz, and F. Spaepen. Structural rearrangements that govern flow in colloidal glasses. *Science*, 318:1895–1899, December 2007.
- [136] J. S. Langer. Shear-transformation-zone theory of plastic deformation near the glass transition. *Phys. Rev. E*, 77:021502, February 2008.
- [137] J. Schroers and W. L. Johnson. Ductile bulk metallic glass. *Phys. Rev. Lett.*, 93:255506, December 2004.
- [138] S. J. Poon, A. Zhu, and G. J. Shiflet. Poisson’s ratio and intrinsic plasticity of metallic glasses. *Appl. Phys. Lett.*, 92(26):261902, June 2008.
- [139] H. S. Chen, J. T. Krause, and E. Coleman. Elastic constants, hardness, and their implications to flow properties of metallic glasses. *J. Non-Cryst. Solids*, 18:157–171, 1975.
- [140] J. J. Lewandowski, W. H. Wang, and A. L. Greer. Intrinsic plasticity or brittleness of metallic glasses. *Philos. Mag. Lett.*, 85(2):77–87, February 2005.
- [141] W. H. Wang. The elastic properties, elastic models and elastic perspectives of metallic glasses. *Prog. Mater. Sci.*, 57:487–656, 2012.
- [142] T. Egami. Universal criterion for metallic glass formation. *Mat. Sci. Eng. A*, 2260228:261–267, 1997.
- [143] T. Egami, S. J. Poon, Z. Zhang, and V. Keppens. Glass transition in metallic glasses: A microscopic model of topological fluctuations in the bonding network. *Phys. Rev. B*, 76:024203, July 2007.

- [144] W. H. Wang. Correlations between elastic moduli and properties in bulk metallic glasses. *J. Appl. Phys.*, 99:093506, 2006.
- [145] J. Q. Wang and H. Y. Bai. High-pressure behaviors of Yb-based bulk metallic glass. *Scripta Mater.*, 61:453–456, 2009.
- [146] W. L. Johnson and K. Samwer. A universal criterion for plastic yielding of metallic glasses with a $(T/T_g)^{2/3}$ temperature dependence. *Phys. Rev. Lett.*, 95:195501, November 2005.
- [147] F. C. Frank and J. S. Kasper. Complex alloy structures regarded as sphere packings. I. Definitions and basic principles. *Acta Cryst.*, 11:184–190, 1958.
- [148] F. C. Frank and J. S. Kasper. Complex alloy structures regarded as sphere packings. II. Analysis and classification of representative structures. *Acta Cryst.*, 12:483–499, 1959.
- [149] A. K. Sinha. *Topologically Close-Packed Structures of Transition Metal Alloys*. Pergamon Press, 1972.
- [150] L. D. Landau and E. M. Lifshitz. *Theory of Elasticity*, volume 7 of *Course of Theoretical Physics*. Butterworth-Heinemann, 3rd edition, 1986.
- [151] S. F. Pugh. Relations between the elastic moduli and the plastic properties of polycrystalline pure metals. *Philos. Mag.*, 45(367):823–843, August 1954.
- [152] X. J. Gu, A. G. McDermott, S. J. Poon, and G. J. Shiflet. Critical Poisson’s ratio for plasticity in Fe-Mo-C-B-Ln bulk amorphous steel. *Appl. Phys. Lett.*, 88(21):211905, May 2006.
- [153] A. Inoue, B. Shen, H. Koshiba, H. Kato, and A. R. Yavari. Cobalt-based bulk glassy alloy with ultrahigh strength and soft magnetic properties. *Nature Mater.*, 2:661–663, October 2003.

- [154] M. Ohtsuki, R. Tamura, S. Takeuchi, S. Yoda, and T. Ohmura. Hard metallic glass of tungsten-based alloy. *Appl. Phys. Lett.*, 84(24):4911–4913, June 2004.
- [155] J. F. Nye. *Physical Properties of Crystals: Their Representation by Tensors and Matrices*. Oxford Science Publications, 2nd edition, 1985.
- [156] R. Zeller and P. H. Dederichs. Elastic constants of polycrystals. *Phys. Status Solidi B*, 55:831–842, 1973.
- [157] R. Hill. The elastic behaviour of a crystalline aggregate. *Proc. Phys. Soc. A*, 65(5):349–354, May 1952.
- [158] C. W. Nan. Physics of inhomogeneous inorganic materials. *Prog. Mater. Sci.*, 37:1–116, 1993.
- [159] Y. Zhang and A. L. Greer. Correlations for predicting plasticity or brittleness of metallic glasses. *J. Alloys Compd.*, 434-435:2–5, 2007.
- [160] B. Zhang, R. J. Wang, D. Q. Zhao, M. X. Pan, and W. H. Wang. Superior glass-forming ability through microalloying in cerium-based alloys. *Phys. Rev. B*, 73:092201, March 2006.
- [161] M. Mihalkovic and M. Widom. Ab-initio calculations of cohesive energies of Fe-based glass-forming alloys. *Phys. Rev. B*, 70:144107, 2004.
- [162] R. Dronskowski and P. E. Blöchl. Crystal Orbital Hamilton Populations (COHP). energy-resolved visualization of chemical bonding in solids based on density-functional calculations. *J. Phys. Chem.*, 97(33):8617–8624, 1993.
- [163] O. Jepsen and O. K. Andersen. Calculated electronic structure of the sandwiched metals LaI_2 and CeI_2 : Application of new LMTO techniques. *Z. Phys. B*, 97:35–47, 1995.

- [164] X. W. Fang, C. Z. Wang, S. G. Hao, M. J. Kramer, Y. X. Yao, M. I. Mendeleev, Z. J. Ding, R. E. Napolitano, and K. M. Ho. Spatially resolved distribution function and the medium-range order in metallic liquid and glass. *Scientific Reports*, 1:194, 2011.
- [165] D. B. Miracle. A physical model for metallic glass structures: An introduction and update. *JOM*, 64(7):846–855, 2012.
- [166] J. M. Walsh and Jr. M. J. Donachie. On a new intermetallic phase in the nickel-tungsten system. *Met. Trans.*, 4:2854–2855, December 1973.
- [167] D. Tromans. Elastic anisotropy of hcp metal crystals and polycrystals. *IJRRAS*, 6(4):462–483, March 2011.
- [168] X. F. Liu, R. J. Wang, and W. H. Wang. Poissons ratio of metallic glasses under pressure and low temperature. *Scripta Mater.*, 62:254–257, 2010.
- [169] B. Gleeson. Alloy degradation under oxidizing-sulfidizing conditions at elevated temperatures. *Mater. Res.*, 7(1):61–69, 2004.
- [170] W. Betteridge and J. Hope. The separation of hydrogen from gas mixtures: A process of absorption and desorption by palladium. *Platinum Met. Rev.*, 19(2):50–59, 1975.
- [171] J. Shu, B. P. A. Grandjean, A. van Neste, and S. Kaliaguine. Catalytic palladium-based membrane reactors: A review. *Can. J. Chem. Eng.*, 69:1036–1060, October 1991.
- [172] T. L. Ward and T. Dao. Model of hydrogen permeation behavior in palladium membranes. *J. Membr. Sci.*, 153:211–231, 1999.
- [173] A. Züttel. Materials for hydrogen storage. *Mater. Today*, pages 24–33, September 2003.

- [174] L. Schlapbach and A. Züttel. Hydrogen-storage materials for mobile applications. *Nature*, 414:353–358, November 2001.
- [175] R. C. Hurlbert and J. O. Konecny. Diffusion of hydrogen through palladium. *J. Chem. Phys.*, 34(2):655–658, February 1961.
- [176] O. Iyoha, R. Enick, R. Killmeyer, and B. Morreale. The influence of hydrogen sulfide-to-hydrogen partial pressure ratio on the sulfidization of Pd and 70 mol% Pd-Cu membranes. *J. Membr. Sci.*, 305:77–92, November 2007.
- [177] B. D. Morreale, B. H. Howard, O. Iyoha, R. M. Enick, C. Ling, and D. S. Scholl. Experimental and computational prediction of the hydrogen transport properties of Pd₄S. *Ind. Eng. Chem. Res.*, 46(19):6313–6319, 2007.
- [178] C.-H. Chen and Y. H. Ma. The effect of H₂S on the performance of Pd and Pd/Au composite membrane. *J. Membr. Sci.*, 362:535–544, 2010.
- [179] D. T. Hughes and I. R. Harris. A comparative study of hydrogen permeabilities and solubilities in some palladium solid solution alloys. *J. Less-Common Met.*, 61:P9–P21, 1978.
- [180] S. Uemiya, T. Matsuda, and E. Kikuchi. Hydrogen permeable palladium-silver alloy membrane supported on porous ceramics. *J. Membr. Sci.*, 56:315–325, 1991.
- [181] J. K. Ali, E. J. Newson, and D. W. T. Rippin. Deactivation and regeneration of Pd-Ag membranes for dehydrogenation reactions. *J. Membr. Sci.*, 89:171–184, 1994.
- [182] H. Amandusson, L.-G. Ekedahl, and H. Dannelun. Hydrogen permeation through surface modified Pd and PdAg membranes. *J. Membr. Sci.*, 193:35–47, 2001.

- [183] J. Piper. Diffusion of hydrogen in copper-palladium alloys. *J. Appl. Phys.*, 37(2):715–721, February 1966.
- [184] B. H. Howard, R. P. Killmeyer, K. S. Rotherberger, A. V. Cugini, B. D. Morreale, R. M. Enick, and F. Bustamente. Hydrogen permeance of palladium-copper alloy membranes over a wide range of temperatures and pressures. *J. Membr. Sci.*, 241:207–218, 2004.
- [185] A. Kulprathipanja, G.-O. Alptekin, J. L. Falconer, and J. D. Way. Pd and Pd-Cu membranes: inhibition of H₂ permeation by H₂S. *J. Membr. Sci.*, 254:49–62, 2005.
- [186] C. P. O’Brien, B. H. Howard, J. B. Miller, B. D. Morreale, and A. J. Gellman. Inhibition of hydrogen transport through Pd and Pd₄₇Cu₅₃ membranes by H₂S at 350 C. *J. Membr. Sci.*, 349:380–384, March 2010.
- [187] B. D. Morreale, M. V. Ciocco, B. H. Howard, R. P. Killmeyer, A. V. Cugini, and R. M. Enick. Effect of hydrogen-sulfide on the hydrogen permeance of palladiumcopper alloys at elevated temperatures. *J. Membr. Sci.*, 241:219–224, 2004.
- [188] D. L. McKinley. Metal alloy for hydrogen separation and purification, November 1967.
- [189] D. R. Alfonso, A. V. Cugini, and D. S. Scholl. Density functional theory studies of sulfur binding on Pd, Cu and Ag and their alloys. *Surf. Sci.*, 546:12–26, 2003.
- [190] P. Kamakoti, B. D. Morreale, M. V. Ciocco, B. H. Howard, R. P. Killmeyer, A. V. Cugini, and D. S. Scholl. Prediction of hydrogen flux through sulfur-tolerant binary alloy membranes. *Science*, 307:569–573, January 2005.
- [191] D. S. Scholl. Using density functional theory to study hydrogen diffusion in metals: A brief overview. *J. Alloys. Compd.*, 446-447:462–468, 2007.

- [192] S. Karup-Møller and E. Makovicky. The phase system Cu-Pd-S at 900, 725, 500, and 400 C. *N. Jb. Miner. Mh.*, 12:551–567, December 1999.
- [193] P. R. Subramanian and D. E. Laughlin. Cu-Pd (copper-palladium). *J. Phase Equilib.*, 12(2):231–243, 1991.
- [194] M. Li, Z. Du, C. Guo, and C. Li. A thermodynamic modeling of the CuPd system. *CALPHAD*, 32(2):439–446, June 2008.
- [195] S. Baärthlein, E. Winning, G. L. W. Hart, and S. Müller. Stability and instability of long-period superstructures in binary Cu-Pd alloys: A first principles study. *Acta Mater.*, 57:1660–1665, 2009.
- [196] G. Ceder, D. de Fontaine, H. Dreysse, D. M. Nicholson, G. M. Stocks, and B. L. Gyorffy. Ab initio study of the Cu-Pd one-dimensional long period superstructure phase diagram. *Acta Metall. Mater.*, 38(11):2299–2308, February 1990.
- [197] B. J. Lee, B. Sundman, S. I. Kim, and K. G. Chin. Thermodynamic calculations on the stability of Cu₂S in low carbon steels. *ISIJ Int.*, 47:163–171, 2007.
- [198] H. Okamoto. Pd-S (palladium-sulfur). *J. Phase Equilib*, 13:106–107, 1992.
- [199] R. Hu, M. C. Gao, Ó. N. Doğan, P. King, and M. Widom. Thermodynamic modeling of the Pd-S system supported by first-principles calculations. *CALPHAD*, 34(3):324–331, September 2010.
- [200] J. P. Perdew, A. Ruzsinszky, G. I. Csonka, O. A. Vydrov, G. E. Scuseria, L. A. Constantin, X. Zhou, and K. Burke. Restoring the density-gradient expansion for exchange in solids and surfaces. *Phys. Rev. Lett.*, April 2008.
- [201] E. A. Owen and E. L. Yates. Precision measurements of crystal parameters. *Philos. Mag*, 15:472–487, 1933.

- [202] I. R. Harris, M. Norman, and W. E. Gardner. The electronic state of cerium in some $\text{CeRh}_3\text{-xPdx}$ alloys. *J. Less-Common Met.*, 29:299–309, November 1972.
- [203] K. Okamura. Lattice modulation in the long period ordered alloys studied by x-ray diffraction. III. Cu_3Pd (α''). *J. Phys. Soc. Jpn*, 28:1005–1014, April 1970.
- [204] H. T. Evans Jr. Djureite ($\text{Cu}_{1.94}\text{S}$) and low chalcocite (Cu_2S): New crystal structure studies. *Science*, 203(4378):356–358, January 1979.
- [205] M. Leon, N. Terao, and F. Rueda. On the phase transition of chalcocite Cu_2S thin films. *Phys. Status Solidi A*, 67:K11–K14, September 1981.
- [206] H. Fjellvåg, F. Grnvold, S. Stlen, A. F. Andresen, R. Müller-Käfer, and A. Simon. Low-temperature structural distortion in CuS . *Z. Krist.*, 184(1-2):111–121, January 1988.
- [207] H. E. King and C. T. Prewitt. Structure and symmetry of CuS_2 (pyrite structure). *Am. Mineral.*, 64(11-12):1265–1271, December 1979.
- [208] F. Grønvold and E. Røst. The crystal structures of Pd_4Se and Pd_4S . *Acta Cryst.*, 15:11–13, January 1962.
- [209] P. Matkovič, M. El-Boragy, and K. Schubert. Kristallstruktur von Pd_{16}S_7 . *J. Less-Common Met.*, 50:165–176, 1976.
- [210] T. F. Gaskell. The structure of braggite and palladium sulfite. *Z. Kristallogr.*, 96:203–213, 1937.
- [211] F. Grønvold and E. Røst. The crystal structure of PdSe_2 and PdS_2 . *Acta Cryst.*, 10:329–331, April 1957.
- [212] A. Janosi. La structure du sulfure cuivreux quadratique. *Acta Cryst.*, 17:311–312, March 1964.

- [213] M. Guymont and D. Gratias. On the stability of periodically antiphased alloys. *Phys. Status Solidi A*, 36:329–334, July 1976.
- [214] E. Røst. The crystal structure of the high-temperature phase Pd₃S. *Acta Chem. Scand.*, 22(3):819–826, 1968.
- [215] A. Soutter, A. Colson, and J. Hertz. Etude cristallographique des phases ordonnés à grande distance et particulièrement des structures antiphases monopériodiques et bipériodiques présentes dans les alliages binaires cuivre-palladium. *Mem. Etud. Sci. Rev. Metall.*, 68:575–591, 1971.
- [216] A. H. Geisler and J. B. Newkirk. Ordering reaction of the Cu₄Pd alloy. *J. Met.*, 6:1076–1082, 1954.
- [217] K. Yamamoto and S. Kashida. X-ray study of the average structures of Cu₂Se and Cu_{1.8}S in the room temperature and the high temperature phases. *J. Solid State Chem.*, 93:202–211, July 1991.
- [218] E. Bruno, B. Ginatempo, and E. S. Giuliano. Fermi surface incommensurate nestings and phase equilibria in Cu-Pd alloys. *Phys. Rev. B*, 63:174107, April 2001.
- [219] C. Wolverton. Crystal structure and stability of complex precipitate phases in Al-Cu-Mg-(Si) and Al-Zn-Mg alloys. *Acta Mater.*, 49(16):3129–3142, 2001.
- [220] J. Friedel. Do metallic quasicrystals and associated Frank and Kasper phases follow the Hume Rothery rules? *Helv. Phys. Acta*, 61:538–555, 1988.
- [221] Jr. M. W. Chase. NIST-JANAF Thermochemical Tables. *J. Phys. Chem. Ref. Data*, 9:1–1951, 1998.
- [222] J. R. Taylor. Phase relationships and thermodynamic properties of the Pd-S system. *Met. Trans. B*, 16B:143–148, March 1985.

- [223] Koun Shirai and S. Emura. Lattice vibrations of boron carbide. *J. Solid State Chem.*, 154:20–5, 2000.
- [224] P. Yu and H. Y. Bai. Poisson’s ratio and plasticity in CuZrAl bulk metallic glasses. *Mater. Sci. Eng. A*, 485:1–4, 2008.
- [225] I.-C. Choi, Y. Zhao, B.-G. Yoo, Y.-J. Kim, J.-Y. Suh, U. Ramamurty, and J.-I. Jang. Estimation of the shear transformation zone size in a bulk metallic glass through statistical analysis of the first pop-in stresses during spherical nanoindentation. *Scripta Mater.*, 66:923–926, 2012.